

CONFRONTING ASTROPHYSICAL
UNCERTAINTIES IN THE DIRECT DETECTION
OF DARK MATTER

BRADLEY J. KAVANAGH

Thesis submitted to the University of Nottingham for the degree of Doctor of
Philosophy

June 27, 2014

Abstract

The identification of dark matter (DM) by direct detection experiments has the potential to shed light on particle physics beyond the Standard Model. However, uncertainties in the DM speed distribution $f_1(v)$ may lead to biased reconstructions of particle physics parameters, such as the DM mass m_χ and interaction cross sections, σ_p^{SI} and σ_p^{SD} . In this work, we aim to determine whether these parameters can be determined from future direct detection data without any prior assumptions about $f_1(v)$.

We study previous methods for parametrising $f_1(v)$ and show that they may still lead to biased reconstructions of the DM parameters. We propose an alternative smooth, general parametrisation, which involves writing the *logarithm* of the speed distribution as a polynomial in v . We test this method using future direct detection mock data sets and show that it allows an unbiased reconstruction of the DM mass over a range of particle physics and astrophysics parameters. However, the unknown fraction of DM particles with speeds below the energy thresholds of the experiments means that only a lower bound can be placed on the interaction cross sections.

By introducing data from neutrino telescope experiments, such as IceCube, this degeneracy in the cross section can be broken, as these experiments probe the low speed DM population. Combined with our parametrisation method, this allows a robust reconstruction of the DM mass and cross sections without relying on any assumptions about the DM speed distribution. The function $f_1(v)$ itself can also be reconstructed, allowing us to probe the phase space of the Milky Way.

Finally, we propose a method of extending this parametrisation to directional data, which should allow even more information to be extracted from future experiments without the need for astrophysical assumptions.

Published work

Parts of the work described in this thesis have appeared in the following published works:

1. *Parametrizing the local dark matter speed distribution: a detailed analysis*
B. J. Kavanagh
Submitted to Phys. Rev. D, arXiv:1312.1852
2. *WIMP physics with ensembles of direct-detection experiments*
A. H. G. Peter, V. Gluscevic, A. M. Green, **B. J. Kavanagh**, S. K. Lee
Submitted to Phys. Dark Universe, arXiv:1310.7039
3. *Model independent determination of the dark matter mass from direct detection*
B. J. Kavanagh and A. M. Green
Phys. Rev. Lett. 111, 031302 (2013), arXiv:1303.6868
4. *Improved determination of the WIMP mass from direct detection data*
B. J. Kavanagh and A. M. Green
Phys. Rev. D 86, 065027 (2012), arXiv:1207.2039

Acknowledgements

*This is dedicated to all of those with big egos
Never fakin', we get the dough and live legal*

—Dr. Dre

Contents

Contents	iv
List of Figures	vii
List of Tables	xii
1 Introduction	1
1.1 Evidence for dark matter	2
1.2 Problems with dark matter	7
1.3 Alternatives to dark matter	8
1.4 Properties of dark matter	9
1.5 Particle dark matter candidates	13
1.6 Detection of dark matter	15
2 Direct detection of dark matter	21
2.1 Introduction	21
2.2 Direct detection formalism	22
2.3 Direct detection experiments	31
2.4 Uncertainties	36
2.5 Conclusion	46
3 Parametrising the WIMP distribution	48
3.1 Attempts to address the uncertainties in $f_1(v)$	49
3.2 Binned speed distribution	52
3.3 Momentum parametrisation for a single experiment	61
3.4 Momentum parametrisation for several experiments	64
3.5 Discussion	76
3.6 Conclusions	78
4 A polynomial parametrisation of the speed distribution	80

4.1	Parametrising the logarithm of $f(v)$	81
4.2	Experiments and benchmark parameters	83
4.3	Results	87
4.4	Varying m_χ	92
4.5	Statistical properties	95
4.6	Reconstructing $f_1(v)$	98
4.7	Discussion	104
4.8	Conclusions	104
5	Neutrino telescopes	106
5.1	Neutrino telescope formalism	107
5.2	Complementarity with direct detection	113
5.3	Benchmarks and experiments	115
5.4	Reconstructions without IceCube	120
5.5	Reconstructions with IceCube	123
5.6	Reconstructing $f(v)$	126
5.7	Discussion	129
5.8	Conclusions	131
6	Directional detection	133
6.1	Directional event rate	134
6.2	Directional experiments	137
6.3	Reconstructing the velocity distribution	140
6.4	Discretising the velocity distribution	141
6.5	Discussion	151
6.6	Conclusion	153
7	Conclusions	155
A	Parameter Reconstruction	160
A.1	Frequentist statistics	161
A.2	Bayesian statistics	163
A.3	Exploring the parameter space	166
A.4	Likelihood examples	169
B	The discrete Radon transform	171
B.1	$N = 2$ discretisation	173
B.2	$N = 3$ discretisation	175

Bibliography	177
--------------	-----

List of Figures

1.1	CMB anisotropies measured by the Planck experiment	4
1.2	Schematic illustration of galaxy rotation curves	6
1.3	Schematic dark matter interactions	16
2.1	Examples of spin-independent event spectra for direct detection experiments	29
2.2	Comparison of spin-dependent and spin-independent rates for a Xenon experiment	30
2.3	Examples of dark matter speed distributions	44
2.4	Biased reconstruction of WIMP parameters	45
3.1	Binned approximation to the SHM	54
3.2	Range of accessible WIMP speeds for mock direct detection experiments	56
3.3	Distribution of reconstructed WIMP masses using the binned speed parametrisation	58
3.4	Reconstructed speed distribution and mean inverse speed using the binned speed parametrisation	59
3.5	Reconstructed mean inverse speed for the SuperCDMS-like experiment	60
3.6	Distribution of the reconstructed scale parameter, D_{rec} , for the Argon experiment using the momentum parametrisation	64
3.7	Reconstructed momentum distribution for a single Argon experiment using a benchmark of a 50 GeV WIMP and the SHM .	65
3.8	Comparison of WIMP masses reconstructed using the binned speed and momentum parametrisations	68
3.9	Reconstructed momentum distribution from all three mock experiments using a benchmark of a 50 GeV WIMP and the SHM	69

3.10	Distribution of reconstructed masses using the binned momentum distribution for a 50 GeV WIMP with SHM, SHM+DD and VL2 distribution functions	70
3.11	Distribution of reconstructed masses using the binned momentum distribution for a 100 GeV WIMP with SHM, SHM+DD and VL2 distribution functions	71
3.12	Reconstructed speed distribution from all three mock experiments using the momentum parametrisation method for a 50 GeV WIMP and SHM distribution function.	73
3.13	As Fig. 3.12 for a 100 GeV WIMP with SHM+DD distribution function using 5 momentum bins (left panels) and 7 momentum bins (right panels). Reproduced from Ref. [1].	74
3.14	Distribution of reconstructed masses using the 7-bin momentum method for a SHM+DD benchmark distribution.	75
3.15	Reconstructed speed distribution from all three mock experiments for a 50 GeV WIMP with SHM distribution. All three benchmark distributions are shown for comparison.	76
4.1	Examples of $\ln f(v)$ polynomial distributions	83
4.2	Several benchmark speed distributions used to test the polynomial $\ln f(v)$ method.	86
4.3	Reconstruction of the WIMP mass and cross section using the polynomial $\ln f(v)$ parametrisation	88
4.4	Benchmark speed distributions used in Sec. 4.3.1 to test the performance of the parametrization as a function of the number and type of basis functions. Reproduced from Ref. [2].	89
4.5	Bayesian information criterion and reconstructed WIMP mass as a function of the number of basis functions for a 50 GeV WIMP with ‘bump’ distribution function	91
4.6	As Fig. 4.5 but for an underlying ‘double-peak’ distribution function. Reproduced from Ref. [2].	91
4.7	Time taken for the reconstruction of the ‘bump’ benchmark as a function of number of basis functions for both the Chebyshev and Legendre bases.	93
4.8	Reconstructed WIMP mass as a function of input WIMP mass for ideal experiments	94

4.9	Reconstructed WIMP mass as a function of input WIMP mass for experiments including the effects of finite backgrounds and energy resolution	95
4.10	Distribution of the reconstructed mass using a 50 GeV WIMP and SHM, SHM+DD and Lisanti et al. distribution functions . .	97
4.11	Reconstructed speed distribution for a single realisation of data using the polynomial $\ln f(v)$ parametrisation	99
4.12	Reconstructed speed distribution for a single realisation of data using the polynomial $\ln f(v)$ parametrisation, normalised to unity above the threshold speed of the experiments	100
4.13	Mean reconstructed values of the rescaled mean inverse speed over 250 realisations for a 50 GeV WIMP with SHM distribution function	101
4.14	Rescaled mean inverse speed for a single realisation of data for a 50 GeV WIMP with SHM distribution function, showing several benchmark speed distributions for comparison	102
4.15	As Fig. 4.14, but using as input a Lisanti et al. speed distribution and an exposure time which is 2.5 times longer. Reproduced from Ref. [2].	103
4.16	As Fig. 4.15, but focusing on the region around $v \sim 400 \text{ km s}^{-1}$. .	104
5.1	Geometry of WIMPs impinging on the Sun	108
5.2	Speed sensitivity ranges of solar capture and direct detection experiments as a function of WIMP mass	114
5.3	2-dimensional profile likelihood for $(m_\chi, \sigma_p^{\text{SI}})$ (left column), $(m_\chi, \sigma_p^{\text{SD}})$ (central column) and $(\sigma_p^{\text{SI}}, \sigma_p^{\text{SD}})$ (right column), obtained using the polynomial $\ln f(v)$ parametrisation with direct detection data only. The shaded area gives the value of the profile likelihood, while the blue contours define the 68% and 95% confidence regions for the particle physics parameters. The 4 rows (from top to bottom) correspond to the 4 benchmarks A, B, C and D. The dashed red lines show the position of the benchmark values from Tab. 5.2 while the green triangle gives the best fit values.	122
5.4	As for Fig. 5.3 but including IceCube mock data. <i>I might over-lay the DD-only contours on here for comparison...</i>	125

5.5	Profile likelihood for the effective cross section σ_{eff} of Germanium (defined in Eq. 5.21) with and without IceCube data for benchmark C. The vertical red dashed line corresponds to the benchmark value while the the vertical dotted black lines correspond to the limits of the 68% and 95% confidence intervals for the case <i>with</i> IceCube data.	126
5.6	Reconstructed 68% and 95% confidence intervals (grey bands) for the directionally-averaged speed distribution $f(v)$ using only direct detection data. We show the SHM distribution (solid blue) and SHM+DD distributions (dashed green). Also shown in dashed red is the best fit form for $f(v)$. We note that for benchmark B, the true distribution is the SHM+DD.	127
5.7	As Fig. 5.6, but for all 4 benchmarks, including data from both direct detection <i>and</i> IceCube experiments. We show the SHM distribution (solid blue) and SHM+DD distributions (dashed green). Also shown in dashed red is the best fit form for $f(v)$. We note that for benchmarks A and C, the true distribution is the SHM, while for benchmarks B and D, the true distribution is the SHM+DD.	128
6.1	Illustration of DM-nucleus scattering	134
6.2	Radon transform examples	138
6.3	Examples of discretised velocity distributions	143
6.4	Exact and approximate integrated Radon transforms for $N = 2$ components in the SHM	147
6.5	Exact and approximate integrated Radon transforms for $N = 2$ components for a stream distribution function	147
6.6	Exact and approximate integrated Radon transforms for $N = 3$ components in the SHM	149
6.7	Exact and approximate integrated Radon transforms for $N = 3$ components for a stream distribution function	150
6.8	True and approximate folded Radon transforms for $N = 3$ components in the SHM	151
A.1	Likelihood-based parameter inference	163
A.2	Posterior-based parameter inference	166

- B.1 Integration limits for Eq. B.14 as a function of $\cos \theta$, for a fixed value of β . The value $\cos \theta' = 0$ is denoted with a horizontal dashed line, while $\cos \theta = 0$ is shown with a vertical dashed line. 174

List of Tables

1.1	Cosmological parameters obtained by the Planck Collaboration	3
2.1	Summary of current and completed direct detection experiments.	36
3.1	Parameter values for the three mock experiments used in Chapter 3	55
3.2	Coverage statistics for the speed and momentum parametrisation methods for a 50 GeV SHM benchmark model.	67
3.3	Confidence interval coverage results for the momentum parametrisation method	72
4.1	Parameter values used for the three mock experiments used in Chapter 4	84
4.2	Summary of speed distribution benchmarks used in Chapter 4	85
4.3	Summary of the MULTINEST sampling parameters used in Chapter 4	86
4.4	Summary of the priors on the parameters used in Chapter 4	87
4.5	Mean bias in the reconstructed log WIMP mass using the polynomial $\ln f(v)$ method	96
4.6	Credible interval coverage results for the polynomial $\ln f(v)$ method	98
5.1	Summary of parameters for mock direct detection experiments used in Chapter 5	116
5.2	Summary of benchmarks used in Chapter 5	119
5.3	Summary of MULTINEST priors used in Chapter 5	120

Nomenclature

$\sigma_{SI(SD)}$ WIMP nucleon spin-independent (spin-dependent) cross section

m_χ WIMP mass

Chapter 1

Introduction

What is dark matter? For a question so central to cosmology and particle physics, the prospects for finding an answer do not at first glance seem promising. The interaction of dark matter (DM) particles must be very weak in order to evade a myriad of bounds set by precision astrophysical and cosmological tests. Our failure to observe dark matter particles thus far tells us that their interactions must be even weaker still. The effort to detect these interactions both on Earth and in the wider Universe is a vast technological and scientific challenge.

However, such efforts are advancing rapidly. The detection of particle DM using terrestrial detectors would give strong clues about the nature and identity of DM. However, the analysis of these so-called ‘direct detection’ experiments is plagued with uncertainties. One such uncertainty is in our understanding of the astrophysical speed distribution of dark matter, which influences the typical energies which would be deposited in a detector in the lab. If these uncertainties can be overcome, direct detection promises to be a powerful probe of both the particle physics and astrophysics of DM.

Without a detection of a possible particle candidate, then, the question ‘What is dark matter?’ is perhaps best answered by reviewing the current evidence for its existence. Evidence for DM is found on scales from the Milky Way up to the cosmological horizon, with a range of observations which cannot be adequately explained with the observed constituents of the Universe. Dark matter is an invisible component introduced to reconcile these observations with the known laws of physics - most importantly, General Relativity.

Beyond this general definition, there are a wide range of particle physics candidates which may play the role of dark matter. These typically derive

from theories of physics beyond the Standard Model (SM), meaning that the study of the properties of dark matter can shed light on theories of high energy physics. Many of these proposed dark matter candidates have weak but non-zero interactions with particles of the Standard Model, leading to several avenues through which it is hoped the non-gravitational detection of dark matter may soon be achieved.

In this chapter, we summarise the evidence in support of the DM paradigm, including constraints from precision cosmology. We discuss some of the features which particle DM must possess, as well as describing a few specific candidates in more detail. Finally, we discuss current progress and constraints from direct and indirect searches for particle dark matter.

1.1 Evidence for dark matter

Dark matter is a key component of the Λ CDM paradigm of modern cosmology. In this framework, the energy density of the Universe today is dominated by the constant and uniform contribution of the vacuum, Λ . This contribution exerts a negative pressure and drives the accelerating expansion of the Universe which was the subject of the 2011 Nobel Prize in Physics [3, 4]. However, the formation of structure in the early Universe is driven by the clustering of a non-interacting, slow moving and as yet undetected matter component [5], Cold Dark Matter (CDM). The fact that DM is non-interacting (or at least, interacts only very weakly) means that it begins to collapse gravitationally earlier in cosmic time than baryonic matter. After decoupling, baryons then fall into the gravitational wells produced by the infalling DM structures. Without DM, the baryonic matter in the Universe could not have had enough time to collapse to form the range of gravitationally bound structures we see today [5, 6]

Cosmological experiments sensitive to the expansion and structure formation history of the Universe allow us to precisely determine the contributions of various different components to the energy density of the Universe (see e. g. WMAP [7], BOOMERanG [8], BOSS [9], BICEP2 [10] and CFHTLenS [11, 12] to name just a few). For example, Baryon Acoustic Oscillations (BAOs) [13] are a feature imprinted on the distribution of matter in the Universe by acoustic waves prior to recombination. BAOs can be measured by using galaxy redshift surveys (such as SDSS [14]) to map out the large scale structure of the Universe and they provide a ‘standard ruler’

Parameter	68% limits
Ω_Λ	0.686 ± 0.020
$\Omega_m h^2$	0.1423 ± 0.0029
$\Omega_b h^2$	0.02207 ± 0.00033
$\Omega_c h^2$	0.1196 ± 0.0031

Table 1.1: Energy density Ω of the cosmological constant (Λ), total matter (m), and separate baryonic (b) and cold dark matter (c) components in units of the critical density, as obtained by the Planck Collaboration [17]. The Hubble parameter is defined as $H_0 = 100 h \text{ km s}^{-1}\text{Mpc}^{-1}$.

for measuring cosmological distances. Type-Ia Supernovae provide ‘standard candles’ which can be used to measure luminosity distances in the Universe. Redshift surveys of these supernovae [15] then allow us to reconstruct these distance scales over cosmic time. Complementary information from these probes and others allow us to constrain the expansion history of the Universe and therefore the various contributions to the density of the Universe.

A particularly sensitive probe for determining the dark matter contribution to the energy budget of the Universe is the measurement of the temperature anisotropies of Cosmic Microwave Background (CMB) photons. These contain an imprint of the acoustic oscillations of the baryon-photon fluid during the era of recombination. The scale of these oscillations is sensitive to the size of the gravitational potential generated in the early Universe by dark matter, which does not interact with the photons [5]. The recent Planck experiment [16] measured the angular power spectrum of these CMB temperature anisotropies. Figure 1.1 shows the results of these measurements, as well as the best fit 6-parameter Λ CDM model. The contributions of the cosmological constant, the total matter component, and the separate baryonic and dark matter components to the total energy density of the Universe are shown in Table 1.1, constrained with an accuracy of less than 3%. These results point to the conclusion that $\sim 84\%$ of the matter content of the Universe is in fact dark.

However, the evidence for dark matter is not purely cosmological. In 1933, Zwicky measured the velocity dispersion of galaxies in the Coma cluster [18]. An application of the Virial Theorem indicated a gravitational mass in the cluster which was several hundred times bigger than that expected from the luminosity of the member galaxies. It is now known that

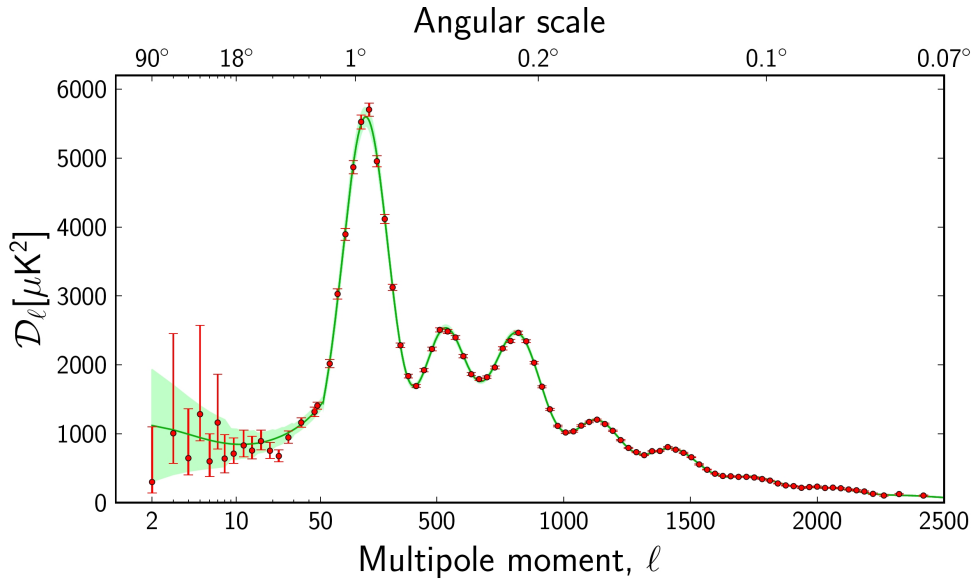


Figure 1.1: Angular power spectrum of CMB temperature anisotropies as measured by the Planck satellite. Data are shown as red points with the best fit Λ CDM cosmological model shown as a green line. Reproduced from Ref. [16].

some of this mass is in the form of hot (\sim 1 million K), X-ray emitting intracluster gas [19]. Nonetheless, a discrepancy remains; current estimates of the mass-to-light ratio of the Coma cluster give a value of roughly 150 times that of the Sun [20, 21]. The Coma cluster does not appear to be unusual. Measurements of the masses of a large number of galaxy clusters using gravitational lensing [22], X-ray observations [23] and dynamical estimates [24] indicate that a significant fraction of a cluster's mass must be dark.

The success of the Λ CDM paradigm is also borne out in results from N-body simulations. These simulations track the evolution of structure in the Universe by modeling the dynamics and gravitational interactions of a large number of particles starting from some initial conditions. These may be cosmological simulations, tracing the collapse of the initial density perturbations after decoupling (such as the Millennium simulation [25]), or galaxy-scale simulations, tracing the formation and growth of a small number of galaxies starting from initial conditions at intermediate redshift (such as the Via Lactea [26] and Aquarius [27] simulations).

Many N-body simulations are DM-only, simulating only the gravitational dynamics of collisionless particles. However, an increasing number

are incorporating baryonic physics such as gas dynamics, as well as stellar evolution, chemical enrichment and a variety of feedback processes (see e.g. [28, 29]). Appropriately accounting for these factors is extremely complex and in some cases the strength of these processes is unknown and must be tuned in the simulations to match observations [30]. Due in part to these difficulties, the impact of baryonic physics on the formation of galaxies and the properties of DM haloes is still uncertain (see for example Refs. [31, 32]). I will revisit this topic - and its consequences for the direct detection of dark matter - in Chapter 2.

A variety of sophisticated computational techniques (such as smoothed particle hydrodynamics [33], adaptive mesh refinement [34] and moving mesh cosmology [35]) have been employed and refined to make such simulations computationally feasible and to allow higher and higher resolutions to be reached. In spite of this, computational limitations mean that the highest resolution simulations still use ‘particle’ masses of the order of $10^5 M_\odot$ [32], many orders of magnitude more massive than the $O(\text{GeV-TeV})$ particles expected to make up the Universe’s dark matter.

In spite of this, a consistent picture has emerged from a vast array of N-body simulations. The distribution of galaxies observed in large scale structure surveys matches that predicted by N-body simulations over a range of distance scales [25]. In addition, N-body simulations have begun to accurately reproduce the observed populations of elliptical and spiral galaxies [29], as well as obtaining Milky Way-like simulated galaxies [28]. This ability of simulations containing DM to reproduce structures observed in the Universe is further evidence in support of the DM paradigm. Such is the accuracy of N-body simulations that they can be used to generate mock galaxy catalogues which allow statistical and systematic errors to be assessed in real galaxy surveys [36].

Further evidence for dark matter comes from observations of the rotation curves of spiral galaxies. In particular, the circular velocity of stars in these galaxies is observed to be approximately constant out to large galactocentric distances [37, 38]. In fact, observations of hydrogen 21cm emission indicate that the constancy of the circular velocity extends well beyond the optical edge of galaxies [39, 40].

This is shown schematically in Fig. 1.2. The majority of the mass of the luminous disc is concentrated at small radii, suggesting that there should be a Keplerian decay of the circular velocity at large radii: $v \sim r^{-1/2}$.

However, the inclusion of an approximately spherically symmetric, non-luminous dark matter halo can reconcile this expectation with the observed flat rotation curves. The density profiles $\rho(r)$ required to provide a good fit to rotation curve data may be consistent with those obtained from N-body simulations, such as the Navarro-Frenk-White profile

$$\rho(r) = \frac{\rho_0}{r/R_s(1+r/R_s)^2}, \quad (1.1)$$

which is described by a characteristic density ρ_0 and scale radius R_s . However, as we discuss in Sec. 1.2, better fits may be obtained by so-called ‘cored’ density profiles. The rotation curve of the Milky Way itself has also been studied [41–43] and found to be almost flat. Using a variety of techniques, it is also possible to measure a non-zero DM density near the Sun’s position. An understanding of this density has significant implications for the study of dark matter detection and we defer a detailed discussion to Chapter 2.

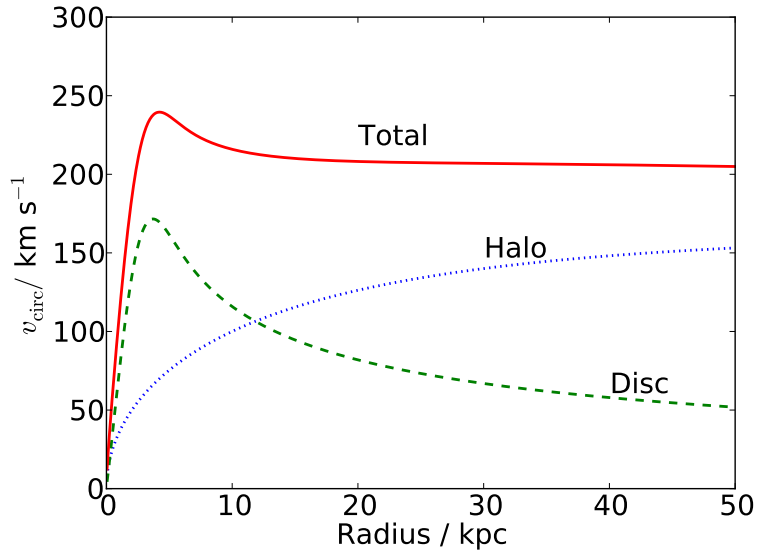


Figure 1.2: Schematic illustration of galaxy rotation curves (circular velocity as a function of galactocentric distance). The contribution to the circular velocity from the luminous disc (green dashed line) and dark matter halo (red dotted line) are shown, as well as the total circular velocity (solid blue line).

We see that evidence for dark matter appears over a wide range of distance scales, from the cosmological horizon down to our own Milky Way. Dark matter is required to explain the formation and growth of large

scale structure, the dynamics of both galaxies and galaxy clusters and the anisotropic temperature distribution of the CMB among others. In spite of this, there remain several problems and unanswered questions with the dark matter paradigm.

1.2 Problems with dark matter

There have emerged several issues with the dark matter dominated model of structure formation as studied with N-body simulations. For example, DM-only simulations predict the existence of a large number of massive subhalos around Milky Way-size galaxies [27]. Using semi-analytical models of galaxy formation Kauffmann et al. [44] predicted that a Milky Way-size halo should host over 100 subhalos massive enough to support observable satellite galaxies. However, the known population of dwarf spheroidal (dSph) satellite galaxies for the Milky Way is on the order of 20 [45], although more ultra-faint satellites are still being discovered (e.g. see Ref. [46]). This discrepancy between the predicted and observed amount of substructure in CDM structure formation is often referred to as the ‘missing satellite problem’ [47].

A related issue is the so-called ‘too big to fail’ problem, which concerns the density of dark matter subhalos. In particular, it is found that the most massive DM subhalos found in N-body simulations are too massive to host the brightest of the Milky Way’s dSph satellites [48]. If the observed dSph galaxies are hosted instead by less massive subhalos, this leaves a large number of more massive DM halos which have not yet been accounted for [49].

Finally, there is also a discrepancy between observed and simulated density profiles for dSphs: the ‘Core-Cusp’ problem (for a review, see Ref. [50]). Cosmological simulations indicate that the DM density should be sharply peaked near the centre of low surface brightness and dSph galaxies [51, 52]. In contrast, observations of the rotation curves of a large number of galaxies suggests the presence of a core - a flat dark matter density profile near the centre [53, 54]. While these results are still under contention (for example, Ref. [55] find rotation curves consistent with *cuspy* density profiles), they may indicate a discrepancy between the process of structure formation in the Universe and that implied by Λ CDM.

A number of possible solutions to these issues have been suggested.

Baryonic effects such as dynamical friction and stellar and supernova feedback (see for example Refs. [56–58]) can lead to the expulsion of DM from the centres of subhalos, reducing the total halo mass and leading to a flatter central density profile. Others have suggested that a *warm* dark matter model may be a better fit to the data [59–61], reducing the amount of structure on small scales, as we will discuss in Sec. 1.4. Whatever the ultimate resolution of these problems, it is clear that dark matter dominated structures such as dSph galaxies are a testing ground for an even more precise understanding of structure formation in the DM paradigm.

There remains one problem which is of a much more theoretical nature. Dark matter is invoked to account for missing mass in a wide range of scenarios. However, this missing mass has not yet been observed indicating that it must interact only very weakly with photons and other particles of the standard model. In fact, as we shall see, there is strong evidence that particles making up the Universe’s dark matter cannot be baryonic and must originate from beyond the Standard Model of particle physics. Before investigating what can be inferred about the nature of particle dark matter, however, we first address an alternative solution to the dark matter problem.

1.3 Alternatives to dark matter

We have discussed a wide range of evidence for the existence of DM, as well as some unresolved problems with the Λ CDM paradigm. Here, we consider the possibility that these observations can be explained not by a new matter species but by a modification to gravity. Milgrom [62–64] proposed the idea of Modified Newtonian Dynamics (MOND): for accelerations smaller than some characteristic value a_0 the usual Newtonian dynamics no longer holds. In particular, for an acceleration \mathbf{a} in a gravitational field Φ_N , this new dynamics can be written

$$\tilde{\mu}(|\mathbf{a}|/a_0)\mathbf{a} = -\nabla\Phi_N. \quad (1.2)$$

The interpolation function $\tilde{\mu}$ tends to unity for large values (the Newtonian limit) but tends to $|\mathbf{a}|/a_0$ for values $|\mathbf{a}| \ll a_0$ (the MOND limit).

At large distances from the centres of galaxies, the acceleration will drop below a_0 and Eq. 1.2 reduces to $a = v_c(r)^2/r = \sqrt{a_0\nabla\Phi_N}$, where v_c is the circular velocity. Assuming that there is no dark matter content,

the mass M enclosed within a radius r becomes constant and we obtain $|\nabla\Phi_N| \approx GM/r^2$. Combining these, we see that

$$v_c(r)^4 \approx GMa_o, \quad (1.3)$$

independent of radius. Thus, a flat rotation curve is obtained without the need to invoke DM. Moreover, Eq. 1.3 is the baryonic Tully-Fisher law, which relates the baryonic mass of a galaxy with the asymptotic rotation velocity, and which does not have an obvious origin in DM-based models [65]. The value for the characteristic acceleration obtained from fits to over 100 galaxies is $a_0 = 1.2 \times 10^{-10} \text{ m s}^{-2}$ [37], which also reproduces the measured proportionality constant in the Tully-Fisher law [66].

The phenomenological approach of MOND can be recast into a fully covariant theory of modified gravity, known as tensor-vector-scalar (TeVeS) gravity [67]. This theory contains new dynamical vector and scalar degrees of freedom and contains a free function, analogous to the interpolation function $\tilde{\mu}$. The formalism for both lensing [68] and cosmological perturbations [69] have both been studied in TeVeS, with perturbations in the new scalar and vector fields allowing structure to form without the need for DM.

How then does MOND compare to DM? MOND can generally give good fits to galaxy rotation curves [37, 70, 71] and can do so with fewer free parameters than DM halo models. MOND can also reduce the tension between the mass in clusters and the dynamical or lensing masses [72, 73], but typically only to within a factor 2, still requiring some collisionless matter to fit data [74]. However, the biggest problem is that relativistic extensions of MOND have yet to reproduce the features of large scale structure and the CMB with the same success as Λ CDM[75–77]. Though the range of possible extensions is large and the cosmological data may yet be explained within such a framework, we will focus here on the DM paradigm for explaining such observations.

1.4 Properties of dark matter

Beyond its gravitational contribution to the Universe, we appear to know little about the nature of particle dark matter. However, the success of modern cosmology and the lack of a confirmed detection so far means that

we do have a grasp on some of the properties of any potential candidate.

For example, DM can have no significant electromagnetic charge, otherwise it would have been seen in a range of searches [78–81]. DM carrying bare color charge can also be excluded due to the disruption it would cause to galaxy formation [82] and the formation of the CMB [83]. Any particle candidate must also be long-lived - otherwise it cannot play the role of dark matter today. For models in which DM is not indefinitely stable, this allows us to place stringent limits on the lifetime of the DM particle [84, 85].

In an effort to summarise what is known about dark matter, Taoso et al. [86] present a ‘10-point test’ which must be passed by any particle before it can be considered as a viable dark matter candidate. Here, I will briefly discuss three of these points, namely, that the DM candidate must be produced with the appropriate relic density, it must be cold and it must be compatible with primordial nucleosynthesis.

1.4.1 Relic density

In order to account for the dark matter in the Universe, a good candidate must be produced with sufficient abundance to match the currently observed value $\Omega_c h^2 = 0.1196 \pm 0.0031$ (see Table 1.1). If produced with a smaller abundance, the candidate cannot account for the entirety of the Universe’s dark matter (though it could still contribute, along with other candidates, as in Ref. [87]). If on the other hand, it is produced with too great an abundance, it could threaten to exceed the DM density constraint set by Planck and overclose the Universe.

The standard scenario for the production of dark matter is referred to as thermal freeze-out [5]. In this scenario, DM particles remain in kinetic and chemical equilibrium with SM particles in the very early Universe by scattering and annihilation processes. Their number density n follows a Maxwell-Boltzmann distribution

$$n \sim (m/T)^{3/2} \exp(-m/T), \quad (1.4)$$

for a mass m and temperature T . As the Universe expands, however, the particles become diluted, reducing the interaction rate until eventually the DM particles become decoupled from the SM particles and are ‘frozen-out’. They are then left with the abundance they had when they decoupled,

which is further diluted by the expansion of the Universe to become the abundance we see today. The exact relic abundance depends on $\langle \sigma_{\text{ann}} v \rangle$, the average annihilation cross section of the DM particles (weighted by the DM speed). If this is small, DM will decouple early when the temperature of the Universe is still high, leading to a large relic abundance. If the annihilation cross section is large, DM will remain in equilibrium for longer, even as the particles become more and more diluted. The DM then freezes out later, with a lower temperature and lower relic abundance. The resulting relic abundance for GeV-scale DM is given approximately by [5]:

$$\Omega_c h^2 \approx \frac{3 \times 10^{-27} \text{ cm}^3 \text{ s}^{-1}}{\langle \sigma_{\text{ann}} v \rangle}, \quad (1.5)$$

leading to a canonical value of around $\langle \sigma_{\text{ann}} v \rangle \approx 3 \times 10^{-26} \text{ cm}^3 \text{ s}^{-1}$ for the annihilation cross section. This coincides well with the value expected for particles with weak-scale interactions (so-called weakly interacting massive particles, or WIMPs), leading some to refer to this argument as the WIMP miracle. In reality, the full differential equations describing the DM number density must be solved [88], accounting for co-annihilations [89], which may boost the total cross section. However, the simplicity of this scenario make such thermal relics an attractive candidate for DM.

Dark matter may also achieve the correct relic abundance through a variety of other mechanisms. ‘Freeze-in’ [90] involves particles which interact so weakly (termed feebly interacting massive particles, FIMPs) that they never reach equilibrium. Instead, a relic population is built up gradually through the production of FIMPs by annihilation of SM particles. In contrast to the freeze-out scenario, the relic abundance of FIMPs increases with increasing annihilation cross section. Dark matter may also be produced gravitationally from vacuum fluctuations during and after inflation [91, 92] or from the decays of heavier meta-stable particles (e.g. Ref. [93]). These possibilities open up the range of candidates which may be considered to include much lighter or much heavier particles than the freeze-out scenario alone might allow.

Is it worth adding a figure to illustrate freeze-out?

1.4.2 Coldness

Dark matter cannot be hot. That is, DM must have been travelling non-relativistically when it was produced in the early Universe. The typical

speed of DM particles in the early Universe defines the so-called *free-streaming length*. Below this length-scale, density perturbations are suppressed due to Landau damping [94]. For non-relativistic species produced by thermal freeze-out, this free-streaming length scales as $m_\chi^{-1/2}$ for thermal relics of mass m_χ [95]. For particle candidates which are too light - and which therefore travel too quickly after decoupling - small scale structures cannot form and cannot match the distribution of structures we see today. Light particles which are produced via a mechanism other than thermal freeze-out may still account for DM (e.g. Ref. [96]), though this alternative mechanism must still ensure that it is not produced with relativistic speeds.

In practise, constraints on the free-streaming length mean that thermally-produced DM cannot have a mass greater than around 1 keV [97]. It is typically assumed that dark matter is significantly heavier than this, decoupling ultra-non-relativistically in the early Universe, rendering it cold. *Warm* dark matter candidates with keV-scale masses have been suggested to explain the subhalo structures at the scale of dSph galaxies (as has already been discussed). However, *hot* dark matter, which decouples at relativistic speeds, is strongly-constrained and cannot make up more than around 1% of the total dark matter component [98, 99].

1.4.3 Primordial nucleosynthesis

Primordial nucleosynthesis (or Big Bang Nucleosynthesis, BBN) describes the production of light nuclei in the first few minutes after the big bang. By solving a set of coupled Boltzmann equations describing the nuclear reactions of protons, neutrons and light nuclei, we can obtain the primordial abundances of these light nuclei and compare with the inferred values [100]. Significantly, these abundances depend strongly on the baryon-photon ratio η and therefore the total baryon density. Fits to data lead to the result $\Omega_b h^2 = 0.017 - 0.024$ [101], independent of the value obtained from CMB measurements (Table 1.1). Thus, the baryonic matter can make up only a fraction of the total matter density of the Universe. This provides further evidence that particle dark matter must consist of some non-baryonic particle.

The results of BBN are also very sensitive to light new species, which can alter the number of relativistic degrees of freedom in the early Uni-

verse and therefore affect the expansion rate. These include, for example, gravitinos [102] and right-handed neutrinos [103]. BBN therefore provides strong constraints on models in which these particles play the role of DM. In addition, the decay of dark matter particles into electromagnetic or hadronic showers during nucleosynthesis can drastically change the primordial abundances of the light elements. BBN can therefore be used to constrain models in which dark matter undergoes early decays (or in which dark matter is produced by the decays of heavier particles) [104].

1.5 Particle dark matter candidates

While *valid* DM candidates need only satisfy the conditions and constraints which have already been discussed, *well-motivated* candidates should derive sensibly from some physical model. In fact, dark matter candidates can be found in a wide range of models of particle physics beyond the standard model. As has already been discussed, massive particles with GeV-scale masses and weak-scale interactions are attractive for obtaining the correct DM relic density. Such a WIMP candidate may be provided by the lightest supersymmetric particle (LSP) in supersymmetric theories [105]. In supersymmetry, each of the known SM particles has a supersymmetric partner (or ‘spartner’), with bosons having fermionic partners and vice versa - this additional symmetry is often invoked to help alleviate the hierarchy problem [106]. In models which possess R-parity (which may be required to protect the proton from decay), particles carry R-parity 1 while supersymmetric particles (‘sparticles’) carry R-parity -1. This means that the lightest sparticle cannot decay into SM particles and is therefore stable, making it a promising DM candidate.

Depending on the parameters of the supersymmetric theory, there are many possibilities for which sparticle will be the LSP. One popular and well-studied possibility is the lightest neutralino χ [107], which is a linear combination of the neutral supersymmetric partners of the W and B with the CP-even higgsinos. The properties of the lightest neutralino can vary dramatically depending on the mixing between these different components and the underlying supersymmetric parameters [108]. In other cases, the LSP may be sneutrino [109], a partner of the standard model neutrino. Another alternative is the gravitino, which provides a good cold DM candidate for masses above around 100 keV [110].

WIMPs also arise in theories of universal extra dimensions, in which the additional dimensions are compactified, leading to a tower of excited states of the standard model particles [111]. These ‘Kaluza-Klein’ (KK) particles also possess a KK-parity, which means that the lightest KK particle (LKP) is stabilised [112]. One possibility for the LKP is the first excitation of the B weak hypercharge boson, $B^{(1)}$. In this case, the WIMP would be a spin-1 particle with a mass of around 1 TeV (in order to be produced thermally with the correct relic abundance) [113]. It has also been shown that the first KK excitations of the photon and neutrino are viable DM candidates if they also have masses at the TeV scale [114]. In contrast to the LSP, the LKP is described by a relatively small parameter space and may be more easily constrained by upcoming experiments [115].

In light of the problems with models of dark matter structure formation on small scales, there are several candidates which may be attractive for constituting warm dark matter. While standard neutrinos (with masses of a few eV [116]) cannot account for a large fraction of the dark matter, keV-scale sterile neutrinos may be viable [117]. Sterile neutrinos interact with ordinary matter via neutrino mixing rather than via electroweak interactions. While attractive for providing warm dark matter, non-thermal production [118] or multiple sterile neutrino species [119] may be required to avoid many astrophysical and cosmological constraints [120, 121].

Another non-WIMP candidate is the axion. The axion was originally introduced by Peccei and Quinn [122] to solve the strong CP problem. It was observed that this spin-zero particle should be produced in abundance in the early Universe via the ‘misalignment mechanism’ and, for masses in the range $10^{-5} - 10^{-3}$ eV, can account for the cosmological dark matter [123]. It was recently noted that axion dark matter would thermalise and form a Bose-Einstein condensate, acting as cold dark matter at late times [124]. Also of interest are axion-like particles (ALPs), which emerge naturally in string theory and are expected to span many orders of magnitude in mass and coupling strength [125]. Searches for axions are currently underway (such as ADMX [126] and CAST [127]), aiming to detect the conversion of axions to photons in a magnetic field.

We mention briefly the possibility that DM could be in the form of primordial black holes (PBHs) [128], which form from the collapse of large density perturbations in the early Universe [129]. PBHs with masses greater than $\sim 10^{-20} M_\odot$ have a lifetime greater than the age of the universe, mean-

ing that they may be able to account for the Universe’s DM. A range of cosmological [130], dynamical [131] and microlensing [132] constraints reduce the allowed mass range for PBHs as the dominant dark matter to $3 \times 10^{-13} - 2 \times 10^{-9} M_{\odot}$. Recent constraints from the capture of PBHs by neutron stars [133] may rule out this remaining window, though PBHs could still act as a subdominant DM component.

As is clear from this discussion, there are a wide range of well-motivated candidates for the dark matter in the Universe. Some further examples include WIMPless dark matter [134], mirror dark matter [135] and little Higgs dark matter [136], as well as minimal approaches to DM [137]. In this work, we focus on the WIMP, not only because of its popularity and generic nature, but because of the large number of experimental searches which provide sensitivity to WIMP dark matter.

The final condition appearing in the ‘10-point test’ of Taoso et al. asks the question ‘Can it be probed experimentally?’ While it may be possible that DM interacts only gravitationally, a wide variety of proposed candidates can interact (however weakly) with the particles of the standard model. While the experimental accessibility of a given DM candidate is not a strict necessity, it allows models to be tested (and either falsified or confirmed) beyond the hypothesis stage. In the next section, we explore the different avenues by which models of particle dark matter may be probed.

1.6 Detection of dark matter

Many of the candidates which have been discussed are expected to interact weakly with the particles of the Standard Model (SM). We note in particular that dark matter particles which are produced by thermal freeze-out in the early Universe must have interactions with SM particles in order to maintain thermal and kinetic equilibrium. These interactions are mediated by Feynman diagrams which can be represented (schematically) as in Fig. 1.3. The existence of production, annihilation and scattering processes between DM and SM particles provides a window into the possible detection of particle DM. Each of these processes leads to a distinct detection strategy, referred to as collider, indirect and direction detection.

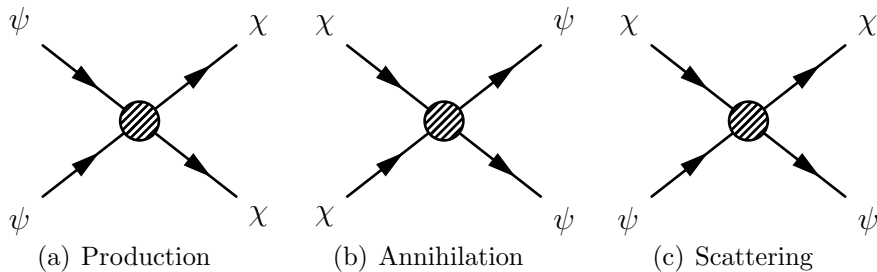


Figure 1.3: Schematic interactions between dark matter particles χ and standard model particles ψ .

1.6.1 Collider production

Searches for dark matter at particle colliders such as the LHC rely on processes such as Fig. 1.3(a), in which SM particles annihilate to produce dark matter particles. However, the weak interactions of the DM means that once produced, it will escape the detectors around the interaction point without being observed. Thus, collider searches for dark matter must look for other signatures.

One approach is to look for signatures which are characteristic of a particular theory. For example, looking for evidence of KK states which are expected in theories of universal extra dimensions [138, 139], or searching for particle signatures from decay chains which are expected from supersymmetry [140, 141]. While this allows constraints to be placed on specific models, the range of models may be large, meaning that each must be constrained separately.

An alternative approach is to look for deviations from the SM expectation and use this to place limits on the operators of an effective field theory (see e.g. [142]). One possible signature is to look for the pair production of DM states, with initial state radiation of a SM particle. It is then possible to search for this initial state radiation (which may be a single jet or a single boson or lepton, depending on which particle was radiated) accompanied by missing energy, which is carried away by the DM. By combining all the possibilities for the form of the initial state radiation, we can place bounds on the effective operators which govern SM-DM interactions [143]. Using such an approach, for example, it is possible to exclude DM with a standard thermal freeze-out cross section for masses $m_\chi < 15$ (75) GeV for vector (axial-vector) couplings to quarks [144].

One advantage of this effective operator approach is that these bounds can be translated into limits on signals at direct and indirect experiments.

allowing collider results to be incorporated with other experimental searches in a complementary fashion [145]. However, it has been noted that caution must be exercised in naively applying the effective field theory approach at the LHC as well as in translating this to other search channels [146, 147].

So far, there has been no evidence observed for the production of dark matter particles at the LHC [148]. The non-observation of supersymmetry at the LHC has also begun to place some tension on the simplest SUSY dark matter models [149], though they are not yet excluded [150]. The proposed International Linear Collider (ILC) [151] should be able to explore more of the possible dark matter parameter space [152, 153].

1.6.2 Indirect detection

The possibility of dark matter annihilation into SM particles (as described in Fig. 1.3(b)) means that DM may be detected indirectly, by searching for these excess annihilation products (and related decay products). Some searches aim to look for the contribution of these products to signals obtained over large survey areas. The Fermi-LAT collaboration have published limits on searches for spectral lines and contributions to the diffuse background of gamma rays [154]. Cosmic ray experiments such as PAMELA [155] have aimed to measure the p^\pm and e^\pm abundances in cosmic rays. The AMS experiment [156] has recently confirmed a rise in the cosmic ray positron fraction at energies above 10 GeV, which was previously observed by PAMELA [157] and Fermi-LAT [158]. This feature has been interpreted as tentative evidence for dark matter annihilations (see e.g. Ref. [159]).

For charged cosmic rays, astrophysical magnetic fields deflect the paths of particles, making it impossible to resolve individual sources [160]. In contrast, photon searches allow specific locations to be targeted. Because the signal rate is proportional to the DM annihilation rate (along the line of sight), the potential signal scales as the square of the dark matter density. Thus, searching in areas where the DM density is expected to be high can boost the signal rate significantly [161]. As has already been discussed, dSph galaxies are dark matter dominated objects and thus represent promising targets for indirect searches. A survey of 25 Milky Way satellite galaxies by the Fermi-LAT telescope [162] has so far found no significant gamma ray excess. However, upper limits on the annihilation

cross section are in some cases close to the thermal freeze-out value of $\langle\sigma_{\text{ann}}v\rangle \approx 3 \times 10^{-26} \text{ cm}^3 \text{ s}^{-1}$, depending on the WIMP mass and annihilation channel. By optimising search regions near the centre of the Milky Way for maximum signal-to-noise, Weniger recently found a bump in the gamma ray spectrum of Fermi-LAT data around 130 GeV [163]. However, subsequent analysis has found that this feature may be a systematic effect in the detector [164] and that it is difficult to reconcile with conventional models for dark matter [165, 166].

Perhaps more promising is a different gamma ray signal coming from the inner regions of the Galaxy, peaking at energies around 1-3 GeV [167, 168]. Fits of the data point towards a dark matter particle with a mass of 31-40 GeV, annihilating predominantly to $b\bar{b}$ with a cross section of $\langle\sigma v\rangle = (1.4 - 2.0) \times 10^{-26} \text{ cm}^3 \text{ s}^{-1}$, approximately matching the value required for a particle created by thermal freeze-out in the early Universe. While it has been suggested that this signal is actually consistent with known sources [169] or as yet unresolved astrophysical sources [170], further analysis has shown that the signal matches the spectrum and morphology expected from DM annihilation [171]. Confirmation of the signal may have to wait until it is corroborated by independent observations, for example a DM annihilation signal from dSph galaxies.

The sensitivity of gamma ray searches can be extended up to TeV-scale masses with ground-based Imaging Atmospheric Cherenkov Telescopes (IACTs). These work by imaging the Cherenkov radiation from charged particles produced when high energy gamma rays impinge on the atmosphere. The current generation of IACTs - HESS [172], MAGIC [173] and VERITAS [174] - have been used to conduct searches for line-like gamma ray spectra as well as searches for signals from dwarf galaxies. However, these limits are typically around two orders of magnitude above the thermal cross section. The planned Cherenkov Telescope Array (CTA) may be able to probe down to this thermal cross section for high WIMP masses [175].

Another potentially rich source of DM annihilations are the Sun and Earth. DM particles may scatter with nuclei in these bodies, losing energy and eventually becoming captured. Eventually, the DM sinks to the centre of the object and annihilates. The only annihilation products which can escape are neutrinos, which can then be detected at neutrino telescopes such as ANTARES [176] and IceCube [177]. Because the neutrino flux

depends on the scattering rate of DM with nuclei, such signals can probe similar parameter spaces to direct detection experiments. Exploring the complementarity between neutrino telescopes and direct detection is the subject of Chapter 5 and treat this subject in more detail there.

1.6.3 Direct detection

Processes described by the diagram in Fig. 1.3(c) lead to the possibility of scattering between DM and SM particles. The principle of direct detection is to look for nuclear recoils due to this scattering in a dedicated detector [178, 179]. WIMPs with GeV-scale masses and speeds $v \sim 10^{-3}c$ are expected to produce keV-scale nuclear recoils. In addition, due to the expected low cross section for such interactions, the predicted rate is less than around 1 event per year per kg of detector mass. Detecting such rare, low energy recoils requires not only large ton-scale detectors, but also sophisticated methods for discriminating signal from background.

Several direct detection experiments have claimed a tentative signal, such as DAMA/LIBRA [180], CoGeNT [181, 182] and CRESST-II [183]. However, these are in tension with null results from other experiments such as the recent LUX report [184]. Due to a range of uncertainties in nuclear physics, particle physics and astrophysics it may be possible to reconcile these results. In any case, a firm understanding of these uncertainties will be necessary to build a coherent picture from future results. The interpretation of direct detection data will be the main focus of this work and the main subject of Chapter 2.

1.6.4 Conclusions

The Λ CDM paradigm has enjoyed great success in explaining observations from galactic to cosmological scales. While discrepancies with observations on smaller scales remain, these are being actively pursued and may prove to be valuable testing grounds for the process of dark matter structure formation.

The identity of dark matter is unknown and cannot be accounted for by any of the known standard model particles. Even so, we know that it must be neutral, long-lived and cold (or possibly warm) and that it must pass a variety of stringent tests coming from BBN and the CMB. There is no lack of well-motivated CDM candidates, including the lightest

supersymmetric and Kaluza-Klein particles, sterile neutrinos, axions and many more. We have focused on the search for weakly interacting massive particles (WIMPs) and described how direct, indirect and collider searches have been used to place limits on the WIMP parameters and soon hope to make the first non-gravitational detection of DM.

Chapter 2

Direct detection of dark matter

2.1 Introduction

The idea that particle dark matter (DM) may be observed in terrestrial detectors was first proposed by Goodman and Witten in 1985 [178] and by Drukier, Freese and Spergel in 1986 [179]. If DM can interact with particles of the Standard Model, the flux of DM from the halo of the Milky Way may be large enough to cause measureable scattering from nuclei. If the subsequent recoils can be detected and their energy spectrum measured, it should be possible to infer some properties of the DM particles.

However, the expected event rate for keV-scale recoils at such a detector would be of the order of 10^{-5} events per kg of detector material per day per keV recoil energy [185]. With such a low event rate, it is imperative that backgrounds can be reduced as much as possible. In addition, detectors should be as large as possible and sensitive to as wide a range of recoil energies as possible, in order to maximise the total number of events observed. Thus, specialised detectors are required to shield the active detector material from backgrounds and to discriminate between these backgrounds and signal events.

There exist at present a wide range of detectors using a variety of different sophisticated techniques for detecting such a weak signal against ubiquitous backgrounds, each probing a slightly different range of DM parameter space. Several of these experiments - such as DAMA/LIBRA [180], CoGeNT [181, 182] and CRESST-II [183] - claim to have observed a signal

indicative of a WIMP with mass ~ 10 GeV. However, a number of other experiments have reported null results creating tension for a dark matter interpretation of these tentative signals. It remains to be seen whether this discrepancy is an experimental effect or a hint of new physics.

There remain a number of uncertainties in the direct detection of dark matter. These come from a variety of sources and can be approximately partitioned into experimental, nuclear, particle and astrophysical uncertainties. Understanding these uncertainties is imperative for properly interpreting the results of direct detection experiments and understanding whether a coherent picture can emerge from a number of different experimental efforts.

In this chapter, I will review the formalism for direct detection which was introduced by Goodman & Witten and Drukier, Freese & Spergel in the 1980s (and subsequently refined). I will then briefly discuss some of the experimental techniques which are used to achieve the required sensitivity for DM searches, as well as summarising current experimental constraints and results. I will also outline some of the uncertainties which afflict the interpretation of direct detection data.

I will focus on astrophysical uncertainties in direct detection. In particular, I will discuss how the local density and distribution of dark matter impacts the direct detection event rate and how well we understand these different factors.

2.2 Direct detection formalism

We wish to obtain the rate of nuclear recoils per unit detector mass due to elastic, non-relativistic scattering from a fermionic weakly interacting massive particle (WIMP). Dark matter is typically assumed to be spin-1/2, though the analysis here can be generalised to particles of arbitrary spin [186]. The differential event rate can be written straightforwardly as

$$\frac{dR}{dE_R} = N_T \Phi_\chi \frac{d\sigma}{dE_R}, \quad (2.1)$$

for recoils of energy E_R , N_T target particles, a DM flux of Φ_χ and a differential scattering cross section of $d\sigma/dE_R$. Per unit detector mass, the number of target particles is simply $N_T = 1/m_N$, for nuclei of mass m_N . The DM flux for particles with speed in the range $v \rightarrow v + dv$ in the labo-

ratory frame is $\Phi_\chi = n_\chi v f_1(v) dv$. Here, n_χ is the number density of dark matter particles χ and $f_1(v)$ is the speed distribution for the dark matter. The orbit of the Earth means that its velocity is time-varying, producing an annual modulation in $f_1(v)$ and therefore in the direct detection event rate [187]. However, this modulation is expected to be a percent-level effect and we consider here only the time averaged distribution.

We can convert from the number density to the mass density ρ_0 by dividing by the DM particle mass m_χ : $n_\chi = \rho_0/m_\chi$. By integrating over all DM speeds, we therefore obtain

$$\frac{dR}{dE_R} = \frac{\rho_0}{m_N m_\chi} \int_{v_{\min}}^{\infty} v f_1(v) \frac{d\sigma}{dE_R} dv, \quad (2.2)$$

where v_{\min} is the minimum speed required to excite a nuclear recoil of energy E_R :

$$v_{\min} = \sqrt{\frac{m_N E_R}{2\mu_{\chi N}^2}}. \quad (2.3)$$

The differential scattering cross section per solid angle in the zero-momentum frame (ZMF), Ω^* , is given by:

$$\frac{d\sigma}{d\Omega^*} = \frac{1}{64\pi^2 s} \frac{p_f^*}{p_i^*} |\mathcal{M}|^2, \quad (2.4)$$

where \mathcal{M} is the scattering amplitude obtained from the Lagrangian. For elastic scattering, the final and initial momenta in the ZMF are equal: $p_f^* = p_i^*$. The centre-of-mass energy squared, s , can be written $s \approx (m_\chi + m_N)^2$, where we have used the non-relativistic approximation. The recoil energy can be written in terms of the ZMF scattering angle θ^* as [185]

$$E_R = \frac{\mu_{\chi N}^2 v^2}{m_N} (1 - \cos \theta^*). \quad (2.5)$$

Noting that $d\Omega^* = d\cos \theta^* d\phi$, we can write:

$$\frac{dE_R}{d\Omega^*} = \frac{\mu_{\chi N}^2 v^2}{2\pi m_N}, \quad (2.6)$$

and therefore

$$\frac{d\sigma}{dE_R} = \frac{1}{32\pi m_N m_\chi^2 v^2} |\mathcal{M}|^2. \quad (2.7)$$

The matrix element \mathcal{M} is obtained from interaction terms in the lagrangian between the DM particle and quarks. This will depend on the

particular DM model under consideration and the full form of these interaction terms is not known. It is typically assumed that these terms can be adequately described by a contact interaction, an implied assumption that the particles mediating the interaction are much more massive than the momentum transferred [188]. The momentum transfer in direct detection experiments is typically less than ~ 200 MeV, suggesting that this assumption should be a valid one. However, we will consider briefly scenarios where this is not the case in Sec. 2.4.2.

Because the WIMPs have speeds of order $10^{-3}c$, the scattering occurs in the non-relativistic limit, leading to some important simplifications. In this limit, the axial-vector interaction simply couples the spins of the WIMP and quark. The scalar interaction induces a coupling of the WIMP to the number of nucleons in the nucleus, with the vector¹ and tensor interactions assuming the same form as the scalar in the non-relativistic limit [105]. All other interactions are typically suppressed by powers of v/c and so will be subdominant. Generically, then, the cross section is written in terms of spin-independent (SI) and spin-dependent (SD) interactions [178]

$$\frac{d\sigma}{dE_R} = \frac{d\sigma_{SI}}{dE_R} + \frac{d\sigma_{SD}}{dE_R}. \quad (2.8)$$

We now discuss the form of the SI and SD cross sections in turn.

2.2.1 SI interactions

Spin-independent interactions are generated predominantly by scalar terms in the effective lagrangian

$$\mathcal{L} \supset \alpha_S^{(q)} \bar{\chi} \chi \bar{q} q, \quad (2.9)$$

for interactions with a quark species q with coupling $\alpha_S^{(q)}$. The operator $\bar{q}q$ is simply the quark number operator, which couples to the quark density. However, we should recall that the quarks are in nucleon bound states. We consider first the contributions from neutrons $|n\rangle$, so we should evaluate $\langle n|\bar{q}q|n\rangle$, adding coherently the contributions from both valence and sea quarks. These matrix elements are obtained from chiral perturbation the-

¹For the case of a Majorana fermion, the vector current vanishes and we need not consider it.

ory [189] or Lattice QCD [190] and can be parametrised in terms of their contribution to the nucleon mass in the form:

$$m_n f_{Tq}^n \equiv \langle n | m_q \bar{q} q | n \rangle . \quad (2.10)$$

Adding the contributions of the light quarks, as well as the heavy quarks and gluons (which contribute through the chiral anomaly [191]), we obtain

$$\langle n | \sum_{q,Q,g} \bar{q} q | n \rangle = \left(\sum_{q=u,d,s} \frac{m_n}{m_q} f_{Tq}^n \alpha_S^q + \frac{2}{27} f_{TQ}^n \sum_{q=c,b,t} \frac{m_n}{m_q} \alpha_S^q \right) \equiv f^n . \quad (2.11)$$

The parameters describing the contributions of the different quarks to the nucleon mass must be determined experimentally. The uncertainties this produces will be discussed shortly in Sec. 2.4.1. *Need to double check this expression and exactly what it's equal to...*

The form factor doesn't depend on the vector \mathbf{q} but on the scalar $|\mathbf{q}|$...

We now consider the matrix elements of the nucleon operators within a nuclear state, $|\Psi_N\rangle : \langle \Psi_N | f^n \bar{n}n | \Psi_N \rangle$. These operators now simply count the number of nucleons in the nucleus N_n , along with a momentum-dependent form factor, $F(\mathbf{q})$, corresponding to the Fourier transform of the nucleon density. This takes into account the loss of coherence for nuclear scattering due to the fact that the nucleus is not point-like. We therefore obtain:

$$\langle \Psi_N | f^n \bar{n}n | \Psi_N \rangle = \langle \Psi_N | \Psi_N \rangle f^n N_n F_n(\mathbf{q}) = 2m_N f^n N_n F_n(\mathbf{q}) , \quad (2.12)$$

where we note that we require the wavefunctions to be normalised to $2E \approx 2m_N$ for a nucleus of mass m_N . We now add the contribution from protons to the matrix element, noting that $F_n \approx F_p = F$ (see Sec. 2.4.1)

$$\langle \Psi_N | f^n \bar{n}n + f^p \bar{p}p | \Psi_N \rangle = 2m_N (f^n N_n + f^p N_p) F(\mathbf{q}) , \quad (2.13)$$

where now N_n and N_p are the neutron and proton numbers of the nucleus respectively.

The corresponding matrix element for the scalar WIMP operator $\bar{\chi}\chi$ is simple in the non-relativistic limit, evaluating to $2m_\chi$ [105]. Combining these, we obtain the scalar matrix element

$$|\mathcal{M}_S|^2 = 16m_\chi^2 m_N^2 |f^p Z + f^n (A - Z)|^2 F_{SI}^2(\mathbf{q}) , \quad (2.14)$$

and the SI cross section

$$\frac{d\sigma_{SI}}{dE_R} = \frac{m_N}{2\pi v^2} |f^p Z + f^n (A - Z)|^2 F^2(\mathbf{q}), \quad (2.15)$$

where we have used the atomic number Z and mass number A to describe the composition of the nucleus. It is conventional to write this in terms of the WIMP-proton SI cross section, which does not depend on the particular (A, Z) of the target nucleus and thus allows easy comparison between experiments. This cross section is given by

$$\sigma_{SI}^p = \frac{\mu_{\chi p}^2}{\pi} (f^p)^2, \quad (2.16)$$

meaning that

$$\frac{d\sigma_{SI}}{dE_R} = \frac{m_N}{2\mu_{\chi p}^2 v^2} |Z + (f^n/f^p)(A - Z)|^2 F^2(E_R). \quad (2.17)$$

2.2.2 SD interactions

The spin-dependent interaction is typically sourced by axial-vector currents of the form

$$\mathcal{L} \supset \alpha_{AV}^{(q)} (\bar{\chi} \gamma^\mu \gamma_5 \chi) (\bar{q} \gamma_\mu \gamma_5 q). \quad (2.18)$$

These result in a coupling of the spins of the WIMP and nucleus. In analogy with the SI case, we can write the neutron quark matrix elements in the form [192, 193]

$$\langle n | \bar{q} \gamma_\mu \gamma_5 q | n \rangle = 2s_\mu^n \Delta_q^n, \quad (2.19)$$

where s_μ is the spin 4-vector and Δ_q parametrises the contribution of quark q to this total spin. Adding the contributions of the different quarks, we can define

$$a_{p,n} = \sum_{q=u,d,s} \frac{\alpha_{AV}^{(q)}}{\sqrt{2} G_F} \Delta_q^{p,n}, \quad (2.20)$$

which are the effective proton and neutron spin couplings.

The full nuclear matrix elements can then be written in the form *This expression isn't quite right - I'm missing a μ index - might need a factor of s_μ - I'll sort it out at some point...*

$$\langle \Psi_N | \sum_{q=u,d,s} \bar{q} \gamma_\mu \gamma_5 q | \Psi_N \rangle = 2\sqrt{2} G_F \frac{a_p \langle S_p \rangle + a_n \langle S_n \rangle}{J} \langle \Psi_N | \hat{J} | \Psi_N \rangle F_{SD}^2(E_R) \quad (2.21)$$

where J is the total nuclear spin, $\langle S_{p,n} \rangle$ the expectation value of the total proton and neutron spin in the nucleus and F_{SD}^2 is a form factor, as in the SI case, which is determined by the internal spin structure of the nucleus. Noting that $\langle \Psi_N | \hat{J} | \Psi_N \rangle = 2J(J+1)m_N$, we obtain for the SD cross section

$$\frac{d\sigma_{SD}}{dE_R} = \frac{4m_N}{\pi v^2} G_F^2 \frac{J+1}{J} |a_p \langle S_p \rangle + a_n \langle S_n \rangle|^2 F_{SD}^2(E_R). \quad (2.22)$$

Again, as in the SI case, it is convenient to rewrite this expression in terms of the proton cross section σ_{SD}^p , which is given by

$$\sigma_{SD}^p = \frac{6G_F^2}{\pi} \mu_{\chi p}^2 (a_p)^2. \quad (2.23)$$

This leads to the final expression for the SD cross section

$$\frac{d\sigma_{SD}}{dE_R} = \frac{2m_N \sigma_{SD}^p}{3\mu_{\chi p}^2 v^2} \frac{J+1}{J} |\langle S_p \rangle + (a_n/a_p) \langle S_n \rangle|^2 F_{SD}^2(E_R). \quad (2.24)$$

2.2.3 The final event rate

It is helpful to collect these various results together to form a coherent picture of the event rate. Combining the SI and SD rates together, we can write

$$\frac{d\sigma}{dE_R} = \frac{m_N}{2\mu_{\chi p}^2 v^2} (\sigma_{SI}^p \mathcal{C}_{SI} F_{SI}^2(E_R) + \sigma_{SD}^p \mathcal{C}_{SD} F_{SD}^2(E_R)), \quad (2.25)$$

where the proton cross sections $\sigma_{SI,SD}^p$ were defined in the previous section, the form factors $F_{SI,SD}^2$ will be discussed in more detail in Sec. 2.4.1 and we have defined the enhancement factors as

$$\mathcal{C}_{SI} = |Z + (f^n/f^p)(A - Z)|^2 \quad (2.26)$$

$$\mathcal{C}_{SD} = \frac{4}{3} \frac{J+1}{J} |\langle S_p \rangle + (a_n/a_p) \langle S_n \rangle|^2. \quad (2.27)$$

We can now incorporate these into the full event rate:

$$\frac{dR}{dE_R} = \frac{\rho_0}{2\mu_{\chi p}^2 m_\chi} (\sigma_{SI}^p \mathcal{C}_{SI} F_{SI}^2(E_R) + \sigma_{SD}^p \mathcal{C}_{SD} F_{SD}^2(E_R)) \int_{v_{\min}}^{\infty} \frac{f_1(v)}{v} dv. \quad (2.28)$$

The shape of the differential event rate then depends on a number of factors: the DM and target nuclear masses, the ratios of the proton and neutron couplings and the shape of the speed distribution $f_1(v)$. This distribution is typically assumed to have a simple form, the so-called Standard Halo Model (SHM). The SHM describes the velocity distribution in the Galactic frame as a Maxwell-Boltzmann distribution, truncated at the Galactic escape speed $v_{\text{esc}} \approx 544 \text{ km s}^{-1}$ [194, 195]. We discuss the SHM in more detail in Sec. 2.4.3. We show in Fig. 2.1 the SI differential event rate for Xenon (solid blue), Germanium (dashed green) and Argon (dot-dashed red) targets and several WIMP masses, assuming equal couplings to protons and neutrons.

As we increase the mass of the target nucleus, we see an increase in the low energy event rate. This is a result of the A^2 enhancement for SI interactions, resulting in the Xenon ($A \approx 131$) spectrum being a factor of around 10 higher than the Argon ($A \approx 40$) spectrum at low energies. As we consider higher energies, however, we observe that the spectrum for heavier targets decays more quickly. This is due to a more sharply falling form factor; the larger size of the nucleus results in a more rapid loss of coherence as the recoil energy is increased. The minimum in the Xenon rate observed in the bottom panel of Fig. 2.1 is also a feature of the Xenon SI form factor.

As we increase the WIMP mass, the recoil spectrum becomes flatter. This is primarily due to the dependence of v_{\min} on m_χ (shown in Eq. 2.3). As we increase m_χ , the reduced mass $\mu_{\chi N}$ increases, meaning that v_{\min} varies more slowly with energy. This means that the integral over the speed distribution also varies more slowly with energy. Physically, low mass WIMPs require a larger speed to impart the same recoil energy and as we increase the recoil energy this required speed grows quickly. The rapid cut-off in the spectrum observed in the $m_\chi = 10 \text{ GeV}$ case (top panel of Fig. 2.1) occurs when there are no more WIMPs below the Galactic escape speed which have sufficient speed to produce recoils of the desired energy.

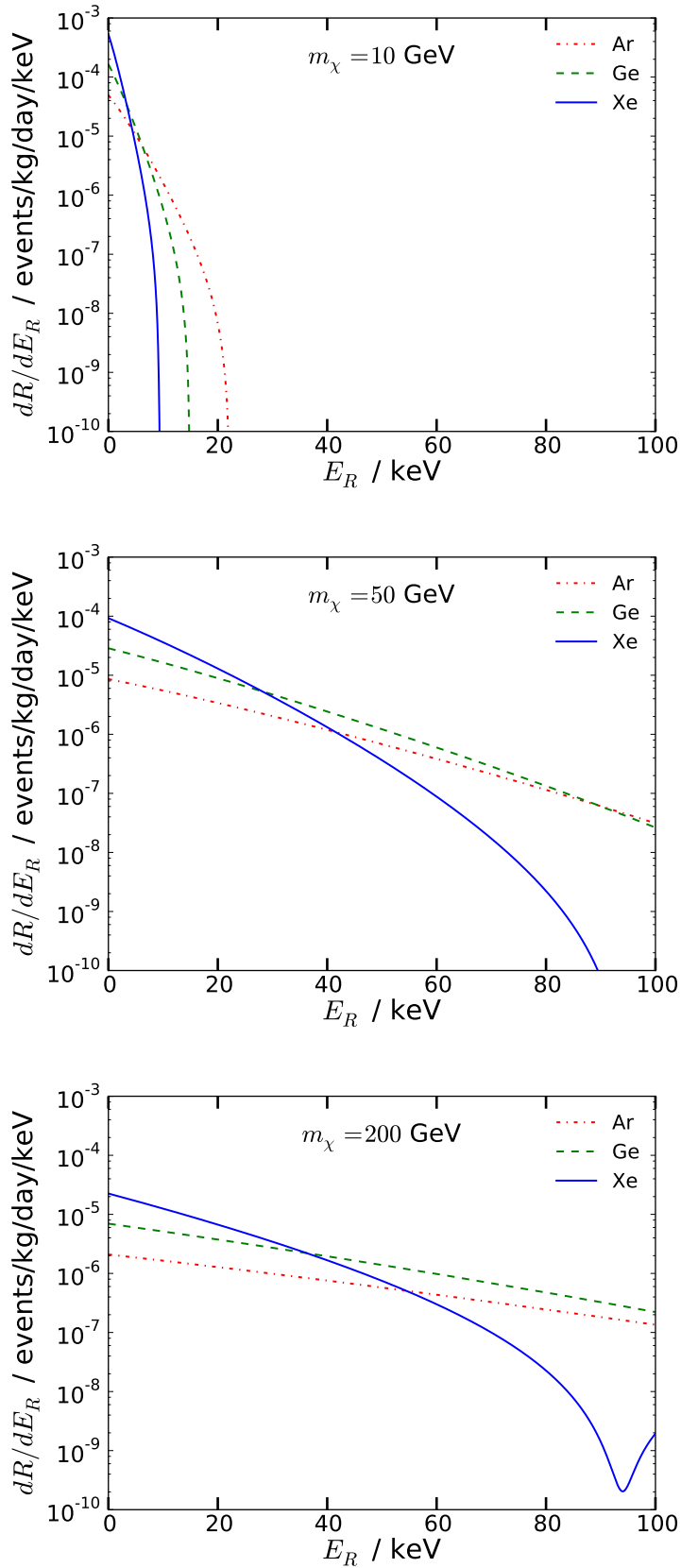


Figure 2.1: Spin-independent differential event rates predicted for the nuclear targets Xenon (solid blue), Germanium (dashed green) and Argon (dot-dashed red) and for several WIMP masses m_χ , assuming $f_p = f_n$. We assume a Standard Halo Model speed distribution, $\rho_0 = 0.3 \text{ GeV cm}^{-3}$ and a spin-independent cross section $\sigma_p^{\text{SI}} = 10^{-45} \text{ cm}^2$. The Helm form factor [196] is assumed (see Sec. 2.4.1).

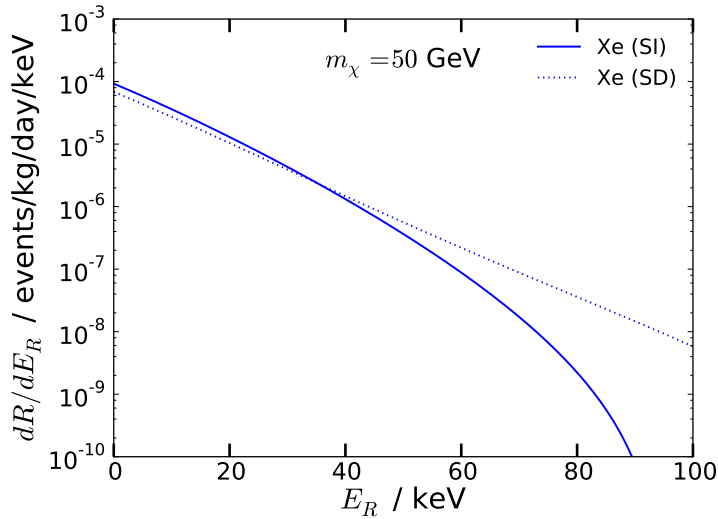


Figure 2.2: Spin-dependent (dotted) and spin-independent (solid) differential event rates predicted for a Xenon nuclear target for a WIMP mass $m_\chi = 50$ GeV, assuming $f_p = f_n$ and $a_p = a_n$. We assume a Standard Halo Model speed distribution, $\rho_0 = 0.3$ GeV cm $^{-3}$ and cross sections $\sigma_p^{\text{SI}} = 10^{-45}$ cm 2 and $\sigma_p^{\text{SD}} = 10^{-40}$ cm 2 . The Helm form factor [196] is assumed for the SI rate, while the SD form factor is taken from Ref. [197] using the NijmegenII calculation (see Sec. 2.4.1).

Finally, in Fig. 2.2, we show the SI and SD rates for a Xenon experiment and a WIMP mass of $m_\chi = 50$ GeV. The SD rate gives a comparable contribution to the SI rate only with a cross section five orders of magnitude larger. This is due to the strong A^2 enhancement of the SI rate for heavy nuclei. For light nuclei such as Fluorine, the SI and SD rates will be closer in magnitude (for a given cross section). Figure 2.2 also shows that the SD spectrum is typically flatter. The SD form factor has an approximately exponential form, while the SI form factor falls more rapidly (see Sec. 2.4.1).

For a real experiment, the detector will be sensitive to recoil energies only in some range E_{\min} to E_{\max} . The total number of events expected is obtained by integrating over this range of recoil energies and multiplying by the exposure time t_{\exp} , detector mass m_{\det} and efficiency (which may also be a function of the recoil energy E_R) $\epsilon(E_R)$:

$$N_e = m_{\det} t_{\exp} \int_{E_{\min}}^{E_{\max}} \epsilon(E_R) \frac{dR}{dE_R} dE_R. \quad (2.29)$$

For the case of a more realistic experiment in which the measurement of energy has only a finite resolution $\sigma(E_R)$, we convolve the event rate with

a resolution function (which we assume to have a Gaussian form) to obtain the observed recoil spectrum $d\tilde{R}/dE_R$,

$$\frac{d\tilde{R}}{dE_R}(E) = \int_{E'=0}^{\infty} \frac{e^{-(E-E')^2/(2\sigma(E'))}}{\sqrt{2\pi}\sigma(E')} \frac{dR}{dE_R}(E') dE'. \quad (2.30)$$

We now turn our attention to the discussion of such ‘realistic experiments’ and the current state of dark matter direct searches.

2.3 Direct detection experiments

In order to measure the event spectrum, a range of obstacles must be overcome. One possible source of backgrounds are high energy cosmic rays. For this reason, direct detection experiments are typically operated underground, such as at the Gran Sasso laboratory in Italy or the Boulby laboratory in the UK, in order to reduce the penetration of these cosmic rays. However, cosmogenic muons and neutrons can still penetrate the experiments, leading to the need for active shields which can detect these particles and provide a veto for any nuclear recoils they produce. It is also possible to veto events which produce multiple-scatters in the detector as WIMPs are expected to scatter only once. Passive shielding also reduces the neutron flux from surrounding rock and other sources. For a detailed analysis of neutron sources at dark matter experiments, see Ref. [198] (CRESST-II) and Ref. [199] (XENON100).

Radioactive decays due to naturally occurring isotopes may cause keV energy nuclear recoils in the detector, meaning that care must be taken to reduce their impact. The radiopurity of the target material is therefore of utmost importance (see for example Ref. [200]), as well as the radiopurity of detector equipment itself [201, 202]. In some cases, the naturally occurring target material is contaminated with a particular radioisotope, such as ^{39}Ar contamination in Argon. In these cases, special sources of the material must be found [203], or the amount of contamination must be carefully monitored and reduced [204, 205].

A major source of backgrounds is also electron recoils, which deposit energy in the detector and must be distinguished from nuclear recoils caused by WIMP interactions. Depending on the design of the detector, different methods are used to discriminate electron from nuclear recoils and to measure the recoil energy itself. We will now summarise some of the techniques which are used.

Cryogenic experiments, such as CDMS [206–209], CRESST [210], CoGeNT [181, 182, 211–213] and EDELWEISS [214], use cryogenic crystals of materials such as Germanium or Silicon as target materials. When a WIMP recoils from a target nucleus phonons are generated in the crystal along with an ionization signal. By summing the energy collected in these two channels (and accounting for any which may be incompletely collected), the total energy of the nuclear recoil can be obtained. The ratio of the total nuclear recoil energy and the ionization signal is referred to as the ‘ionisation yield’ and can be used to discriminate electron from nuclear recoils; electron recoils deposit more energy into ionisation. However, care must be taken to identify so-called ‘surface events’ - events occurring close to the detector surface which result in an incomplete collection of ionisation signal and can thus mimic a WIMP signal.

Noble liquid experiments use liquid (or two-phase) noble elements such as Xenon and Argon as target materials. Completed or operational Xenon detectors include ZEPLIN [215], XENON [216] and LUX [184]. In these detectors, Xenon recoils produce a scintillation signal (S_1) which can be observed directly using photomultiplier tubes. Ionisation electrons are also produced, which drift in an applied electric field, producing an electroluminescence signal (S_2) in the gas phase. The sum of these signals can be used to reconstruct the total recoil energy, while the ratio S_1/S_2 is used to discriminate electron from nuclear recoils. The two signals can also be used to localise the event within the detectors. A fiducial volume is then defined within the detector - only events inside this volume are considered in data analysis. This allows liquid Noble detectors to be self-shielding; the fiducial volume is shielded by the remaining detector volume. Experiments utilising Argon [217, 218] and Neon [219] are currently under development, using either the scintillation to ionisation signal as a discriminant or using timing of the scintillation signal (pulse shape discrimination).

Superheated liquid detectors such as COUPP [220], SIMPLE [221] and PICASSO [222] use a detector volume filled with droplets of superheated liquid such as C_4F_{10} . The deposition of kinetic energy by a WIMP will induce the nucleation of a bubble producing an acoustic signal which is detected by piezoelectric transducers. Energy deposition by other particles such as muons and γ - and β -radiation typically occurs over longer length scales and thus does not register a signal. The temperature and pressure of the detector can be tuned to specify the threshold energy, the minimum

energy which must be deposited before nucleation occurs. As such, superheated liquid detectors cannot measure the energy of specific events but rather the total event rate above the energy threshold. However, by ramping up the energy threshold, the recoil spectrum can effectively be measured. Due to the light targets such as Fluorine used by these experiments, they are typically more sensitive to light WIMPs with SD interactions.

Crystal scintillator experiments [223] such as DAMA/LIBRA [180, 224, 225] and KIMS [226] use crystals such as Thallium-doped Sodium Iodide ($\text{NaI}(\text{Tl})$) as the detector material. When a nuclear recoil occurs with the nuclei in the crystal, scintillation occurs. The light is collected by photomultiplier tubes, with the total recoil energy being related to the amount of scintillation light produced. In the case of DAMA/LIBRA, electron-nuclear recoil discrimination is not employed. Instead, the experiment aims to observe the annual modulation of the signal which is expected due to the periodic motion of the Earth through the WIMP halo. In other cases, such as NAIAD [227], pulse shape discrimination has been used to distinguish nuclear and electronic recoils.

A final class of direct detection experiments are known as ‘directional’ direct detection experiments. These aim to measure not only the energy deposited by WIMP scattering events but also the direction of the nuclear recoils. It is hoped that a recoil spectrum peaked in the direction opposite to the Earth’s motion will provide strong evidence for a DM origin for the recoils. One possibility for this is the use of specialised gas time projection chambers (TPCs), which allow measurable track lengths from which the recoil direction can be determined. The directional detection of dark matter is the subject of Chapter ?? and we defer a more detailed discussion of directional experiments until then.

2.3.1 Current limits and results

The first major dark matter detection to be reported was that of DAMA/NaI [228] and its successor DAMA/LIBRA. The experiments observed an annual modulation over 13 annual cycles, with a phase matching that expected from a dark matter signal. The detection of the annual modulation has been reported at the 8.9σ confidence level over an energy range of 2–6 keV. The modulation signal was only found in single-hit events at low energies, again suggesting a dark matter origin for the signal. It has been

suggested that the signal may be explained by a dark matter particle of mass $m_\chi \sim 10$ GeV and SI cross section $\sigma_{SI} \sim 10^{-41}$ cm 2 [229] scattering off Sodium (or a heavier WIMP around 80 GeV scattering off Iodine [230]). An annual modulation signal was also observed in the CoGeNT experiment [182, 212]. In this case too, the period and phase are consistent with expectations, though, the amplitude of the annual modulation is approximately 5 times larger than expected.

Excesses above the expected backgrounds have also been observed in a number of experiments. The CoGeNT experiment observed an exponentially rising excess of events at low energies, down to 0.5 keV $_{ee}$. A maximum likelihood analysis [213] pointed towards a 10 GeV WIMP interpretation, with a cross section of around $\sigma_{SI} \sim 5 \times 10^{-42}$ cm 2 , though the significance of the ‘signal’ lies at only 2.9σ . CRESST-II [210] observe 67 events in the nuclear recoil signal region but expect a background of only one event due to leakage of electron recoils into this window. Taking into account other backgrounds, the CRESST-II collaboration estimate that 25-30 of these events may be due to a WIMP signal. A fit to the data produces two minima in the likelihood function: one at $m_\chi \approx 25$ GeV (in which scattering from Tungsten is appreciable) and another at $m_\chi \approx 12$ GeV (where Tungsten recoils lie below the energy threshold). In both cases, the fitted cross section is in the range $\sigma_{SI} \approx 10^{-42} - 5 \times 10^{-41}$ cm 2 . Finally, a recent analysis of the Silicon detector data from CDMS-II [209] finds 3 events in the signal region. However, the very low expected backgrounds mean that this small number of events may be significant. The probability of the known backgrounds producing these three events has been calculated at 5.4% and a likelihood analysis shows consistency with a WIMP with $m_\chi \approx 9$ GeV and $\sigma_{SI} \approx 2 \times 10^{-41}$ cm 2 .

While it appears that a reasonably consistent picture of a low mass WIMP is emerging from several experiments [231], a large number of competing experiments have reported null results. Results from CDMS-II (Ge), XENON100, LUX, SuperCDMS [232] and others set upper limits on the standard WIMP cross section several orders of magnitude lower than the claimed signal. Several explanations for this discrepancy have been offered. One possibility is background contamination of the experiments claiming to have observed a signal, which has been suggested in the case of CRESST-II [202]. A recent analysis of the CoGeNT excess [233] finds evidence for DM at less than 1σ using an improved method for rejecting surface events. In

the case of DAMA/LIBRA, it has been suggested that ion-channeling in the detector crystals may affect the collected ionisation signal and therefore alter the signal [234]. The DAMA/LIBRA signal has also been attributed to an annually modulated muon signal [235, 236].

An alternative explanation is that the claimed signals *are* due to a dark matter particle, but that its properties are not as simple as in the canonical case, explaining why it has not been observed in all experiments. One possibility is that the astrophysical distribution of dark matter does not match the standard assumptions. We will discuss this astrophysical distribution in more detail shortly in Sec. 2.4.3. However, it appears that even with this additional freedom, the different results cannot be reconciled [237–240]. A number of particle physics models have also been considered to explain the results, including spin-dependent interactions [241], isospin violating dark matter (for which $f^p \neq f^n$) [242], inelastic dark matter [243] and mirror dark matter [244]. However, a consistent picture which reconciles all experimental datasets remains elusive [245].

We summarise some of the completed and current direct detection experiments in Table 2.1. The most stringent limits on the SI WIMP-proton cross section are set by LUX [184], who find a limit of $\sigma_{SI}^p \leq 7.6 \times 10^{-46} \text{ cm}^2$ at a mass of $m_\chi = 33 \text{ GeV}$. The best limit for the SD cross section is set by XENON100 [246]: $\sigma_{SD}^p \leq 3.5 \times 10^{-40} \text{ cm}^2$. The confirmation or falsification of the signals which have been claimed thus far may have to wait for the next generation of dark matter experiments, or for corroboration from collider or indirect searches.

I could potentially add in a plot of some limits, depending on space/time.

2.3.2 Future experiments

Experiments which are planned or under construction typically aim to scale up the size of current detectors and reduce unwanted backgrounds (in order to increase the sensitivity to lower cross sections) or decrease the energy threshold (which increases sensitivity to lower masses). There are a number of ton scale detectors either in operation or planned, including XENON1T [248], DEAP-3600 [249], LZ [250], EURECA [251, 252] and DARWIN [253]. With this next generation of detectors, the aim is to achieve sensitivity to the SI WIMP-proton cross section down to $\sigma_{SI}^p = 10^{-48} \text{ cm}^2$. Below this value, irreducible backgrounds from neutrinos (predominantly from

Experiment	Target	Status
CDMS-II (Ge) [206–208]	Ge	Null result
CDMS-II (Si) [209]	Si	Excess
SuperCDMS [232]	Ge	Null result
CoGeNT [181, 182, 211–213]	Ge	Excess & annual modulation
CRESST-II [210]	CaWO ₄	Excess
EDELWEISS-II [214]	Ge	Null result
ZEPLIN-III [215]	Xe	Null result
XENON100 [216, 247]	Xe	Null result
LUX [184]	Xe	Null result
PICASSO [222]	C ₄ F ₁₀	Null result
SIMPLE-II [221]	C ₂ ClF ₅	Null result
COUPP [220]	CF ₃ I	Null result
DAMA/LIBRA [180, 224, 225]	NaI(Tl)	Annual modulation
NAIAD [227]	NaI(Tl)	Null result
KIMS [226]	CsI(Tl)	Null result

Table 2.1: Summary of current and completed direct detection experiments.

the Sun) become important and the identification of a DM signal becomes more difficult [254, 255].

There have also been a number of proposals for novel methods of directly detecting dark matter. These include using DNA-based detectors to provide high spatial resolution [256], using nano-scale explosives [257] or charged-coupled devices [258] to achieve very low energy thresholds and using proton-beam experiments as a source for dark matter source for direct detection experiments [259]. It has also been suggested the direct detection experiments could be used to search for DM interactions with electrons, rather than nuclei (see e.g. Refs. [260, 261]). Clearly, there are a range of approaches being pursued both in refining current technologies and developing new ones.

2.4 Uncertainties

Calculation of the DM differential event rate dR/dE_R requires not only a knowledge the dark matter parameters m_χ and $\sigma_{SI,SD}$ but a number of other factors which also enter into the calculation. It is important to understand how uncertainties in these different factors and parameters propagate into the event rate in order to ensure that the conclusions we draw from di-

rect detection experiments are unbiased. These uncertainties are typically partitioned into three separate classes: nuclear physics, particle physics and astrophysics.

2.4.1 Nuclear physics uncertainties

As we have already seen, nuclear physics enters into the calculation of the nucleon matrix elements $m_n f_{Tq}^n \equiv \langle n | m_q \bar{q} q | n \rangle$. The factors f_{Tq}^n must be determined experimentally, and have values

$$f_{Tu}^p = 0.020 \pm 0.004; f_{Td}^p = 0.026 \pm 0.005; f_{Ts}^p = 0.118 \pm 0.062, \quad (2.31)$$

with $f_{Tu}^p = f_{Td}^n$, $f_{Td}^p = f_{Tu}^n$ and $f_{Ts}^p = f_{Ts}^n$. The main uncertainties stem from determinations of the π -nucleon sigma term, determined either experimentally from low energy pion-nucleon scattering [189, 262, 263] or from lattice QCD calculations [190, 264]. Similarly for the spin contributions Δ_q to the nucleus, values must be obtained experimentally [193, 265–267],

$$\Delta_u^p = 0.77 \pm 0.08; \Delta_d^p = -0.38 \pm 0.08; \Delta_s^p = -0.09 \pm 0.08, \quad (2.32)$$

although efforts are being made to obtain these values directly via calculation [268, 269]. It should be noted that these nucleon matrix elements are only necessary if we wish to deal directly with quark-level couplings and interactions. If, instead, we consider the nucleon-level effective operators (and equivalently the WIMP-nucleon cross sections), these values are not required.

Nuclear physics also enters into the calculation of form factors, describing the internal nucleon and spin structures of the nuclei. For the SI case, the form factor is obtained from the Fourier transform of the nucleon distribution in the nucleus. The form typically used is due to Helm [196]

$$F_{SI}^2(E_R) = \left(\frac{3j_1(qR_1)}{qR_1} \right)^2 e^{-q^2 s^2}, \quad (2.33)$$

where $j_1(x)$ is a spherical bessel function of the first kind,

$$j_1(x) = \frac{\sin x}{x^2} - \frac{\cos x}{x}. \quad (2.34)$$

Nuclear parameters due to Lewin and Smith [270], based on fits to muon spectroscopy data [271] are typically used:

$$R_1 = \sqrt{c^2 + \frac{7}{3}\pi^2 a^2 - 5s^2}, \quad (2.35)$$

$$c = 1.23A^{1/3} - 0.60\text{fm}, \quad (2.36)$$

$$a = 0.52\text{fm}, \quad (2.37)$$

$$s = 0.9\text{fm}. \quad (2.38)$$

Muon spectroscopy and electron scattering data [272] are used as a probe of the *charge* distribution in the nucleus. However, detailed Hartree-Fock calculations indicate that the charge distribution can be used as a good proxy for the nucleon distribution (especially in the case $f_p \approx f_n$) and that using the approximate Helm form factor introduces an error of less than $\sim 5\%$ in the total event rate [273]. Studies also indicate that errors due to distortions in nuclear shape away from sphericity are negligible [274].

In the SD case, however, the situation is more complicated. In order to calculate the SD cross section, we require the proton and neutron spin content $\langle S_{p,n} \rangle$ as well as the form factor F_{SD}^2 . The form factor can be written in the form

$$F_{SD}^2(E_R) = S(E_R)/S(0), \quad (2.39)$$

in terms of the response function $S(E_R)$. This response function can in turn be decomposed into three spin-dependent structure functions (SDSFs)

$$S(E_R) = a_0^2 S_{00}(E_R) + a_0 a_1 S_{01}(E_R) + a_1^2 S_{11}(E_R), \quad (2.40)$$

where $a_0 = a_p + a_n$ is the isoscalar coupling and $a_1 = a_p - a_n$ is the isovector coupling. The zero momentum transfer value $S(0)$ is related to the proton and neutron spin expectation values by [275]

$$S(0) = \frac{2J+1}{\pi} \frac{J+1}{J} |a_p \langle S_p \rangle + a_n \langle S_n \rangle|^2. \quad (2.41)$$

We can therefore rearrange the SD cross section of Eq. 2.24 as

$$\frac{d\sigma_{SD}}{dE_R} = \frac{2\pi}{3} \frac{m_N \sigma_{SD}^p}{\mu_{\chi p}^2 v^2} \frac{1}{2J+1} \frac{S(E_R)}{(a_p)^2}. \quad (2.42)$$

The nuclear physics is now encapsulated in a single response function $S(E_R)$ (or equivalently two SDSFs S_{00} and S_{11}).²

²In Ref. [275], it is noted that the SDSFs are not independent and that the function S_{01} can be written in terms of the other two.

The functional form for S_{ij} can be calculated from shell models for the nucleus [197]. However, there are a number of competing models (such as the Odd Group Model [276], Interacting Boson Fermion Model [277] and Independent Single Particle Shell Model [278] among others). These models use different methods for accounting for forces between quarks, leading to different forms for the SDSFs and therefore to significant uncertainty in the spin-dependent cross section. This issue was explored by Cerdeño et al. [279], who developed a parametrisation for the spin structure functions in terms of the parameter $u = (qb)^2/2$, where q is the momentum transfer and $b = \sqrt{41.467/(45.0A^{-1/3} - 25.0A^{-2/3})}$ is the oscillator size parameter. This parametrisation takes the form

$$S_{ij} = N((1 - \beta)e^{-\alpha u} + \beta), \quad (2.43)$$

where the range of the parameters $\{N, \alpha, \beta\}$ is chosen such that S_{ij} spans the different possible forms presented in the literature. It was shown that this parametrisation was able to mitigate the uncertainties in the SD cross section and accurately recover the remaining particle physics parameters when the true form for the SDSFs was unknown.

2.4.2 Particle physics uncertainties

Apart from the unknown values for the WIMP mass m_χ and cross sections $\sigma_{SI,SD}$, the ratios of proton to neutron couplings are also *a priori* unknown. In the case of SI scattering, the dominant contribution comes from the coupling to strange quarks f_{Ts} , which is equal for protons and neutrons. It is therefore typically assumed that $f^p = f^n$, though isospin violating dark matter models have been considered [242, 280, 281]. Similarly, for the SD interaction, a specific relation is typically assumed between the proton and neutron couplings, such as $a_p/a_n = \pm 1$. While specific models often predict such a relation [105], it should be noted that this ratio is *a priori* unknown and fixing it is a model choice.

Further uncertainty is derived from the form of the interaction terms themselves. Here, we have considered the dominant contributions to scattering in the case of non-relativistic contact interactions. Extensions including mediator particles have been considered [282, 283], as well as models in which DM can interact electromagnetically with nuclei [284, 285]. There has also been significant effort towards developing a general non-

relativistic field theory for the interaction of WIMPs with nuclei [186, 188, 286, 287]. Current limits can be translated into limits on the couplings associated with a range of effective operators. While this approach significantly widens the parameter space of dark matter direct detection, it is more general and does not rely on (potentially poor) assumptions about DM interactions.

2.4.3 Astrophysical uncertainties

Astrophysical uncertainties enter into the direct detection event rate through the local dark matter density ρ_0 and the speed distribution $f_1(v)$.

DM density, ρ_0

The DM mass density sets the overall scale of the scattering rate. As we shall discuss in Chapter 3, the DM density is degenerate with the interaction cross section, meaning that an accurate determination is important. One method of obtaining the value of ρ_0 is by mass modelling of the Milky Way (MW). One builds a model for the Galaxy incorporating various sources of mass, including the stellar bulge and disc, dust and a dark matter halo [288]. It is then possible to use various data such as the total MW mass, local surface mass density and the velocities of tracers to fit the parameters of this model and thereby extract ρ_0 . Estimates using this method tend to have a wide uncertainty, typically lying in the range $0.2 - 0.4 \text{ GeV cm}^{-3}$ (e.g. Ref. [288, 289]). A more recent determination using state-of-the-art data obtains a more precise but higher value of $\rho_0 = 0.47^{+0.05}_{-0.06} \text{ GeV cm}^{-3}$ [290] (though this depends on the choice of halo density profile).

An alternative method is to use local stellar kinematic data to constrain the gravitational potential near the Sun and thus obtain an estimate of ρ_0 . Using kinematic data from roughly 2000 K-dwarfs, Garbari et al. [291] obtain the value $\rho_0 = 0.85^{+0.57}_{-0.50} \text{ GeV cm}^{-3}$ while Zhang et al., using a larger sample of 9000 K-dwarfs, obtain $0.28 \pm 0.08 \text{ GeV cm}^{-3}$. Including microlensing data, the range of allowed values at 1σ is $\rho_0 = 0.20 - 0.56 \text{ GeV cm}^{-3}$ [292]. A further model independent method was proposed by [293]. The advantage of such approaches is that one does not need to assume a particular form for the DM halo density profile. However,

they may be more sensitive to assumptions about local equilibrium near the Sun’s position.

In 2012, Moni Bidin et al. [294] used the dynamics of thick disk stars to constrain the DM density, finding a result consistent with no dark matter at the Sun’s radius. However, a subsequent reanalysis by Bovy and Tremaine [295] showed that this result derived from a poor assumption about the velocity of stellar tracers as a function of Galactic radius. Using the same data with more reasonable assumptions, the value $0.3 \pm 0.1 \text{ GeV cm}^{-3}$ was obtained.

In spite of the large number of determinations, no consistent value appears to be emerging, with values ranging from $0.2\text{--}0.85 \text{ GeV cm}^{-3}$. There also remain a number of uncertainties in these determinations, including the shape of the DM halo and assumptions about the local equilibrium of the Galaxy (for a recent review, see Ref. [296]). The ‘standard’ value assumed in the analysis of direct detection experiments is 0.3 GeV cm^{-3} , though the exact origin of this number is unclear [297].

Speed distribution, $f_1(v)$

The speed distribution enters into the direct detection rate in the integral,

$$\eta(v_{\min}) \equiv \int_{v_{\min}}^{\infty} \frac{f_1(v)}{v} dv, \quad (2.44)$$

which is referred to as the ‘velocity integral’ or the ‘mean inverse speed’. Direct detection experiments are traditionally analyzed within the framework of the Standard Halo Model (SHM), in which WIMPs are assumed to have a Maxwell-Boltzmann velocity distribution in the Galactic frame. In the Earth’s frame, this takes the form

$$f_{\text{SHM}}(\mathbf{v}) = N \exp\left(-\frac{(\mathbf{v} - \mathbf{v}_{\text{lag}})^2}{2\sigma_v^2}\right) \Theta(v_{\text{esc}} - |\mathbf{v} - \mathbf{v}_{\text{lag}}|), \quad (2.45)$$

where \mathbf{v}_{lag} specifies the velocity of the Earth frame with respect to the Galactic rest frame and σ_v the velocity dispersion. The SHM distribution is obtained assuming a spherical, isothermal DM halo with density profile $\rho \sim r^{-2}$ and results in the relation $\sigma_v = v_{\text{lag}}/\sqrt{2}$. The distribution is truncated above the escape speed v_{esc} in the Galactic frame and the factor

N is required to satisfy the normalization condition:

$$\int f(\mathbf{v}) d^3\mathbf{v} = 1. \quad (2.46)$$

By integrating over directions we obtain $f(v)$ and the speed distribution is then given by

$$f_1(v) = f(v)v^2 = \int f(\mathbf{v})v^2 d\Omega_v. \quad (2.47)$$

Within the SHM, there is some uncertainty on the parameters describing $f_1(v)$. The parameter v_{lag} is given by the local circular speed $v_c = 218 \pm 7 \text{ km s}^{-1}$ [298, 299] plus a contribution from the peculiar motion of the Sun and the Earth's orbital motion. This lag speed is typically assumed to be close to the local circular speed, though more recent determinations of the solar velocity point towards higher values [300, 301] of $240 - 250 \text{ km s}^{-1}$. The Galactic escape velocity can be estimated from the radial velocities of MW stars; the RAVE survey obtain the range $v_{\text{esc}} = 533^{+54}_{-41} \text{ km s}^{-1}$ at 90% confidence [194, 195]. Moreover, the relation $\sigma_v = v_{\text{lag}}/\sqrt{2}$ is obtained from solving the Jeans equation assuming $\rho \sim r^{-2}$ [302]. Relaxing this assumption means that this relation no longer holds and that σ_v is no longer as well constrained.

Even taking into account these uncertainties, the SHM is unlikely to be an accurate representation of the DM halo. Observations and N-body simulations indicate that the halo should deviate from a $1/r^2$ profile and may not be spherically symmetric. As a result alternative models have been proposed. Speed distributions associated with triaxial halos [303] or with more realistic density profiles [304] have been suggested, as well as analytic parametrisations which should provide more realistic behaviour at low and high speeds [305]. Self-consistent distribution functions reconstructed from the potential of the Milky Way have also been obtained [306, 307].

It is also possible to extract the speed distribution from N-body simulations. Such distribution functions tend [308–310] to peak at lower speeds than the SHM and have a more populated high speed tail. There are also indications that DM substructure may be significant, causing ‘bumps’ in the speed distribution, or that DM which has not completely phase-mixed - so-called ‘debris flows’ - may have a contribution [311]. *May include one of these in Fig. 2.3.*

It should be noted that N-body simulations do not probe down to the sub-milliparsec scales which are probed by direct detection experiments. There may be a concern then that the local dark matter distribution could be dominated by localised subhaloes or streams which are not captured by these simulations and which may affect the interpretation of direct detection experiments [312]. However, an analysis of N-body simulations has found that no individual subhalos should dominate the local distribution [313]. Vogelsberger et al. [314] study the geodesic deviation of individual particles in N-body simulations, giving access to information about the ultra-local DM distribution. They find that the local distribution should be made up of a large number of streams ($\sim 10^5$), meaning that it can effectively be treated as smooth.

Another result obtained from N-body simulations is the possibility of a dark disk. When baryons are included in simulations of galaxy formation, this results in the tidal disruption of DM subhaloes which are then preferentially dragged into the disk plane [315, 316]. The resulting dark disk corotates with approximately the same speed as the baryonic matter, though with a smaller velocity dispersion $\sigma_v^{DD} \sim 50 \text{ km s}^{-1}$. This dark disk is expected to contribute an additional density 0.2-1.0 times the density of the halo. However, this value is dependent on the merger history of the Milky Way, with more massive and numerous mergers leading to an enhance disk density. The more recent ERIS results [32], comparing hydrodynamic and DM-only simulations, report a relatively quiet merger history for a Milky Way-like galaxy. The result is a smaller dark disk density of just 10% that of the DM halo.

In Fig. 2.3, we show some examples of possible dark matter speed distributions in the Earth frame. We show the directionally averaged velocity distribution $f(v)$ in the top panel, the speed distribution $f_1(v)$ in the middle panel and the corresponding $\eta(v)$ in the bottom panel. The population of low speed WIMPs in the SHM + dark disk (dashed green) distribution causes the mean inverse speed (and therefore the event rate) to rise more rapidly at low speeds than the SHM alone (solid blue). A sharp stream distribution function (dotted magenta) leads to step-like form for η ; for v_{\min} above the speed of the stream almost no WIMPs can contribution to the scattering, while for v_{\min} below the speed of the stream almost all can. Each of these possible distributions will produce a distinct event spectrum in a detector.

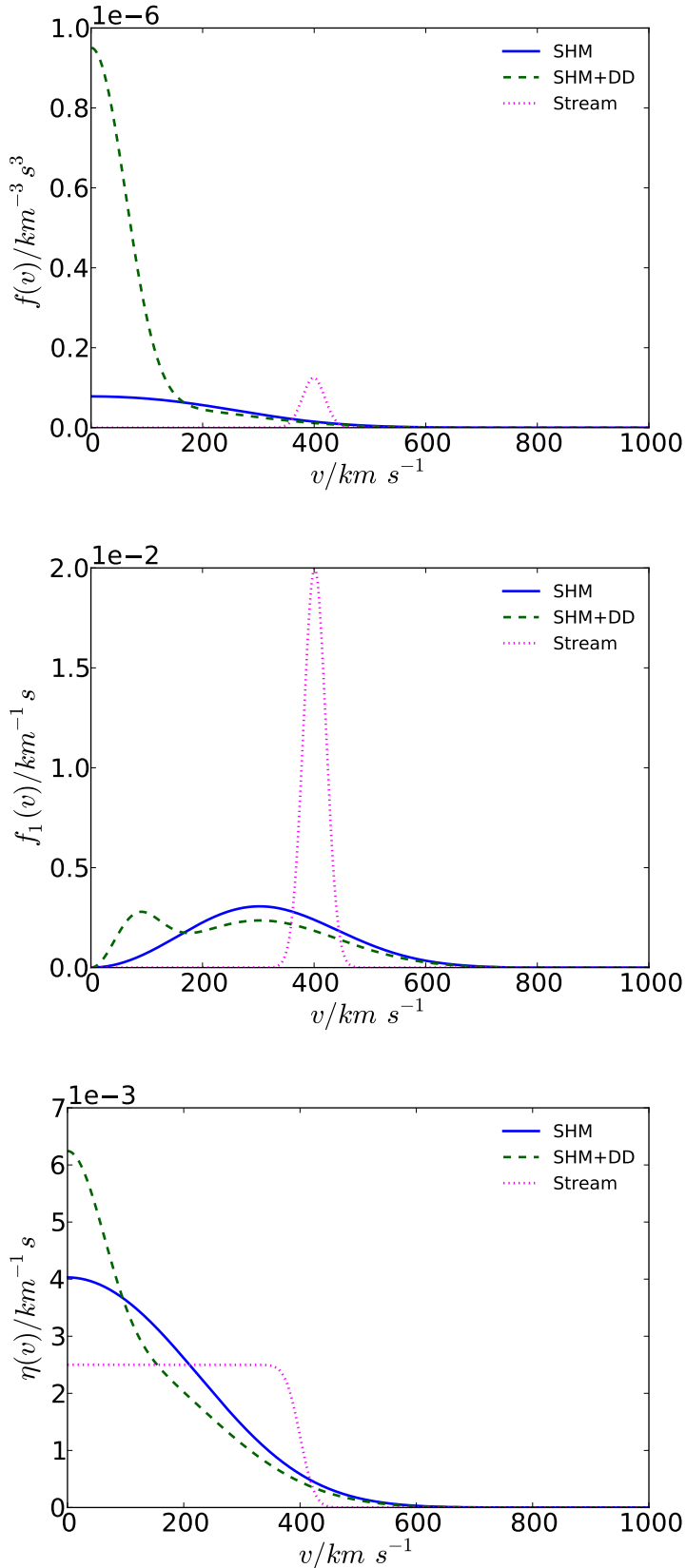


Figure 2.3: Some examples of possible dark matter speed distributions including the Standard Halo Model (SHM), SHM with a 30% dark disk overdensity (SHM+DD), and a stream centred around 400 km s^{-1} . We show the directionally averaged velocity distribution $f(v)$ (top panel), the speed distribution $f_1(v)$ (middle panel) and mean inverse speed $\eta(v)$ (bottom panel).

The impact of such uncertainties in the WIMP speed distribution has been much studied (see e.g. Refs. [317–319]) and it has been shown that poor assumptions about the speed distribution may result in biased reconstructions of the DM mass and cross sections from future direct detection data. Peter attempted to reconstruct the WIMP mass and SI cross section from mock data sets based on future direct detection experiments [318]. In order to generate the data, an SHM distribution function with an additional contribution from a dark disk was assumed. However, the posterior distribution for m_χ and σ_p^{SI} was obtained assuming that $f_1(v)$ could be well described by a single Maxwell-Boltzmann (MB) distribution (with average speed and speed dispersion included as nuisance parameters). The resulting marginalised 68% and 95% contours for m_χ and σ_p^{SI} are shown in Fig. 2.4, with the true parameter values given by the black crosses.

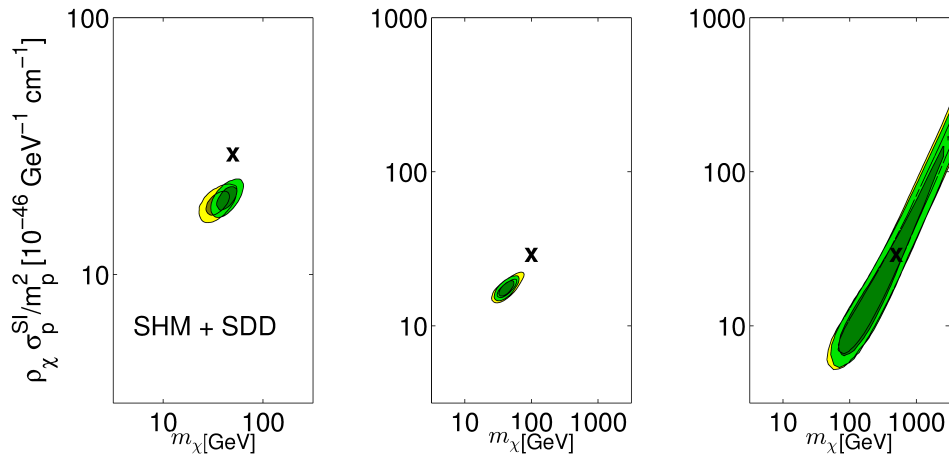


Figure 2.4: Reconstructed WIMP mass m_χ and SI cross section σ_p^{SI} using mock data from three future detectors. Data was generated assuming an SHM distribution with a contribution from a dark disk. However, the reconstruction was performed assuming that a Maxwell-Boltzmann speed distribution. Yellow regions show the 68% and 95% marginalised credible contours for conservative values of the maximum energy of the experimental search window, while green contours are the results extending the search window up to $E_{\text{max}} = 1$ MeV. Reproduced from Ref. [318].

Even including some uncertainties in the shape of the MB speed distribution, there is still a clear bias in the reconstructed WIMP parameters. The MB speed distribution cannot reproduce the shape of the event spec-

trum closely and the WIMP mass and cross section move to different values to compensate and improve the fit. Not only is there a bias, but the resulting contours are relatively small. In this case, if we trust the ansatz of an MB distribution, we would mistakenly believe that we had reconstructed the WIMP parameters accurately with a high precision.

It is unknown which, if any, of the many distributions discussed here best describes the true Galactic DM speed distribution. It is therefore imperative that we model the uncertainties in $f_1(v)$ in a general way to avoid bias in the reconstructed WIMP parameters. Chapter 3 addresses the various attempts to achieve this in the literature and explores what is required for such a general approach.

2.5 Conclusion

We have discussed the dark matter direct detection formalism, focusing on the contribution from scalar and axial-vector contact interactions. The non-relativistic speeds involved means that the event rate can be divided into a spin-dependent and spin-independent contribution. A number of sophisticated experiments have been and continue to be developed which should allow the rare nuclear recoils produced by these interactions to be detected. The use of different channels such as scintillation, ionisation and phonons not only allows the energy of these events to be measured but also aids discrimination against electronic recoils which can act as a significant background.

Tentative hints of a signal from the DAMA/LIBRA, CRESST-II and CoGeNT experiments have been interpreted as evidence for a WIMP with mass $m_\chi \sim 10$ GeV and cross section $\sigma_{SI} \sim 10^{-41}$ cm 2 . However, null results from XENON, CDMS and other experiments are in tensions with this claimed signal. The origin of this discrepancy may lie in unidentified backgrounds or in an unconventional model for DM; corroboration from indirect and collider experiments may be needed before such a signal can be confirmed.

Finally, there are a number of uncertainties associated with calculating direct detection event rates and therefore with interpreting data from these experiments. Nuclear uncertainties are typically more important for the SD rate than for the SI, though the method of Cerdeño et al. may be able to reduce the impact of such uncertainties. Particle physics uncertainties

are significant, though the standard contact operator approach should be a good first approximation and effective field theories extending beyond this standard approach are being developed. Uncertainties in the *number* of dark matter particles, embodied in the local DM density ρ_0 , lead to a factor of roughly 2 uncertainty in the total direct detection rate.

In contrast, uncertainties in the speed distribution of dark matter are poorly controlled. Theoretical and computational considerations indicate that the benchmark assumption - the SHM - is not a good description of the WIMP distribution and while a large number of alternatives are available, it is unclear which, if any, of these may be correct. The wide range of possibilities for $f_1(v)$, as well as the consequences for misinterpreting future data, indicate that taking these uncertainties into account in a general way is essential.

Chapter 3

Parametrising the WIMP distribution

As we have explored in Chapter 2, there are a number of uncertainties associated with calculating the direct detection event rate. These translate directly into uncertainties in the analysis of direct detection results, present and future. If these uncertainties are properly accounted for, they can provide more realistic estimates of uncertainties on the WIMP cross sections σ_p^{SI} and σ_p^{SD} and WIMP mass m_χ . If, however, our assumptions do not reflect the underlying nuclear physics, particle physics or astrophysics of dark matter, this can lead to a bias in the WIMP parameters. Understanding these uncertainties and how to mitigate them is therefore of great importance.

The WIMP speed distribution $f_1(v)$ enters into the direct detection event rate as it influences both the typical flux of dark matter particles and the typical recoil energy imparted during a scattering event. Unfortunately, the typical flux and recoil energy are also strongly dependent on the WIMP mass m_χ . This leads to a strong degeneracy between m_χ and $f_1(v)$ and, as discussed in Sec. 2.4.3, the possibility of significant bias in the reconstruction of the WIMP mass.

Because the speed distribution is so poorly constrained, an ideal goal would be to construct the most general parametrisation for $f_1(v)$ which can accommodate a wide range of possibilities for the true functional form. In Sec. 3.1, we explore previous attempts in the literature to account for uncertainties in the speed distribution and consider the properties which are required of any parametrisation of the speed distribution. A very gen-

eral approach was explored by Peter [318], who wrote down an empirical parametrisation for $f(v)$ as a series of constant bins in v . However, this still resulted in a bias in the reconstructed WIMP parameters. In Sec. 3.2, we analyse in more detail the performance of this method and attempt to explain where this bias comes from.

In Sec. 3.3 and Sec. 3.4, we discuss a method analogous to that of Peter but for parametrising the WIMP *momentum* distribution in terms of a series of constant bins. This transformation helps remove some of the degeneracy between the WIMP mass and distribution function and improves reconstructions of the mass compared to binning in $f(v)$. We also discuss how the speed distribution can be extracted from the momentum parameters. Finally, we discuss the weaknesses of this momentum parametrisation, highlighting where remaining work is needed.

3.1 Attempts to address the uncertainties in $f_1(v)$

Direct detection experiments are typically analysed within the framework of the Standard Halo Model (SHM), described in Chapter 2. A first step in extending the SHM is to incorporate uncertainties in v_{lag} , σ_v and v_{esc} in reconstructions. Strigari and Trotta [320] introduce a simple model of the Milky Way mass distribution, from which SHM velocity parameters can be derived. They then use projected stellar kinematics and direct detection data to fit both the model parameters and the dark matter properties. A more direct approach is to directly fit the SHM velocity parameters, incorporating their uncertainties into the fitting likelihood. This method has been considered by Peter [321], and is typically used as a simple model of astrophysical uncertainties (especially in studies which focus on other aspects of direct detection, e.g. Ref. [322]). These methods allow bias in the reconstructed WIMP parameters to be eliminated when the underlying speed distribution is indeed in the SHM form. However, as shown by Peter [318], these methods fail when the distribution function differs from the standard Maxwellian case.

There have also been attempts to incorporate and fit more realistic distribution functions. Pato et al. [323] incorporate astrophysical uncertainties by using the distribution function of Lisanti et al. [305] and fitting the

various shape parameters associated with it. In a more recent paper, Pato et al. [324] use projected direct detection data to fit a model of the Milky Way mass distribution, from which they derive a self-consistent distribution function (SCDF) using Eddington’s formula. This means that the resulting speed distribution will be consistent with the underlying potentials of the galaxy’s bulge, disk and dark matter, incorporating a broader range of shapes than the SHM alone. However, as the authors point out, velocity distributions from cosmological N-body simulations differ significantly from those expected from Eddington’s formula. As with the Standard Halo Model, fitting a realistically-motivated distribution function is likely to result in biased reconstructions if the true distribution deviates significantly from the functional form used for fitting.

Methods which make no assumptions about the functional form of the speed distribution have had mixed success. Drees and Shan [325, 326] developed a method for estimating the WIMP mass by calculating moments of the speed distribution. However, this method still introduces a bias into the reconstructed WIMP mass and performs more poorly for heavier WIMPs and when finite energy thresholds are considered. An empirical ansatz for the speed distribution has also been suggested, specifically dividing the WIMP speed into a series of bins, with the distribution being constant within each bin [318]. However, both of these still result in a significant bias in the reconstructed mass and cross section. A recent proposal by Feldstein and Kahlhoefer [327] is to fit the velocity *integral* rather than the speed distribution. This proposal is the most promising so far and appears to give an unbiased reconstruction of the mass, though reconstructing the speed distribution itself remains problematic.

Finally, a method for analysing existing data has been developed by various authors [239, 240, 328]. At a given mass, a given experiment is sensitive only to speeds in a fixed range, set by $v_{\min}(E_{\min})$ and $v_{\min}(E_{\max})$. By considering only the range of speeds where two or more experiments overlap, one can ensure that the astrophysical contribution to both experiments is equal. This method has typically been used to assess the compatibility of different data sets and to set more robust limits on the WIMP interaction cross sections. Recently it has also been extended to accomodate more general forms for the WIMP interactions [329].

3.1.1 Considerations in parametrising $f_1(v)$

Given the range of possibilities for the form of the speed distribution, we want to consider parametrisations which are as general as possible. We discuss now some of the challenges and considerations which must be taken into account for such parametrisations. We can write the integral over the speed distribution as

$$\eta(v_{\min}) \equiv \int_{v_{\min}}^{\infty} \frac{f_1(v)}{v} dv, \quad (3.1)$$

where v_{\min} is given by

$$v_{\min} = v_{\min}(E_R, m_\chi, m_N) = \sqrt{\frac{m_N E_R}{2\mu_{\chi N}^2}}. \quad (3.2)$$

If we treat $f_1(v)$ as a free function (subject to the condition that it be normalised to unity and everywhere positive), this is equivalent to treating $\eta(v_{\min})$ as a free function (subject to the equivalent condition that η be a monotonically decreasing function of v_{\min}). This represents an entirely agnostic approach to $f_1(v)$, assuming that we know nothing at all about its functional form. Unfortunately, if we fix m_N , any change in the form of η can be counteracted by a change in m_χ (and a resulting change in v_{\min}) leading to the same spectral shape $\eta(E_R)$. This means that for a single experiment, the WIMP mass and $f(v)$ are exactly degenerate and we need multiple experiments to disentangle the two [326]. We will phrase this in more concrete terms later in Sec. 3.3.

Another consideration when parametrising $f_1(v)$ is the range of sensitivity of the experiments. Each experiment will have a window of recoil energies to which it is sensitive $[E_{\min}, E_{\max}]$ (though the recoil detection efficiency may vary across this window). This means that for a given WIMP mass, each experiment will be sensitive only a range of WIMP speeds $[v_{\min}(E_{\min}), v_{\min}(E_{\max})]$. WIMPs with speeds smaller than $v_{\min}(E_{\min})$ do not contribute to the velocity integral defined in Eq. 3.1. WIMPs with speeds above $v_{\min}(E_{\max})$ can contribute to the overall spectrum, but they contribute only a constant, additive rate; the experiment is not sensitive to the *shape* of the speed distribution above this maximum speed. If we wish to probe the shape of $f_1(v)$, the range of speeds probed by each experiment must have some overlap. Otherwise, the $f_1(v)$ can be varied independently across each speed range and the degeneracy between m_χ and $f_1(v)$ remains.

In order to get a handle on $f_1(v)$ (and simultaneously the WIMP mass and cross sections) we therefore need several direct detection experiments, which use different target materials but which probe overlapping WIMP speeds. However, we must come up with a way of writing our general function $f_1(v)$ which allows us to reconstruct it by fitting to the data. Such a parametrisation should correspond to a physical distribution function. This gives two important conditions on the speed distribution:

- (i) it should be normalised to unity

$$\int_0^\infty f_1(v) \, dv , \quad (3.3)$$

- (ii) and it should be everywhere positive

$$f_1(v) \geq 0 \text{ for all } v . \quad (3.4)$$

Subject to these constraints, we should try to write down a parametrisation which spans a wide range of underlying distribution functions and which does not introduce any additional bias into attempts to reconstruct the WIMP parameters. For this reason, it is necessary to carefully test any proposed parametrisation. We now explore in more detail several proposals for what such a general parametrisation could look like.

3.2 Binned speed distribution

Peter proposed the use of an empirical speed distribution in the form of series of bins in speed v in order to fit to data. Explicitly, we write the directionally-averaged velocity distribution (in the Earth frame), as a series of N bins of constant value, with bin edges $\{\tilde{v}_i\}$:

$$f(v) = \sum_{i=1}^N g_i W(v; \tilde{v}_i, \Delta v) , \quad (3.5)$$

where the top-hat function, W , is defined as:

$$W(v; \tilde{v}_i, \Delta v) = \begin{cases} 1 & v \in [\tilde{v}_i, \tilde{v}_i + \Delta v] \\ 0 & \text{otherwise.} \end{cases} \quad (3.6)$$

We must choose a maximum speed $v_{\max} = N\Delta v$ up to which we parametrise. Beyond this speed, we set $f(v)$ to zero, so we should choose a conservative value which does not risk truncating the speed distribution prematurely. Based on the results of the RAVE surveys [194, 195], the Galactic escape speed is estimated to be $v_{\text{esc}} < 587$ at the 90% confidence level. Assuming a local circular speed of $v_c \sim 220 \text{ km s}^{-1}$ [298, 299], this means that in the Earth frame, particles with speeds significantly higher than $v_c + v_{\text{esc}} \sim 800 \text{ km s}^{-1}$ should not be gravitationally bound. This is consistent with results for the local escape speed obtained in N-body simulations [309]. We therefore choose a value $v_{\max} = 1000 \text{ km s}^{-1}$ as a conservative upper limit for the parametrisation.

The form for the distribution function given in Eq. 3.5 is the directionally-averaged WIMP velocity distribution, $f(v)$. The WIMP *speed* distribution is then given by

$$f_1(v) = \sum_{i=1}^N g_i v^2 W(v; \tilde{v}_i, \Delta v). \quad (3.7)$$

Imposing normalisation of the speed distribution, we obtain the following constraint on the $\{g_i\}$:

$$\sum_{i=1}^N g_i \left[(\tilde{v}_i + \Delta v)^3 - \tilde{v}_i^3 \right] / 3 = 1. \quad (3.8)$$

For notational convenience, we also define

$$\hat{g}_i = g_i \left[(\tilde{v}_i + \Delta v)^3 - \tilde{v}_i^3 \right] / 3, \quad (3.9)$$

such that the normalisation condition becomes

$$\sum_{i=1}^N \hat{g}_i = 1. \quad (3.10)$$

We illustrate the form of this binned distribution for $f(v)$ in Fig. 3.1. We show the Standard Halo Model in the Earth frame (blue line) as well as the binned approximation to the SHM (red line). This approximation is obtained by integrating the WIMP speed distribution over each of the bins:

$$\hat{g}_i^{\text{approx}} = \int_{\tilde{v}_i}^{\tilde{v}_i + \Delta v} f_1^{\text{SHM}}(v) dv. \quad (3.11)$$

This allows us to examine how closely the binned parametrisation can be used to approximate the SHM. However, in a realistic scenario, these bin parameters $\{\hat{g}_i\}$ would form part of the parameter space, along with m_χ and σ_p , which must be explored based on the data.

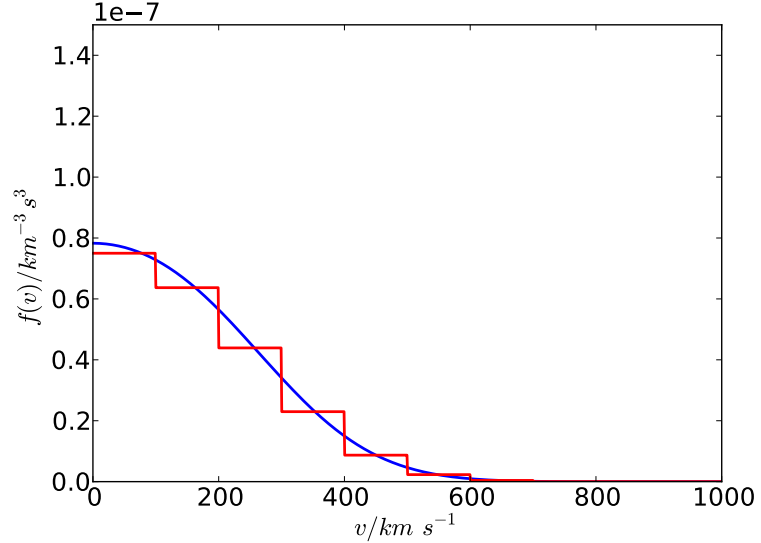


Figure 3.1: Binned approximation to the SHM in the Earth frame. The bin heights are obtained from Eq. 3.11. We note that shown here is $f(v)$, the directionally-averaged velocity distribution. We must multiply by v^2 to obtain the speed distribution $f_1(v)$.

In Ref. [318], Peter found evidence that this method still leads to a bias in the reconstructed WIMP mass and cross section, despite the apparent generality of this binned distribution function. Increasing the number of speed bins did not appear to alleviate this problem. Here, we explore this method further. In particular, we consider a large number of realisations of data sets from hypothetical future experiments, assuming some fiducial benchmark model. We then attempt to reconstruct the WIMP mass for each realisation, allowing us to determine how the method performs statistically and whether the bias found by Peter is present in all data sets or only in a small number of Poissonian realisations.

3.2.1 Experiments and benchmark parameters

We consider three next-generation detectors, modelled on experiments which are currently in development: XENON1T [330], WArP [331] and SuperCDMS [332]. Each experiment is characterised by the (suitably averaged)

Experiment	Target Mass, A	Detector Mass (fid.), m_{det}/kg	Efficiency, ϵ	Energy Range/keV
Xenon	131	1000	0.17	2-30
Argon	40	1000	1.0	30-130
Germanium	73	100	0.3	10-100

Table 3.1: Parameter values for the three mock experiments used in this chapter, chosen to closely match those used in Ref. [318]. The Xenon experiment is modelled on Xenon1T [330], the Argon experiment on WArP [331] and the Germanium experiment on SuperCDMS [332]. An exposure of $t_{\text{exp}} = 1$ years is used for all 3 experiments. The meanings of the experimental parameters are described in Sec. 3.2.1.

mass number A of the target nucleus, a fiducial detector mass m_{det} , an efficiency ϵ , and a pair of energies, E_{\min} and E_{\max} , which mark the extent of the signal region. The efficiency of each experiment incorporates information about detection efficiency, as well as data cuts and detector down-time. Table 3.1 shows the experimental parameters used in this chapter, which are chosen to approximately match those used by Peter [318]. For all three experiments, we assume an exposure time of $t_{\text{exp}} = 1$ year.

We assume that the detector efficiency is independent of energy. We also assume perfect energy resolution and zero backgrounds. For a real experiment, these assumptions will almost certainly not hold, for example due to variations in the relative scintillation efficiency of Xenon [333], but the results presented here should be viewed as a proof of principle in the ideal case.

Figure 3.2 shows the minimum and maximum accessible WIMP speeds for each experiment. All three experiments rapidly become insensitive to WIMPs with speeds less than $\sim 1000 \text{ km s}^{-1}$ as the WIMP mass drops below $m_\chi \sim 10 \text{ GeV}$. This suggests that the experiments considered here generically have a low sensitivity to such light WIMPs, producing too few events for accurate parameter reconstruction.

For comparison with later methods, we consider here a single benchmark model: $m_\chi = 50 \text{ GeV}$, $\sigma_p^{\text{SI}} = 10^{-44} \text{ cm}^2$ and the SHM (with $v_{\text{lag}} = 220 \text{ km s}^{-1}$).¹ We assume that the spin-dependent contribution to the event

¹At the time that Ref. [318] and Ref. [1] were published this value of the cross section had not yet been probed. However, the value $\sigma_p^{\text{SI}} = 10^{-44} \text{ cm}^2$ has since been excluded

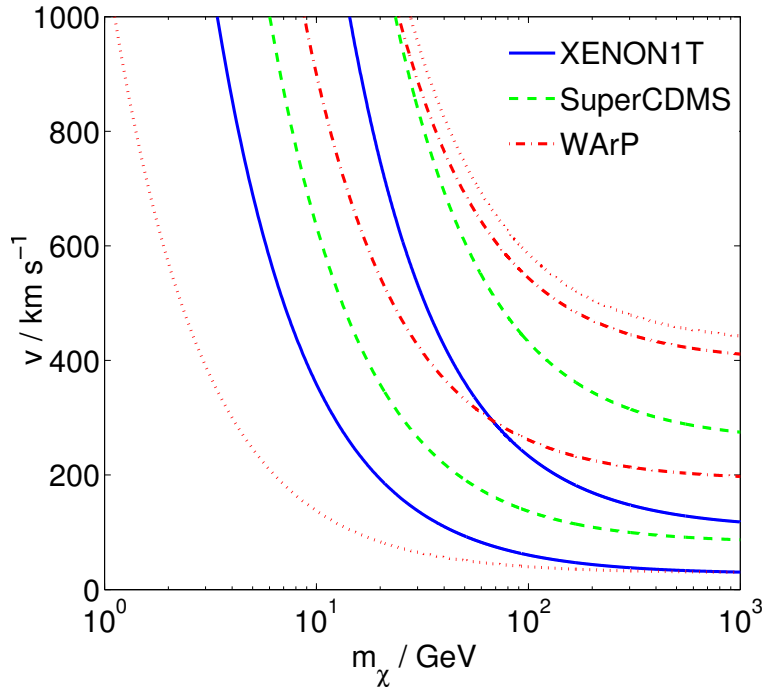


Figure 3.2: Range of accessible WIMP speeds for each of the three mock experiments: XENON1T-like (solid blue), SuperCDMS-like (dashed green) and WArP-like (dot-dashed red). Each pair of lines corresponds to the maximum and minimum accessible WIMP speeds for a given experiment. The outermost dotted red lines show the accessible speeds for the adjusted parametrisation range described in Sec. 3.4. Reproduced from Ref. [1].

rate is negligible, as the A^2 enhancement leads to SI rate to dominate for heavy targets. This also allows us to disentangle degeneracy between σ_p^{SI} and σ_p^{SD} from the astrophysical uncertainties we consider here. We assume a fixed value for the local DM density $\rho_0 = 0.3 \text{ GeV cm}^{-3}$. **Check this**
*–*As will be explained in Sec. 3.4, the precise values of σ_p^{SI} and ρ_0 are not particularly important due to the degeneracy between these two parameters. The total number of events from all three detectors combined typically ranges from around 300 to 600 for the different benchmark parameters which will be considered in this chapter.

3.2.2 Parameter reconstruction

We generate 250 mock data sets using the experiments described above. Each realisation of the mock data is generated as follows:

by several experiments [184, 247].

1. Calculate the number of expected events N_e , given $\{m_\chi, \sigma_p^{\text{SI}}, f(v)\}$, using Eq. 2.29,
2. Pick the number of observed events N_o from a Poisson distribution with mean N_e ,
3. Pick recoil energies $\{E_1, E_2, \dots, E_{N_o}\}$, from the distribution $P(E_R)$

$$P(E_R) = \frac{\epsilon m_{\text{det}} t_{\text{exp}}}{N_e} \frac{dR}{dE_R}, \quad (3.12)$$

4. Repeat for all three experiments.

We then use the Markov Chain Monte Carlo (MCMC) package CosmOMC [334] to make parameter inferences on the parameters $m_\chi, \sigma_p^{\text{SI}}, \{\hat{g}_i\}$, where \hat{g}_i are the bin parameters for a 5 bin speed distribution function. We sample the WIMP mass and cross-section logarithmically in the ranges $[10, 1000]$ GeV and $[10, 10000] \times 10^{-47}$ cm 2 respectively, with log-flat priors on both. We sample the \hat{g}_i linearly in the range $[0, 1]$, subject to the normalisation constraint of Eq. 3.10. In order to ensure adequate exploration of the parameter space, we perform the MCMC at a temperature $T = 2$. That is, we explore the high temperature likelihood $\mathcal{L}^{1/T}$ and subsequently ‘cool’ the chains back down to $T = 1$ (see e.g. Refs. [335, 336]). We sample using a total of 3×10^5 chain positions, which is then thinned by a factor of 50.

The likelihood function used to generate the Markov chains is the same unbinned form used by CDMS [206] and XENON100 [216], which for a single experiment is:

$$\mathcal{L}_1 = \frac{N_e^{N_o} e^{-N_e}}{N_o!} \prod_j^{N_o} P(E_j). \quad (3.13)$$

The full likelihood \mathcal{L} is then the product of the likelihoods for the three separate experiments.

The distribution of MCMC chain positions gives the posterior probability distribution $\mathcal{P}(\theta)$ for the parameters θ . The value which maximises the posterior probability is taken as a best estimate of the underlying parameter. In order to obtain 1-dimensional parameter limits, we consider the marginalised posterior distribution $\mathcal{P}_m(\theta)$, which is obtained by integrating $\mathcal{P}(\theta)$ over all the parameters other than the parameter of interest. We then construct minimal credible intervals for the parameter of interest at the $p\%$ level.

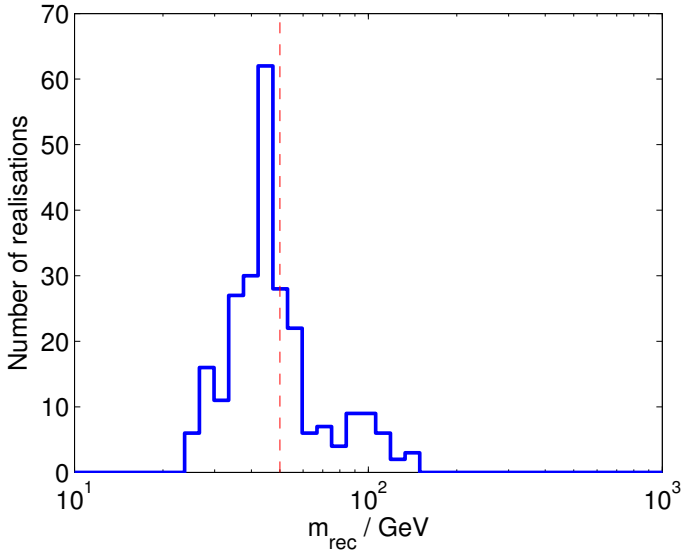


Figure 3.3: WIMP masses reconstructed using the binned speed parametrisation method from 250 realisations. The benchmark speed distribution is the SHM. The true mass of 50 GeV is shown as a dashed vertical line. Reproduced from Ref. [1].

3.2.3 Results

Figure 3.3 shows the fitted values for the WIMP mass, m_{rec} , obtained from 250 mock datasets. This distribution shows a peak around 45 GeV, as well as a significant number of datasets reconstructed at ~ 100 GeV. As pointed out by Ref. [337], some mock datasets will not be representative of the underlying benchmark parameters, having more events at high energies than expected, for example. This can lead to ‘bad’ reconstructions with a fitted WIMP mass higher than the benchmark value. Thus, the reconstructions near 100 GeV do not necessarily signify a failure of the reconstruction method.

However, we can also study the coverage of the $p\%$ credible intervals: the fraction of reconstructions for which the true WIMP mass lies within the $p\%$ interval. For the 68% and 95% confidence intervals, this method shows significant under-coverage: $36 \pm 3\%$ coverage and $63 \pm 3\%$ coverage respectively. This indicates that while the mass reconstructions appear to be distributed close to the true value (within around 5-10 GeV), the corresponding error estimates must be too small. The bias noted by Peter is therefore a real effect and is sizeable compared to the statistical uncertainty on m_χ . We therefore cannot trust the WIMP mass reconstructed using this parametrisation.

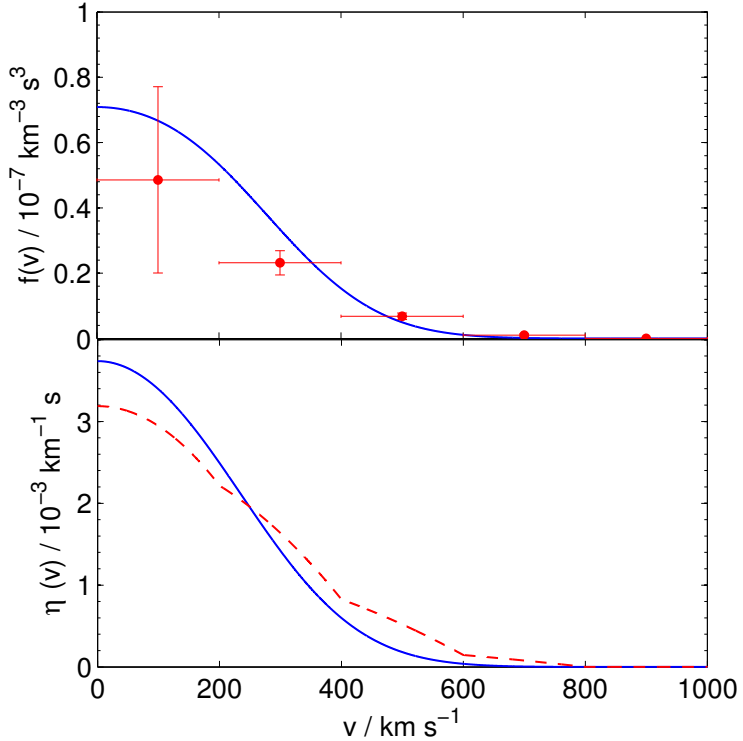


Figure 3.4: Reconstructed speed distribution, $f(v)$, and mean inverse speed, $\eta(v)$, using the speed parametrisation method. The benchmark model used was a 50 GeV WIMP with an SHM speed distribution. The upper panel shows the underlying SHM speed distribution (solid blue) and the fitted values of the speed bin parameters (red points). The lower panel shows the mean inverse speed corresponding to these fitted values (dashed red line) and the true mean inverse speed (solid blue). Reproduced from Ref. [1].

Figure 3.4 shows the reconstructed speed distribution for a typical realisation using this method. The reconstructed mass is $m_{\text{rec}} = 30.2^{+4.5}_{-3.9} \text{ GeV}$, compared to the benchmark value of 50 GeV. The mean inverse speed is under-estimated in the range $0 - 200 \text{ km s}^{-1}$ and slightly over-estimated at higher speeds. However, the reduced m_{rec} increases the minimum accessible speed of the experiments, meaning that the experiments are less sensitive to the shape of the speed distribution at low speeds. Moreover, a reduced value of the reconstructed mass serves to steepen the spectrum, reconciling the flattened $\eta(v_{\text{min}})$ at high speeds with the data. This is because varying the mass of the WIMP ‘rescales’ the spectrum, due to the relation $E_{\text{R}} \propto \mu_{\chi N}^2 v_{\text{min}}^2$.

In Fig. 3.5, we plot η/m_{χ} as a function of recoil energy, E_{R} , for the SuperCDMS-like experiment. We rescale η by $1/m_{\chi}$ because this factor

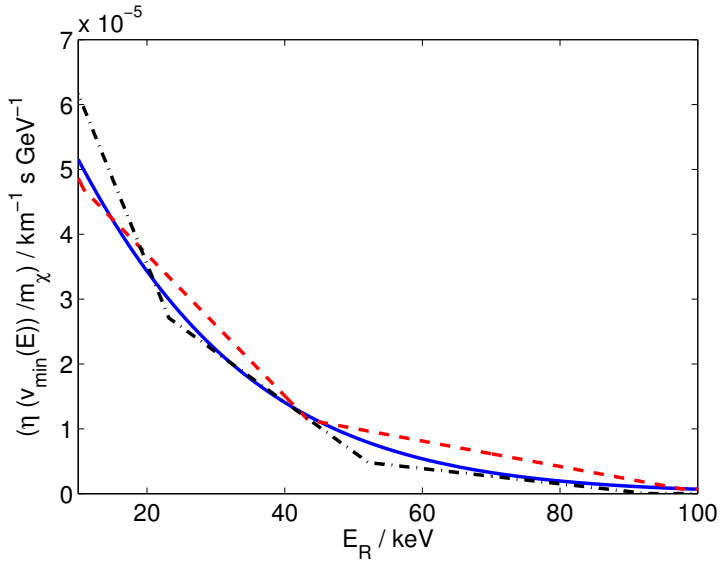


Figure 3.5: The rescaled mean inverse speed, η/m_χ , measured in the SuperCDMS-like experiment as a function of recoil energy, E_R . The same mock dataset was used as in Fig. 3.4. The underlying Standard Halo Model distribution (solid blue) uses the true WIMP mass of 50 GeV, as does the binned approximation to the SHM (dashed red). The reconstructed mean inverse speed (dot-dashed black) uses the reconstructed value of 30 GeV. Reproduced from Ref. [1].

appears in the event rate and we are then able to compare the spectra of events from different models. The solid line shows the mean inverse speed in the SHM, using the true WIMP mass of 50 GeV. We also show a binned approximation to the SHM (dashed line) obtained using the ‘true’ values of the bin parameters $\{g_i^{\text{approx}}\}$ and the true WIMP mass. Finally, we show the reconstructed mean inverse speed (dot-dashed line) using the reconstructed WIMP mass of 30 GeV. We see that the binned approximation to the SHM, which should represent a ‘good’ reconstruction, actually recovers the spectrum poorly compared to the reconstructed values. In particular, we note the energy range of the experiment spans two bins in the binned approximation to the SHM, but three bins in the MCMC reconstruction, allowing a closer approximation to the true spectrum.

Thus, the speed distribution parameters can be explored to provide a good fit to the data, with the reconstructed mass varying to compensate. As can be seen from Fig. 3.5, for a fixed bin width in velocity space, the size of bins in energy space can be reduced by moving to lower masses. This should allow a closer fit to the data and may explain why there appears to be a bias towards lower mass values. In the next section, we explore a

possible way to reduce this bias by attempting to size of the bins from the value of m_χ .

3.3 Momentum parametrisation for a single experiment

When considering the speed distribution of the WIMPs, we see that each experiment has a different range of sensitivity and that varying the WIMP mass changes this range. However, we can instead consider a ‘reduced WIMP-nucleus momentum’,

$$\mathbf{p}_N = \mu_{\chi N} \mathbf{v}, \quad (3.14)$$

defined separately for each target nucleus. We now note that the accessible range in \mathbf{p}_N for each experiment is independent of the WIMP mass:

$$p_{\min}(E_R) = \mu_{\chi N} v_{\min}(E_R) = \sqrt{\frac{m_N E_R}{2}}. \quad (3.15)$$

We therefore rewrite the differential event rate in terms of the new momentum variable:

$$\frac{dR}{dE_R} = \frac{\rho_0 \sigma_p \mu_{\chi N}}{2 \mu_{\chi p}^2 m_\chi} A^2 F^2(E_R) \tilde{\eta}(p_{\min}), \quad (3.16)$$

where $\tilde{\eta}$ is the mean inverse *momentum* associated with the reduced momentum distribution, $\tilde{f}(\mathbf{p})$:

$$\tilde{\eta}(p_{\min}) = \int_{p_{\min}}^{\infty} \frac{\tilde{f}(\mathbf{p})}{p} d^3 \mathbf{p} = \frac{1}{\mu_{\chi N}} \eta(p_{\min}/\mu_{\chi N}). \quad (3.17)$$

The event rate can be rewritten as:

$$\frac{dR}{dE_R} = \frac{\rho_0}{2} D(\sigma_p, m_\chi, m_N) A^2 F^2(E_R) \tilde{\eta}(p_{\min}), \quad (3.18)$$

where we have defined

$$D(\sigma_p, m_\chi, m_N) = \frac{\sigma_p \mu_{\chi N}}{\mu_{\chi p}^2 m_\chi}, \quad (3.19)$$

which encodes all information about the WIMP mass and cross-section and controls the overall scale of the event rate.

If we consider only a single experiment, is it possible to parametrise $\tilde{f}(\mathbf{p})$ and therefore reconstruct the value of D ? We can again define a

directionally averaged momentum distribution, $\tilde{f}(p) = f(p/\mu_{\chi N})/\mu_{\chi N}^3$, and parametrise this in terms of 5 constant bins, with bin values $\{h_i\}$. It is then only necessary to parametrise $\tilde{f}(p)$ over the range of sensitivity of the experiment: $p \in [p_a, p_b]$, where $p_{a,b} = p_{\min}(E_{\min,\max})$. This means that we need not make any assumptions about the distribution function outside the range of sensitivity of the experiment. However, we still wish to impose some normalisation constraint on the momentum distribution parameters. Each experiment now probes a well-defined (but unknown) fraction of WIMPs, α_N , given by

$$\alpha_N = \int_{p_a}^{p_b} f(p) p^2 dp. \quad (3.20)$$

The momentum parameters are therefore normalised according to

$$\sum_{i=1}^N \hat{h}_i = \alpha_N, \quad (3.21)$$

where \hat{h}_i is defined analogously to \hat{g}_i in Eq. 3.10. We absorb the unknown α_N into D , such that the momentum distribution parameters, $\{\hat{h}_i/\alpha_N\}$, are normalised to unity and

$$D(\sigma_p, m_\chi, m_N) = \alpha_N \frac{\sigma_p \mu_{\chi N}}{\mu_{\chi p}^2 m_\chi}. \quad (3.22)$$

Finally, it is necessary to introduce a parameter A which models the constant contribution to η from WIMPs with momenta greater than p_b :

$$A = \int_{p_{\min}(E_{\max})}^{\infty} \frac{\tilde{f}(\mathbf{p})}{p} d^3\mathbf{p}. \quad (3.23)$$

Because the precise form of $\tilde{f}(p)$ above the upper energy threshold is undetermined by the experiment, the contribution of A to the normalisation, α_N , cannot be calculated and is therefore not considered. Instead, we include conservative constraints on A such that its contribution alone cannot exceed the normalisation of $\tilde{f}(p)$:

$$A < (p_{\min}(E_{\max}))^{-1}. \quad (3.24)$$

We also note that

$$\int_{p_a}^{p_b} \frac{\tilde{f}(\mathbf{p})}{p} d^3\mathbf{p} \leq \frac{\alpha_N}{p_b}, \quad (3.25)$$

and thus impose the following additional constraint on the parameters:

$$\frac{1}{\alpha_N} [\eta(p_a) - \eta(p_b)] \leq \frac{1}{p_b}. \quad (3.26)$$

We therefore perform parameter reconstructions using the parameters D , $\{h_i/\alpha_N\}$ and A/α_N . Because the fraction of high momentum WIMPs is expected to be relatively low, we sample the parameter A logarithmically, with a log-flat prior.

3.3.1 Results

We consider again a single set of benchmark parameters, namely a 50 GeV WIMP with an SHM speed distribution. We apply the momentum parametrisation to mock datasets from the WArP-like Argon experiment. The reconstructed D values, D_{rec} , are shown in Fig. ?? in units of $10^7 \text{ cm}^2 \text{ kg}^{-2}$. In all reconstructions, the posterior distribution is unimodal, having separate parameters to describe the scale (D) and shape ($\{h_i\}$) of the event rate. The number of reconstructions is peaked at the correct value. The average reconstructed value is $\log_{10}(D)_{\text{rec}} = 1.865 \pm 0.004$, compared to the input value of $\log_{10}(D)_{\text{true}} = 1.878$. This represents a slight bias (of less than 1%) towards smaller values of $\log_{10}(D)$.

However, this is smaller than the typical statistical uncertainty in a single reconstruction, which is $\sim 4\%$. In addition, this method results in *overcoverage* of the true parameter, with values of $76 \pm 2\%$ and $98 \pm 1\%$ respectively for the 68% and 95% confidence intervals. This method therefore allows us to place reliable conservative estimates on the parameter D .

We show in Fig. 3.7 the reconstructed momentum distribution and mean inverse momentum for a typical realisation, for which the reconstructed $\log_{10}(D)$ value is $1.81^{+0.09}_{-0.05}$. The underlying momentum distribution has been rescaled by $1/\alpha_{\text{Ar}}$ to allow a comparison to the reconstructed values. We see that the the momentum distribution is well reconstructed and the mean inverse momentum is accurately recovered at low and high momenta. In the middle of the momentum range, however, $\tilde{\eta}(p_{\min})$ exceeds the true value. Because only a single experiment is being used, the measured spectrum is particularly susceptible to Poisson fluctuations. The mock dataset used here has a slight excess of events around $E_R \approx 60 \text{ keV}$, corresponding to $p_{\text{Ar}} \approx 30 \text{ MeV}$, which may explain the reconstructed excess.

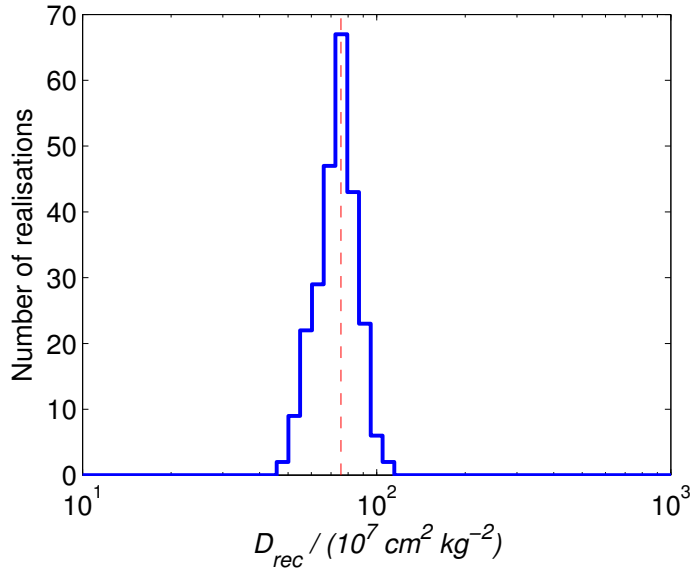


Figure 3.6: Reconstructed values for the scale parameter, D_{rec} , for the Argon experiment using the momentum parametrisation method from 250 realisations. The benchmark speed distribution is the SHM. The value of $D_{\text{true}} = 75.6 \times 10^7 \text{ cm}^2 \text{ kg}^{-2}$ is shown as a dashed vertical line. Reproduced from Ref. [1].

In addition, this may be a consequence of the particular parametrisation. The constant-bin parametrisation of $\tilde{f}(p)$ leads to a parametrised $\tilde{\eta}(p_{\min})$ which is concave downwards in each bin, while the underlying function is strictly convex downwards in this region. Thus, $\tilde{\eta}(p_{\min})$ tends to be slightly overestimated, leading the scale parameter D to be reduced to compensate for this. With datasets containing more events, the number of bins could be increased, in order to reduce this bias on D and maintain it at below the level of the statistical uncertainty.

3.4 Momentum parametrisation for several experiments

The reduced momentum method allows us to extract information from a single experiment, making no assumptions about the underlying velocity (or momentum) distribution. However, information about the mass and cross-section are encoded in the parameter, D , and cannot be extracted using a single experiment alone. We now extend the method to use data from several detectors.

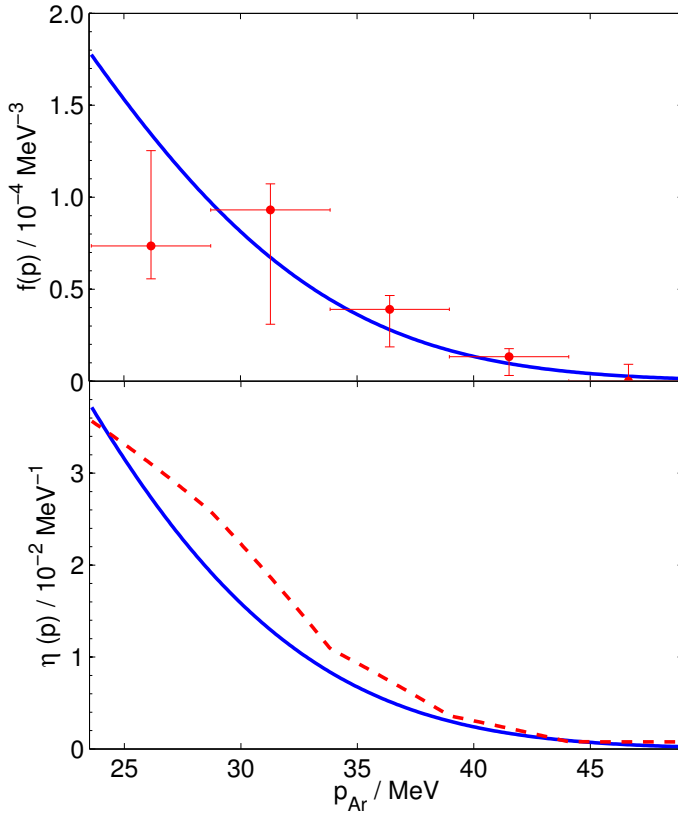


Figure 3.7: Reconstructed momentum distribution for a single Argon experiment using a benchmark of a 50 GeV WIMP and the SHM. The upper panel shows the SHM momentum distribution (solid blue) and reconstructed bin values (red points). Because the posterior is unimodal, we also display vertical errorbars showing the extent of the 68% confidence region for each bin. Note that these errors are strongly correlated. The lower panel shows the corresponding reconstructed mean inverse momentum (dashed red) and the mean inverse momentum in the SHM (solid blue). The underlying distribution has been rescaled by $1/\alpha_{\text{Ar}}$ for comparison to the reconstructed values. Reproduced from Ref. [1].

Because a different momentum variable p_N can be defined for each experiment, it is necessary to choose a single experiment and parametrise the momentum distribution defined with respect to that experiment. It may be necessary to adjust the lower and upper limits of the parametrisation (beyond the values of E_{\min} and E_{\max} used in the experiment) to accommodate as much of the data as possible from all experiments. In the single experiment considered in Section 3.3, the WIMP-Ar momentum was parametrised in the range $p_{\text{Ar}} \in [23.6, 49.2]$ MeV, to match the sensitivity of the Argon experiment. However, as can be seen in Fig. 3.2, this

sensitivity window does not match that of the other experiments. If we extend this interval, and parametrise in the range $p_{\text{Ar}} \in [3.6, 53.0]$ MeV, we can enclose the sensitivity regions of all three experiments as closely as possible, as shown by the dotted curves in Fig. 3.2. We again use 5 bins in momentum space, with an additional parameter to control a constant offset.

In theory, any of the three experiments could have been chosen to define the momentum variable. However, some choices of experiment are less practical. For example, in order to use the XENON1T-like experiment, it would be necessary to parametrise the momentum over the range $p_{\text{Xe}} \in [11, 162]$ MeV. This is because at high WIMP masses the remaining two experiments have maximum accessible speeds of $\sim 500 \text{ km s}^{-1}$. This corresponds to very high values of the WIMP-Xe reduced momentum because of Xenon’s comparatively higher mass. A large number of bins would be required to cover this wide momentum range and accurately model structures in the distribution function. Owing to the Galactic escape speed, many of these bins would have a value of zero, making parametrisation with respect to the XENON1T-like experiment a poor choice.

By comparison, using the WArP-like Argon experiment allows us to parametrise only as much of the momentum space as required to accommodate data from all three experiments. In the speed parametrisation method, varying the WIMP mass altered the size and number of energy bins to which the experiments were sensitive. However, for a given range of reduced WIMP-Argon momenta, the corresponding energy range probed by each experiment depends less strongly on m_χ (and is independent of m_χ for the Argon experiment itself). This means that the number of bins probed by each experiment should not vary significantly as a function of WIMP mass. For a fixed bin width in momentum space, the bin width in energy space is also much less sensitive to the WIMP mass. This should help reduce the bias observed in the binned speed parametrisation.

Unfortunately, this method does not allow the WIMP-nucleon cross-section to be extracted; because the contributing WIMP fraction, α , is unknown, we can only obtain a lower bound. This is a fundamental limitation of any method which makes no assumptions about the underlying speed distribution. Without knowing the fraction of WIMPs with speeds within the signal window of the experiment, we cannot determine the cross-section. However, the cross-section appears in the event rate only through

	Speed Method	Momentum Method
68% Coverage	$36 \pm 3\%$	$71 \pm 3\%$
95% Coverage	$63 \pm 3\%$	$92 \pm 2\%$

Table 3.2: Coverage statistics for the speed and momentum parametrisation methods for a 50 GeV SHM benchmark model.

the degenerate combination $\sigma_p \rho_0$. As discussed in Sec. 2.4.3, estimates of ρ_0 typically carry a factor of around 2 uncertainty. Thus, any estimate of the WIMP-nucleon interaction cross-section would have an inherent uncertainty in any case.

3.4.1 Results

We first compare results for the momentum method to the speed parametrisation method presented in Section 3.2. We use the same mock datasets generated for the 50 GeV, SHM benchmark presented previously. The results of both the momentum and speed methods are shown in Fig. 3.8. In the case of the momentum method, the distribution of realisations is now more closely peaked around the true mass of 50 GeV. Furthermore, the momentum method produces substantially improved coverage properties, as summarised in Table 3.2. It should be noted that compared to the speed method, the momentum method leads to a larger number of reconstructions at high WIMP mass. It is not clear whether this signals a failure of the momentum method in certain cases or whether these are representative of ‘bad’ reconstructions, as will be discussed shortly.

Figure 3.9 shows the reconstructed WIMP-Argon momentum distribution using the same mock dataset as used for Fig. 3.4. The benchmark distributions have been rescaled by α so that they can be compared to the reconstructed values. In this case, $\alpha = 0.995$, so we can reconstruct both the mass and cross section accurately: $\log_{10}(m_{\text{rec}}/\text{GeV}) = 1.62 \pm 0.31$ and $\log_{10}(\sigma_p/10^{-47} \text{ cm}^2) = 2.99 \pm 0.18$, compared to the true values of $\log_{10}(m_{\text{true}}/\text{GeV}) = 1.699$ and $\log_{10}(\sigma_p/10^{-47} \text{ cm}^2) = 3.0$. While there is no way to know *a priori* whether α will be close to unity, the accurate reconstruction of the mass, cross-section and momentum distribution show that momentum parametrisation can offer a significant improvement over the speed parametrisation method.

We now present the results of the momentum method for a wider range

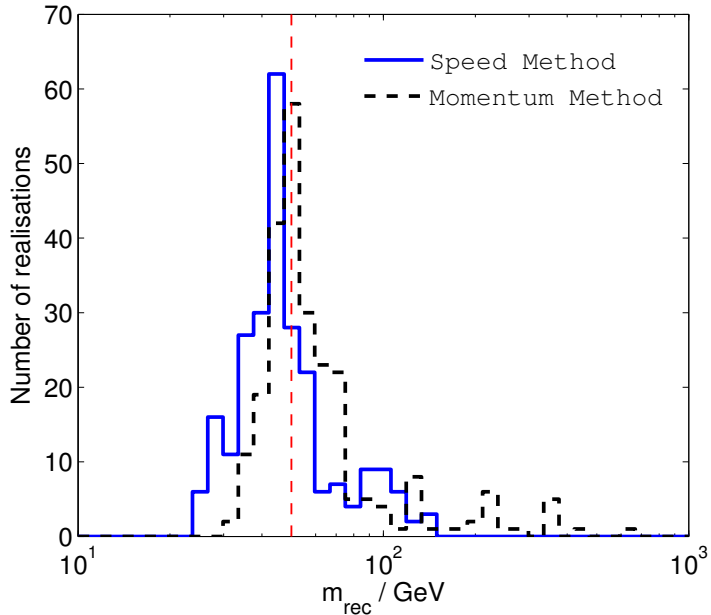


Figure 3.8: WIMP masses reconstructed using the speed and momentum parametrisation methods from 250 realisation. The benchmark speed distribution is the SHM. The true mass of 50 GeV is shown as a dashed vertical line. Reproduced from Ref. [1].

of benchmarks. In order to ensure the robustness of the method, we use two possible WIMP masses of 50 GeV and 100 GeV, as well as three benchmark models for the velocity distribution:

- (i) the Standard Halo Model (SHM), with $\sigma = 156 \text{ km s}^{-1}$ and $v_{\text{lag}} = 230 \text{ km s}^{-1}$;
- (ii) a 50% Standard Halo Model with a 50% contribution from a dark disk (SHM+DD);
- (iii) rescaled Via Lactea II data (VL-2).

We model the dark disk velocity distribution as a Maxwellian with $\sigma = 50 \text{ km s}^{-1}$ and $v_{\text{lag}} = 60 \text{ km s}^{-1}$, similar to the typical values obtained by Ref. [338]. A 50% contribution from the dark disk is at the upper limit of the range presented by Ref. [316] and we consider this as an extreme case. The third benchmark is the distribution function as extracted from the Via Lactea 2 (VL-2) N-body simulation [339] and presented in Ref. [309]. It is averaged over galactic radius in the range $7.5 < R < 9.5 \text{ kpc}$ and measured in bins of width 10 m s^{-1} . VL-2 is a DM-only simulation

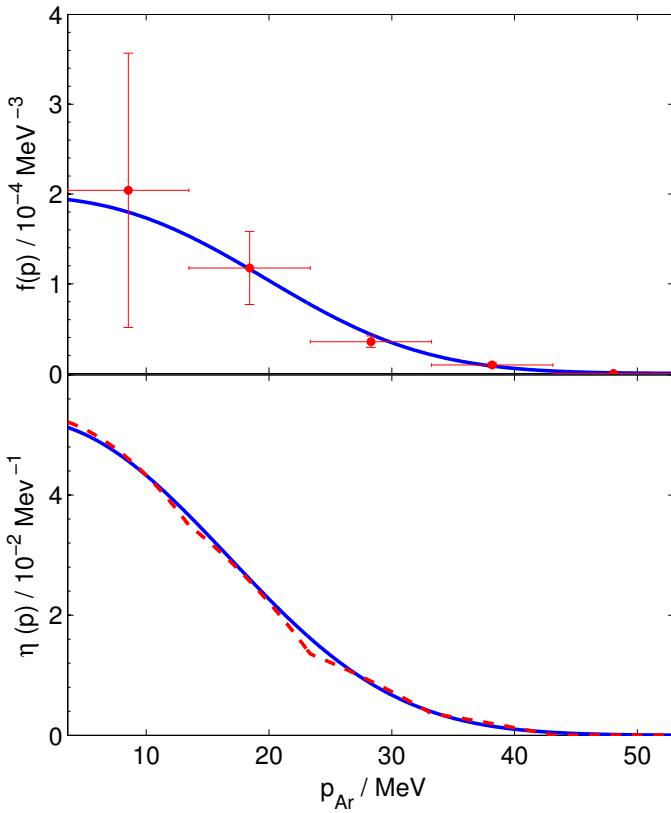


Figure 3.9: Reconstructed momentum distribution from all three mock experiments using a benchmark of a 50 GeV WIMP and the SHM. The upper panel shows the SHM momentum distribution (solid blue) and reconstructed bin values (red points). The lower panel shows the corresponding reconstructed mean inverse momentum (dashed red) and the mean inverse momentum in the SHM (solid blue). The reconstructed values have been rescaled by α for comparison to the true distribution. Reproduced from Ref. [1].

and thus leads to a lower peak speed than the SHM. Including the effects of baryons should deepen the galactic potential and raise this peak speed closer to that observed in the Milky Way. In order for a fairer comparison, we therefore rescale the VL-2 data such that $f_1(v)$ peaks at the same speed as in the SHM, allowing us to probe the departures from Maxwellian form which appear in N-body simulations.

The distributions of reconstructed masses are shown in Fig. 3.10 for the 50 GeV WIMP and Fig. 3.11 for the 100 GeV WIMP. For the 50 GeV benchmark, the distribution of reconstructions is peaked at the true value, though in all three cases there are a number of datasets reconstructed at higher masses. For some of the mock datasets, the posterior distribution for the WIMP mass is multimodal, with a peak near the true value as well

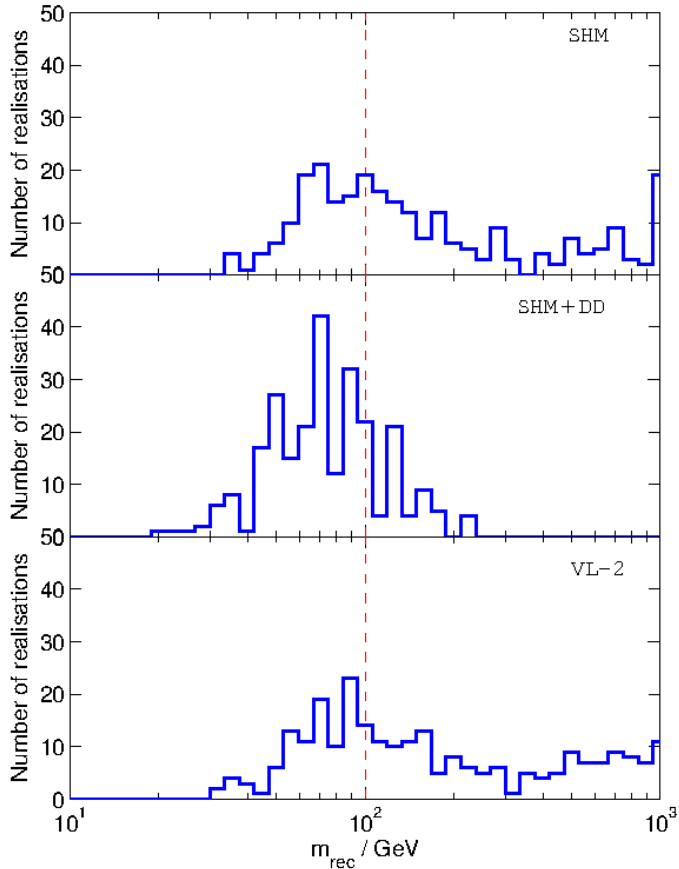


Figure 3.10: Distribution of reconstructed masses, m_{rec} , using the momentum method for 250 reconstructions. The true mass of 50 GeV is shown as a dashed vertical line. Reproduced from Ref. [1].

as a peak above ~ 100 GeV. For reconstructions using a fixed speed (or momentum) distribution, these may correspond to ‘bad’ reconstructions, as mentioned previously, in which the spectrum of events is flatter than expected. When the momentum distribution is allowed to vary, as here, the event rate can be well fit by more than one region of the mass parameter space. We also note a larger number of reconstructions at high masses in the case of the VL-2 benchmark. This is because of the flatter recoil spectrum in this case, which is more easily mimicked by a higher WIMP mass.

For the 100 GeV benchmark, the SHM and VL-2 models show similar structures, with a broad peak of reconstructions at or near the correct values, as well as a smaller tail up to masses of 1000 GeV, the upper limit of the prior. The 100 GeV datasets contain fewer events than their 50 GeV counterparts, so we would expect the spread of reconstructed values to be

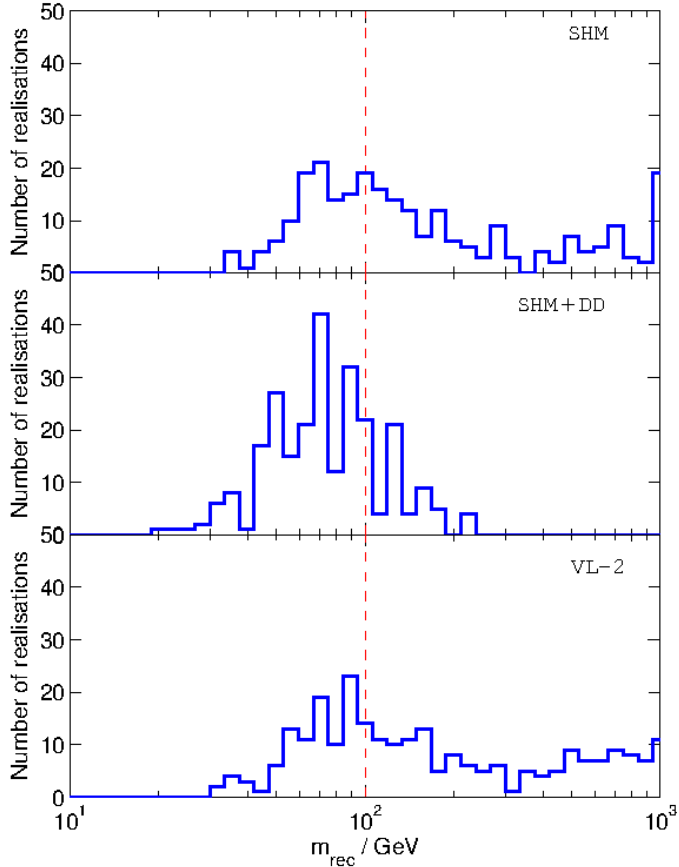


Figure 3.11: As Fig. 3.10 for $m_\chi = 100$ GeV. Reproduced from Ref. [1].

broader. Also, as the WIMP mass exceeds the mass of the target nucleus, v_{\min} becomes less sensitive to the value of the m_χ [318]. The result is that the shape of the event spectrum becomes roughly independent of the WIMP mass. The largest nuclear mass used here is $A_{\text{Xe}} = 131$, meaning that for values of m_{rec} significantly above $m_\chi \approx 131$ amu ≈ 122 GeV, the posterior distribution becomes roughly flat. Reconstructions in the high-mass tail occur when the maximum of the posterior occurs in this approximately flat region, and we expect the tail to extend up to arbitrarily high masses. In this case, we can only place a lower bound on the WIMP mass and, when calculating coverage statistics, we use 1-tailed limits (i.e. a $p\%$ confidence limit encloses $\frac{1}{2}(1 + p)\%$ of the marginalised posterior).

We report coverage statistics for the various benchmarks in Table 3.3. For the SHM, there is approximately exact coverage for both 50 and 100 GeV WIMPs, while for the VL-2 benchmark exact coverage is observed for the 100 GeV WIMP. The remaining benchmark parameters display

WIMP Mass		
	50 GeV	100 GeV
SHM	71 \pm 3%	65 \pm 3%
	92 \pm 2%	94 \pm 1%
SHM+DD	61 \pm 3%	58 \pm 3%
	94 \pm 1%	91 \pm 2%
VL-2	72 \pm 3%	65 \pm 3%
	90 \pm 2%	94 \pm 2%

Table 3.3: 68% and 95% confidence interval coverage results for the momentum parametrisation method using a variety of benchmark parameters, as defined in Sec. 3.2.1.

some undercoverage, though still much improved over that achieved by the speed parametrisation method. The poorest coverage is achieved for the 100 GeV SHM+DD benchmark, for which the 68% confidence interval has a coverage of $58 \pm 3\%$. This is to be expected from the poorly distributed reconstructions shown in Fig. 3.11. For the 100 GeV dark disk benchmark, there appears to be a significant bias in the distribution of reconstructed values, which peaks around 70 GeV. We explore the origin of this bias in the next section, where we examine the speed distributions reconstructed using this method.

3.4.2 Recovering the speed distribution

We will now consider how the speed distribution can be reconstructed from the momentum parametrisation. For a set of constant bins in momentum space, the positions and widths of bins in velocity space are dependent on the WIMP mass. It is therefore difficult to extract precise statistical information on the speed distribution, as the bin values will be very strongly correlated with the WIMP mass. Instead, we take the reconstructed WIMP mass as fixed and use this to obtain a speed distribution from the momentum distribution parameters. Without treating the covariance of the WIMP mass and the bin parameters in full, the reconstructed speed distribution will depend strongly on the reconstructed mass value. However, this naive approach should give an indication of whether accurate reconstructions are possible.

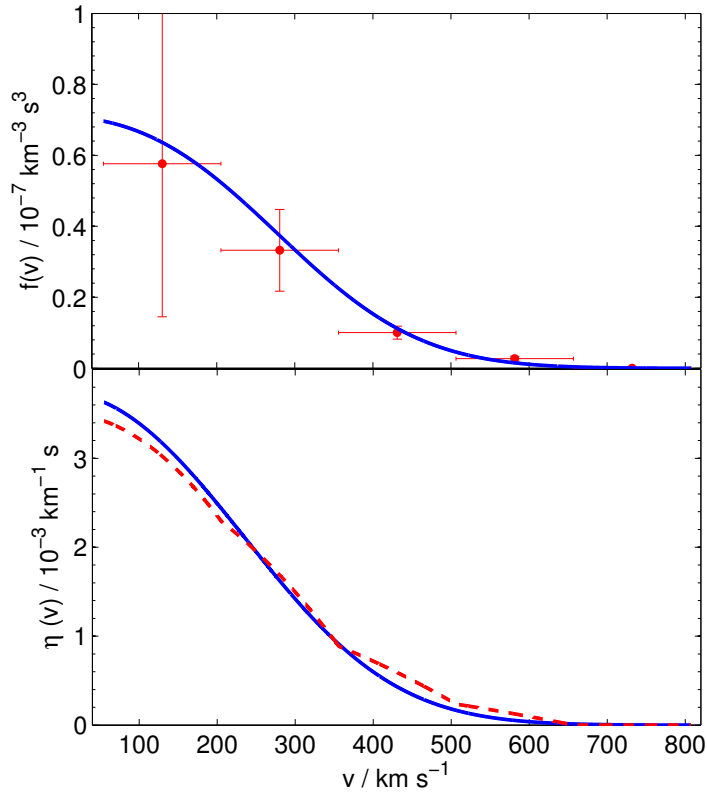


Figure 3.12: Reconstructed speed distribution from all three mock experiments using the momentum parametrisation method. The benchmark is a 50 GeV WIMP and the SHM distribution function. The upper panel shows the underlying SHM speed distribution (solid blue) and the fitted values of the speed bin parameters (red points). The lower panel shows the mean inverse speed corresponding to these fitted values (dashed red line) and the true mean inverse speed (solid blue). The underlying distributions have been rescaled by α for comparison to the reconstructions. Reproduced from Ref. [1].

First, we consider a 50 GeV WIMP with SHM distribution, as an archetypal WIMP model with a well-behaved distribution function. We show a typical reconstructed speed distribution in Fig. 3.12, using the same mock dataset as Fig. 3.9. In this case, the reconstructed value of m_{rec} is 42 GeV and the speed distribution appears to be accurately reconstructed within the error estimates.

Next, we consider a reconstruction for a 100 GeV WIMP with SHM+DD distribution function. One example is shown in the left-hand panels of Fig. 3.13, for a dataset with reconstructed mass $\log_{10}(m_{\text{rec}}/\text{GeV}) = 1.83 \pm 0.15$, compared to the true value of $\log_{10}(m_{\chi}/\text{GeV}) = 2$. The speed distribution appears to be well recovered at all speeds. However, there is a significant

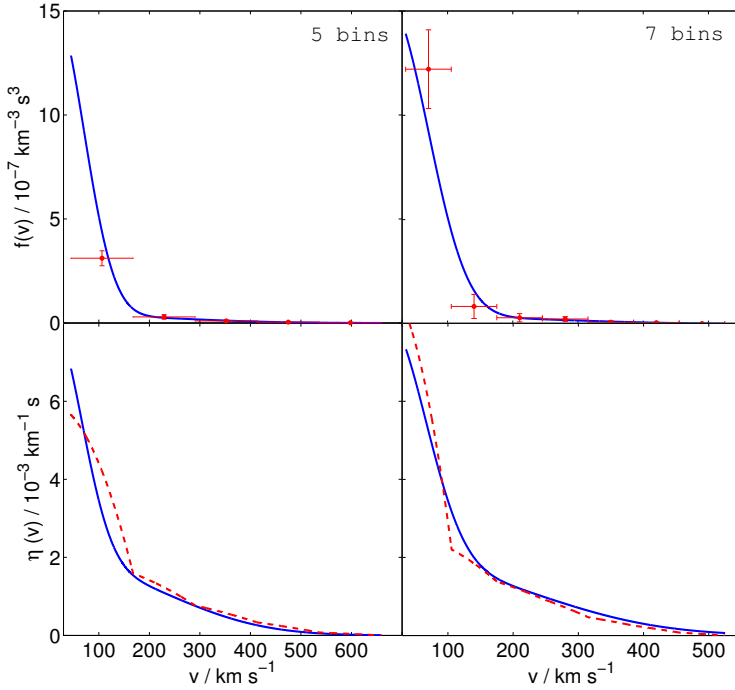


Figure 3.13: As Fig. 3.12 for a 100 GeV WIMP with SHM+DD distribution function using 5 momentum bins (left panels) and 7 momentum bins (right panels). Reproduced from Ref. [1].

discrepancy in the mean inverse speed below $\sim 150 \text{ km s}^{-1}$. This is because the SHM+DD distribution function is very rapidly varying at low v , meaning that the ansatz of constant bins can no longer be applied. As observed in the speed parametrisation method, the event spectrum can be steepened by moving to lower mass values and this may explain why there is significant bias and poor coverage for this set of benchmark parameters.

In the right-hand panels of Fig. 3.13, we show results from the same mock dataset reconstructed using 7 bins in momentum space. The reconstructed mass is now $\log_{10}(m_{\text{rec}}/\text{GeV}) = 2.21 \pm 0.27$, with the mean inverse momentum more closely reconstructed than for the 5 bin case. Figure 3.14 shows the distribution of reconstructed masses for a 100 GeV WIMP with a SHM+DD distribution function using 7 bins in momentum space. The reconstructed masses are now more broadly distributed around the benchmark value, with improved coverage compared to the 5 bin case: $67 \pm 3\%$ and $94 \pm 1\%$. We have found that increasing the number of bins for the 50 GeV SHM benchmark leaves the coverage properties and distribution of reconstructions largely unchanged, indicating that increasing the number of bins can be used to check the robustness of the reconstructions.

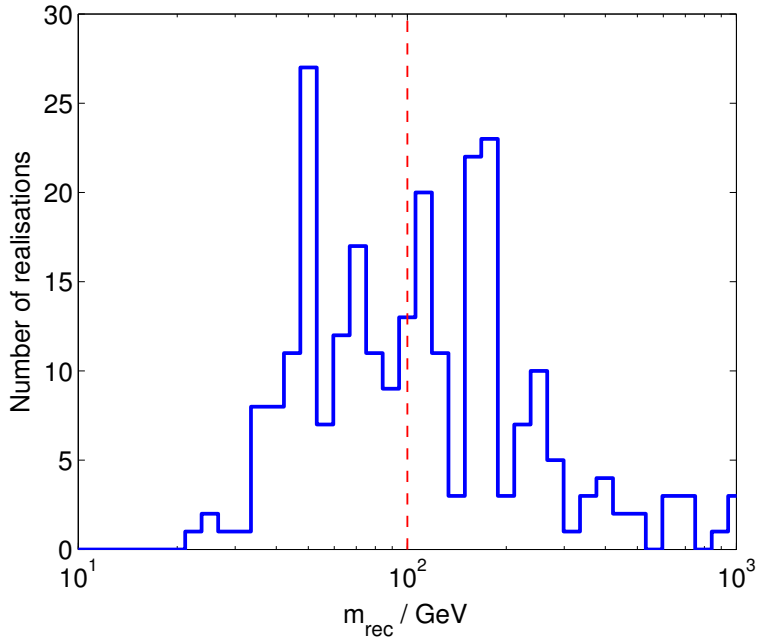


Figure 3.14: Distribution of reconstructed masses using the 7-bin momentum method for 250 reconstructions for a SHM+DD benchmark distribution. The true mass of 100 GeV is shown as a dashed vertical line. Reproduced from Ref. [1].

Finally, we consider the discriminatory power of the reconstructions. Returning to the 50 GeV SHM benchmark, we plot a single speed distribution reconstruction in Fig. 3.15, as well as all three benchmark speed distributions for comparison. The reconstruction is reasonably consistent with both the SHM and VL-2 models and displays only mild tension with the SHM+DD model. In addition, the benchmark distributions in Fig. 3.15 have been rescaled by the true value of α for comparison with the reconstructed values. In a real experiment, the value of α is unknown, further reducing the potential to discriminate between different models. Only in the case of more extreme distribution functions, such as a dark disk, might it be possible to make a distinction between the many possible underlying models. Thus, while the momentum parametrisation method can provide good constraints on the mass of the WIMP, it remains difficult to probe the speed distribution function.

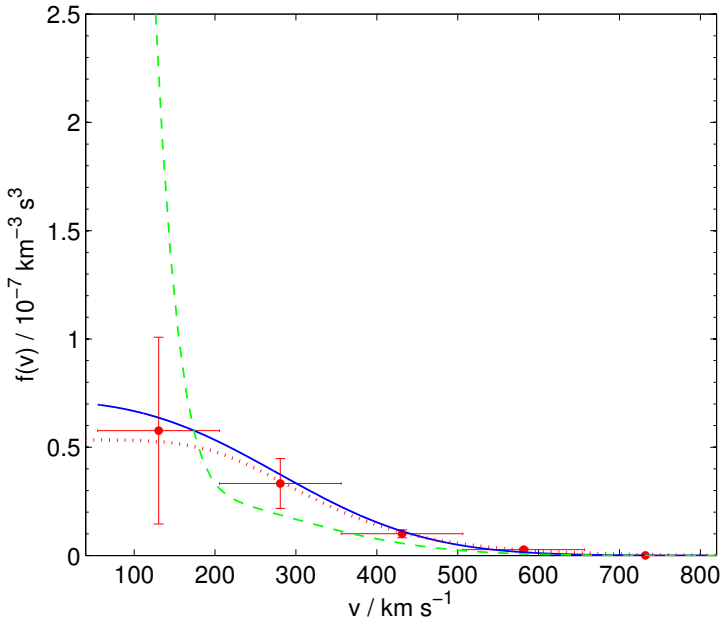


Figure 3.15: Reconstructed speed distribution from all three mock experiments using a benchmark of a 50 GeV WIMP with SHM distribution. The reconstructed values have been rescaled by α for comparison to the true distribution. The three different benchmark speed distributions defined in Sec. 3.2.1 have been overlaid: SHM (solid blue), SHM+DD (dashed green) and VL-2 (dotted red). Reproduced from Ref. [1].

3.5 Discussion

We have explored the simple, empirical parametrisation proposed by Peter and showed that it produces a significant bias and underestimates the errors on m_χ , even for simple benchmarks. This appears to be due to the dependence of $\eta(E_R)$ on m_χ . For a fixed bin width in v , reducing the WIMP mass leads to smaller bins in E_R . This means that $\eta(E_R)$ can provide a better fit to the observed data, as demonstrated in Fig. 3.5.

As an alternative we have proposed binning the *momentum* distribution. For a single experiment, the inverse momentum distribution $\tilde{\eta}(E_R)$ is independent of the WIMP mass and the scale (controlled by the parameter D of Eq. 3.22) and shape of the recoil distribution can be effectively decoupled. This allows D to be reconstructed with minimal bias. The D values from many different experiments can then potentially be used to place bounds on the values of the WIMP mass and cross-section.

However, to directly constrain the WIMP mass, it is necessary to combine data from multiple experiments simultaneously. This is done by

parametrising the reduced momentum distribution of the WIMPs with respect to only one of the experiments. In this work, we choose to parametrise $p_{\chi Ar}$. The result is that the shape of the recoil spectrum depends only weakly on the WIMP mass. This is because the recoil energy can now be written as

$$E_R = \frac{2p_{\chi Ar}^2}{m_N} \left(\frac{\mu_{\chi N}}{\mu_{\chi Ar}} \right)^2. \quad (3.27)$$

For a fixed bin width in $p_{\chi Ar}$, the bin width in recoil energy now scales with $\mu_{\chi N}^2/\mu_{\chi Ar}^2$, which has a weaker dependence on m_χ than when we consider fixed bins in v . This reduces the bias induced in the reconstructed WIMP mass.

The momentum method also allows us to probe a more constrained range of speeds. This is done by parametrising $p_{\chi Ar}$ only over the range to which the experiments are sensitive. While this cannot be done exactly for more than one experiment, it means that as many of the momentum bin parameters as possible contribute to the rate. Varying the WIMP mass does not strongly impact the number of bins to which the experiments are sensitive, again reducing bias in the reconstructed value of m_χ . This is similar to the method of Drees and Shan [326], which uses an algorithm to attempt to match the sensitivity ranges of multiple experiments.

Unfortunately, for low WIMP masses the range of speeds (and therefore momenta) probed by each experiment grows rapidly (see Fig. 3.2). A significant portion of this range is expected to be significantly higher than the maximum expected WIMP speed of $\sim 800 \text{ km s}^{-1}$. If we hope to parametrise the entire range of sensitivity of the experiments, this means that only a very small fraction of this range will be non-zero. A very large number of bins would be required to capture this ‘low’ momentum population (as discussed briefly in Sec. 3.4 for the case of a Xenon experiment). Thus, the momentum binning method appears not to be feasible for low mass WIMPs. Even in the case of intermediate mass WIMPs, it may not always be clear what the optimum range of momenta will be.

In Sec. 3.4.2, we have attempted to reconstruct the WIMP speed distribution from the corresponding momentum distribution. In doing so, we fixed the WIMP mass to its maximum posterior value, in order to avoid the strong correlations between m_χ and $\tilde{f}(p)$ associated with converting p to v . However, in order to make robust statistical inferences about the speed

distribution, it is necessary to take these correlations into account. This will be especially important when distinguishing between similar forms for $f(v)$, as in Fig. 3.15. In future, it will be necessary to study these correlations in detail or find a parametrisation with which we can reconstruct $f(v)$ directly.

Finally, while the momentum bin parametrisation provides significant improvements in coverage and reduced bias over the speed bin parametrisation, it may not work in every scenario. For example, the method still suffers from some under-coverage for more extreme distribution functions, such as the dark disk. This can be improved by increasing the number of bins, at the cost of significantly widening the range of reconstructed masses. These residual problems mean that the momentum binning method should be applied with caution.

3.6 Conclusions

We have discussed the current state of the art in accounting for astrophysical uncertainties in the analysis of direct detection data. In particular, we have emphasised the need for a general, empirical parametrisation for the WIMP distribution function and we have studied one such proposal in detail: a binned parametrisation for $f(v)$, developed by Peter. We show that this method produces a significant bias in reconstructions of the WIMP mass. This parametrisation introduces a fixed scale (the bin width) into the distribution function. Converting from speed bins to energy bins depends on the WIMP mass, introducing a bias into the analysis. We propose an alternative method: a binned parametrisation of the WIMP momentum distribution.

In the case of a single experiment, this method can be applied exactly and allows one to extract information about the shape of the distribution function, at the cost of losing access to information about either the WIMP mass or cross-section separately. For multiple experiments, the range of the parametrisation must be extended to cover the sensitivity regions of all experiments. For estimation of the WIMP mass, this allows us to achieve significant improvements in coverage and reduction in bias over previous methods. Without making any assumptions about the WIMP speed distribution, however, we cannot estimate the interaction cross-section due to its degeneracy with the fraction of WIMPs accessible to the experiments.

This is an unavoidable problem for any method hoping to analyse direct detection data without astrophysical assumptions.

Reconstruction of the WIMP speed distribution remains difficult. The finite sensitivity window of direct detection experiments means that information on the normalisation of $f(v)$ is lost, making comparison to theoretical models difficult. At the event rates studied here, it does not appear to be possible to distinguish between different distribution functions. A more thorough treatment of the correlation between m_χ and the momentum bin parameters would be required for robust inferences.

This technique represents a significant step towards developing model-independent methods for determining the WIMP mass. However, caution must be exercised, as the method is expected to perform poorly for low mass WIMPs, where the range of momenta probed by the experiments is large. There is also evidence that residual bias may remain, especially in the case of more extreme distribution functions.

Chapter 4

A polynomial parametrisation of the speed distribution

In an attempt to mitigate astrophysical uncertainties in the analysis of direct detection experiments, a number of parametrisations for the WIMP speed distribution have been proposed. In Chapter 3, we explored two such empirical parametrisation which aim to fit the WIMP distribution without making any *a priori* assumptions about its form. These methods involved writing the WIMP speed and momentum distributions as a series of constant bins.

However, the introduction of a fixed scale, in the form of the bin width, results in a bias in the reconstruction of the WIMP mass. While binning the momentum rather than speed distribution helps to reduce this problem, there may remain residual bias. Furthermore, the method is expected to fail for low mass WIMPs and the choice of momentum range to parametrise may not always be clear.

In this chapter, we propose an alternative parametrisation for the speed distribution which is smooth and can fit a wide range of possible functional forms of $f(v)$. This method involves parametrising the *logarithm* of $f(v)$ as a polynomial in the WIMP speed v . We describe the parametrisation in detail in Sec. 4.1.

We test the parametrisation, as in Chapter 3, using mock data sets from future experiments, generated from a range of particle physics and astrophysics benchmarks, outlined in Sec. 4.2. We show in Sec. 4.4, that the parametrisation allows an unbiased reconstruction of the WIMP mass, even when Poisson noise and realistic experimental parameters are incorporated

in the analysis. We show the performance of the method as a function of WIMP mass and also outline how to determine the optimal number of basis functions for the polynomial parametrisation.

Finally, in Sec. 4.6, we show how the speed distribution can be reconstructed using this parametrisation. A lack of information about the normalisation of $f(v)$ impairs our ability to reconstruct its absolute value. However, we propose a method for reconstructing the *shape* of the mean inverse speed $\eta(v_{\min})$ even when information about the overall normalisation is not available.

4.1 Parametrising the logarithm of $f(v)$

We would like to write down a general parametrisation, treating $f(v)$ as a free function. However, the speed distribution is subject to two constraints in order to qualify as a physical distribution function:

- (i) it must be normalised (or at least should be capable of being normalised), and
- (ii) it must be everywhere greater than or equal to zero.

Motivated by (ii), we propose parametrising the *natural logarithm* of the speed distribution. The properties of the logarithm will ensure that the speed distribution remains everywhere positive. Moreover, logarithmic dependence on the parameters means that a wide range of shapes for the speed distribution can be spanned by the parametrisation.

We parametrise $\ln f(v)$ as a polynomial in v . That is, we wish to write

$$\ln f(v) = \sum_{k=0}^{N-1} a_k P_k(v), \quad (4.1)$$

leading to the speed distribution

$$f_1(v) = v^2 \exp \left(\sum_{k=0}^{N-1} a_k P_k(v) \right), \quad (4.2)$$

where we use N polynomial basis functions $P_k(v)$, multiplied by the coefficients a_k . Normalisation is imposed by fixing a_0 once the remaining parameters have been chosen. By using enough basis functions for the polynomial parametrisation, we can approximate any smooth, bounded

function arbitrarily well [340], so this choice provides complete generality. However, which polynomial basis should be used? We see immediately that a naive power series of the form

$$\ln f(v) \approx a_0 + a_1 v + a_2 v^2 + a_3 v^3 + \dots, \quad (4.3)$$

is not practical for the purposes of parameter estimation. Higher powers of v will have rapidly growing contributions to $\ln f$, meaning that the associated coefficients must be rapidly decreasing in order to suppress these contributions. Fitting to the SHM using just 5 terms, the range of values for the a_k in the case of a simple power series would span around 13 orders of magnitude. Ideally, we would like to specify an identical prior on each of the coefficients. However, in this scenario this would result in a highly inefficient exploration of the parameter space when some of the terms are so small.

This problem can be significantly improved by rescaling v . We choose to rescale by a factor of $v_{\max} = 1000 \text{ km s}^{-1}$ and cut off the distribution function at v_{\max} . We should choose v_{\max} to ensure that $f_1(v)$ is negligible above the cut off. However, too high a choice of v_{\max} will result in $f_1(v)$ being close to zero over a large range of the parametrization, making fitting more difficult. We use the value $v_{\max} = 1000 \text{ km s}^{-1}$, which lies significantly above the Galactic escape speed, as discussed in Chapter 3. The basis functions $(v/v_{\max})^k$ are now less than unity by construction and the coefficients a_k are now dimensionless:

$$\ln f(v) \approx a_0 + a_1(v/v_{\max}) + a_2(v/v_{\max})^2 + a_3(v/v_{\max})^3 + \dots. \quad (4.4)$$

We now address the problem of *conditioning* of the polynomial basis (see e.g. Refs. [341, 342]). Conditioning is a measure of how much the value of a polynomial changes, given a small change in the coefficients. For a well-conditioned polynomial, small changes in the coefficient are expected to lead to small changes in the value of the polynomial. This is ideal for parameter estimation as it leads to a more efficient exploration of the parameter space. Orthogonal polynomial basis functions typically have improved conditioning [341] and we consider two specific choices: the Legendre polynomials and the Chebyshev polynomials. The Legendre polynomials are a familiar series of orthogonal basis functions. The Chebyshev polynomials

are used extensively in polynomial approximation theory [343] and are expected to be well conditioned [341]. We examine both which polynomials perform best and how many basis functions are required in Sec. 4.3.1.

We plot in Fig. 4.1 some examples of distribution functions which can be described by the polynomial $\ln f(v)$ parametrisation with $N = 5$ basis functions. These examples were generated by randomly picking values for the $\{a_i\}$ values. Clearly this parametrisation can reproduce a wide range of shapes, peaking at different values of v . However, we wish to determine how well we can *fit* these parameters, along with the WIMP mass and cross section, to data. As in the case of the binned distribution of Chapter 3, we now define a series of theoretical and experimental benchmarks which we use to generate mock data sets and test the parametrisation.

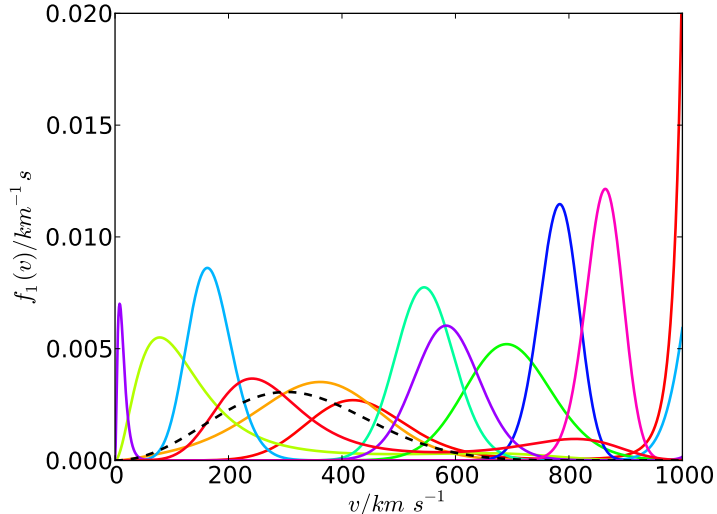


Figure 4.1: Examples of speed distributions $f_1(v)$ generated using the polynomial parametrisation for $\ln f(v)$ with $N = 5$ basis functions. The SHM distribution function in the Earth frame is shown as a black dashed line for comparison.

4.2 Experiments and benchmark parameters

In order to generate mock data sets, we consider three idealized mock experiments, loosely based on detectors which are currently in development. The three target materials we consider here are Xenon, Argon and Germa-

Experiment	Target Mass, A	Detector Mass (fid.), m_{det}/kg	Efficiency, ϵ	Energy Range/keV
Xenon	131	1100 [248]	0.7 [247]	7-45 [344]
Argon	40	1000	0.9 [345]	30-100 [346]
Germanium	73	150 [347]	0.6 [348]	8-100 [348]

Table 4.1: Summary of experimental parameters used in this work, defined in Sec. 4.2. An exposure of $t_{\text{exp}} = 2$ years is used for all 3 experiments.

nium. As in Chapter 3, we describe each experiment in terms of the mass number A of the target nucleus, fiducial detector mass m_{det} , efficiency ϵ and energy sensitivity window $[E_{\min}, E_{\max}]$. We consider a total exposure time for all experiments of $t_{\text{exp}} = 2$ years. The experimental parameter values used in this chapter are summarized in Tab. 4.1. We note that these values may be slightly adjusted or updated compared to those used in Chapter 3 as a result of updated experimental results and projections. We have tried to indicate the source of the values used in Tab. 4.1.

As in Chapter 3, we assume that SI interactions dominate and use a single value of the interaction cross section $\sigma_p^{\text{SI}} = 10^{-45} \text{ cm}^2$. However, we will consider a range of WIMP masses from 10 GeV, below which the sensitivity of current direct detection experiments decreases dramatically, up to 1000 GeV above which sensitivity to the precise WIMP mass is lost.

We consider several benchmark speed distributions in this chapter, including the SHM and the SHM with the addition of a moderate dark disk which accounts for 23% of the total WIMP density [32]. For the SHM, we assume a fixed DM density of $\rho_0 = 0.3 \text{ GeV cm}^{-3}$. However, we treat the dark disk as an overdensity contributing an *additional* WIMP population, bringing the local density up to $\rho_0 = 0.39 \text{ GeV cm}^{-3}$. In addition, we also use the speed distribution of Lisanti et al. [305], which has the following form in the Earth's frame:

$$f(\mathbf{v}) = N \left[\exp \left(\frac{v_{\text{esc}}^2 - |\mathbf{v} - \mathbf{v}_0|^2}{kv_0^2} \right) - 1 \right]^k \Theta(v_{\text{esc}} - |\mathbf{v} - \mathbf{v}_0|). \quad (4.5)$$

We use the parameter values $k = 2$ and $v_0 = 220 \text{ km s}^{-1}$ in this work. In all cases, we assume a fixed value of the escape speed $v_{\text{esc}} = 544 \text{ km s}^{-1}$ (see

Speed distribution benchmark	Fraction	$v_{\text{lag}}/\text{km s}^{-1}$	$\sigma_v/\text{km s}^{-1}$
SHM	1	220	156
SHM+DD	0.77	220	156
	0.23	50	50
Stream	1	400	20
Bump	0.97	220	156
	0.03	500	20
Double-peak	0.5	200	20
	0.5	400	20
Lisanti et al.		$v_0 = 220 \text{ km s}^{-1}$	$k = 2$

Table 4.2: Summary of speed distribution benchmarks used in this work. Some benchmarks are modelled as mixtures of two gaussian components, for which we give the fractional contribution of each component (labelled ‘Fraction’). The remaining parameters are defined in Sec. 2.4.3, as well as Eq. 4.5 and the accompanying text. The ‘bump’ and ‘double-peak’ distributions are discussed in Sec. 4.3.1. For each benchmark distribution, we fix $v_{\text{esc}} = 544 \text{ km s}^{-1}$.

Chapter 2). We summarize in Tab. 4.2 the different speed distributions considered. We also plot several of these in Fig. 4.2 for reference.

4.2.1 Parameter sampling

The parameter space of the polynomial $\ln f(v)$ parametrisation is much larger than for the binned method and is poorly explored using conventional MCMC methods. We therefore make parameter inferences using the publicly available MULTINEST nested sampling package [349–351]. This allows us to map out both the likelihood $\mathcal{L}(\theta)$ and posterior probability distribution $\mathcal{P}(\theta)$ for the model parameters θ . We summarize in Tab. 4.3 the MULTINEST sampling parameters used. We also summarize the priors used in this work in Tab. 4.4.

In Sec. 4.5 and Sec. 4.6, we consider many realisations of data, including the effects of Poisson noise. We therefore use the unbinned likelihood of Eq. 3.13 in MULTINEST. As in Chapter 3, we make parameter inferences from the marginalised posterior distribution \mathcal{P}_m . We take the mode of the distribution to be the reconstructed parameter value and construct p% *minimal* credible intervals. This method performs well for small numbers

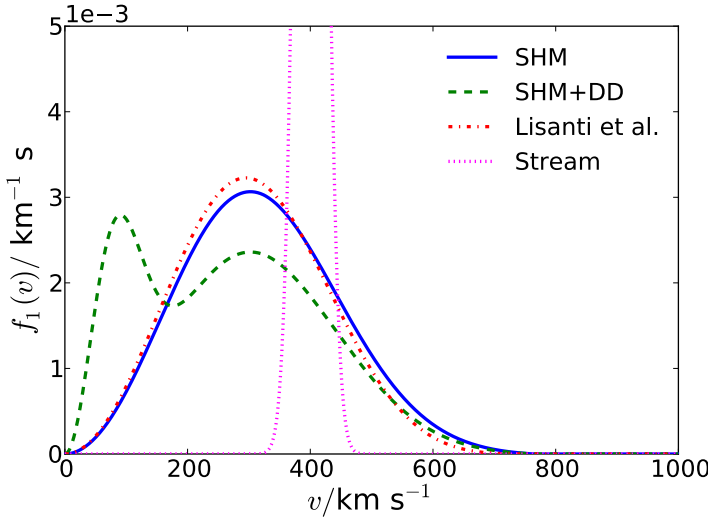


Figure 4.2: Several of the benchmark speed distributions used in this chapter. They are defined in Eqs. 2.45 and ?? with parameters from Tab. 4.2. These distributions are the SHM (solid blue), SHM+DD (dashed green), Lisanti et al. (dot-dashed red) and the stream (dotted magenta). Reproduced from Ref. [2].

Parameter	Value
N_{live}	10000
efficiency	0.25
tolerance	10^{-4}

Table 4.3: Summary of the MULTINEST sampling parameters used in this chapter.

of observations (compared to the number of free parameters in the fit). It is therefore a sensible choice here, where in some cases the number of events observed in an experiment is less than 10.

In Sec. 4.3.1 and Sec. 4.4, we consider the effects of varying the form of the parametrization and of varying the input WIMP mass. In order to eliminate the effects of Poisson noise, we use Asimov data [352] for these sections. This means that we divide the energy window of each experiment into bins of width 1 keV. We then set the observed number of events N_o^i in bin i equal to the expected number of events N_e^i and use the binned

Parameter	Prior type	Prior range
m_χ / GeV	log-flat	$[10^0, 10^3]$
σ_p / cm^2	log-flat	$[10^{-46}, 10^{-42}]$
$\{a_k\}$	linear-flat	$[-50, 50]$
R_{BG}/dru	log-flat	$[10^{-12}, 10^{-5}]$

Table 4.4: Summary of the priors on the parameters used in this chapter. The background rate R_{BG} is defined in Sec. 4.4 while the $\{a_k\}$ are the polynomial coefficients used in the parametrisation.

likelihood

$$\mathcal{L} = \prod_{i=1, N_{\text{bins}}} \frac{(N_e^i)^{N_o^i}}{(N_o^i)!} e^{-N_e^i}, \quad (4.6)$$

for each experiment. In these sections, we have a very large number of observations, namely the exact (non-integer) event numbers in each energy bin. We can therefore use the best fit point (i.e. the point which maximises the likelihood) as the reconstructed value. To obtain confidence intervals on some subset of the full parameter space, we use the profile likelihood \mathcal{L}_p , obtained by maximising \mathcal{L} over the remaining nuisance parameters. We then construct confidence intervals using the asymptotic χ^2 distribution of the profile likelihood [353].

4.3 Results

Before we consider in detail the properties of the parametrisation, we show a single reconstruction of m_χ and σ_p^{SI} using as input a WIMP of mass 50 GeV and the SHM distribution function. We generate Asimov data for this benchmark and fit using $N = 5$ basis functions and a basis of Chebyshev polynomials (see Sec. 4.3.1). If the polynomial $\ln f(v)$ parametrisation cannot produce an unbiased reconstruction of the WIMP parameters for the simple and smooth SHM benchmark, it is unlikely to be useful for more complicated distribution functions.

The results of this reconstruction are shown in Fig. 4.3. There is very good agreement between the best fit point (green triangle) and the benchmark values (dashed red lines). The WIMP mass is well reconstructed, with an uncertainty of about 30% at the 1σ level. However, we notice that

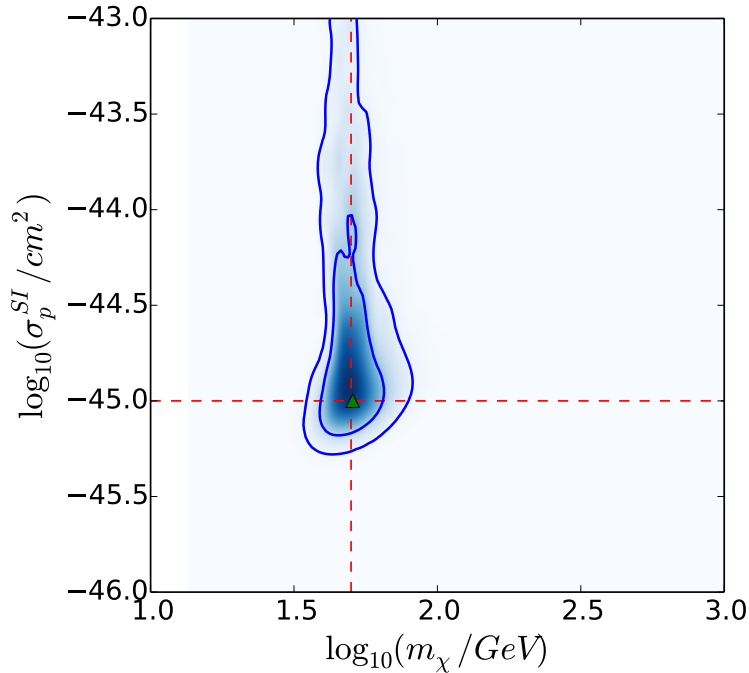


Figure 4.3: Reconstruction of the WIMP mass and cross section using the polynomial $\ln f(v)$ parametrisation with 5 basis functions. Asimov data was generated for a WIMP with $m_\chi = 50$ GeV and $\sigma_p^{\text{SI}} = 10^{-45}$ cm 2 (shown as dashed red horizontal and vertical lines) and the SHM speed distribution. The shaded blue shows the value of the profile likelihood (with darker values corresponding to higher likelihood), along with the 68% and 95% confidence contours. The best fit point is shown as a green triangle.

there is a significant degeneracy, with the reconstruction for σ_p^{SI} extending up to large values. This problem was discussed briefly in Chapter 3. We have no information about the shape of $f(v)$ below the energy thresholds of the experiments. This means that distributions which have a large WIMP population at low speeds can be made to fit the data as well as those which do not, as long as the value of the cross section is adjusted to compensate. While we can reconstruct m_χ using this method, we can only place a lower limit on σ_p^{SI} unless we make further assumptions about the low speed WIMP population. We will now explore in more detail the properties of this new parametrisation method.

4.3.1 Testing the parametrisation

We now consider the two questions: (i) how many basis functions are required and (ii) which polynomial basis should be used? In order to answer

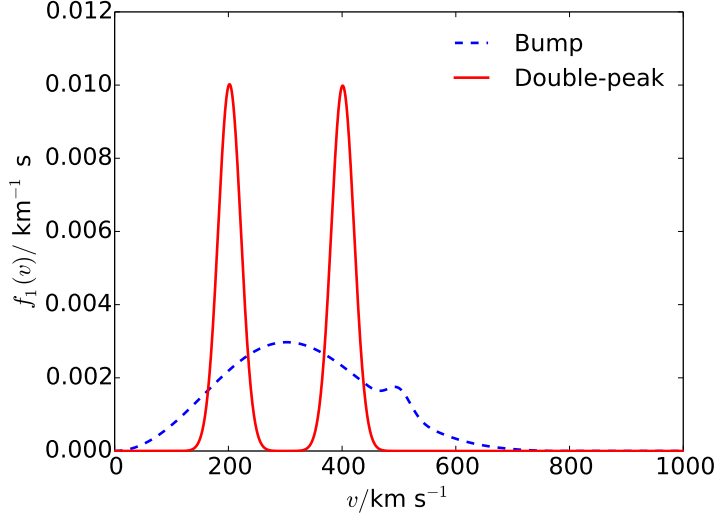


Figure 4.4: Benchmark speed distributions used in Sec. 4.3.1 to test the performance of the parametrization as a function of the number and type of basis functions. Reproduced from Ref. [2].

these questions, we use the two benchmark distribution functions illustrated in Fig. 4.4. We have chosen these benchmarks not because they are necessarily realistic distribution functions but because they should be difficult to fit using standard techniques and fitting functions (e.g. [305]). The first distribution (referred to as ‘bump’) is a SHM distribution with the addition of a small bump, which contributes just 3% of the total WIMP population and could correspond to a small sub-halo or stream [308]. This should be difficult to fit because it represents only a very small deviation from the standard scenario. The second distribution (referred to as ‘double-peak’) has a sharp and rapidly varying structure, which we anticipate should be difficult to capture using a small number of basis functions.

Varying the number of basis functions

We first investigate how the reconstructed WIMP mass m_{rec} and uncertainty varies with the number of basis functions N . For now, we fix our choice of basis to shifted Legendre polynomials¹:

$$P_k(v) = L_k \left(2 \frac{v}{v_{\max}} - 1 \right), \quad (4.7)$$

where L_k is the Legendre polynomial of order k .

¹We use the shifted argument $2v/v_{\max} - 1$ in order to enforce the orthogonality of the polynomials over the range $v \in [0, v_{\max}]$.

The lower panel of Fig. 4.5 shows the best fit mass and 68% confidence intervals as a function of N , using as input a WIMP of mass 50 GeV and the ‘bump’ distribution function. The reconstructed mass very rapidly settles close to the true value, using as few as three basis functions. This is because adding the bump near $v \sim 500 \text{ km s}^{-1}$ still leaves the mean inverse speed relatively smooth, so a large number of basis functions is not required. The correct mass is reconstructed and we emphasize in the lower panel of Fig. 4.5 that the reconstruction is stable with the addition of more basis functions.

We should also consider how the quality of the fit changes as a function of N . We would expect that adding fit parameters should always lead to a better fit. Eventually, the fit should be good enough that adding additional basis functions will no longer improve it significantly. We can then be confident that our reconstruction is accurate and not an artifact of using too few basis functions. In order to investigate this, we utilise the Bayesian Information Criterion (BIC) [354], which is given by:

$$BIC = 2N_p \ln(N_m) - \ln(\mathcal{L}_{\max}), \quad (4.8)$$

where N_p is the number of free parameters, N_m is the number of measurements or observations and \mathcal{L}_{\max} is the maximum likelihood value obtained in the reconstruction. For the case of binned data, N_m corresponds simply to the total number of energy bins across all experiments. This criterion penalises the inclusion of additional free parameters and in comparing several models, we should prefer the one which minimises the BIC.

The upper panel of Fig. 4.5 shows the BIC (in arbitrary units) as a function of the number of basis functions for the ‘bump’ distribution function. The BIC is comparable for the cases of $N = 2$ and $N = 3$, indicating that the quality of the fit is improved slightly by the addition of another basis function. However, adding further basis functions does not have a significant impact on the maximum likelihood, leading to an increase in the BIC. This coincides with the stabilization of the reconstructed mass around the true value and we conclude that only two or three basis functions are required to provide a good fit to the data.

Figure 4.6 shows the corresponding results for the ‘double-peak’ distribution function. Here, we note that the bias induced by using too small a number of basis functions is larger than for the case of the ‘bump’ distribution, due to the more complicated structure in this case. The BIC

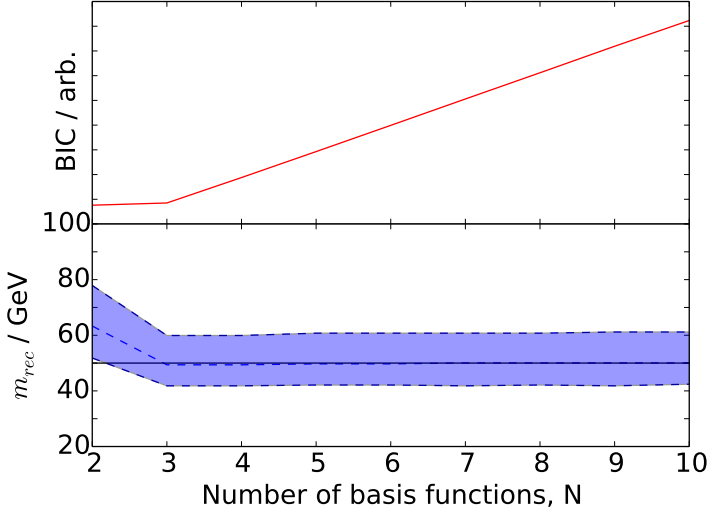


Figure 4.5: Bayesian information criterion (BIC) as a function of the number of basis functions for an underlying ‘bump’ distribution function, 50 GeV WIMP and using Legendre polynomial basis functions (upper panel). Also shown (lower panel) are the reconstructed WIMP mass (dashed blue line), 68% confidence interval (shaded blue region) and underlying WIMP mass (solid horizontal black line). Reproduced from Ref. [2].

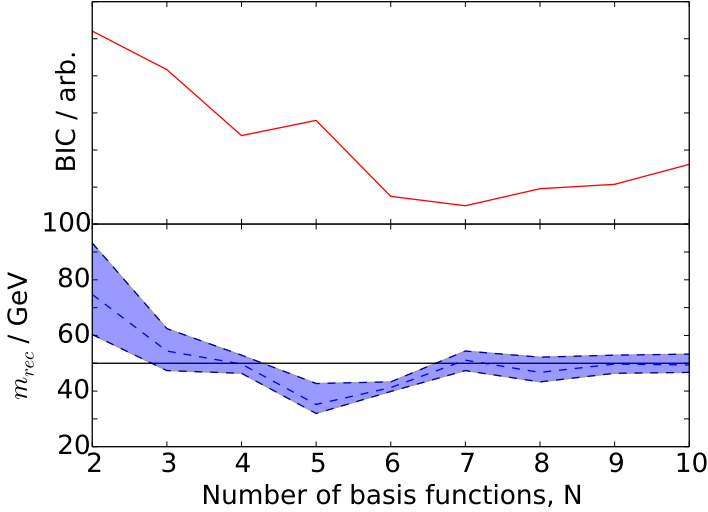


Figure 4.6: As Fig. 4.5 but for an underlying ‘double-peak’ distribution function. Reproduced from Ref. [2].

is minimized for $N = 7$, indicating that additional basis functions do not significantly improve the quality of the fit to data. This suggests that the shape of the speed distribution can be well fit by $N \geq 7$ basis functions.

As shown in the lower panel of Fig. 4.6, the reconstruction of the WIMP mass is stable around the true mass for these values of N .

We propose that such a procedure should be used in the case of real data should a dark matter signal be observed at multiple detectors. We have shown that by analyzing the reconstructed mass as a function of N we can recover the true mass and that by using the BIC we can be confident that we have obtained an adequate fit to data.

Choice of basis functions

We now consider the second question posed at the start of Sec. 4.3.1: which polynomial basis should be used? As previously mentioned, we test two different polynomial bases: Legendre and Chebyshev polynomials. We have checked that the reconstruction results using Chebyshev polynomials are largely indistinguishable from the case of Legendre polynomials for both the ‘bump’ and ‘double-peak’ distributions and as a function of N . This leads us to conclude that the accuracy of the reconstruction is independent of the specific choice of basis. However, the reconstruction was much faster in the case of the Chebyshev basis. This is illustrated in Fig. 4.7, which shows the time taken for reconstruction of the ‘bump’ benchmark as a function of N . The time taken grows much more slowly for the Chebyshev basis (roughly as N^2) than for the Legendre basis (roughly as N^3). This is consistent with the common use of the Chebyshev basis in polynomial approximation problems [343]. We have also checked that this difference is not an artifact of how we calculate the basis functions. These results indicate that this choice of basis provides both reliable and efficient reconstruction for the WIMP mass and we therefore use the Chebyshev basis in the remainder of this work.

4.4 Varying m_χ

We now consider the performance of the parametrisation over a wide range of WIMP masses. We generate Asimov data for WIMP masses of 10, 20, 30, 40, 50, 75, 100, 200 and 500 GeV and reconstruct the best fit WIMP mass m_{rec} and 68% and 95% confidence intervals from the profile likelihood. We use the SHM as a benchmark distribution function and use a fixed number of $N = 5$ basis functions. The results are shown in Fig. 4.8, along with the

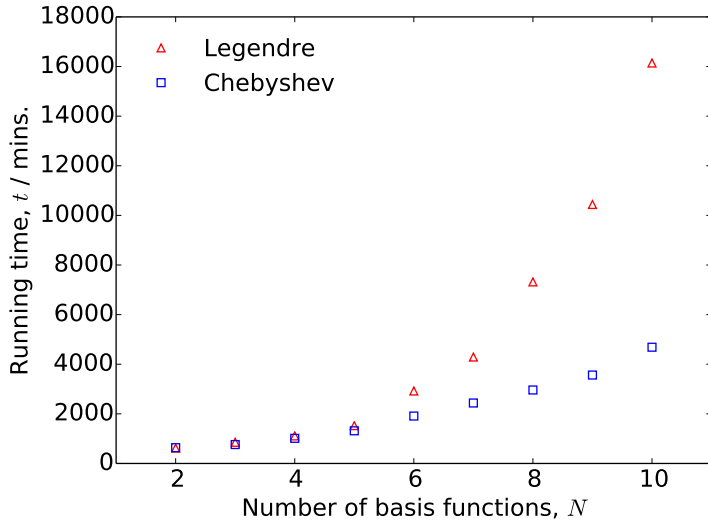


Figure 4.7: Time taken (using 4 processors in parallel) for the reconstruction of the ‘bump’ benchmark, as a function of number of basis functions. The time taken using the Chebyshev basis (blue squares) grows more slowly with N than for the Legendre basis (red triangles). Reproduced from Ref. [2].

line $m_{\text{rec}} = m_\chi$ for reference.

For large values of m_χ , the shape of the event spectrum becomes independent of m_χ [355], which results in a widening of the confidence intervals as the WIMP mass increases. For low mass WIMPs, fewer events are observed in each bin, again resulting in wider confidence intervals. It should be noted that for this analysis we have used Asimov data, in which the exact (non-integer) number of events is recorded in each bin. For low mass WIMPs, this means that the spectrum (and therefore the correct WIMP mass) is still well reconstructed using Asimov data, in spite of the small number of events. The tightest constraints are obtained when the input WIMP mass is close to the masses of several of the detector nuclei (in the range 30-80 GeV). There also appears to be no bias in the WIMP mass: the reconstruction matches the true mass across all values considered.

So far, we have only considered idealized direct detection experiments. We now apply the method to more realistic mock detectors, taking into account the effects of finite energy resolution, as well as unrejected background events. We assume here that each experiment has a gaussian energy resolution with fixed width $\sigma_E = 1$ keV (see Sec. 2.2.3 for details). We also assume a constant flat background rate for each experiment $R_{\text{BG}} = 10^{-6}$

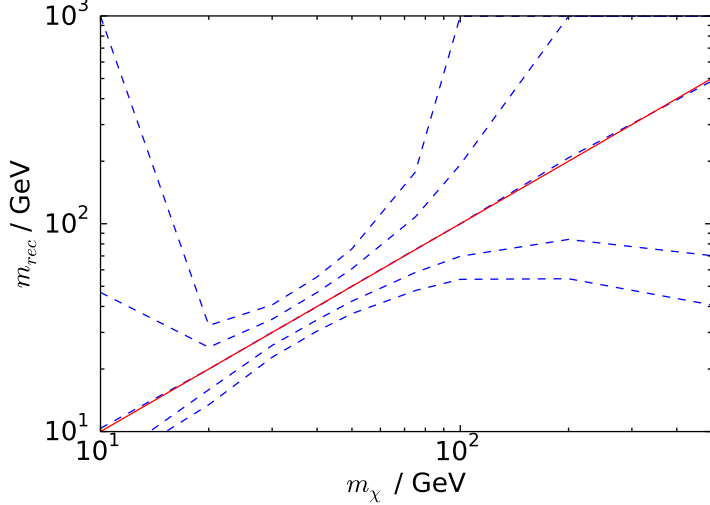


Figure 4.8: Reconstructed WIMP mass m_{rec} (central dashed blue line) as a function of input WIMP mass m_χ as well as 68% and 95% intervals (inner and outer blue dashed lines respectively). The line $m_{\text{rec}} = m_\chi$ (solid red line) is also plotted for reference. Reproduced from Ref. [2].

events/kg/keV/day (which has been suggested as a possible background rate for Xenon1T [344] and WArP-100L [346]) when generating mock data sets. However, we allow the flat background rate in each experiment to vary as free parameters during the fit.

We have chosen relatively generic resolution and background parameters in this work, because the precise details of energy resolution and background shape and rate will depend on the specific experiment under consideration. Instead, we hope to show that the inclusion of more realistic experimental setups does not introduce an additional bias or otherwise spoil the good properties of the method presented here.

Figure 4.9 shows the reconstructed mass as a function of input mass in this more realistic scenario. The 68% and 95% confidence intervals are now wider and the reconstructed mass does not appear to be as accurate. For input masses above ~ 100 GeV, the uncertainties become very wide, with only a lower limit of $m_{\text{rec}} > 20$ GeV being placed on the WIMP mass. Due to the poorer energy resolution the shape of the energy spectrum is less well-determined. In addition, a flat background contribution can mimic a higher mass WIMP, as it leads to a flatter spectrum. This leads to a strong degeneracy, as a wide range of mass values can provide a good fit to the data. For high input masses, the profile likelihood is approximately

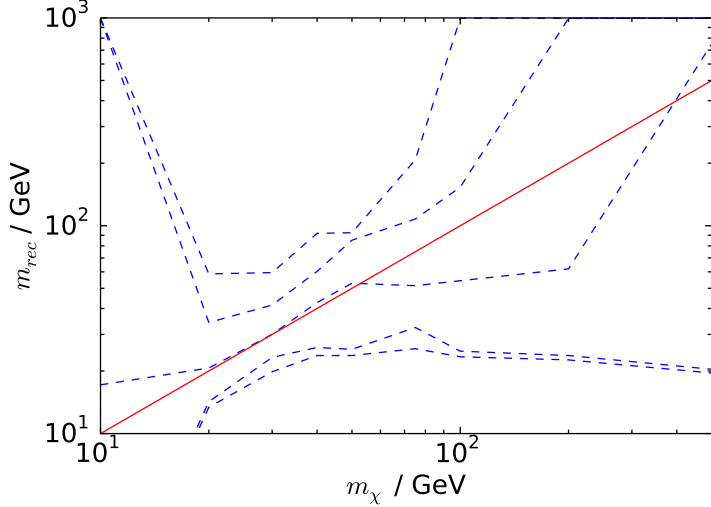


Figure 4.9: As fig. 4.8 but including the effects of finite energy resolution and non-zero backgrounds, as described in the text. Reproduced from Ref. [2].

constant above $m_{\text{rec}} \sim 20$ GeV, indicating that there is no sensitivity to the underlying WIMP mass.

In spite of this, the true mass values still lie within the 68% and 95% confidence intervals. In addition, the poor values for the reconstructed mass for heavy WIMPs are a side effect of the loss of sensitivity. Because the profile likelihood is approximately flat, the maximum likelihood point is equally likely to be anywhere within the 68% interval. These effects would be present even if we had considered a fixed form for the speed distribution. However, when we allow for a range of possible speed distributions, the effects become more pronounced. These results show that for more realistic experimental scenarios, the method presented in this paper remains reliable over a range of masses, though its precision may be significantly reduced.

4.5 Statistical properties

We now consider the impact of statistical fluctuations on the reconstruction of the WIMP mass. In reality, the number of events observed N_o at a given experiment will be Poisson distributed about the expected value N_e , while the observed distribution of recoil energies will not exactly match that expected from the calculated event rate. The fundamental statistical limitations of future direct detection experiments have been studied in

Benchmark distribution	Mean bias $\langle b \rangle$
SHM	0.002 ± 0.008
SHM+DD	0.005 ± 0.007
Lisanti et al.	0.01 ± 0.01

Table 4.5: Mean bias $\langle b \rangle$ in the reconstructed log WIMP mass (Eq. 4.9). This was calculated over 250 realisations using three different benchmark speed distributions.

detail in Ref. [337]. As in Chapter 3, we generate 250 realisations of data from the mock experiments described in Tab. 4.1.

For each realisation, we then use the polynomial $\ln f(v)$ parametrisation (using $N = 5$ basis functions) to reconstruct the WIMP mass and 68% and 95% credible intervals. Figure 4.10 shows the distribution of reconstructed masses for an input mass of 50 GeV for three benchmark speed distributions: SHM, SHM+DD and Lisanti et al. as described in Sec. 4.2. In all three cases, the reconstructions are peaked close to the true value, regardless of the underlying distribution.

In order to assess the accuracy of the reconstructed value of the mass m_{rec} , we also calculate the bias b for each realisation:

$$b = \ln(m_{\text{rec}}/\text{GeV}) - \ln(m_{\text{true}}/\text{GeV}). \quad (4.9)$$

We compare the logarithms of the mass values because we have used logarithmically-flat priors on the WIMP mass. In Tab. 4.5 we show the average bias across all 250 realisations for each of the three benchmark distributions. In all three cases, the average bias is consistent with zero. Even in the SHM+DD case, which shows larger fluctuations away from the true value, there is no statistical bias.

We also test the *coverage* of the credible intervals which have been constructed. Table 4.6 shows the coverage values for the 68% and 95% intervals obtained in this section. In each case, there is very close to exact coverage. We have also checked that these intervals only provide exact coverage for the true WIMP mass of 50 GeV. Other values of m_{rec} are contained within the intervals less frequently than the true value, again indicating that this parametrization allows for unbiased and statistically robust reconstructions of the WIMP mass.

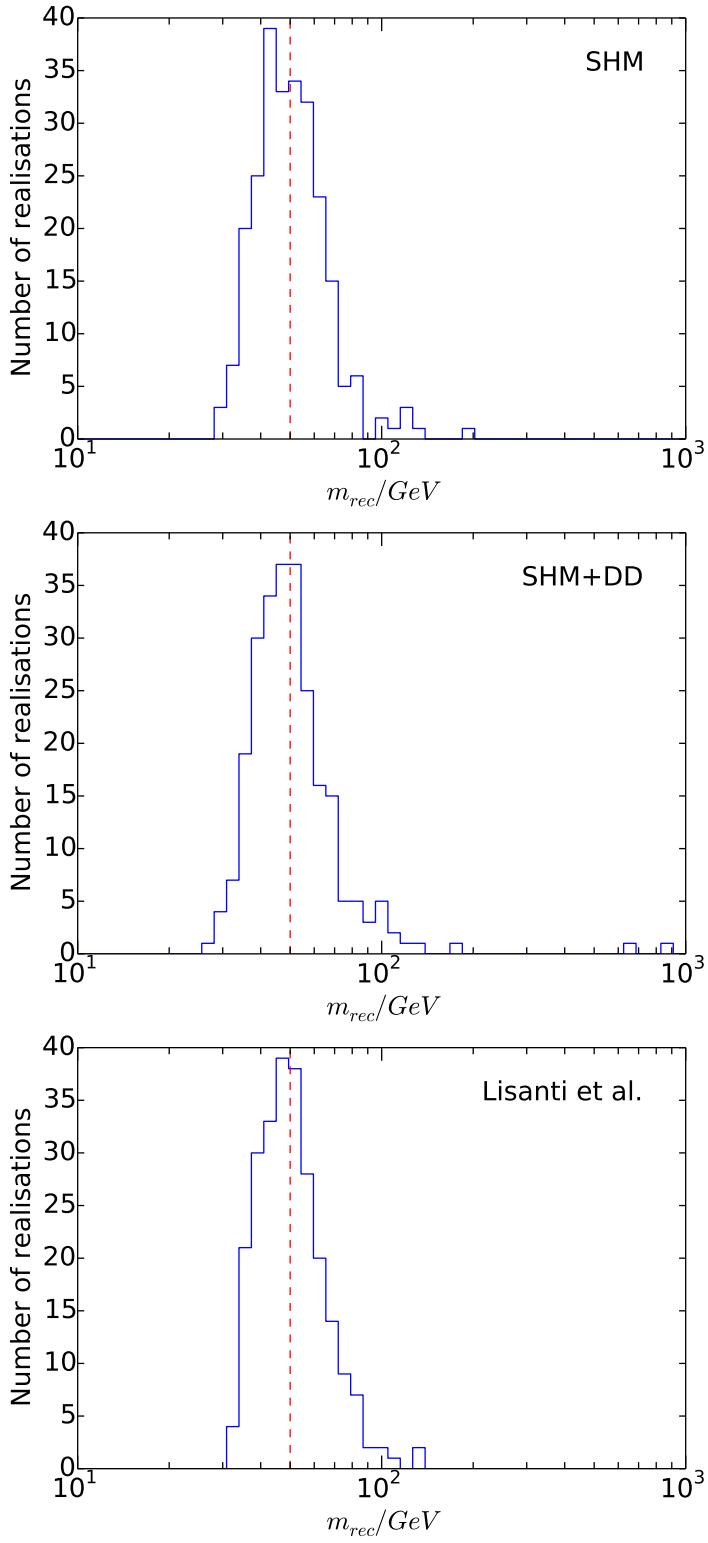


Figure 4.10: Distribution of the reconstructed mass m_{rec} for 250 mock data sets generated using several benchmark speed distributions, defined in Sec. ???. These are the SHM (top), SHM+DD (middle) and Lisanti et al. (bottom) distributions. The input WIMP mass of $m_\chi = 50$ GeV is shown as a vertical dashed red line. Reproduced from Ref. [2].

Benchmark speed distribution	68% coverage	95% coverage
SHM	$71 \pm 3 \%$	$94 \pm 3 \%$
SHM+DD	$68 \pm 3 \%$	$91 \pm 4 \%$
Lisanti et al.	$70 \pm 3 \%$	$95 \pm 3 \%$

Table 4.6: Coverage of 68% and 95% credible intervals calculated from 250 data realisations each for three benchmark speed distributions. The concept of coverage is described in the text of Sec. 4.5.

4.6 Reconstructing $f_1(v)$

Using the method described in this chapter, we can obtain the posterior probability distribution for the coefficients $\{a_1, \dots, a_{N-1}\}$ given the data, which we refer to as $P(\mathbf{a})$. We would like to be able to present this information in terms of the distribution function $f_1(v)$ in order to compare with some known distribution or look for particular features in the distribution. However, due to the fact that the distribution function is normalized, the values of f_1 at different speeds will be strongly correlated. We illustrate here how robust comparisons with benchmark distributions can be made.

As a first step, we can attempt to sample from $P(\mathbf{a})$, in order to obtain $P(f_1(v))$. This is the probability distribution for the value of f_1 at a particular speed v , marginalizing over the values of f_1 at all other speeds. We can repeat for a range of speeds to obtain 68% and 95% credible intervals for the whole of $f_1(v)$. The result of this procedure is presented in Fig. 4.11, for a randomly selected realisation from the SHM ensemble of Sec. 4.5. The underlying SHM distribution is shown as a solid line, while the 68% and 95% marginalized intervals are shown as dark and light shaded regions respectively. In this naive approach, we see that there is little shape information which can be recovered from the reconstruction, with only upper limits being placed on the speed distribution.

This method performs poorly because, as initially mentioned in Sec. 4.3, we have no information about the fraction of dark matter particles below the energy threshold of our experiments. Varying $f_1(v)$ will change this fraction. There is thus a degeneracy between the shape of the speed distribution and the cross-section, meaning that we can only probe the shape of

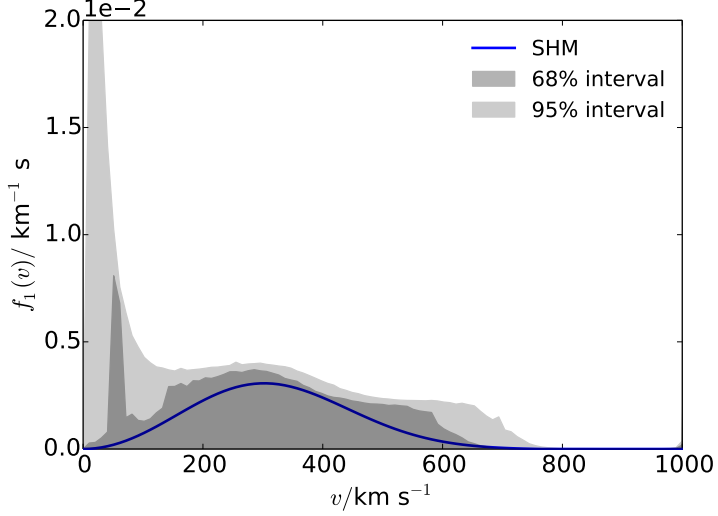


Figure 4.11: Reconstructed speed distribution for a single realisation of data, generated for a 50 GeV WIMP. 68% and 95% credible intervals are shown as dark and light shaded regions respectively, while the underlying SHM distribution function is shown as a solid blue line. Reproduced from Ref. [2].

$f_1(v)$, rather than its overall normalization. This degeneracy has not been accounted for in Fig. 4.11. We can attempt to correct for this by adjusting the normalization of $f_1(v)$. If we fix $f_1(v)$ to be normalized to unity above v_a (where $v_a \approx 171 \text{ km s}^{-1}$ is the lowest speed probed by the experiments for a WIMP of mass 50 GeV), we can compare the shapes of the underlying and reconstructed distribution functions. This is illustrated in Fig. 4.12, which shows that we now broadly reconstruct the correct shape of $f_1(v)$. Below v_a , the value of $f_1(v)$ is poorly constrained, because the experiments provide no information about the shape of the distribution below threshold.

There remain several issues with this approach. In order to utilize this method, we must know the approximate value of the lowest speed probed by the experiments. However, this value is set by the WIMP mass. We could determine v_a using the reconstructed WIMP mass, but this would be subject to significant uncertainty. In addition, direct reconstructions of the speed distribution may be easily biased. The upper limit of the energy windows of the experiments corresponds to a particular WIMP speed (for a given WIMP mass). WIMPs above this speed still contribute to the total event rate, but contribute no spectral information. The reconstructed shape of the high speed tail of the distribution is therefore not constrained

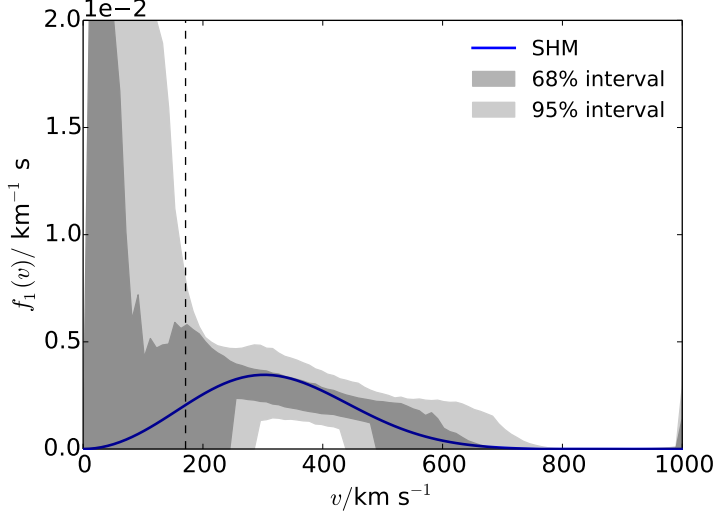


Figure 4.12: Reconstructed speed distribution for the same realisation of data as Fig. 4.11. In this case, we have also normalized $f_1(v)$ to unity above $v_a \approx 171 \text{ km s}^{-1}$ (vertical dashed line). This is the lowest speed accessible to the experiments for a WIMP of mass 50 GeV. 68% and 95% credible intervals are shown as dark and light shaded regions respectively, while the underlying SHM distribution function is shown as a solid blue line. Reproduced from Ref. [2].

by the data, but may affect the reconstructed value of f_1 at lower speeds.

An alternative approach is to reconstruct the mean inverse speed $\eta(v)$ (defined in Eq. 2.44) at some speed v . Because $\eta(v)$ is an integral function of f_1 , it is less prone to bias as it takes into account the full shape of the distribution at speeds greater than v . However, we do not know the normalization of f_1 and so we must normalize η appropriately. For each point sampled from $P(\mathbf{a})$, we calculate η . We then divide by $\alpha(v)$, the fraction of WIMPs above speed v , calculated using the same parameter point:

$$\alpha(v) = \int_v^\infty f_1(v') \, dv'. \quad (4.10)$$

We will write this rescaled mean inverse speed as $\eta^*(v) = \eta(v)/\alpha(v)$. The value of $\eta^*(v)$ is a measure of the shape of the distribution function above v . However, some information about the normalization of the distribution has been factored out by dividing by $\alpha(v)$. We no longer need to know the value of v_a in order to obtain information about the shape of the distribution at higher speeds. We may still need to decide the speed down to which we trust our reconstruction, but this no longer relies on an

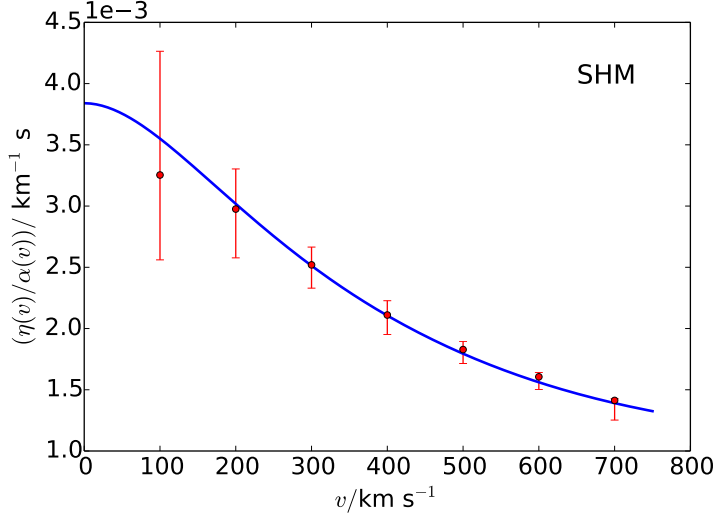


Figure 4.13: Mean reconstructed values of the rescaled mean inverse speed $\eta(v)/\alpha(v)$ at several values of v , calculated over 250 realisations of data using a 50 GeV WIMP and underlying SHM distribution function. Errorbars indicate the mean upper and lower limits of the 68% credible intervals. The underlying form of $\eta(v)/\alpha(v)$ obtained from the SHM is shown as a solid blue line. Reproduced from Ref. [2].

arbitrary choice of v_a to normalize the reconstructions at all speeds.

In Fig. 4.13, we plot the mean reconstructed value of η^* at several values of v , using 250 realisations of the 50 GeV SHM benchmark. We also show the mean upper and lower limits of the 68% credible intervals as errorbars. The form of η^* for the SHM is shown as a solid blue line. In all cases except for $v = 100 \text{ km s}^{-1}$, the mean reconstructed value is close to the true value, indicating that η^* can be reconstructed without bias using this method. At low speeds, the reconstructed value deviates from the true value. In addition, the credible intervals lead to *undercoverage* in the $v = 100 \text{ km s}^{-1}$ case. However, this point lies below the lowest speed to which the experiments are sensitive and therefore we cannot trust the reconstruction at this low speed. We have checked that for the remaining values of v the method provides exact or overcoverage, indicating that at higher speeds we can use η^* as a reliable and statistically robust measure of the shape of the distribution.

In the case of a single realisation of data, we would like to compare the probability distribution for $\eta^*(v)$ (obtained from $P(\mathbf{a})$) to the value calculated from some test distribution. We note that several distributions may produce the same value of $\eta^*(v)$ at a given value of v . Thus, we

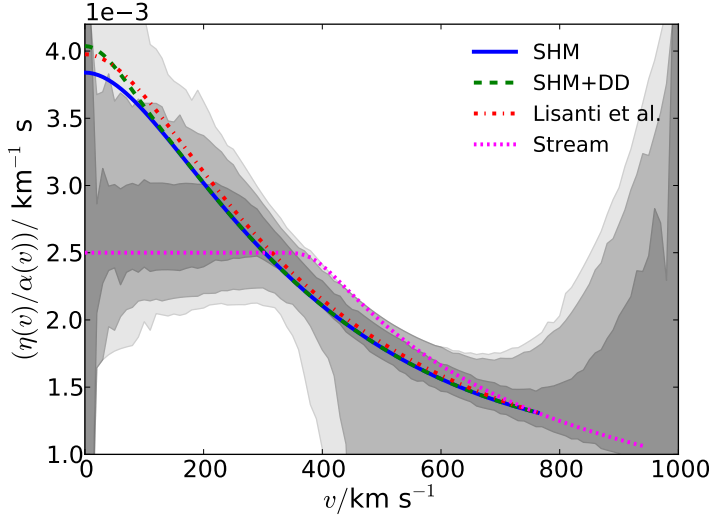


Figure 4.14: Rescaled mean inverse speed $\eta(v)/\alpha(v)$, reconstructed from a single realisation of data using a 50 GeV WIMP and underlying SHM distribution function. At each value of v we calculate 68%, 95% and 99% credible intervals (shown as shaded intervals). We also show the calculated values of $\eta(v)/\alpha(v)$ for several possible benchmark speed distributions: SHM (solid blue), SHM+DD (dashed green), Lisanti et al. (dot-dashed red) and stream (dotted magenta). The benchmark curves are truncated when the underlying distribution function goes to zero. Reproduced from Ref. [2].

may fail to reject a distribution function which is not the true distribution. However, if the calculated value of $\eta^*(v)$ does lie outside the $p\%$ interval, we can reject it at the $p\%$ level.

We can increase the discriminating power of this method by repeating this reconstruction over all speeds and checking to see if the benchmark value of η^* is rejected at any value of v . The result of this procedure is shown in Fig. 4.14 for a single realisation of data generated using an SHM distribution (the same data as in Figs. 4.11 and 4.12). We plot the 68%, 95% and 99% credible intervals as shaded regions, as well as the values of $\eta^*(v)$ calculated from several benchmark speed distribution. We will focus on the intermediate speed range ($v \gtrsim 200 \text{ km s}^{-1}$), as we do not know *a priori* the lowest speed to which the experiments are sensitive.

The reconstructed intervals are consistent with a range of possible distribution functions. The SHM and SHM+DD distributions are identical over a wide range of speeds. This is because above $\sim 200 \text{ km s}^{-1}$, the two distributions differ in normalization but not in shape. Differences appear

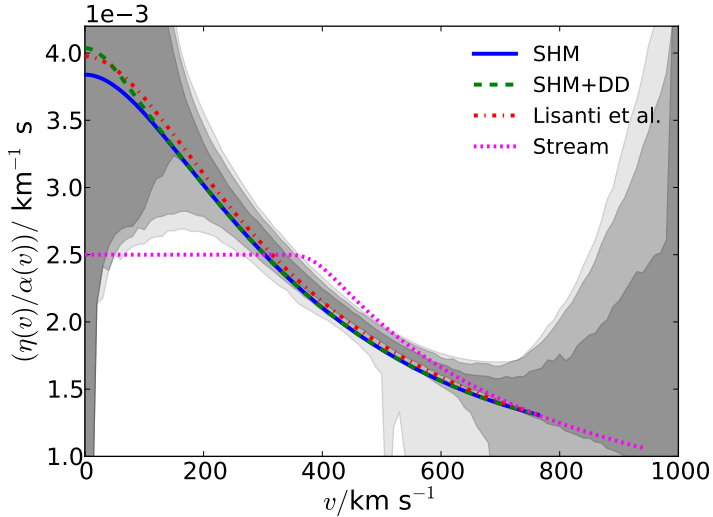


Figure 4.15: As Fig. 4.14, but using as input a Lisanti et al. speed distribution and an exposure time which is 2.5 times longer. Reproduced from Ref. [2].

between the two at low speeds where their shapes diverge. The Lisanti et al. distribution results in a larger deviation from the SHM, but not sufficiently large to differentiate between the two distributions given the size of the uncertainties. Finally, the stream distribution results in a significantly different form for $\eta^*(v)$. At approximately 400 km s^{-1} , the curve for the stream distribution lies outside the reconstructed 99% credible interval. We can therefore use this method to reject the stream distribution at the 99% confidence level.

Figure 4.15 shows the results of a reconstruction using a larger exposure. In this case, we generate data using the Lisanti et al. distribution and an exposure increased by a factor of 2.5, resulting in approximately 1000 events across the three detectors. As expected, the resulting credible intervals are now substantially narrower. The stream distribution now lies significantly outside the 99% interval. In Fig. 4.16, we show the same results, but focusing in on the region around $v \sim 400 \text{ km s}^{-1}$. At certain points, the SHM and SHM+DD distributions now lie outside the 95% credible interval, suggesting that with a number of events of the order of 1000, we may be able to reject these benchmarks.

While the method displayed in Fig. 4.12 allows the approximate shape of the speed distribution to be reconstructed, reconstructions of $\eta^*(v)$ allow more statistically robust statements to be made about the underlying speed

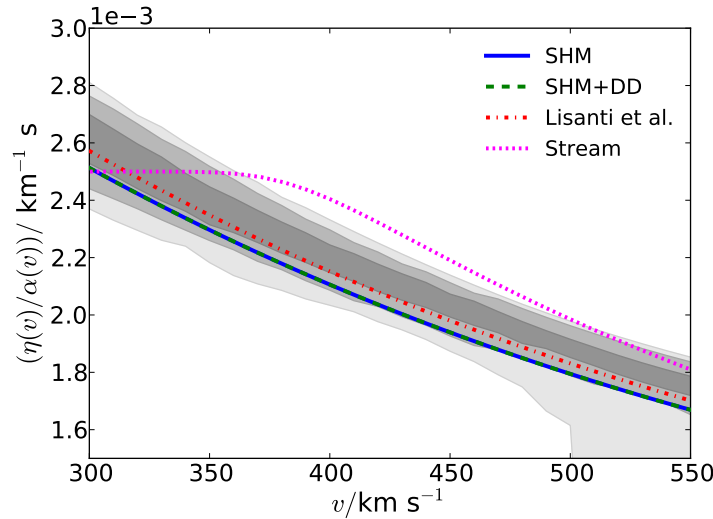


Figure 4.16: As Fig. 4.15, but focusing on the region around $v \sim 400 \text{ km s}^{-1}$. Notice that in the range $400 - 550 \text{ km s}^{-1}$, both the SHM and SHM+DD curves lie at or below the lower limit of the 95% credible interval. Reproduced from Ref. [2].

distribution. In particular, Fig. 4.16 illustrates that with larger exposures deviations from Maxwellian speed distributions can be detected in a model-independent fashion.

4.7 Discussion

Is it worth having a comparison between this method and the speed binning and momentum binning methods? As in showing a table where I reconstruct the WIMP mass using all three? And then explain why (and in what ways) this one works better.

4.8 Conclusions

We have studied in detail a new parametrization for the local dark matter speed distribution. This method involves writing the logarithm of the speed distribution as a polynomial in speed v and fitting the polynomial coefficients (along with the WIMP mass and cross section) to the data. We have attempted to disentangle in this paper the influence of different benchmark speed distributions, different benchmark WIMP masses and different forms for the parametrization.

We have shown how the number of basis functions in the parametrisation can be chosen in a systematic way by minimising the Bayesian Information Criterion. We have also shown that the results are insensitive to the precise choice of basis functions, but that the Chebyshev polynomials can be used to efficiently explore the parameter space and result in a faster reconstruction than other choices.

We have demonstrated that the WIMP mass can be reconstructed without bias in this method, using values in the range 10-500 GeV to test this. The inclusion of more realistic experimental uncertainties reduces the precision of the reconstructions, but does not introduce any bias. We have further tested the statistical properties of the WIMP mass reconstructions and have shown them to be robust over a range of possible speed distributions.

We have presented several ways of displaying the reconstructed WIMP speed distribution using this method. In order to make robust statistical inferences about the speed distribution, we calculate the probability distribution of $\eta(v)/\alpha(v)$. This is the mean inverse speed $\eta(v)$, rescaled by the fraction of WIMPs $\alpha(v)$ above speed v . This can be used as a measure of the *shape* of the distribution function, from which the unknown normalization has been factored out. We can then compare to the expected value of $\eta(v)/\alpha(v)$ from a given benchmark speed distribution, allowing us to distinguish between different underlying models.

Unfortunately, due to the finite threshold energies of direct detection experiments, we cannot probe the low speed population of WIMPs. If we make no assumptions, we have no information about the form of $f(v)$ below threshold and therefore little information about the overall normalisation of $f(v)$. This translates to an unavoidable degeneracy in the WIMP interaction cross section σ_p^{SI} . In spite of this, the completely general parametrisation presented in this Chapter can be used both to reconstruct the WIMP mass and probe the shape of the speed distribution in an unbiased and robust way.

Chapter 5

Breaking the cross section degeneracy: neutrino telescopes

The presence of dark matter (DM) in the Solar neighbourhood provides us with the opportunity to directly detect its scattering in terrestrial detectors. As we have investigated in Chapter 4, this may give us a handle on both the DM mass and speed distribution, providing we use a range of detector materials. However, the finite energy thresholds of direct detection experiments means that we cannot probe the entire range of DM speeds. With no sensitivity to low speed WIMPs, we also cannot know what fraction of WIMPs are probed by the experiments, resulting in a loss of sensitivity to the DM interaction cross section.

The local DM population may also scatter with nuclei in the Sun, becoming gravitationally captured if enough energy is lost in the interaction [356–360]. These can then annihilate and produce neutrinos, which may be observed at neutrino telescope (NT) experiments such as IceCube. Importantly, capture occurs preferentially for WIMPs with low energy or, equivalently, low speed. Such a signal at an NT experiment would provide complementary sensitivity to the low speed WIMP population, hopefully breaking the degeneracy in the DM interaction cross section.

In this chapter, we discuss the formalism for calculating the solar capture rate, as well as the processes of neutrino production, propagation and detection. We focus on calculating the event rate at the IceCube detector [177]. We then test the polynomial $\ln f(v)$ parametrisation presented in

Chapter 4 using both direct detection and IceCube mock data. In particular, we test the ability of these data sets to constrain the DM interaction cross sections and the DM mass, without making assumptions about the WIMP speed distribution. We note that due to the high abundance of spin-1/2 hydrogen in the Sun, we must consider both spin-independent (SI) and spin-dependent (SD) couplings in the analysis.

In Sec. 5.1, we describe the IceCube event rate formalism. We then describe several particle physics and astrophysical benchmarks for the dark matter population in Sec. 5.3, along with the experimental parameters used in the analysis. We explore the complementarity between NT and direct detection experiments in Sec. 5.2. In the remaining sections, we consider reconstructions of particle physics parameters first without IceCube data (Sec. 5.4) and then with IceCube data (Sec. 5.5), before discussing the prospects for reconstructing $f(v)$ itself (Sec. 5.6).

5.1 Neutrino telescope formalism

Calculation of the expected spectrum of neutrinos at an NT experiment can be broadly decomposed into 3 contributions. The first is the rate at which WIMPs scatter and are captured in the Sun. The second is the subsequent thermalisation of the solar WIMP population and their eventual annihilation into neutrinos. Third, we must model the detection of neutrinos at the IceCube detector. We now consider each of these in turn, focusing on the first, as this is where the WIMP cross sections and speed distribution enter into the calculation.

5.1.1 Solar capture

In calculating the solar capture rate, we follow closely the treatment of Gould [361, 362]. WIMPs are captured by the Sun when they elastically scatter off one of its constituent nuclei and end up with a speed lower than the solar escape velocity (which at the surface is equal to $v_{\text{esc}}^{\odot} = 617.5 \text{ km s}^{-1}$ [363]). These WIMPs then enter bound orbits intersecting the Sun, ensuring further scatters with solar nuclei during subsequent passes. WIMPs may become unbound in subsequent scatters (this possibility will be discussed later) but typically lose energy until they collect and thermalise around the Sun’s core.

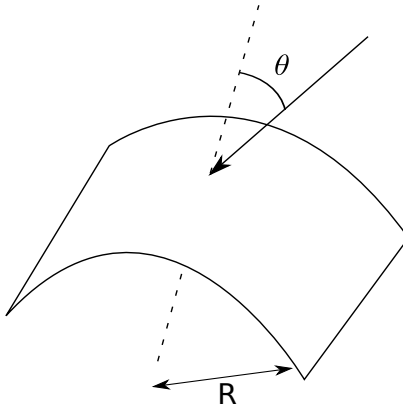


Figure 5.1: Illustration of the geometry of WIMPs impinging on the Sun

In order to calculate this ‘first-scatter’ probability, we consider a spherical surface of radius R , large enough that the gravitational field at R is negligible. This geometry is illustrated schematically in Fig. 5.1. The number density of WIMPs with speed v is $n_\chi f_1(v) dv$. Because of the spherical symmetry of the problem, we can assume that the WIMP velocity distribution is isotropic without loss of generality. The fraction of WIMPs with direction $\cos \theta \rightarrow \cos \theta + d \cos \theta$ relative to the perpendicular direction is $\frac{1}{2} d \cos \theta$ (normalised over all values of $\cos \theta$). The WIMP speed perpendicular to the surface is given by $v \cos \theta$, meaning that the WIMP flux inward through the surface (per unit area) can be written:

$$\frac{n_\chi}{2} f_1(v) v \cos \theta dv d \cos \theta = \frac{n_\chi}{4} f_1(v) v dv d \cos^2 \theta, \quad \theta \in [0, \frac{\pi}{2}]. \quad (5.1)$$

We change variables to angular momentum per unit mass, $J = Rv \sin \theta$, and integrate over all area elements on the surface of the shell to obtain the inward WIMP flux per unit time

$$4\pi R^2 \frac{\rho_0}{m_\chi} \frac{1}{4} f_1(v) v dv \frac{dJ^2}{R^2 v^2}. \quad (5.2)$$

We now consider an inner shell of radius r and thickness dr . If the escape velocity at the shell is $v_{\text{esc}}(r)$, then a WIMP with speed v at infinity will have speed $w = \sqrt{v^2 + v_{\text{esc}}^2(r)}$ at this inner shell. The total time the WIMP spends in the shell is

$$\frac{dl}{w} = \frac{2}{w \cos \theta} \Theta(1 - \sin \theta) dr = \frac{2}{w} \left[1 - \left(\frac{J}{rw} \right)^2 \right]^{-1/2} \Theta(rw - J) dr, \quad (5.3)$$

where the Heaviside step function Θ appears because the WIMP crosses the shell either twice or not at all. If the rate at which a single WIMP travelling at velocity w is scattered down to a speed less than the escape speed v_{esc} is given by $\Omega_{v_{\text{esc}},i}^-(w)$, then we can write the WIMP capture rate per unit time as

$$\begin{aligned} 2\pi \, dr \frac{\rho_0}{m_\chi} \frac{f_1(v)}{v} \, dv \frac{\Omega_{v_{\text{esc}},i}^-(w)}{w} \int_0^{(rw)^2} \left[1 - \left(\frac{J}{rw} \right)^2 \right]^{-1/2} d(J^2) \\ = 4\pi r^2 \, dr \frac{\rho_0}{m_\chi} \frac{f_1(v)}{v} \, dv w \Omega_{v_{\text{esc}},i}^-(w). \end{aligned} \quad (5.4)$$

The ‘first scatter’ rate is then given by integrating over the radius of the Sun:

$$C_\odot = \frac{\rho_0}{m_\chi} \int_0^{R_\odot} dr \sum_i \frac{dC_i}{dV} 4\pi r^2, \quad (5.5)$$

where the capture rate per unit shell volume is

$$\frac{dC_i}{dV} = \int_0^{v_{\text{max}}} dv \frac{f_1(v)}{v} w \Omega_{v_{\text{esc}},i}^-(w). \quad (5.6)$$

The index i labels the various nuclei in the Sun. The integration limit is

$$v_{\text{max}} = \frac{\sqrt{4m_\chi m_{N_i}}}{m_\chi - m_{N_i}} v_{\text{esc}}(r). \quad (5.7)$$

WIMPs above this speed cannot lose enough energy in a recoil to drop below the escape speed.

We now calculate the factor $\Omega_{v_{\text{esc}},i}^-(w)$, which gives the rate at which a single WIMP travelling at velocity w is scattered down to a speed less than the escape speed v_{esc} . This rate can be written as:

$$\Omega_{v_{\text{esc}},i}^-(w) = \Phi_\chi N_T \sigma_{v_{\text{esc}}} \quad (5.8)$$

where $\Phi_\chi N_T$ is the WIMP flux multiplied by the number of target nuclei. For a single WIMP and a number density of nuclei n_N , this becomes $\Phi_\chi N_T = w n_N$. The cross-section for the process $\sigma_{v_{\text{esc}}}$ is given by:

$$\sigma_{v_{\text{esc}}} = \int_{E_{v_{\text{esc}}}}^{E_{\text{max}}} \frac{d\sigma}{dE_R} dE_R \quad (5.9)$$

where $E_R = \Delta E$ is the energy lost by the scattering WIMP. The limits of integration run from the minimum energy loss required to reduce the WIMP speed below v_{esc} ,

$$E_{v_{\text{esc}}} = \frac{m_\chi}{2} (w^2 - v_{\text{esc}}^2) = \frac{m_\chi}{2} v^2, \quad (5.10)$$

to the maximum possible energy loss in the collision,

$$E_{\max} = \frac{2\mu_{\chi N}^2}{m_N} w^2. \quad (5.11)$$

As in the direct detection case, we can decompose the differential cross section into SI and SD components. While all of the constituent elements of the Sun are sensitive to the SI interaction, only spin-1/2 Hydrogen is sensitive to SD scattering. The differential cross section is therefore given by

$$\frac{d\sigma}{dE_R} = \frac{m_{N_i}}{2\mu_{\chi p}^2 v^2} \begin{cases} \sigma_p^{\text{SI}} + \sigma_p^{\text{SD}} & \text{for } A = 1 \\ \sigma_p^{\text{SI}} A_i^2 F_i^2(E_R) & \text{for } A > 1. \end{cases} \quad (5.12)$$

No form factor is needed for Hydrogen ($A = 1$), which consists of only a single nucleon. For the remaining nuclei, we approximate the form factor as [361]

$$F_i^2(E_R) = \exp(-E_R/E_i); \quad E_i = \frac{3}{2m_{N_i} R_i^2}, \quad (5.13)$$

where R_i is the nuclear radius (see Sec. 2.4.1). These expressions allow Eq. 5.9 to be calculated analytically and introduce an error in the total capture rate of at most a few percent. In addition to the effects which have already been described, we can also consider a number of other factors which may impact the WIMP capture rate. The fact that nuclei in the Sun have a finite temperature has been neglected so far. However, detailed calculation [356, 361] shows that this gives a correction to the capture rate of only around 1% for WIMP masses above around 10 GeV. The gravitational influence of other bodies in the Solar system may also have an impact [364]. For example, Peter [365] found that WIMPs whose bound orbits reach out as far as Jupiter can be perturbed by the planet and become unbound. This leads to so-called *Jupiter depletion* for WIMPs heavier than around 1 TeV. However, a recent study by Sivertsson and Edsjö [366] showed using Liouville's theorem that such depletion processes must be accompanied by an inverse diffusion process. The net result is that for Solar capture we can treat the WIMP population as being free.

5.1.2 Evolution of the WIMP population

Once a WIMP has scattered to below the escape speed at a given solar position, it will be in a bound orbit and will enter the population of WIMPs

captured by the Sun. Subsequent scatters with the nuclei in the Sun should lead to an approximately thermal distribution. There are then two processes which will tend to deplete this population: WIMP evaporation and annihilation.

Evaporation occurs when WIMPs scatter into the high speed tail of the thermal distribution, above the Solar escape velocity, and become unbound. It has been shown that for a WIMP mass of around 4 GeV, the evaporation timescale is approximately equal to the lifetime of the Sun (~ 4.7 billion years) [367]. For WIMPs significantly heavier than this, the evaporation rate is negligible compared to the capture rate. For WIMPs lighter than this, the tail of the Maxwell-Boltzmann distribution lying above the escape velocity becomes significant and evaporation can no longer be neglected [368, 369]. As we will see, the IceCube detector is sensitive to WIMPs with masses above around $m_\chi > 20$ GeV, meaning that we can safely ignore the effects of evaporation.

The population of WIMPs will also undergo annihilation (either with their anti-particle partners or with themselves if they are Majorana particles). The evolution of the total number $N(t)$ of WIMPs in the Sun can then be written as [360]:

$$\frac{dN}{dt} = C_c - \frac{1}{2}C_a N^2 - C_e N. \quad (5.14)$$

The parameter C_c is the total capture rate and the parameters C_a and C_e determine the annihilation and evaporation rates. As we have discussed, we can safely neglect evaporation, so we set C_e to zero. The parameter C_a and therefore the annihilation rate will depend on the velocity-averaged annihilation cross section $\langle\sigma v\rangle$ which is *a priori* unknown. Over a long period of time, equilibrium between the capture and annihilation will be achieved and a steady state scenario for the WIMP population will be reached. This timescale is set by the equilibration time $\tau = 1/\sqrt{C_c C_a}$. If this is sufficiently short compared to the lifetime of the Sun, the WIMP population will currently be in equilibrium with the annihilation rate Γ_a set by the capture rate as

$$\Gamma_a = \frac{1}{2}C_a. \quad (5.15)$$

Crucially, in this case, the annihilation rate no longer depends on the unknown annihilation cross section, but is related only to the WIMP-

nucleus scattering cross sections. We will assume in the rest of this chapter that the annihilation cross section is sufficiently high that the equilibrium assumption is valid.

Standard Model (SM) particles are produced in these annihilations, the majority of which cannot escape the Sun. However, some of these particles may decay to neutrinos or neutrinos may be produced directly in the WIMP annihilation. These neutrinos can escape the Sun and may be detected at NT experiments on Earth. It is important to account for the production and propagation of neutrinos in the dense medium of the Sun, as well as the propagation of these neutrinos from the Sun to the Earth [370]. The spectrum of neutrinos reaching Earth can be written as

$$\frac{dN_\nu}{dE_\nu} = \frac{\Gamma_a}{4\pi D^2} \sum_f B_f \frac{dN_\nu^f}{dE_\nu}, \quad (5.16)$$

where D is the Earth-Sun distance, dN_ν^f/dE_ν is the neutrino spectrum produced in the Sun for a particular final state f and B_f is the branching ratio into that final state. The branching ratios will depend on the specific form of the dark matter interactions with baryons. Typically, in order to set constraints on the WIMP interaction cross sections, we consider annihilation into only one channel at a time, assuming $B_f = 1$ for that particular channel during the analysis. Finally, the neutrino spectrum produced in the annihilation dN_ν^f/dE_ν can be obtained using particle physics event generators (such as PYTHIA [371]) and propagated to Earth using neutrino Monte Carlo simulations (such as WimpSim [370]). We perform these calculations (and the capture rate calculation) using a modified version of the publicly available DARKSUSY package [372, 373].

5.1.3 Detection

Neutrinos which escape the Sun can be detected at terrestrial NT experiments [177, 374]. We focus in this work on the IceCube experiment [177, 375], which can detect the Čerenkov radiation produced by high energy particles traveling through ice. Muon neutrinos interact via charged-current interactions in the ice to produce relativistic muons. These in turn produce Čerenkov light, which is collected by digital optical modules (DOMs) mounted on strings in the ice. The amount and pattern of lit DOMs allows the energy and direction of the incoming neutrino to be

reconstructed.

In addition to the main IceCube array, a small region of the detector is instrumented with additional strings. This region has a DOM density roughly 5 times greater than the rest of the detector and is known as DeepCore [376]. The increased Čerenkov light collection means that DeepCore lowers the threshold energy of the detector down to roughly 10 GeV. This gives the detector sensitivity to DM particles with mass down to around 20 GeV. Data from the 79-string IceCube experiment including DeepCore have been able to set upper limits of $\sigma_p^{\text{SI}} < 1.45 \times 10^{-43} \text{ cm}^2$ and $\sigma_p^{\text{SD}} < 1.34 \times 10^{-40}$ at the 90% confidence level, for masses in the range 200-500 GeV and annihilation to W^+W^- [377].

5.2 Complementarity with direct detection

The complementarity between direct detection and NT data has been studied in the past [322]. In particular, the high abundance of hydrogen can help to constrain the spin-dependent cross section and, even in cases where no signal is observed at IceCube, limits from NT experiments can help to reduce the size of the allowed parameter space. Here, we explore further this complementarity by looking at the range of speeds which are probed by NT experiments.

As can be seen from Eq. 5.6, WIMPs with speeds from $v = 0$ up to $v = v_{\max}$ have the possibility of being captured by the Sun. In particular, with increasing WIMP speed the capture probability decreases, further suppressed by the loss of coherence in the SI case. As pointed out in Ref. [378], direct detection experiments probe a complementary range of the WIMP speed distribution, defined by the energy range of the WIMP search window. If the ranges of speeds probed by direct detection and NT experiments overlaps, this means that the entire WIMP speed distribution can be probed.

In Fig. 5.2, we show the WIMP speeds to which two experiments are sensitive as a function of WIMP mass. As a blue band, we show the region probed by a Xenon direction detection experiment. The lower and upper limits of the band are set by $v_{\min}(E_{\min})$ and $v_{\min}(E_{\max})$, where E_{\min} and E_{\max} define the extent of the WIMP signal window. In this chapter, we consider a window of $[5, 45]$ keV. WIMPs with speeds above the blue band still contribute to the overall event rate (so there is still some sensitivity to

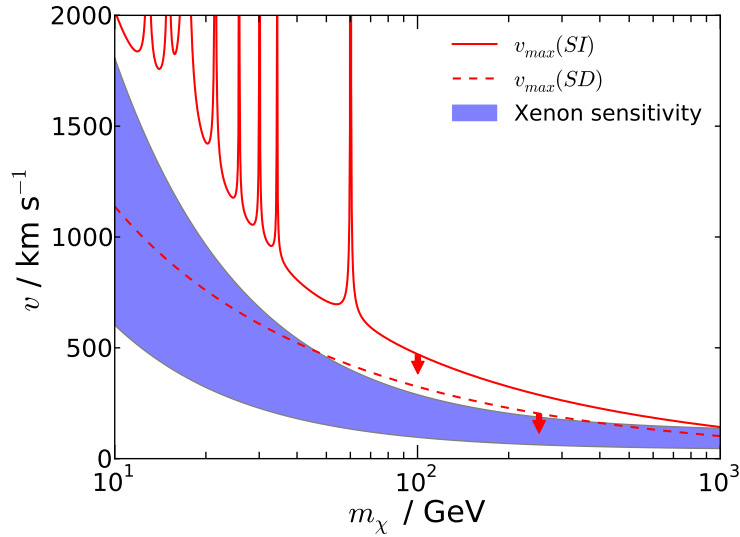


Figure 5.2: Sensitivity ranges of solar capture and direct detection experiments. We show as a blue band the range of speeds to which a Xenon detector is sensitive using an energy window of [5, 45] keV. The maximum speed to which solar WIMP capture is sensitive is shown as a solid (dashed) red line for SI (SD) interactions (see the text for more details).

them). However, there is no information on the *shape* of the distribution at higher speeds, as we are not sensitive to the event spectrum above E_{\max} .

Also shown in Fig. 5.2 are the values of v_{\max} involved in the Solar capture rate for SI and SD interactions. In the SD case, the maximum speed is set by the hydrogen mass m_H :

$$v_{\max} = \frac{\sqrt{4m_{\chi}m_H}}{m_{\chi} - m_H} v_{\text{esc}} . \quad (5.17)$$

The escape speed v_{esc} depends on radius within the Sun so we use an average value, weighted by the hydrogen density as a function of radius. In the SI case, the situation is more complex, as more than one nucleus contributes to the capture rate. We therefore consider the average value of v_{\max} weighted by the mass fraction f_i of each species

$$\langle v_{\max} \rangle = \sum_i f_i \frac{\sqrt{4m_{\chi}m_{N_i}}}{m_{\chi} - m_{N_i}} v_{\text{esc}} , \quad (5.18)$$

where again v_{esc} is evaluated at the average radius of each species i . This gives an indication of the typical value of v_{\max} experienced by WIMPs in the Sun.

In the SD case, the decreasing value of v_{\max} with m_χ reflects the kinematics of the $\chi - H$ interaction. As the WIMP mass increases, scattering with hydrogen becomes less efficient at transferring energy. In the SI case, the value of v_{\max} is typically higher because the WIMP is closer in mass to the heavier nuclei in the Sun. However, there is still a significant SI interaction with hydrogen and the same fall off with m_χ is observed as in the SD case. In addition, there are resonances in v_{\max} , corresponding to perfect mass matching between the WIMP and one of the nuclei in the Sun. In these cases, energy transfer is highly efficient and WIMPs of any speed can scatter into bound orbits.

The key point of Fig. 5.2 is that in both the SI and SD dominated cases, v_{\max} never falls below the lower limit of the blue band. This means that the combination of NT and direct detection data should provide sensitivity to the full range of WIMP speeds over a range of masses. The level of sensitivity may vary with WIMP speed, due for example to a falling capture contribution from higher speeds or form factor suppression in direct detection experiments. However, in principle, we can probe the full WIMP speed distribution and hopefully break the degeneracy in the cross section described in Chapter 4. The inclusion of data sets from additional direct detection experiments should only improve this sensitivity.

5.3 Benchmarks and experiments

In order to test this complementarity and determine how well the WIMP parameters can be recovered, we generate mock data sets for a set of hypothetical direct detection experiments as well as for IceCube. In Table 5.1, we show the parameters used in this chapter for three direct detection experiments chosen to mimic next-generation detectors currently in development. Each experiment is described by the range of nuclear recoil energies it is sensitive to and the total exposure (the product of the fiducial detector mass, the exposure time and the experimental and operating efficiencies). We also include a gaussian energy resolution of $\sigma_E = 1$ keV and a flat background rate of 10^{-7} events/kg/day/keV. This results in 1-2 background events in each detector.

Compared to Chapter 4, we use a slightly lower threshold for the Xenon experiment. This is in light of the low threshold energy achieved by the LUX experiment [184]. We use an exposure time $t_{\text{exp}} = 2$ years for all 3

Experiment	Target Mass, A	Detector Mass (fid.), m_{det}/kg	Efficiency, ϵ	Energy Range/keV
Xenon	131	1000	0.5	5-45
Argon	40	1000	0.5	30-100
Germanium	73	300	0.5	10-100

Table 5.1: Summary of parameters for mock direct detection experiments. All experiments have a constant energy resolution of $\sigma_E = 1 \text{ keV}$ and a flat background rate of $10^{-7} \text{ events/kg/day/keV}$. An exposure of $t_{\text{exp}} = 2 \text{ years}$ is used for all 3 experiments.

experiments and a constant 50% efficiency. The methods presented here would be used after a dark matter signal has been confirmed in multiple channels, once a sufficient number of events has been detected. We therefore choose not to model the energy resolution, background rates and efficiencies too closely on current experiments. Instead, we consider what may be possible with several somewhat-idealised future detectors.

For the spin-dependent scattering in Xenon and Germanium, we assume natural abundances of each of the isotopes and use the parametrisation of Cerdeno et al. [279],

$$S_{ij} = N((1 - \beta)e^{-\alpha u} + \beta), \quad (5.19)$$

which is described in more detail in Sec. 2.4.1. The values we use for the parameters (N, α, β) for the S_{00} spin structure functions are (0.0595, 3.75, 0.0096) for Xe-129, (0.035, 3.925, 0.12) for Xe-131 and (0.195, 4.25, 0.07) for Ge-73. These were chosen to approximately reproduce the median values obtained from a range of spin structure function calculations [197, 379–381]. We focus in this work on understanding the impact of astrophysical uncertainties, so we keep the SD nuclear parameters fixed at these median values during the reconstructions.

We divide the energy range of each experiment into bins and generate Asimov data [352] by setting the observed number of events in each bin equal to the expected number of events. While this cannot correspond to a physical realisation of data as the observed number of events will be non-integer, it allows us to disentangle the effects of Poisson fluctuations from the properties of the parametrisation under study.

To generate neutrino telescope data, we consider the IceCube 86-string configuration. We use an exposure time of 900 days (corresponding to five 180 day austral winter observing seasons, as in Ref. [322]). We use an angular cut around the solar position $\phi_{\text{cut}} = 3^\circ$. This results in approximately 217 background events over the full exposure. As with the direct detection experiments, we set the observed number of events equal to the expected number of signal plus background events. We use only the observed number of events as data and not the energies of the individual events. Event-level likelihood methods have previously been developed [382] for use with IceCube 22-string data [375]. However, a similar analysis has not been performed for IceCube-86. In particular, the probability distributions for the number of lit digital optical modules (DOMs) as a function of neutrino energy are not yet available for IceCube-86. Nonetheless, using the number of observed events at IceCube is a first step towards using neutrino telescope data to help constrain the WIMP speed distribution.

5.3.1 Benchmarks

We use four benchmark models to generate mock data sets, which are summarised in Table 5.2, along with the number of events expected for each model. In all cases, we use an SI WIMP proton cross section of $\sigma_p^{\text{SI}} = 10^{-45} \text{ cm}^2$ and SD cross-section of $\sigma_p^{\text{SD}} = 2 \times 10^{-40} \text{ cm}^2$, both of which are close to the current best exclusion limits [184, 246]. For simplicity, we assume that the WIMP-proton and WIMP-neutron couplings are equal in both the SI and SD cases. We could allow the ratio of these couplings to vary as free parameters, but this would introduce additional degeneracies into the analysis. Here we focus on the degeneracy associated with the WIMP speed distribution.

Benchmark A represents an intermediate mass WIMP which annihilates to W^+W^- , which is similar to benchmark B used by Ref. [322]. As we will see, even with this intermediate mass there is already a strong degeneracy in the reconstructed WIMP mass. We therefore choose not to consider a benchmark model with higher mass, which would result in an even poorer sensitivity to the reconstructed WIMP mass. We do, however, consider a lighter WIMP in benchmark C, which annihilates to $\nu_\mu\bar{\nu}_\mu$. The IceCube detector (with DeepCore) is sensitive to WIMPs with masses down to about 20 GeV. We therefore use a 30 GeV WIMP mass, as WIMPs much lighter

than this cannot feasibly be detected by IceCube.

Benchmarks A and C assume an SHM speed distribution described by $v_{\text{lag}} = 230 \text{ km s}^{-1}$ and $\sigma_v = 163 \text{ km s}^{-1}$. Benchmarks B and D assume the same particle physics parameters as A and C respectively, but assuming an SHM distribution with a moderate dark disk overdensity (SHM+DD). We model the dark disk as contributing an additional 30% dark matter density to the SHM, with parameters $v_{\text{lag}} = 50 \text{ km s}^{-1}$ and $\sigma_v = 50 \text{ km s}^{-1}$. As shown in Ref. [109], the capture rate in the Sun is not strongly dependent on variations in the shape of $f(v)$ (such as the differences between distribution functions extracted from different N-body simulations). However, significant enhancement of the capture rate can be achieved with the presence of a low speed dark disk, which we investigate using these two astrophysical benchmarks.

5.3.2 Parameter sampling

We perform parameter scans using a modified version of the publicly available MULTINEST 3.6 package [349–351]. This allows us to map out the likelihood $\mathcal{L}(\theta)$ for the model parameters θ . We use $N_{\text{live}} = 20000$ live points in the scans and a tolerance of 10^{-4} . We show in Table 5.3.2 the priors on the various model parameters used in this work.

In the polynomial $\ln f(v)$ parametrisation, we use 6 basis polynomials (5 free coefficients, with one fixed by normalisation). This is because, with the addition of SD interactions, the parameter space is significantly larger than in the SI-only case. As we will see, using 6 basis functions still allows a wide range of speed distributions to be explored and can provide a good fit to the data. With increasing numbers of events, it would be feasible to increase the number of basis functions and more precisely parametrise the form of the speed distribution.

The likelihood function we use for each experiment is:

$$\mathcal{L}(\theta) = \left(\prod_{i=1, N_{\text{bins}}} \frac{(N_e^i)^{N_o^i}}{(N_o^i)!} e^{-N_e^i} \right)^w, \quad (5.20)$$

where the signal region is divided into N_{bins} bins with N_e^i events expected and N_o^i events observed in the i th bin. We weight the likelihood by a factor $w = N_{\text{tot}}/(N_{\text{expt}} N_{\text{bins}})$, where N_{tot} is the total number of bins across all experiments. This means that the direct detection experiments (for

Benchmark	m_χ (GeV)	Speed dist.	Ann. channel	$N_{\text{Xe}}(\text{SI})$	$N_{\text{Xe}}(\text{SD})$	$N_{\text{Ar}}(\text{SI})$	$N_{\text{Ar}}(\text{SD})$	$N_{\text{Ge}}(\text{SI})$	$N_{\text{Ge}}(\text{SD})$	N_{IC}
A	100	SHM	W^+W^-	154.9	262.7	16.1	0	25.4	18.7	43.3
	100	SHM+DD	W^+W^-	167.1	283.9	16.2	0	25.7	18.9	242.9
C	30	SHM	$\nu_\mu \bar{\nu}_\mu$	175.1	301.1	6.2	0	20.5	16.1	13.2
	30	SHM+DD	$\nu_\mu \bar{\nu}_\mu$	175.0	300.9	5.8	0	20.4	16.0	40.2

Table 5.2: Summary of benchmarks. In all cases, we consider only isospin conserving interactions (i.e. $f_p = f_n$ and $a_p = a_n$). Also listed are the number of events foreseen in each detector. For direct detection targets we separate between recoils induced by SI and SD interactions.

Parameter	Prior range	Prior type
m_χ (GeV)	10–1000	log-flat
σ_{SI}^p (cm 2)	$10^{-48} – 10^{-42}$	log-flat
σ_{SD}^p (cm 2)	$10^{-43} – 10^{-37}$	log-flat
Polynomial coefficients $\{a_k\}$	–20 – 20	linear-flat

Table 5.3: Summary of MultiNest priors used in this chapter.

which there are a large number of bins in energy) receive the same weight as the IceCube experiment (for which $N_{\text{bins}} = 1$). More details are given in Appendix A. The total likelihood is then the product over all experiments under consideration.

5.4 Reconstructions without IceCube

In Fig. 5.3, we show the 2-dimensional profile likelihood plots for the parameters $(m_\chi, \sigma_p^{\text{SI}})$, $(m_\chi, \sigma_p^{\text{SD}})$ and $(\sigma_p^{\text{SI}}, \sigma_p^{\text{SD}})$ reconstructed using the polynomial $\ln f(v)$ parametrisation. We use data from the three direct detection experiments described in Sec. 5.3 *without* any additional information from IceCube. Each row corresponds to a different benchmark and the contours enclose the 68% and 95% confidence regions. The benchmark parameter values are shown as dashed red line, while the best fit is indicated as a green triangle. These results are distinct from the results of Chapter 4 in that we are also including a contribution to the rate from spin-dependent interactions.

For Benchmark A (top row), there is a strong degeneracy in the WIMP mass. The benchmark value $m_\chi = 100$ GeV is larger than the target masses for Argon and Germanium, leading to a loss in sensitivity to the reconstructed WIMP mass. This is exacerbated by the degeneracy between m_χ and the shape of $f(v)$. In spite of this, the best fit value is close to this benchmark value, indicating that the inclusion of SD scattering does not introduce any bias in the reconstruction of m_χ .

The inclusion of σ_p^{SD} in the scan, however, does introduce an additional degeneracy in the overall event rate. At large masses the contours for σ_p^{SD} extend down to low values and we do not obtain a closed contour. The complementarity of different experiments has previously been studied

in Ref. [383]. Because each target nucleus has a different response to SI and SD interactions, we should be able to determine the values of σ_p^{SI} and σ_p^{SD} separately. However, this depends on the uncertainties on the number of events at each experiment. For large m_χ , the range of speeds probed by each experiment has less overlap (see e.g. Fig. 3.2). Because the experiments do not all probe the same range of speeds, there is more freedom, in varying $f(v)$, to reproduce the observed event numbers in each experiment. This means that a large σ_p^{SI} and a small σ_p^{SD} can account for the observed data. The same is not true for small values of σ_p^{SI} and large values of σ_p^{SD} . This is because σ_p^{SI} is constrained by the (small) number of events in the Argon experiment which couples only via SI interactions. A direct detection target such as Fluorine which is sensitive predominantly to SD scattering would allow the bounds on σ_p^{SD} to be improved.

Should I include reconstructions with fixed $f(v)$ - I could overlay them...

The results for benchmark B (second row of Fig. 5.3) share many features with those of benchmark A. This is because the majority of the dark disk population (which is present in benchmark B) lies at speeds below the energy thresholds of the experiments. However, a major difference is the extension of the contours up to large values of both σ_p^{SI} and σ_p^{SD} . This is particularly evident in the top right corner of the right-most plot. This is an illustration of the problem described in both Chapter 3 and Chapter 4: the shape of $f(v)$ is unconstrained at low v , which means that the fraction of WIMPs above the experimental thresholds is unconstrained.

Why does this degeneracy not appear in benchmark A? This is because for a finite number N of basis functions, the parametrisation we use for $f(v)$ cannot approximate all functional forms arbitrarily well. For large m_χ , the lowest WIMP speed probed by the experiments is relatively small, with the Xenon experiment probing down to $v \approx 100 \text{ km s}^{-1}$. Distributions which fit the data down to this low speed and then rise rapidly below it may not necessarily be well explored by the parametrisation. In benchmark B, the dark disk population causes a rise in $f(v)$ above $v \approx 100 \text{ km s}^{-1}$, which leads to an excess in the data above the SHM-only case. For benchmark B, then, the parametrisation explores speed distributions which rise at low v in order to reproduce the data. The unconstrained WIMP fraction below the threshold then leads to the observed cross section degeneracy.

We note that the cross section degeneracy is a real effect in the case of benchmark A, meaning that the reconstructed cross sections which appear

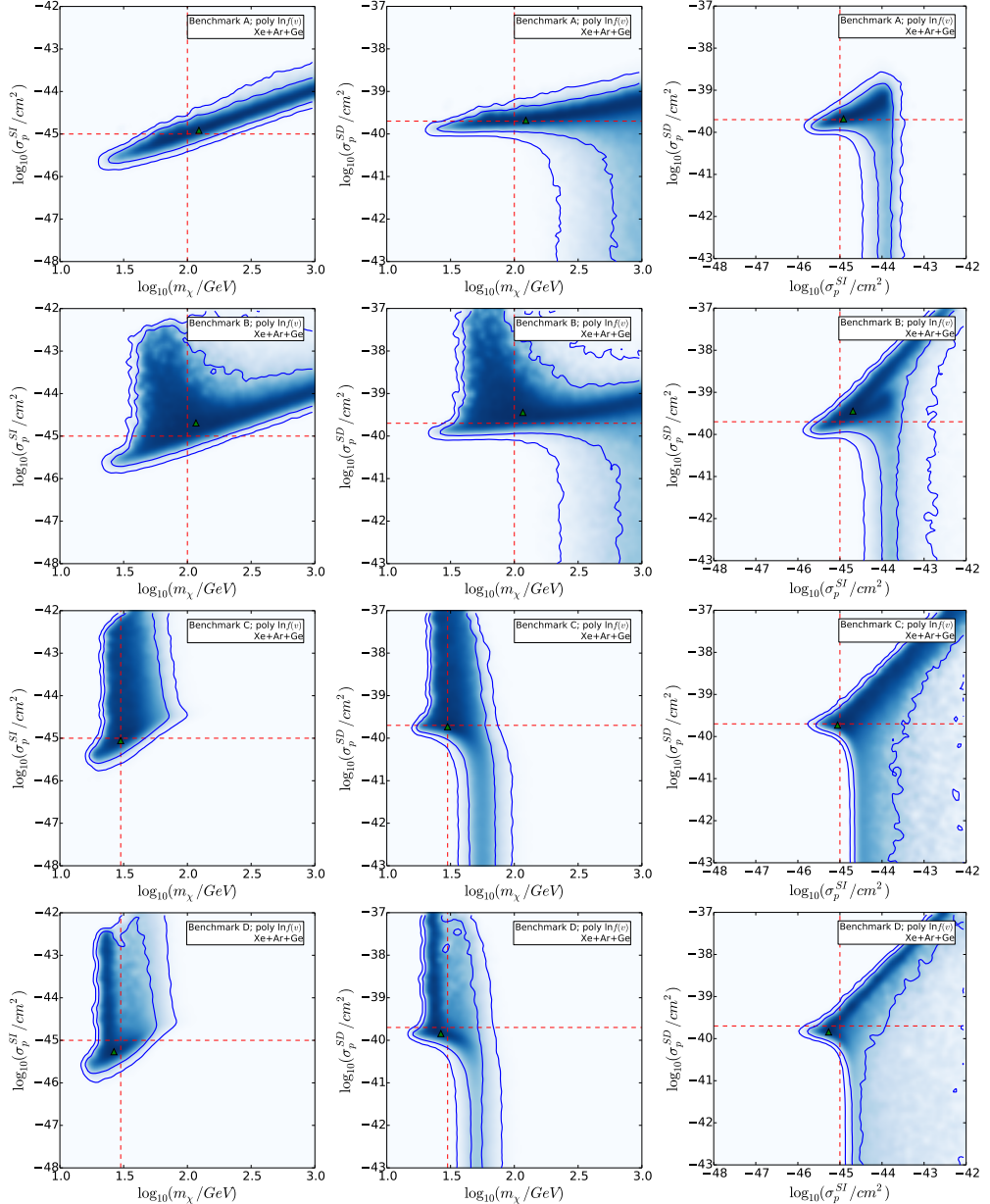


Figure 5.3: 2-dimensional profile likelihood for $(m_\chi, \sigma_p^{\text{SI}})$ (left column), $(m_\chi, \sigma_p^{\text{SD}})$ (central column) and $(\sigma_p^{\text{SI}}, \sigma_p^{\text{SD}})$ (right column), obtained using the polynomial $\ln f(v)$ parametrisation with direct detection data only. The shaded area gives the value of the profile likelihood, while the blue contours define the 68% and 95% confidence regions for the particle physics parameters. The 4 rows (from top to bottom) correspond to the 4 benchmarks A, B, C and D. The dashed red lines show the position of the benchmark values from Tab. 5.2 while the green triangle gives the best fit values.

in the top row of Fig. 5.3 must be taken as lower limits. The fact that this degeneracy does not appear in the profile likelihood is a consequence of the high WIMP mass and the finite number of basis functions used in the parametrisation. The degeneracy should become apparent with increasing N , but this would not improve the fit with the data, as it would simply explore a wider range of shapes for $f(v)$ below the experimental thresholds.

In benchmarks C and D (bottom two rows of Fig. 5.3), the cross section degeneracy is pronounced, as the experiments now only probe down to $v \sim 200 \text{ km s}^{-1}$ as a result of the lighter WIMP mass. The lighter WIMP mass also means that the rate is more sensitive to the reconstructed m_χ value. Thus, there is now an upper limit on m_χ , though we can only constrain m_χ to within a factor of ~ 4 at the 68% level. As in the case of heavier WIMP masses, σ_p^{SD} is not bounded from below due to the degeneracy between σ_p^{SI} and σ_p^{SD} .

5.5 Reconstructions with IceCube

In Fig. 5.4, we show the profile likelihood reconstructed using the polynomial $\ln f(v)$ parametrisation (as in Fig. 5.3) but now using both direct detection *and* IceCube mock data.

The results for benchmark A (top row) show that the best fit point is very close to the benchmark parameter values. One of the modes of the likelihood is peaked at the true WIMP mass and allows m_χ to be constrained to within a factor of 2 at the 1σ level. This is because the IceCube rate depends on m_χ in a different way to the direct detection experiments, leading to complementarity between the two experiments and allowing m_χ to be recovered more precisely.

However, there is also a second mode in the likelihood, at large values of m_χ and low values of σ_p^{SD} . This is evident in the bottom right corner of the central panel on the top row. We have already discussed this scenario in the case of direct detection-only data. In addition, large WIMP masses result in higher energy neutrinos being produced in WIMP annihilations and therefore an increased number of events above the IceCube threshold [322]. This means that the lower value of σ_p^{SD} can also reproduce the observed IceCube data. Furthermore, distributions which rise rapidly at low v can boost the capture rate further and therefore widen the allowed range of σ_p^{SD} to lower values.

The results for benchmark B (second row of Fig. 5.4) are almost indistinguishable from the results of benchmark A. This indicates that the uncertainties in $f(v)$ are being well accounted for in each case. For benchmark B, the most striking difference when compared with the direct detection-only reconstructions is that the degeneracy of the cross sections up to large values has now been broken. Upper limits can now be placed on σ_p^{SI} and σ_p^{SD} at the 95% level. Those points with large cross sections and a large WIMP population below the direct detection threshold would now over-produce events at IceCube, which is sensitive to this low speed WIMP population.

For the light benchmarks (C and D, bottom two rows of Fig. 5.4), the results are again largely indistinguishable, indicating good control over the astrophysical uncertainties. In both cases, the reconstruction of the mass is improved compared to the direct detection-only case, especially at low m_χ . Due to the energy threshold at IceCube, the detector is only sensitive to the annihilation of WIMPs with masses above ~ 25 GeV. WIMPs lighter than this cannot explain the number of excess events observed at IC.

As in benchmarks A and B, we cannot place lower limits on σ_p^{SD} due to the remaining freedom in $f(v)$ at low speeds, which can boost N_{IC} . However, also as in the heavier benchmarks, the degeneracy in the cross sections up to high values is broken. We would like to determine the effect of IceCube data on the determination of the cross section. Due to the degeneracy between σ_p^{SI} and σ_p^{SD} , we will define an effective cross section σ_{eff} , which incorporates both cross sections and controls the overall event rate. Due to the different response of each detector to SI and SD couplings, we can define a different σ_{eff} for each experiment (including IceCube). Here, we look at the effective cross section as seen by Germanium:

$$\sigma_{\text{eff}} = \sum_i f_i A_i^2 \sigma_p^{\text{SI}} + f_{73} \frac{16\pi}{3} \frac{\sigma_p^{\text{SD}}}{2J+1} S_{00}(0), \quad (5.21)$$

where f_i is the mass fraction of isotope i . In Fig. 5.5, we show the profile likelihood for σ_{eff} with and without IceCube data (as solid and dashed lines respectively) for benchmark C. Without IceCube data, the profile likelihood of σ_{eff} is almost entirely flat, with roughly 3 orders of magnitude uncertainty in the total WIMP interaction strength. Including IceCube data, the profile likelihood becomes sharply peaked, with the value of σ_{eff} constrained to within a factor of 4 at the 68% level. Clearly, the inclusion

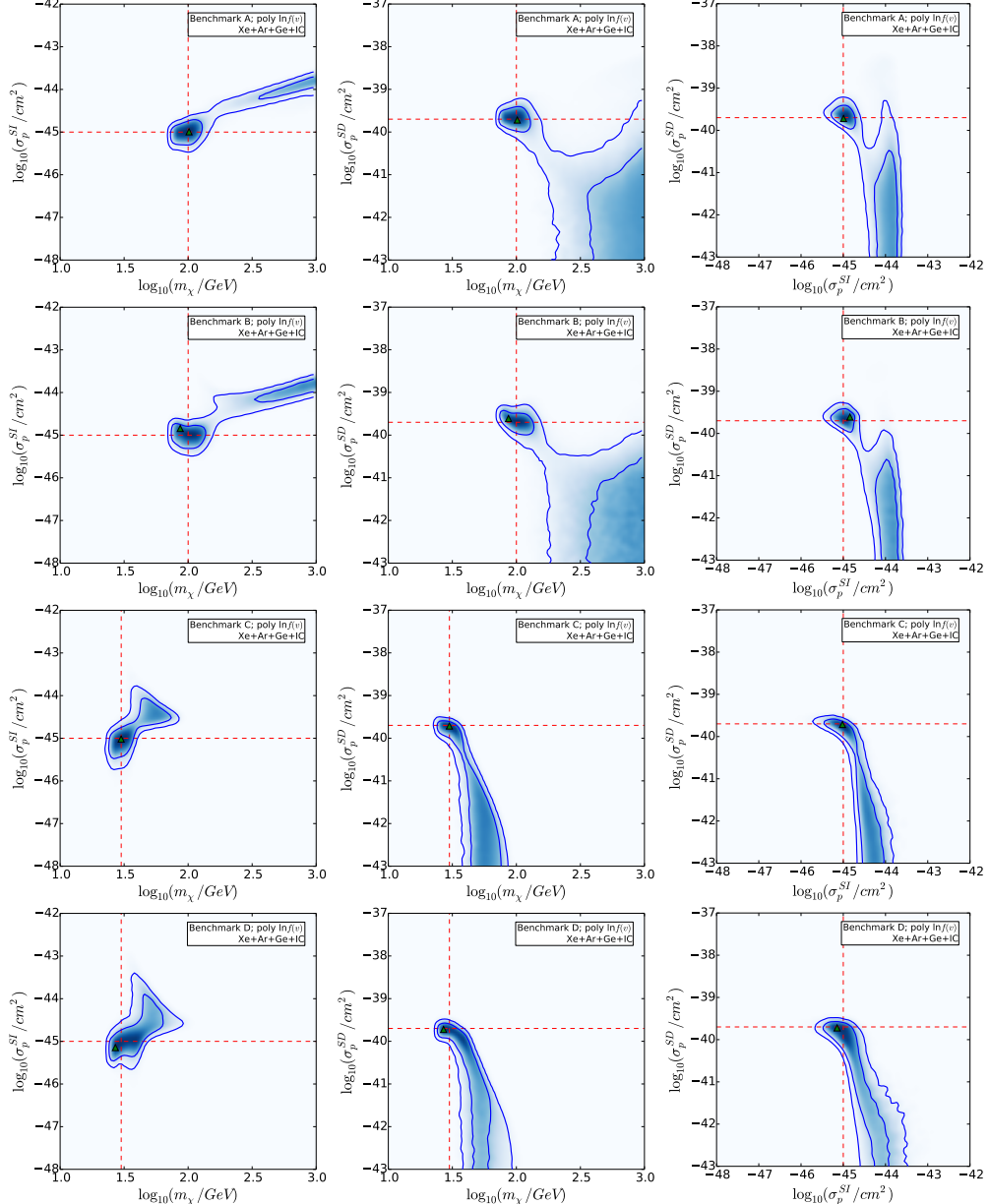


Figure 5.4: As for Fig. 5.3 but including IceCube mock data. *I might overlay the DD-only contours on here for comparison...*

of IceCube data means that we can now reconstruct the value of the cross sections, rather than simply placing a lower limit.

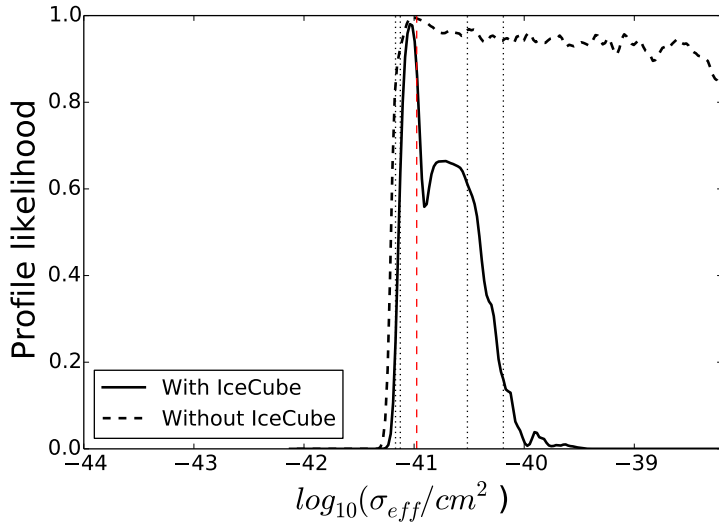


Figure 5.5: Profile likelihood for the effective cross section σ_{eff} of Germanium (defined in Eq. 5.21) with and without IceCube data for benchmark C. The vertical red dashed line corresponds to the benchmark value while the the vertical dotted black lines correspond to the limits of the 68% and 95% confidence intervals for the case *with* IceCube data.

5.6 Reconstructing $f(v)$

As we are sensitive to the full range of WIMP speeds, we can now probe not only the shape of the speed distribution, as in Chapter 4, but the absolute value of $f(v)$. We show in Fig. 5.6 the 68% and 95% confidence intervals (as grey bands) for the values of $f(v)$ using only direct detection data in benchmark B. These confidence intervals extend down to zero across almost the entire range of speeds, meaning that we cannot place any lower limit on $f(v)$. The degeneracy in the cross sections up to high values corresponds to a degeneracy in $f(v)$ down to low values. The results for the remaining benchmarks suffer from the same problem.

Including data from IceCube, the results are shown in Fig. 5.7 for all 4 benchmarks. These result in significantly improved constraints on $f(v)$. For the case of A and B, the tightest constraints are obtained around $v \sim 100 \text{ km s}^{-1}$. This is because for $m_\chi = 100 \text{ GeV}$ and the energy thresholds considered here, this is approximately the minimum speed probed by the

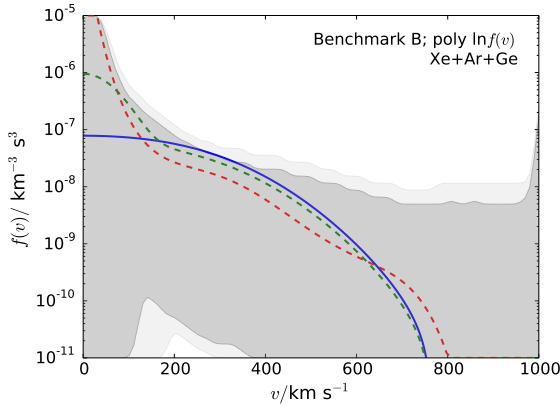


Figure 5.6: Reconstructed 68% and 95% confidence intervals (grey bands) for the directionally-averaged speed distribution $f(v)$ using only direct detection data. We show the SHM distribution (solid blue) and SHM+DD distributions (dashed green). Also shown in dashed red is the best fit form for $f(v)$. We note that for benchmark B, the true distribution is the SHM+DD.

experiments. This is where the most spectral information is available, as the rate decays with increasing energy. For the lower mass benchmarks (C and D), the best constraints are obtained for higher values of v , with a maximum sensitivity in the range $v = 200 - 400 \text{ km s}^{-1}$.

The shape of $f(v)$ is less well constrained at low speeds because the IceCube data contains no spectral information. The capture rate is a single number, but depends on a combination of m_χ , σ_p^{SI} , σ_p^{SD} and a series of integrals over $f(v)$. Thus, the precise shape of $f(v)$ at low speeds cannot be extracted, but the approximate magnitude of $f(v)$ can be inferred when IceCube and direct detection data are combined.

For benchmarks B and D, which have a SHM+DD distribution function, the best fit traces the benchmark distribution closely. In particular, the rise in the best fit $f(v)$ at low speeds indicates that we have achieved sensitivity to this low speed WIMP population. In the regions of maximum sensitivity, the value of $f(v)$ can be constrained to within a factor of around 4 at the 68% level. We see that this uncertainty in the value of $f(v)$ is the source of the remaining uncertainty in the effective WIMP cross section σ_{eff} described in the previous section, which can also be determined to within a factor of ~ 4 . In spite of this remaining uncertainty, it may be possible to distinguish between different distribution functions.

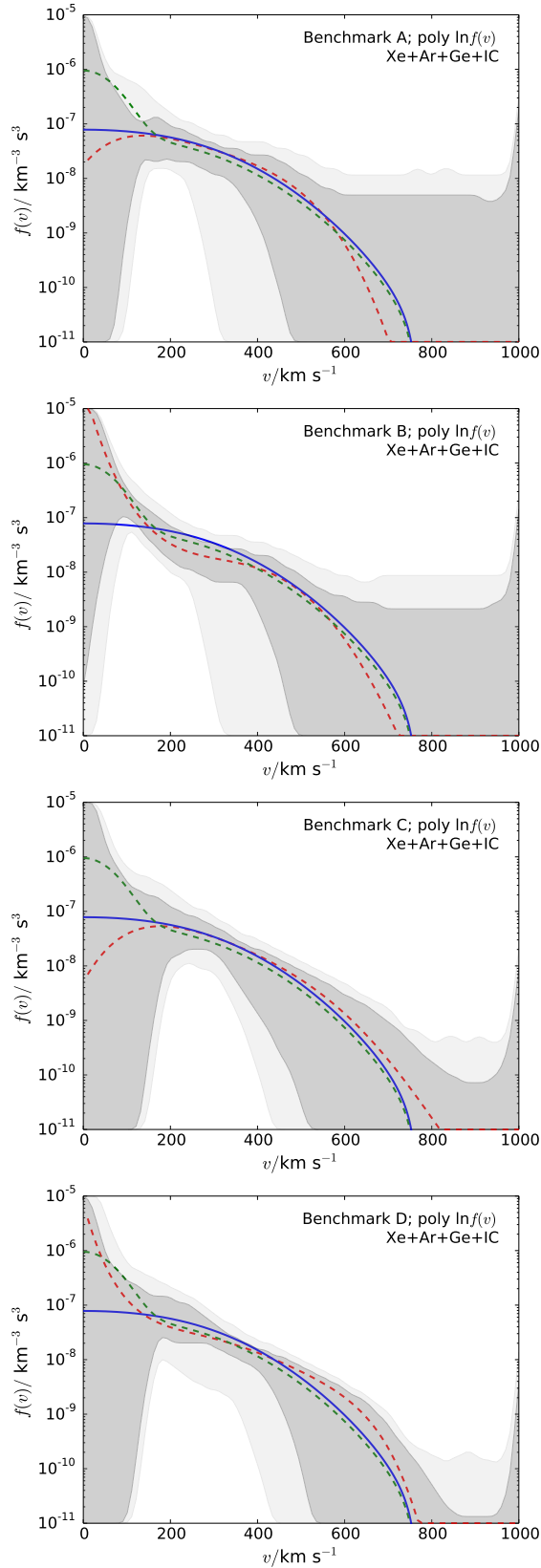


Figure 5.7: As Fig. 5.6, but for all 4 benchmarks, including data from both direct detection *and* IceCube experiments. We show the SHM distribution (solid blue) and SHM+DD distributions (dashed green). Also shown in dashed red is the best fit form for $f(v)$. We note that for benchmarks A and C, the true distribution is the SHM, while for benchmarks B and D, the true distribution is the SHM+DD.

5.7 Discussion

We have demonstrated that for the benchmarks considered here, the WIMP mass can be better constrained with the inclusion of IceCube data and that the degeneracy in the cross sections up to high values (which is inherent in any astrophysics-independent analysis of data) can be broken.

The benchmarks we have considered in this chapter all result in a signal at IceCube. However, in benchmark C, the number of signal events is just 13, which is consistent with the observed background at just over 1σ . Even with a signal of such low significance, we can still break the degeneracy between the cross section and $f(v)$. If we consider lighter WIMPs, which lie below the IceCube detection threshold, these would produce no events at IceCube regardless of the scattering cross sections and speed distribution. Thus, while we can use information from IceCube even with no significant signal, this would only give an improvement in constraints if the WIMP is heavy enough to potentially give a signal at IceCube.

Assuming that a signal is observed at IceCube, there is more information which can be extracted beyond simply the number of events. With the future release of information about energy reconstruction using the IceCube 86-string configuration, it should be possible to include spectral information in the analysis. This should significantly improve constraints on the mass and annihilation channel of the WIMPs, consequently improving constraints on the remaining parameters. However, because the capture rate depends only on an integral over the speed distribution, this additional spectral information will not allow us to significantly improve the shape reconstruction of $f(v)$ at low speeds.

We note that we have made several assumptions in this work. We have neglected uncertainties in spin-dependent form factors, which may result in wider uncertainties on the particle physics parameters. Using the parametrisation of Cerdeno et al. [279] will allow us to take this into account, as well as to compare the relative importance of nuclear and astrophysical uncertainties. Further simplifications we have used include the assumptions of equilibrium between the capture and annihilation rates in the Sun, and the approximation that annihilations occur into a single channel. These uncertainties could be relaxed and incorporated as additional fitting parameters. However, we have shown here what may be possible in an ideal case.

The success of the method we have used here opens up the question of whether the inclusion of IceCube data can improve the performance of other speed distribution parametrisation methods. We could consider, for example, the case of the binned speed distribution studied by Peter [318] and studied in detail in Chapter 3. In that case, it was observed that the number and size of bins to which the experiments were sensitive depends in a specific way on the WIMP mass. The IceCube rate not only probes the low speed bins which are not accessible to direct detection experiments, but also depends on m_χ in a different way. This complementarity may therefore allow the bias caused by using the binned speed distribution to be reduced; lowering the WIMP mass will have a significant impact on the IceCube rate which may not result in a good fit to data. This perhaps opens up the possibility of using several different parametrisations to constrain the particle physics parameters as a consistency check.

Finally, the prospects for reconstructing the speed distribution seem good. In Fig. 5.7, for benchmark A, the SHM+DD distribution function falls outside the 68% band. Similarly, for benchmark B, the SHM distribution lies outside the 68% band at several different speeds. It is difficult to estimate the significance of rejecting these distributions. The bands in Fig. 5.7 are calculated from the 1-dimensional profile likelihood separately at each value of v . However, the uncertainties at different values of v are strongly correlated due to the normalisation of $f(v)$. This means that not all shapes falling within the 68% band are consistent with the data at the 68% level. However, if a speed distribution falls outside the 68% band at some value of v , it can be rejected at at least the 68% level. Further statistical analysis is required to determine the precise significance of the results of the $f(v)$ reconstructions.

Even if it is not possible reject these distributions with high significance using the data sets considered here, these results show that such a rejection should be possible with additional data. In Chapter 4, where only the *shape* of $f(v)$ could be reconstructed, the SHM and SHM+DD distributions were almost indistinguishable. Including IceCube data we probe the low speed distribution, presenting the possibility of discriminating between the two astrophysical models and testing the existence of a dark disk in the Milky Way.

5.8 Conclusions

We have explored the possibility of combining neutrino telescope and direct detection data to probe a wider range of WIMP speeds. Neutrino telescopes, such as IceCube, are sensitive to the annihilations of WIMPs captured in the Sun. WIMPs with lower speeds are preferentially captured, meaning that IceCube probes a range of speeds complementary to those probed in direct detection experiments. In particular, this should allow the absolute value of $f(v)$ to be constrained, as well as breaking the degeneracy between the WIMP cross sections and the fraction of WIMPs above the detection threshold.

The inclusion of this data means that an upper limit can now be placed on the WIMP interaction cross sections, reducing the uncertainty on the total cross section by 2-3 orders of magnitude. However, the necessary inclusion of spin-dependent interactions opens up a new degeneracy direction. For the experiments considered here, it may not be possible to constrain the spin-dependent cross section from below. An increased exposure or a different choice of targets may improve this situation. However, this is not a problem associated with unknown astrophysics and has been previously observed even when no astrophysical uncertainties are taken into account [383].

Because we now probe the entire range of speeds of interest, we see improved constraints on the absolute value of $f(v)$. The maximum sensitivity is achieved near the threshold speeds of the direct detection experiments, where the most spectral information is available. This allows us to reconstruct $f(v)$ to within a factor of 4, opening up the possibility to distinguish the SHM from the SHM with an additional dark disk contribution, which was not previously feasible using direct detection-only data.

Constraints on the WIMP mass are also improved, with the complementarity between IceCube and direct detection experiments allowing us to break the high mass degeneracy and begin to constrain m_χ to within a factor of 2 even for WIMP masses around 100 GeV. This is even possible with no significant signal observed at IceCube, although IceCube is insensitive to very low mass WIMPs and would therefore not improve constraints if the WIMP is lighter than around 20 GeV. The PINGU upgrade to IceCube [384] should lower the IceCube threshold and therefore allow a wider range of the parameter space to be explored and constrained.

We have demonstrated that combining direct detection data with IceCube, we can probe the entire range of WIMP speeds and reconstruct without bias the WIMP mass, SI and SD cross sections *and* the values of the speed distribution itself, without making any astrophysical assumptions.

Chapter 6

Velocity parametrisation for directional experiments

While many direct detection experiments seek to measure the recoil energies deposited by weakly interacting massive particles (WIMPs) scattering off detector nuclei, *directional* experiments aim to measure both the energy and direction of the recoil. While the recoil distribution of typical backgrounds is expected to be roughly isotropic, the WIMP-induced recoil distribution is expected to be highly directional. The motion of the Sun through the Galactic dark matter (DM) halo generates a so-called ‘WIMP wind’, leading to an event rate peaked in the opposing direction, the direction of the constellation Cygnus.

The ability of directional detection to distinguish background from signal and to provide a model independent confirmation of the dark matter origin of the signal make it a promising search strategy. However, measuring the direction of rare, low energy recoils remains challenging. A number of directional detectors are currently in development and a number of novel methods for directional detection have also been proposed.

Measuring the directional recoil spectrum allows us to probe not just the energy distribution of WIMPs in the Galactic halo (embodied in the speed distribution $f_1(v)$), but the full 3-dimensional velocity distribution $f(\mathbf{v})$. This may allow us to gain new insight into the phase space distribution of the Milky Way’s DM halo. However, it also introduces new uncertainties into calculating the event rate. While non-directional detection leaves us with a single free function in the form of $f_1(v)$, the directional case relies upon the *a priori* unknown function of a 3-dimensional vector, $f(\mathbf{v})$.

In this chapter, we will first introduce the formalism by which the directional rate is calculated. Specifically, we introduce the Radon transform which relates the WIMP velocity distribution to the corresponding nuclear recoil distribution. We then discuss the current state of directional detection technology and the progress of several directional experiments. We summarise previous approaches to mitigating the uncertainties associated with the velocity distribution. Finally, we consider a new method for parametrising $f(\mathbf{v})$, which allows it to be written in terms of a finite number of one-dimensional functions, and how to calculate the Radon transform of this new, discretised distribution function.

I should probably say something about why it would be nice to measure $f(\mathbf{v})$ itself.

Some of the plots have $\hat{f}(v)$ on the axes, which should be $\hat{f}(v_{\min})$.

6.1 Directional event rate

We wish to calculate the directional event spectrum in a dark matter detector. We follow the treatment of Gondolo [385], noting that similar calculations were performed previously by Copi, Heo and Krauss [386] and later by Copi and Krauss [387]. The scattering of a WIMP with a nucleus is illustrated in Fig. 6.1.

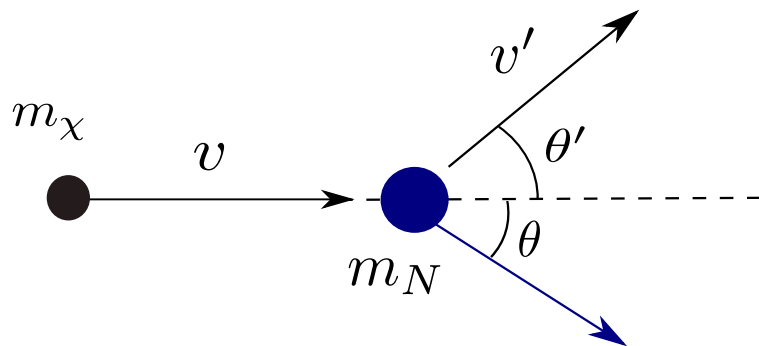


Figure 6.1: Illustration of the scattering of a DM particle of mass m_χ from a nucleus of mass m_N .

We consider a DM particle of mass m_χ impinging with velocity $\mathbf{v} = v(1, 0)$ on a stationary target nucleus of mass m_N . The dark matter scatters with velocity $\mathbf{v}' = v'(\cos \theta', \sin \theta')$ and the nucleus scatters with final momentum $\mathbf{q} = q(\cos \theta, \sin \theta)$. From conservation of linear momentum we obtain:

$$m_\chi v' \cos \theta' = m_\chi v - q \cos \theta , \quad (6.1)$$

$$m_\chi v' \sin \theta' = q \sin \theta . \quad (6.2)$$

We can eliminate θ' by summing the squares of Eqs. 6.1 and 6.2, to obtain:

$$v'^2 = v^2 - \frac{2vq \cos \theta}{m_\chi} + \frac{q^2}{m_\chi^2} . \quad (6.3)$$

From energy conservation, we obtain:

$$v'^2 = v^2 - \frac{q^2}{m_\chi m_N} . \quad (6.4)$$

Combining these, we see that the recoil momentum of the target nucleus is given by

$$q = 2\mu_{\chi N} v \cos \theta , \quad (6.5)$$

where $\mu_{\chi N} = m_\chi m_N / (m_\chi + m_N)$ is the DM-nucleus reduced mass.

For a WIMP-nucleus interaction cross section which is independent of velocity, we can write the differential cross section as

$$\frac{d\sigma}{dE_R} = \frac{m_N \sigma_p}{2\mu_{\chi p}^2 v^2} \mathcal{C} F^2(E_R) , \quad (6.6)$$

where E_R is the nuclear recoil energy, σ_p is the WIMP-proton interaction cross section (which may be spin-dependent (SD) or spin-independent (SI)) and \mathcal{C} and F^2 are the corresponding enhancement factor and nuclear form factor (see Eq. 2.25). We then require a Dirac δ -function to impose the condition in Eq. 6.5:

$$\frac{d\sigma}{dE_R d \cos \theta} = \frac{m_N \sigma_p}{2\mu_{\chi p}^2 v^2} \mathcal{C} F^2(E_R) \delta(\cos \theta - q/2\mu_{\chi N} v) . \quad (6.7)$$

The collision is azimuthally symmetric, so that $d\Omega_q = 2\pi d \cos \theta$. Rewriting the δ -function as

$$\delta(\cos \theta - q/2\mu_{\chi N} v) = v \delta(v \cos \theta - q/2\mu_{\chi N}) , \quad (6.8)$$

we obtain the double differential cross-section $d\sigma/dE_R d\Omega_q$:

$$\frac{d\sigma}{dE_R d\Omega_q} = \frac{m_N \sigma_p}{4\pi \mu_{\chi p}^2 v} \mathcal{C} F^2(E_R) \delta(v \cos \theta - v_{\min}) , \quad (6.9)$$

where v_{\min} is the minimum WIMP speed required to excite a recoil of momentum q or, equivalently, energy E_R :

$$v_{\min} = \frac{q}{2\mu_{\chi N}} = \sqrt{\frac{m_N E_R}{2\mu_{\chi N}^2}}. \quad (6.10)$$

To obtain the differential rate per unit detector mass, we divide by the mass of the target nucleus and multiply by the WIMP flux at velocity \mathbf{v} ,

$$\frac{\rho_0}{m_\chi} v f(\mathbf{v}) d^3 \mathbf{v}, \quad (6.11)$$

where ρ_0 is the local dark matter mass density, before integrating over all velocities. Combining these, we obtain:

$$\frac{dR}{dE_R d\Omega_q} = \frac{\rho_0 \sigma_p}{4\pi \mu_{\chi p}^2 m_\chi} \mathcal{C}F^2(E_R) \hat{f}(v_{\min}, \hat{\mathbf{q}}), \quad (6.12)$$

where $\hat{f}(v_{\min}, \hat{\mathbf{q}})$ is the Radon Transform of the velocity distribution, defined as:

$$\hat{f}(v_{\min}, \hat{\mathbf{q}}) = \int \delta(v_{\min} - \mathbf{v} \cdot \hat{\mathbf{q}}) f(\mathbf{v}) d^3 \mathbf{v}. \quad (6.13)$$

Geometrically, this is the integral of $f(\mathbf{v})$ over a plane perpendicular to $\hat{\mathbf{q}}$ at a distance v_{\min} from the origin. In physical terms, for a given recoil angle and energy, we integrate over all WIMP velocities satisfying the kinematic constraint given by Eq. 6.5.

6.1.1 Examples

We consider several examples of velocity distributions and their corresponding Radon transforms. For an isotropic Maxwell-Boltzmann distribution with dispersion σ_v ,

$$f(\mathbf{v}) = \frac{1}{(2\pi\sigma_v^2)^{\frac{3}{2}}} \exp\left[-\frac{\mathbf{v}^2}{2\sigma_v^2}\right], \quad (6.14)$$

the Radon transform is also isotropic,

$$\hat{f}(v_{\min}, \hat{\mathbf{q}}) = \frac{1}{(2\pi\sigma_v^2)^{\frac{1}{2}}} \exp\left[-\frac{v_{\min}^2}{2\sigma_v^2}\right]. \quad (6.15)$$

If we take this form to describe the DM velocity distribution in the Galactic frame, we must transform to the laboratory frame using the relation [385]

$$\hat{f}_{\text{lab}}(v_{\min}, \hat{\mathbf{q}}) = \hat{f}_{\text{gal}}(v_{\min} - \mathbf{v}_{\text{lag}} \cdot \hat{\mathbf{q}}, \hat{\mathbf{q}}), \quad (6.16)$$

where \mathbf{v}_{lag} is the velocity of the peak of the Galactic distribution with respect to the laboratory. We therefore obtain the Radon transform of the Standard Halo Model (SHM):

$$\hat{f}(v_{\min}, \hat{\mathbf{q}}) = \frac{1}{(2\pi\sigma_v^2)^{\frac{1}{2}}} \exp\left[-\frac{(v_{\min} - \mathbf{v}_{\text{lag}} \cdot \hat{\mathbf{q}})^2}{2\sigma_v^2}\right]. \quad (6.17)$$

This can be extended to incorporate a cut off at the Galactic escape speed, or for more general anisotropic velocity distributions [385].

Another interesting velocity distribution is that of a stream

$$f(\mathbf{v}) = \delta(\mathbf{v} - \mathbf{v}_s), \quad (6.18)$$

which has Radon transform

$$\hat{f}(v_{\min}, \hat{\mathbf{q}}) = \delta(v_{\min} - \mathbf{v}_{\text{lag}} \cdot \hat{\mathbf{q}}). \quad (6.19)$$

This results in a highly directional signal, producing a spherical recoil spectrum centred on $\mathbf{v} = \mathbf{v}_s/2$.

In Fig. 6.2, we illustrate the Radon transform of the SHM (top), the SHM with a 23% contribution from a dark disk (middle), and a stream (bottom) with $v_{\text{lag}} = 400 \text{ km s}^{-1}$. In each case, we have integrated over the ϕ direction and show $\hat{f}(v, \cos \theta)$. In the case of the SHM and the stream, there is a clear anisotropy and the two scenarios should be easily distinguishable. This highlights the discriminatory power of directional detection. It has previously been demonstrated that only of order 10 events would be required to distinguish a directional WIMP signal from an isotropic background. Furthermore, with of order 100 events, it should be possible to detect any deviation in peak recoil direction due to a stream [388]. In the case of the SHM with a dark disk contribution, the spectrum is more isotropic. This is because the Radon transform is dominated by the dark disk contribution, which has a lower value of $v_{\text{lag}} = 50 \text{ km s}^{-1}$ and therefore appears more isotropic in the Earth frame.

6.2 Directional experiments

Directional experiments are still in the prototype stage. A number of experiments use time projection chamber (TPC) technology to achieve directional sensitivity. These include DRIFT [389, 390], NEWAGE [391, 392], MIMAC [393, 394], DMTPC [395, 396] and D3 [397]. These detectors are

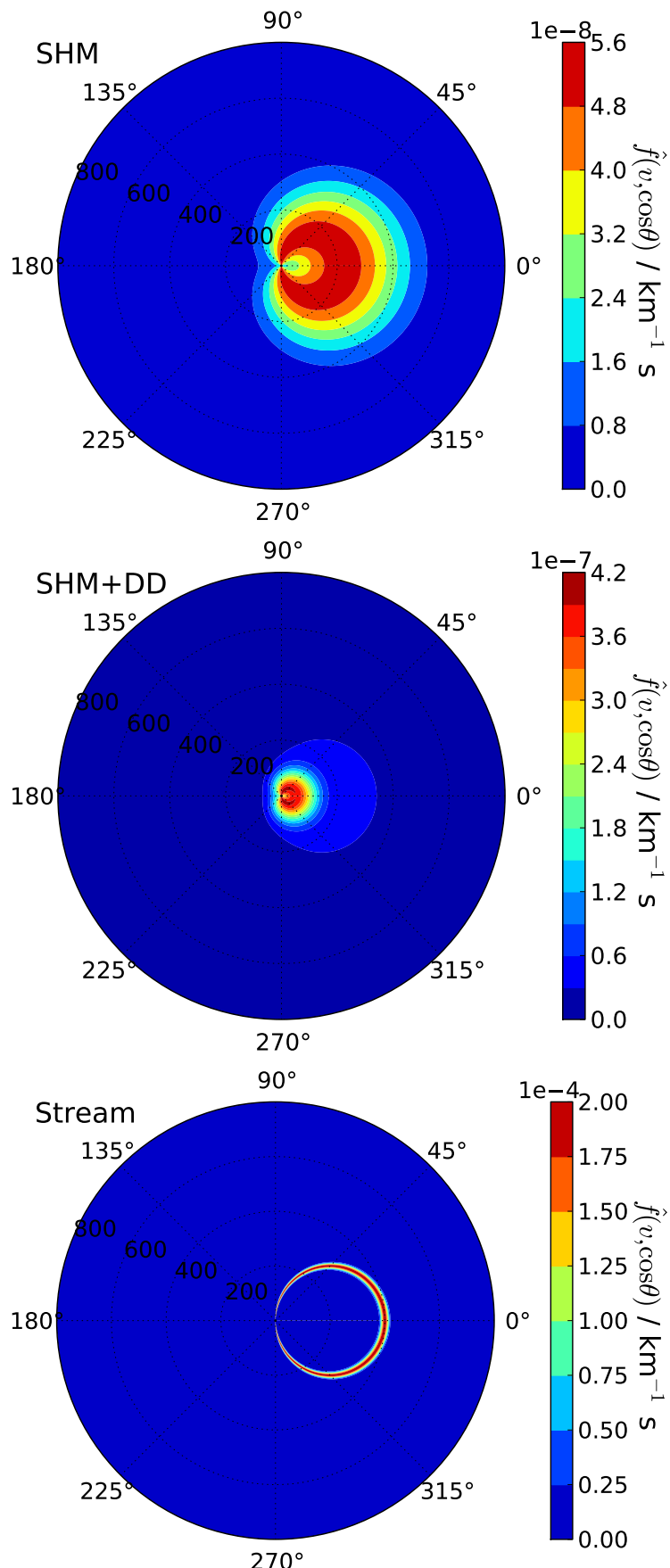


Figure 6.2: Radon transform $\hat{f}(v, \cos \theta)$ of the SHM (top), SHM with a dark disk contribution (middle) and stream (bottom) distribution functions. We have integrated over the ϕ angle. In each case \mathbf{v}_{lag} is aligned along $\theta = 0$. Note the different scale in each plot.

less than 1 m³ in size, with hopes for a scale up to larger experiments (possibly up to ton-scale) in the future.

In order to have directional sensitivity, a detector must image the tracks produced by the recoiling nucleus in the detector. The typical range of a WIMP-nucleus recoil is only \sim 100nm, however, which makes track reconstruction difficult. The above directional experiments therefore operate in the low pressure gas phase (around 0.05 atm [390]) in order to maximise the distance travelled by a recoiling nucleus. The detector is filled with a target gas (such as CF_4 in the case of the DRIFT experiment) which provides sensitivity predominantly to spin-dependent interactions. Nuclear recoils in the detector ionize the target gas. The freed electrons are drifted under an electric field to an anode at one face of the detector where the charge is collected. An electron transport gas (CS_2 in the DRIFT experiment) may also be added, which attracts the free electrons forming ions which are then collected.

The energy of the recoil can be recovered from the total amount of ionisation in the event. The three dimensional track (which is only a few mm long) can be reconstructed from the distribution of charge detected at the anode, with information about the z-direction obtained from the timing of the charges arriving at the anode. This method allows an angular resolution of 20°-80° using current prototypes [398], with higher resolution at higher recoil energies. However, the sense of the recoil is much more difficult to determine, requiring sensitivity to tiny asymmetries between the start and end of the track. While sense discrimination has previously been demonstrated [399], it cannot be achieved with 100% efficiency. Even for high energy (100 keV) recoils, studies suggest that only partial sense recognition may be possible (with only a 65% probability of correctly determining the sense) [398]. Without sense discrimination the anisotropy of the WIMP signal is reduced and roughly 3 times more events are required to establish the directionality of the signal and distinguish from an anisotropic background [355, 388].

A number of other directional technologies have also been suggested. Nuclear emulsion experiments use as a target silver halide crystals suspended in gelatin [400]. The emulsion required must be composed of very fine grains in order to image dark matter recoil tracks smaller than 1 μ m. However, angular resolutions below 20° may be achievable. DNA based experiments [256] have also been proposed which may be able to achieve

directional sensitivity. The collaborations running the main TPC-based experiments have proposed a joint project to construct a ton-scale ‘CYGNUS’ detector [401] in the future.

6.3 Reconstructing the velocity distribution

With promising developments in directional detector technology, it is interesting to ask what information about the velocity distribution we could, in principle, extract from a directional signal. Alves, Hendri and Wacker [402] investigated the possibility of describing $f(\mathbf{v})$ in terms of a series of special functions of integrals of motion (energy and angular momentum). These can then be fit to data, with around 1000 events required to distinguish between the SHM and a Via Lactea II distribution function [403]. However, the special, separable form of the velocity distribution requires that the dark matter halo is in equilibrium. Moreover, this method requires prior knowledge of the DM mass (for example from earlier non-directional detectors or from collider experiments).

A more general parametrisation for the velocity distribution was recently proposed by Lee [404]. In this approach, the velocity distribution is decomposed into products of Fourier-Bessel functions and spherical harmonics. This is completely general and does not require that the halo is completely virialised. Lee also gives an analytic expression for the Radon transform of the Fourier-Bessel basis, making this approach computationally efficient. However, this basis does not guarantee that the resulting $f(\mathbf{v})$ is everywhere positive and therefore not all combinations of coefficients correspond to physical distribution functions.

In fact, any decomposition in terms of spherical harmonics leads to this problem, because the spherical harmonic basis functions can have negative values. It is unclear how this issue will affect parameter reconstruction. Without some criteria which determines which coefficients of the spherical harmonics lead to strictly positive distribution functions, it may be necessary to numerically test each parametrised distribution function for negative values. However, for a real function of three parameters $f(\mathbf{v}) = f(v_x, v_y, v_z)$ this would require a very large number of evaluations, which may not be computationally feasible. In addition, it is not clear

how this property would affect an exploration of the parameter space using, for example, Markov Chain Monte Carlo or Nested Sampling (see Appendix A). Physical distribution functions may occupy only a small fraction of the total space of parameters or may be distributed over a large number of irregular regions in the parameter space, making sampling from them difficult.

In order to fit to data, it is necessary to decompose $f(\mathbf{v})$ into a series of angular components A^i :

$$f(\mathbf{v}) = f^1(v)A^1(\theta', \phi') + f^2(v)A^2(\theta', \phi') + f^3(v)A^3(\theta', \phi') + \dots \quad (6.20)$$

We then truncate the series at some order, leaving only a finite number of 1-D functions $f^i(v)$ which are unknown. This reduces the problem of attempting to fit a function of the 3-dimensional variable \mathbf{v} to the problem of parametrising a series of 1-dimensional functions, which is much more tractable. Of course, we should be careful that this truncation preserves enough angular information to still provide a good approximation to $f(\mathbf{v})$. However, as more data becomes available, we can add more terms to the series to capture more angular features in the distribution.

As we have discussed, the spherical harmonic basis may not be an appropriate choice for this decomposition. In the next section, I will present an alternative decomposition which can guarantee that the velocity distribution is everywhere positive and therefore represents a promising and general method for extracting information from directional experiments.

6.4 Discretising the velocity distribution

In order to ensure that the velocity distribution is everywhere positive, we propose that the velocity distribution be discretised into N angular components:

$$f(\mathbf{v}) = f(v, \cos \theta', \phi') = \begin{cases} f^1(v) & \text{for } \theta' \in [0, \pi/N] , \\ f^2(v) & \text{for } \theta' \in [\pi/N, 2\pi/N] , \\ \vdots & \\ f^k(v) & \text{for } \theta' \in [(k-1)\pi/N, k\pi/N] , \\ \vdots & \\ f^N(v) & \text{for } \theta' \in [(N-1)\pi/N, \pi] . \end{cases} \quad (6.21)$$

Over each bin in θ' , $f(\mathbf{v})$ has no angular dependence and depends only on a single function of the WIMP speed. We consider for simplicity only a discretisation in $\cos \theta'$, though this can be extended to an additional discretisation in ϕ' if required.

We show in Fig. 6.3 an example of this discretised velocity distribution. We show the full SHM velocity distribution (top), as well as the $N = 2$ (middle) and $N = 3$ (bottom) discretised approximations. These approximations are obtained by averaging the full velocity distribution over each bin in θ' .

The motivation for this description is that the simplest signal (beyond an isotropic $N = 1$ signal) which can be observed with a directional detector is an asymmetry between the event rates in, say, the forward and backward directions. Shortly after the confirmation of a dark matter signal at a directional detector, the number of events may still be quite small (for example, the roughly 10 events required to distinguish from an isotropic background). In this small statistics scenario, constraining a large number of free functions is not feasible. However, if we discretise $f(\mathbf{v})$ into $N = 2$ angular components, it should be possible to extract some meaningful directional information with only a small number of events. With larger numbers of events, N can be increased to allow more directional information to be extracted.

Because angular information is being lost from the velocity distribution, the full Radon transform of this discretised distribution is unlikely to provide a good fit to the data on an event by event basis. Instead, we should consider integrated Radon transforms of the form:

$$\hat{f}_k(v_{\min}) = \int_{\phi=0}^{2\pi} \int_{(k-1)\pi/N}^{k\pi/N} \hat{f}(v_{\min}, \hat{\mathbf{q}}) d\cos \theta d\phi, \quad (6.22)$$

where $\hat{\mathbf{q}} = (\cos \theta, \phi)$. Thus, we will be using a discretised version of the Radon transform (or equivalently, the event rate and, ultimately, data) in order to constrain the functional form of the discretised velocity distribution. While binning the data in this way results in a loss of angular information, it should reduce the error which is introduced by using a binned approximation to the velocity distribution. This in turn allows us to parametrise the v -dependence of each angular bin and mitigate uncertainties in the velocity distribution.

What form should be used for the free functions $f^k(v)$? This dis-

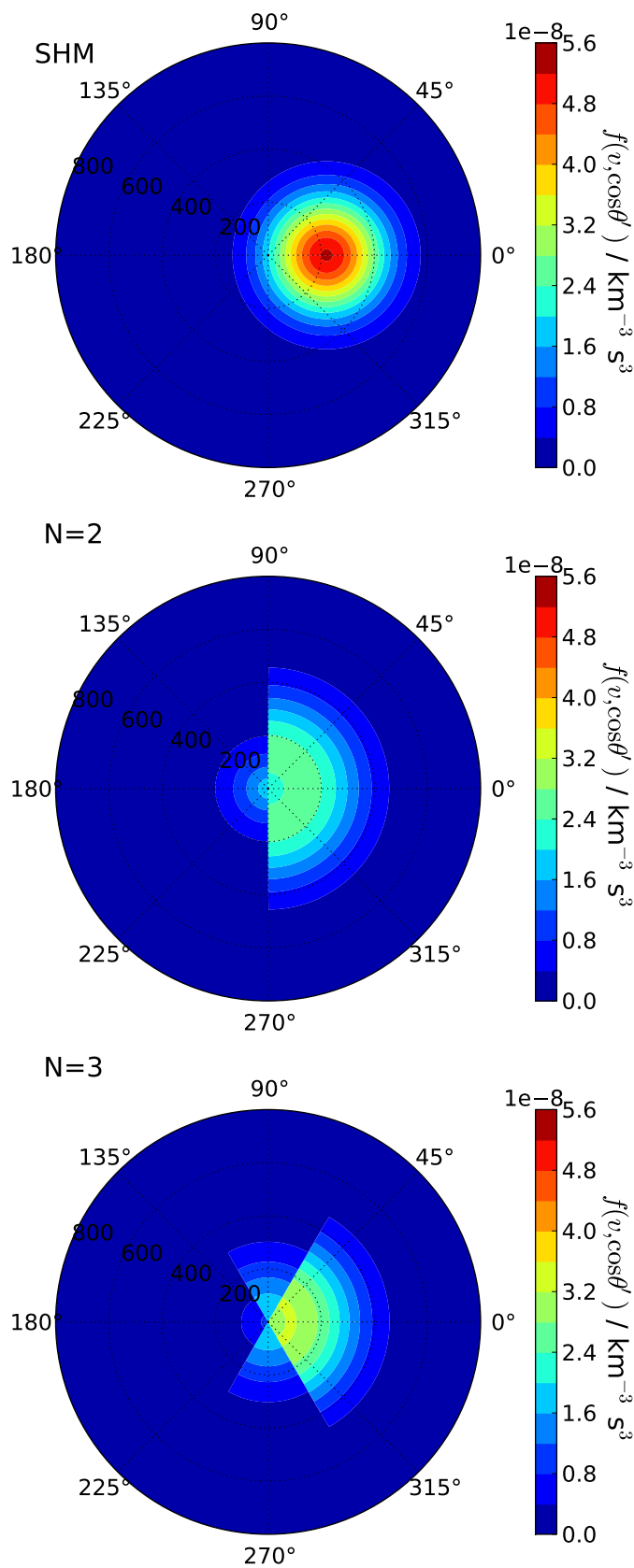


Figure 6.3: The SHM velocity distribution (top) as well as $N = 2$ (middle) and $N = 3$ (bottom) discretised approximations. In each case, we have integrated over the ϕ' direction and only show $f(v, \cos \theta')$. The vector \mathbf{v}_{lag} is aligned along $\theta' = 0$. The same colour scale is used in each plot.

cretisation scheme does not depend on choosing a particular form for the v -dependence of the velocity distribution. We can therefore choose any parametrisation for $f^k(v)$ - such as the polynomial parametrisation described in Chapter 4 - as long as it is everywhere positive and we are convinced that it introduces no bias into the fitting procedure. The question we will now address is what errors are introduced by this angular discretisation. We will now demonstrate for the cases of $N = 1, 2, 3$ how the corresponding Radon transform is calculated and how it compares to the true Radon transform for some benchmark cases.

6.4.1 $N = 1$ discretisation

The $N = 1$ case corresponds to the assumption that $f(\mathbf{v})$ is isotropic. That is, we could consider setting $f(\mathbf{v})$ equal to its angular average:

$$f(\mathbf{v}) = \bar{f}(v) \equiv \frac{1}{4\pi} \int f(\mathbf{v}) d\Omega_v. \quad (6.23)$$

The Radon transform then reduces to

$$\hat{f}(v_{\min}, \hat{\mathbf{q}}) = \int \delta(v_{\min} - \mathbf{v} \cdot \hat{\mathbf{q}}) \bar{f}(v) d^3\mathbf{v}. \quad (6.24)$$

We can rewrite the delta function as

$$\delta(v_{\min} - \mathbf{v} \cdot \hat{\mathbf{q}}) = \frac{1}{v} \delta(v_{\min}/v - \hat{\mathbf{v}} \cdot \hat{\mathbf{q}}), \quad (6.25)$$

which means that Eq. 6.24 becomes

$$\hat{f}(v_{\min}, \hat{\mathbf{q}}) = \int_{v=0}^{\infty} \frac{v^2 \bar{f}(v)}{v} \oint \delta(v_{\min}/v - \hat{\mathbf{v}} \cdot \hat{\mathbf{q}}) d\Omega_v dv. \quad (6.26)$$

The angular integral evaluates to unity as long as $v_{\min}/v = \hat{\mathbf{v}} \cdot \hat{\mathbf{q}}$ for some value of $\hat{\mathbf{v}}$ in the domain of integration. Because we integrate over all directions $\hat{\mathbf{v}}$, this is guaranteed to be satisfied for some value, as long as $v > v_{\min}$ (because $\hat{\mathbf{v}} \cdot \hat{\mathbf{q}}$ cannot exceed 1). Thus,

$$\oint \delta(v_{\min}/v - \hat{\mathbf{v}} \cdot \hat{\mathbf{q}}) d\Omega_v = \Theta(v - v_{\min}), \quad (6.27)$$

and

$$\hat{f}(v_{\min}, \hat{\mathbf{q}}) = \int_{v=v_{\min}}^{\infty} \frac{v^2 \bar{f}(v)}{v} dv. \quad (6.28)$$

Finally, to obtain the directionally averaged Radon transform $\hat{f}(v_{\min})$, we integrate over all directions $\hat{\mathbf{q}}$. As the Radon transform is isotropic in this case, this gives a contribution of 4π . Replacing the expression for $\bar{f}(v)$ from Eq. 6.23, we therefore obtain

$$\hat{f}(v_{\min}) = \int_{v=v_{\min}}^{\infty} \frac{f(\mathbf{v})}{v} d^3\mathbf{v}. \quad (6.29)$$

This matches the expression for the total non-directional scattering rate. We therefore see that in the $N = 1$ case, the angular-discretised ‘approximation’ is in fact exact and leads to the correct angular-averaged Radon transform.

6.4.2 $N = 2$ discretisation

For the $N = 2$ case, we are considering a forward-backward asymmetry in the velocity distribution:

$$f(\mathbf{v}) = \begin{cases} f^1(v) & \text{for } \theta' \in [0, \pi/2] \\ f^2(v) & \text{for } \theta' \in [\pi/2, \pi] \end{cases} \quad (6.30)$$

From these, we wish to obtain the integrated Radon transforms for the forward and backward directions. Specifically:

$$\hat{f}^1(v_{\min}) = \int_0^1 \hat{f}(v_{\min}, \cos \theta) d \cos \theta \quad (6.31)$$

$$\hat{f}^2(v_{\min}) = \int_{-1}^0 \hat{f}(v_{\min}, \cos \theta) d \cos \theta. \quad (6.32)$$

Full details of the calculation are given in Appendix B. However, the result takes the relatively straightforward form:

$$\hat{f}^1 = 4\pi \int_{v_{\min}}^{\infty} v \left\{ \pi f^1(v) + \tan^{-1} \left(\frac{\sqrt{1 - \beta^2}}{\beta} \right) (f^2(v) - f^1(v)) \right\} dv \quad (6.33)$$

$$\hat{f}^2 = 4\pi \int_{v_{\min}}^{\infty} v \left\{ \pi f^2(v) + \tan^{-1} \left(\frac{\sqrt{1 - \beta^2}}{\beta} \right) (f^1(v) - f^2(v)) \right\} dv, \quad (6.34)$$

where $\beta = v_{\min}/v$. We have also checked using Monte Carlo calculations that these are the correct forms of the forward and backward integrated Radon transforms in the case of a discretised velocity distribution.

We now wish to compare these approximate Radon transforms with the Radon transforms obtained from the full (non-discretised) velocity distribution. To do this, we select a benchmark velocity distribution (such as the SHM) and calculate the $f^{1,2}$ of Eq. 6.30 by averaging over $\cos \theta'$ in the forward and backward directions as in Fig. 6.3. We then insert these into Eq. 6.33 to obtain the forward and backward Radon transform. We refer to these as the *approximate* forward and backward Radon transforms. For comparison, we use the full Radon transform of Eq. 6.17 to obtain the *exact* forward and backward Radon transforms by integrating over $\cos \theta$.

The results of this comparison for an SHM model with $v_{\text{lag}} = 220 \text{ km s}^{-1}$ and $\sigma_v = 156 \text{ km s}^{-1}$ are shown in Fig. 6.4. While the general features are reproduced, there are some discrepancies. In particular, the forward Radon transform obtained using the approximate method is roughly 80% of the correct result, while the backward Radon transform is up to 100% larger using the approximate method. The reason for this is clear from Fig. 6.3, which shows that the discretised velocity distribution has a greater fraction of WIMPs with velocities at right angles to the forward direction ($\theta' = 0$). Thus, the discretised velocity distribution has a greater chance of producing scatters in the backward direction. Overall, the discretised distribution is less focused in the forward direction, resulting in a reduced asymmetry between the forward and backward scattering rates.

We show in Fig. 6.5 the forward and backward Radon transforms for a stream distribution function, with $v_{\text{lag}} = 400 \text{ km s}^{-1}$ and $\sigma_v = 20 \text{ km s}^{-1}$. The discrepancy between the approximate and exact results is significantly worse in this case. This is because the stream is highly directional and a simple $N = 2$ discretisation of the velocity distribution is not sufficient to capture the angular features of the stream

6.4.3 $N = 3$ discretisation

Given the discrepancies in the $N = 2$ case, we will now consider the $N = 3$ discretisation, which should improve the fit between the true and approximate transforms. In addition, $N = 3$ will allow us to employ this methodology to the case where sense discrimination of recoils is not possible. With-

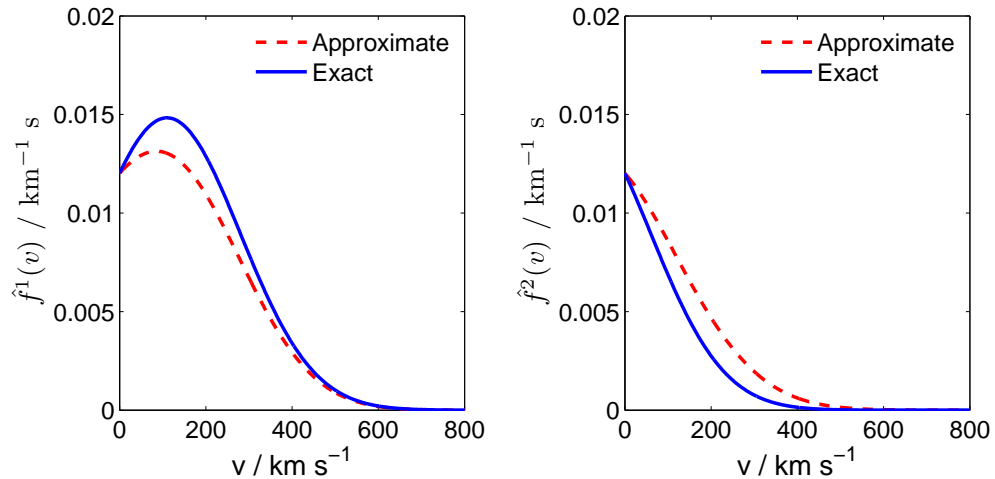


Figure 6.4: Exact and approximate forward and backward Radon transforms, \hat{f}^1 and \hat{f}^2 , for the SHM. The approximate Radon transforms are obtained by discretising the full velocity distribution into $N = 2$ angular bins. The vector \mathbf{v}_{lag} is aligned along $\theta' = 0$.

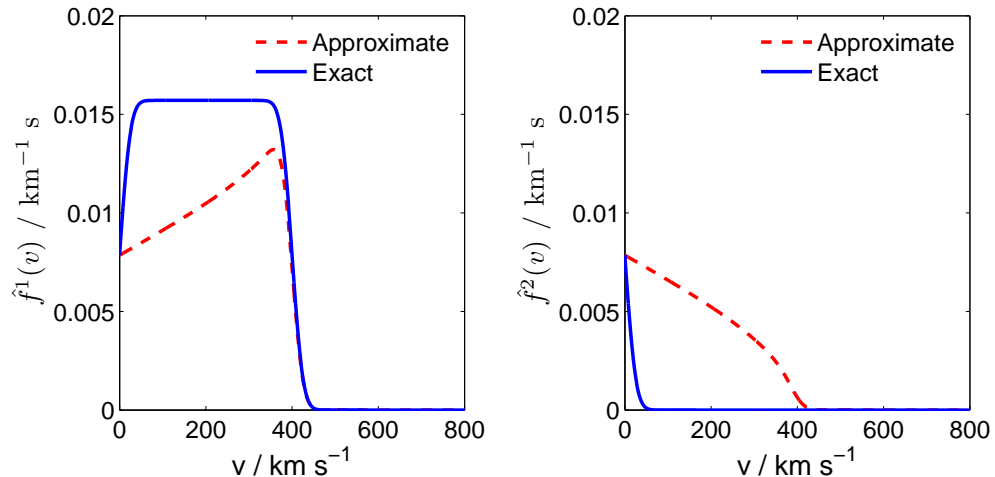


Figure 6.5: As Fig. 6.4, but for a stream distribution with $v_{\text{lag}} = 400 \text{ km s}^{-1}$ and $\sigma_v = 20 \text{ km s}^{-1}$.

out sense discrimination, the forward and backward directions cannot be distinguished and the $N = 2$ discretisation provides no directional sensitivity. As we shall see shortly, directional sensitivity is possible in the $N = 3$ case.

We write the velocity distribution in discretised form as

$$f(\mathbf{v}) = \begin{cases} f^1(v) & \text{for } \theta' \in [0, \pi/3] \\ f^2(v) & \text{for } \theta' \in [\pi/3, 2\pi/3] \\ f^3(v) & \text{for } \theta' \in [2\pi/3, \pi]. \end{cases} \quad (6.35)$$

If we interpret this discretisation as an averaging of the underlying velocity distribution, as before, we obtain the distribution in the bottom panel of Fig. 6.3 for the SHM. Following the same procedure as for the $N = 2$ case, we can obtain the corresponding forward, backward and transverse integrated Radon transforms. The exact form of these is complicated (and not particularly instructive), so we do not include it in full here. However, as in the $N = 2$ case, we can test these approximate transforms against the exact forms.

The results for the SHM are shown in Fig. 6.6. Compared to the $N = 2$ case, the Radon transforms are reproduced much more closely, with a discrepancy of at most 15% between the true and approximate distributions. As can be seen in the bottom panel of Fig. 6.3, the $N = 3$ discretised velocity distribution is more focused in the forward direction and fewer particles have velocities perpendicular \mathbf{v}_{lag} . In Fig. 6.7, we show the corresponding results for the stream distribution. These show a slight improvement over the $N = 2$ case (particularly in the backward rate). However, there are still significant differences between the exact and approximate Radon transforms.

The folded distribution

As discussed in Sec. 6.2, sense discrimination between forward and backward-going recoils may not be possible with near-future detectors. In this case then, all that can be measured is the so called ‘folded’ recoil spectrum

$$\frac{dR}{dE_R d|\cos \theta|} = \frac{dR}{dE_R d\cos \theta} + \frac{dR}{dE_R d(-\cos \theta)}. \quad (6.36)$$

As a result, we are concerned not with the full Radon transform of $f(\mathbf{v})$, but the folded Radon transform $\hat{f}(v_{\min}, |\cos \theta|)$. In the case of $N = 2$ discretisation, this folded Radon transform would have no directional information (because the forward and backward scattering rates differ only

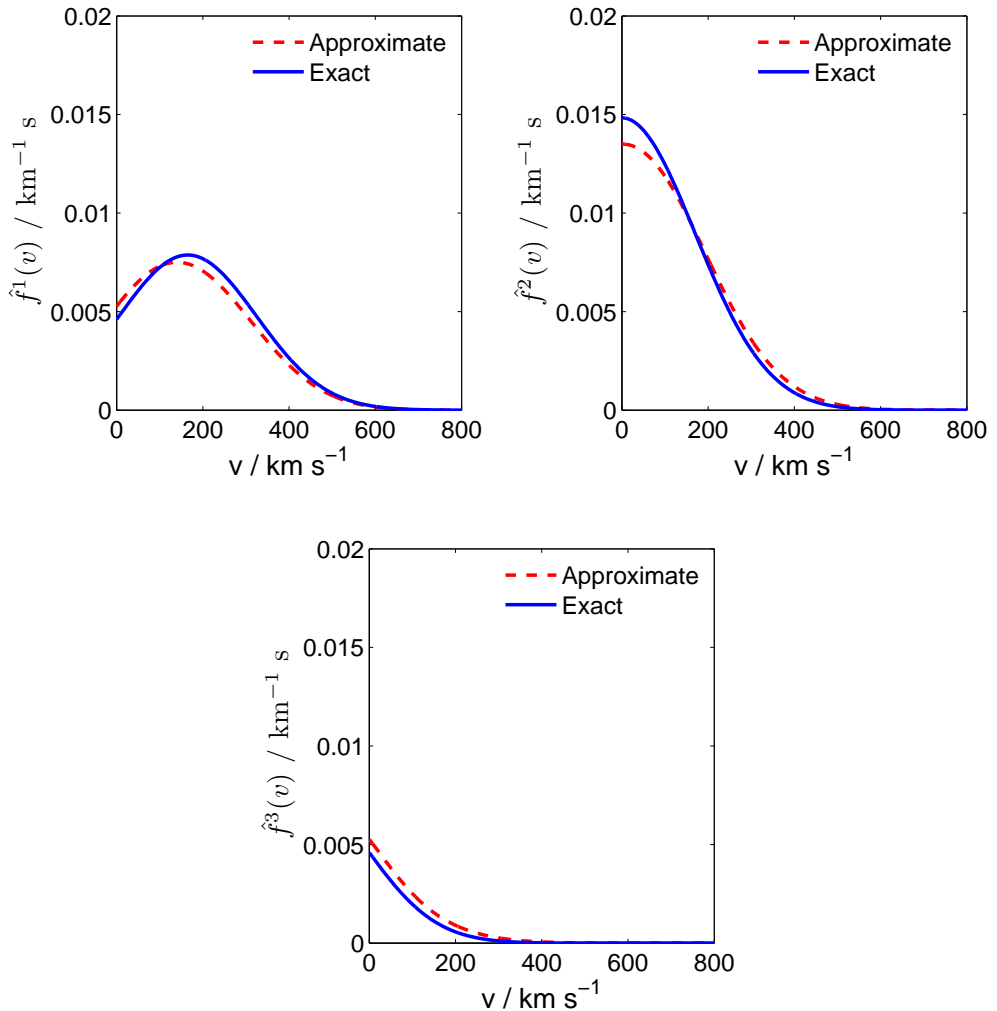


Figure 6.6: Exact and approximate forward, transverse and backward Radon transforms, \hat{f}^1 , \hat{f}^2 and \hat{f}^3 , for the SHM. The approximate Radon transforms are obtained by discretising the full velocity distribution into $N = 3$ angular bins. The vector \mathbf{v}_{lag} is aligned along $\theta' = 0$.

in the sign of $\cos \theta$). However, in the $N = 3$ case, the transverse Radon transform, given by

$$\hat{f}^T(v_{\min}) = \hat{f}^2(v_{\min}) = \int_{-1/2}^{1/2} \hat{f}(v_{\min}, \cos \theta) d \cos \theta, \quad (6.37)$$

is invariant under $\hat{f}(v_{\min}, \cos \theta) \rightarrow \hat{f}(v_{\min}, -\cos \theta)$. That is, the transverse event rate ‘folds’ back onto itself. Thus, even without sense discrimination, directional experiments will still be sensitive to this transverse scattering rate. By comparison, if the forward and backward directions cannot be distinguished, the remaining two integrated Radon transforms (the top left

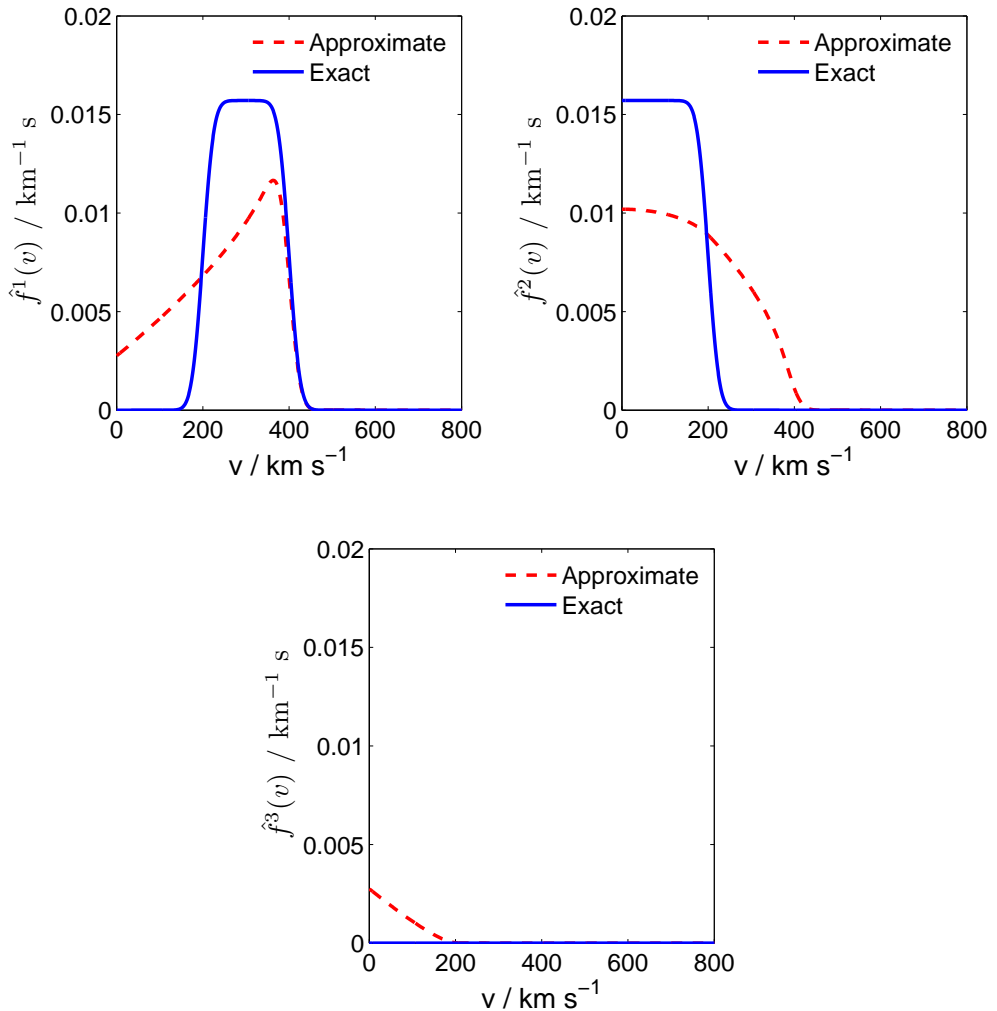


Figure 6.7: As Fig. 6.6, but for a stream distribution with $v_{\text{lag}} = 400 \text{ km s}^{-1}$ and $\sigma_v = 20 \text{ km s}^{-1}$.

and bottom panels in Fig. 6.6) are folded together, to obtain the longitudinal rate

$$\hat{f}^L(v_{\min}) = \int_{-1}^{-1/2} \hat{f}(v_{\min}, \cos \theta) d \cos \theta + \int_{1/2}^1 \hat{f}(v_{\min}, \cos \theta) d \cos \theta. \quad (6.38)$$

We plot the transverse and longitudinal integrated Radon transforms in Fig. 6.8 for the SHM. As expected, the two rates are now more similar in shape as we have lost some directional information. The approximate Radon transforms, obtained from the discretisation, match the true transforms closely for speeds above $v_{\min} \approx 200 \text{ km s}^{-1}$. For a Fluorine target with a 20 keV energy threshold [389], these low speeds will be below the threshold energy for all WIMP masses and the bias introduced by this

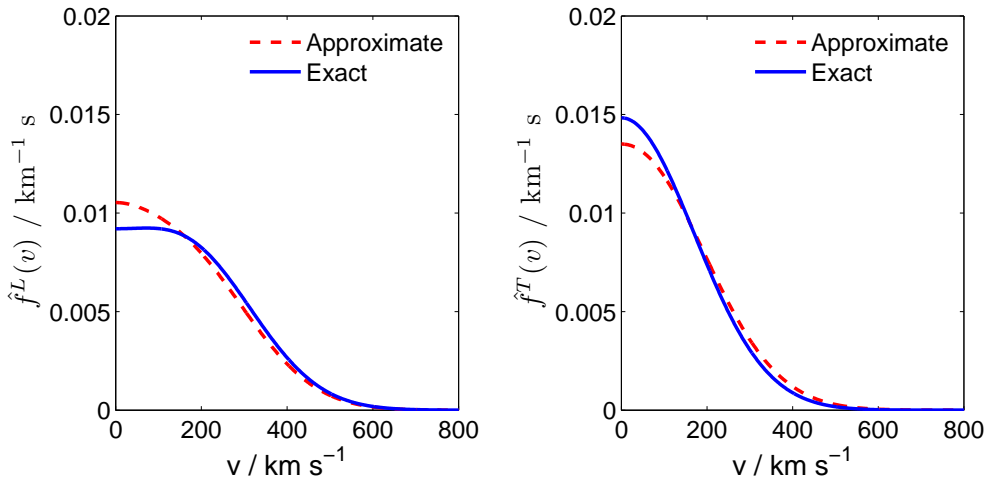


Figure 6.8: Exact and approximate folded transforms when the full SHM velocity distribution is discretised into $N = 3$ directional pieces. In the ‘longitudinal’ case (\hat{f}^L) $|\cos \theta| \in [1/2, 1]$ while in the ‘transverse case’ (\hat{f}^T) $|\cos \theta| \in [0, 1/2]$. The vector \mathbf{v}_{lag} is aligned along $\theta' = 0$.

discrepancy should be minimal.

We note that in this folded case, we would fit to two data sets, corresponding to the longitudinal and transverse event rates. However, our original discretisation required 3 free functions of v : $f^{1,2,3}(v)$. However, due to the properties of the Radon transform, the longitudinal rate is not a function of $f^1(v)$ and $f^3(v)$ but of the sum $f^1(v) + f^3(v) \equiv f_L(v)$. Thus, we have only two free functions $f^{L,T}(v)$ to fit.

6.5 Discussion

We have demonstrated that for smooth SHM-like distributions, the discretised velocity distribution allows us to obtain a good approximation to the discretised Radon transform. This means that we should be able to parametrise the speed distributions in each angular bin $f^k(v)$ and account for astrophysical uncertainties without introducing a large error in the recoil spectrum. An additional dark disk contribution would further reduce the error between the exact and approximate Radon transforms, as the dark disk is expected to approximately corotate with the Earth and would thus appear more isotropic than the SHM. However, strongly peaked velocity distributions, such as the stream studied in the previous sections, would introduce a much larger error in the Radon transform. While such

distributions are not considered likely (see Sec. 2.4.3), we should bear in mind that a larger value of N may be required for these more extreme distributions.

The decomposition we have presented in this chapter is coordinate dependent (as is a spherical harmonic decomposition). That is, we must specify which direction corresponds to $\theta' = 0$. In a real experiment, we would want to choose this direction to maximise the directional signal, in order to obtain the most information from the data. Therefore, we would ideally like to choose $\theta' = 0$ along the direction of the mean WIMP velocity. In the SHM, this is parallel to \mathbf{v}_{lag} , which corresponds to the direction of the Earth's motion in the Galactic frame, which has been calculated [405]. It might also be possible to use the median recoil direction to determine the mean WIMP velocity and thereby fix θ' . We note that for the results presented in this chapter we have fixed $\theta' = 0$ parallel to \mathbf{v}_{lag} . If we instead choose a different direction for $\theta' = 0$, this would decrease the forward-backward asymmetry of the discretised velocity distribution, reducing the error between the exact and approximate Radon transforms. Thus, the results presented would not be spoiled by a different choice of θ' .

Another consideration we have not yet address is the fact that in an experiment, we measure the directional recoil spectrum, not the Radon transform. Thus, we must multiply by the appropriate form factor and apply realistic thresholds in order to apply the methods presented here to directional data. Perhaps more important, however, is finite angular resolution. As discussed in Sec. 6.2, directional detectors have angular resolutions of 20° - 80° . In future work, this should be taken into account to determine the true directional recoil spectrum measured in an experiment. This angular smoothing will make the measured spectrum less anisotropic which again should reduce the error induced by considering a discretised velocity distribution.

Finally, in order to accommodate more strongly peaked distribution functions (or to obtain more directional information as the amount of data increases), it will be necessary to consider discretised distributions with $N > 3$. In future, we must develop an algorithm for generating the discrete Radon transforms from discrete velocity distributions of arbitrary N . As outlined in Appendix B, the angular integrals can be performed explicitly for any value of N , leaving only a series of 1-dimensional integrals over elementary functions of the WIMP speed v . Thus, it should be possible to

extend this framework to arbitrary N without requiring any (potentially slow) numerical integration over the angular variables.

6.6 Conclusion

Directional direct detection experiments should allow us to probe the full WIMP velocity distribution. However, as in the non-directional case, this introduces significant uncertainties into the analysis of data. Parametrising the velocity distribution and therefore reconstructing its structure requires a very large number of parameters, as $f(\mathbf{v})$ is a function of the 3-dimensional vector \mathbf{v} . It is therefore necessary to decompose $f(\mathbf{v})$ into some angular basis and parametrise the corresponding coefficients. Previous attempts in this direction have required equilibrium assumptions about the Galactic halo, or have made use of a spherical harmonic basis. An expansion in this basis does not necessarily lead to a physical distribution function, as it does not ensure that $f(\mathbf{v})$ is everywhere positive.

We have presented an alternative decomposition of $f(\mathbf{v})$ into angular bins. Over each bin, the velocity distribution has no angular dependence. As long as the parametrisation for the radial part of $f(\mathbf{v})$ is everywhere positive, so too will be full velocity distribution. We have demonstrated how the corresponding binned Radon transforms can be calculated for the case of $N = 1, 2, 3$ and compared these with the exact Radon transforms obtained from the full distribution.

In the $N = 2$ case, the discretised approximation underestimates the forward rate and overestimates the backward rate. However, this is improved in going to the $N = 3$ case, for which the exact and approximate Radon transforms agree to within 10-15%. For $N = 3$, it should also be possible to extract directional information even when sense recognition is not possible. For a more sharply peaked distribution, such as a stream, the error induced by using the discretised velocity distribution is significant. It would therefore be necessary to go to higher values of N in order to capture the strongly anisotropic features of such a distribution.

We have presented here a framework for parametrising the directional part of the velocity distribution. In future, it will be necessary to test this method using mock data from directional detectors in order to determine how well the WIMP parameters and the distribution itself can be reconstructed. This will require us to determine the mean WIMP direction, as

well as to include realistic experimental effects, such as angular resolution. However, we have argued that the good agreement between the exact and approximate rates for the case of smooth distributions should not be spoiled by these effects. Finally, it will be necessary to extend this framework to higher values of N to capture more angular information if larger numbers of events are observed at directional detectors.

Chapter 7

Conclusions

The presence of dark matter (DM) in the Universe has been postulated to explain a range of observations. Data from Cosmic Microwave Background anisotropies, the growth of large scale structure and the dynamics of galaxies and clusters all point towards a dark universe, with roughly 5 times as much dark matter as baryonic matter. So far, however, the detection of dark matter has only been through its gravitational influence. A number of experiments - so called direct detection experiments - are underway or in development which hope to detect weakly interacting massive particles (WIMPs) through their non-gravitational interactions in terrestrial detectors.

Once such a detection is confirmed, the next stage will be to try and measure the properties of the DM particles, such as their mass and interaction cross sections. This should help us to unravel the identity of the DM and begin to probe the structure of physics beyond the Standard Model of particle physics. However, the analysis of direct detection data is fraught with uncertainties. In this work, we have focused on astrophysical uncertainties, particularly those coming from the local speed distribution of dark matter $f_1(v)$. This distribution is *a priori* unknown and a wide range of proposals having been put forward for its correct form. We cannot hope to accurately reconstruct the DM properties without first addressing these uncertainties.

Previous attempts to parametrise the DM speed distribution have been unsatisfactory. As we discuss in Chapter 3, these methods typically assume some specific functional form for the speed distribution, motivated by N-body simulations or assumptions of equilibrium. However, if the true shape of the speed distribution is poorly fit by the functional form assumed

in the parametrisation, the particle physics parameters we are aiming to reconstruct will be biased. The aim then should be to develop a general, empirical parametrisation for the speed distribution which can be fit according to the data and which allows the DM mass and interaction cross sections to be reconstructed without bias. Such a parametrisation was first proposed by Peter [318], in the form of a binned approximation to the speed distribution. However, this was shown to result in a bias in the reconstructed WIMP mass.

In Chapter 3, we demonstrated that this bias stems from the interplay between the WIMP mass and the size of the bins in energy. For a fixed bin width in speed, varying the WIMP mass affects not only the size of the corresponding bins in energy but also the number of bins to which an experiment is sensitive. The result is that the best fit to the data may not be provided by the true underlying WIMP mass.

This problem can be alleviated by using a binned parametrisation of the DM *momentum* distribution. The range of momenta probed by a given experiment is independent of the WIMP mass, meaning that the overall shape and normalisation of the event spectrum can be probed separately. To pin down the WIMP mass, multiple experiments are required. In this case, the size and number of bins probed by each experiment depend only weakly on the WIMP mass, significantly reducing the bias seen in the binned speed parametrisation. We have also seen that the values of the momentum bin parameters may allow us to reconstruct the WIMP speed distribution itself. However, going from the reconstructed momentum distribution to the speed distribution is non-trivial. Moreover, the momentum binning method is expected to fail at low WIMP masses. Finally, this method requires a choice of the momentum range over which to parametrise, which may not always be obvious.

What properties then do we require of a general parametrisation of the WIMP distribution? It must be a physical distribution function, meaning that it must be everywhere non-negative and must be normalised. From our study of binned parametrisations, we are also lead to conclude that it should not have any fixed length scales, as these may result in a biased WIMP mass reconstruction. We have proposed that the *logarithm* of directionally-averaged velocity distribution $f(v)$ should be written as a polynomial in the speed v in the Earth frame. The resulting speed distri-

bution takes the form

$$f_1(v) = v^2 \exp\left(-\sum_{i=0}^{N-1} a_k P_k(v)\right). \quad (7.1)$$

This ensures that $f_1(v)$ is not only strictly positive, but also a smooth function of v . The shape of the speed distribution is controlled by the parameters a_k and the N basis functions P_k . Logarithmic dependence on the parameters also means that a wide range of functional forms can be approximated.

In Chapter ??, we have demonstrated that using the parametrisation the WIMP mass can be reconstructed without bias over a range of benchmark masses from 10 to 500 GeV. We have also demonstrated the method for a number of possible underlying distribution functions and shown that it has the correct statistical properties when Poisson fluctuations are included. We have also set out how best to choose the basis polynomials P_k and the number of basis functions.

However, direct detection experiments have finite energy thresholds, which corresponds to a minimum WIMP speed to which they are sensitive. Without information about the speed distribution below this threshold, it remains unconstrained by the experiments. This means that we do not know what fraction of WIMPs can contribute to scattering events in the detector. If we observe a small number of events at a detector, we cannot know whether they were caused by WIMPs with a low cross section or by WIMPs with a larger cross section but whose population is concentrated at low speeds. This results in a degeneracy between the cross section and the shape of the speed distribution. This degeneracy is a generic consequence of any general parametrisation of the WIMP speed distribution and means that we can only use direct detection experiments to place a lower bound on the interaction strengths of DM particles. As a consequence of this, we can only probe the *shape* but not the normalisation of the WIMP speed distribution. In spite of this, it may still be possible to distinguish the Standard Halo Model from N-body speed distributions using around 1000 events.

In Chapter 5, we explore a method for breaking the speed distribution-cross section degeneracy. The capture of DM particles in the Sun is described by the same interaction cross sections which control the scattering rate in direct detection experiments. However, in the case of DM capture, it is those WIMPs with the lowest speeds which are more easily

captured. Captured WIMPs then annihilate in the Sun and produce neutrinos, which can be detected at neutrino telescope experiments, such as IceCube. By combining future neutrino telescope and direct detection data, we can probe the entire range of the WIMP speed distribution. We have demonstrated this for several benchmarks. This allows us to constrain the fraction of low speed WIMPs and therefore break the degeneracy in the cross section. We have also been able to closely reconstruct the WIMP speed distribution over the entire range of interest. **Finish...**

Need better statistical techniques to reject speed distributions...

Finally, in Chapter ??, we began to explore how such a parametrisation method could be extended to directional experiments. Such experiments depend on the full 3-dimensional velocity distribution $f(\mathbf{v})$. Parametrising such a function is unfeasible and would require a huge number of parameters. It is therefore necessary to decompose $f(\mathbf{v})$ into a smaller number of basis functions. A spherical harmonic decomposition has been suggested previously. However, the spherical harmonic basis is not strictly positive, meaning that we cannot ensure that the velocity distribution is physical at every point in parameter space.

As an alternative, we propose an angular discretisation of the velocity distribution. As a first approximation, we have considered the forward- and backward-going distributions. However, with increasing amounts of data, it would be possible to increase the number of discretised pieces in $f(\mathbf{v})$. This method allows us to constrain a small number of 1-dimensional functions $f_j(v)$, rather than a much larger space of 3-dimensional functions. We have laid out the framework for calculating the directional event rate from such a discrete parametrisation and have shown that with as few as $N = 3$ discrete pieces, the event spectrum can be well fit by this approximation.

Further work is needed to understand how this discrete approximation behaves when confronted with mock data sets. In particular, we must combine this angular discretisation with the polynomial parametrisation we have developed for the speed distribution. This will allow us to determine how many discrete pieces are required for real data sets to ensure a close enough approximate to the true recoil spectrum. We can also combine directional with non-directional data sets using the same parametrisation. The isotropic speed distribution will simply be given by the sum of each of the discrete directional pieces. Though this method remains to be tested,

we have established a framework which should allow the velocity distribution to be parametrised in a tractable way.

Need more ‘further work’...Combining with other uncertainties - particle physics...

In this work, we have demonstrated for the first time that uncertainties in the WIMP speed distribution can be confronted and overcome in a completely general way. The polynomial $\ln f(v)$ parametrisation which we have proposed allows the WIMP mass to be reconstructed without bias, which we have demonstrated with a wide range of particle physics and astrophysics benchmarks. The introduction of neutrino telescope data allows us to probe the low speed population of WIMPs and therefore constrain not only the WIMP mass but also the WIMP interaction cross sections. We have also outlined how such a framework can be extended to incorporate directional data. This work is the first demonstration that both particle physics parameters *and* the form of the speed distribution can be extracted from data from DM search experiments. **Need a punchy end...**

Appendix A

Parameter Reconstruction

In this appendix, we address the problem of parameter reconstruction. Given a set of data \mathcal{D} , we would like to make some statement about the values of a set of model parameters $\boldsymbol{\theta}$. Due to statistical and systematic uncertainties, this will be a probabilistic statement about which values of $\boldsymbol{\theta}$ are more likely. Here, we consider what is meant by ‘more likely’. We then demonstrate how parameter estimates and uncertainty intervals are constructed and how the parameter space of $\boldsymbol{\theta}$ can be explored to obtain these estimates.

In general, there are two approaches to parameter estimation. In *frequentist* inference, there is only a single, fixed set of true values for the model parameters $\boldsymbol{\theta}$. We imagine that the experiment (which produced the data \mathcal{D}) can be repeated a large number of times, giving independent results each time. The ‘probability’ associated with each set of parameters $\boldsymbol{\theta}$ is a measure of how frequently our experiment would produce data which looked similar to \mathcal{D} if $\boldsymbol{\theta}$ is the true value. In a frequentist framework, the true model parameters are fixed but unknown and we make statements about how confident we are that these true parameters lie in a particular range.

An alternative approach is *Bayesian* inference. The true parameter value is treated as a random variable and we use Bayes’ theorem to determine its probability distribution from the data:

$$P(\boldsymbol{\theta}|\mathcal{D}) = P(\boldsymbol{\theta}) \frac{P(\mathcal{D}|\boldsymbol{\theta})}{P(\mathcal{D})}. \quad (\text{A.1})$$

In doing so, we need to know $P(\boldsymbol{\theta})$, known as the prior on the model parameters. This is a measure of our beliefs about the true value of $\boldsymbol{\theta}$ and may be motivated by theoretical considerations or information from

other experiments. In a Bayesian framework, we combine the data with information about our prior expectations to make statements about the probability of $\boldsymbol{\theta}$ having a particular value.

A.1 Frequentist statistics

In frequentist statistics, the most important quantity to consider is the *likelihood* of a given point in parameter space, $\mathcal{L}(\boldsymbol{\theta})$, defined as the probability of obtaining the data \mathcal{D} , assuming that $\boldsymbol{\theta}$ is the true parameter value. The likelihood often takes a very small value (because the probability of obtaining a particular data set out of all possible data sets is typically very small), and so it is convenient to work with the log-likelihood $l(\boldsymbol{\theta}) = \ln(\mathcal{L}(\boldsymbol{\theta}))$. The absolute value of $\mathcal{L}(\boldsymbol{\theta})$ carries no significance. However, the likelihood value of a particular point, relative to another, can be interpreted as a measure of the relative goodness of fit of the points. While the likelihood is not a probability distribution, in the limit of a large number of samples $l(\boldsymbol{\theta})$ follows a χ^2 distribution (as we shall discuss shortly) and therefore can have a probabilistic interpretation.

Often, we may not be interested in all of the parameters of $\boldsymbol{\theta}$. For example, we may partition the parameters into parameters of interests $\boldsymbol{\psi}$ and so-called nuisance parameters $\boldsymbol{\phi}$: $\boldsymbol{\theta} = (\boldsymbol{\psi}, \boldsymbol{\phi})$. These nuisance parameters may be parameters which we are not directly interested in, but which must be included in the analysis to account for all the relevant uncertainties. We often want to reduce the dimensionality of $\boldsymbol{\theta}$ to consider only how the likelihood varies as a function of $\boldsymbol{\psi}$.

One method of doing this is by maximizing the full likelihood function over the nuisance parameters:

$$\mathcal{L}_p(\boldsymbol{\psi}) = \max_{\boldsymbol{\phi}} \mathcal{L}(\boldsymbol{\psi}, \boldsymbol{\phi}). \quad (\text{A.2})$$

That is, for each value of $\boldsymbol{\psi}$, we select the maximum value of \mathcal{L} obtained from all possible values of $\boldsymbol{\phi}$. This projection onto the subset of parameters $\boldsymbol{\psi}$ is referred to as the profile likelihood.

An alternative method of reducing the dimensionality of the full parameter space is to calculate the mean likelihood:

$$\mathcal{L}_m(\boldsymbol{\psi}) = \frac{\int \mathcal{L}(\boldsymbol{\psi}, \boldsymbol{\phi}) d\boldsymbol{\phi}}{\int d\boldsymbol{\phi}}. \quad (\text{A.3})$$

The mean likelihood allows us to take into account the structure of the likelihood function in the nuisance directions. The profile likelihood simply selects the largest likelihood value at each value of ψ , even if this value is only realised over a small range of values in ϕ . By comparison, the mean likelihood receives a greater contribution from wide ranges of ϕ which have a moderate likelihood value.

A.1.1 Parameter estimates

In frequentist statistics, the point estimate of a parameter is relatively unambiguous. This point estimate is given by the best fit point, or maximum likelihood estimate (MLE), $\hat{\theta}$, such that:

$$\max \mathcal{L}(\theta) = \mathcal{L}(\hat{\theta}). \quad (\text{A.4})$$

This estimate is the same whether we use the full likelihood or the profile likelihood, while using the mean likelihood may lead to a different value. In parameter inference, it is useful to consider the relative log-likelihood l_r :

$$l_r(\theta) = \ln \left(\frac{\mathcal{L}(\theta)}{\mathcal{L}(\hat{\theta})} \right). \quad (\text{A.5})$$

The logarithm is a monotonically increasing function and therefore the maximum of the likelihood and the relative log-likelihood are obtained for the same parameter values $\hat{\theta}$. According to Wilks' theorem [353], l_r is asymptotically χ^2 -distributed as the number of samples N in the data tends to infinity,

$$-2l_r \sim \chi_k^2, \quad (\text{A.6})$$

where the number of degrees of freedom k is equal to the dimensionality of the space $\psi = (\psi_1, \dots, \psi_k)$. This asymptotic behaviour applies equally well for the full likelihood and the profile likelihood [406] and allows us to construct confidence intervals.

We construct a $p\%$ interval from all values of ψ for which

$$l_r(\psi) \leq -\frac{1}{2}\gamma(p\%; k), \quad (\text{A.7})$$

where $\gamma(p\%; k)$ satisfies

$$\int_0^{\gamma(p\%; k)} P(\chi_k^2) d\chi_k^2 = p\%, \quad (\text{A.8})$$

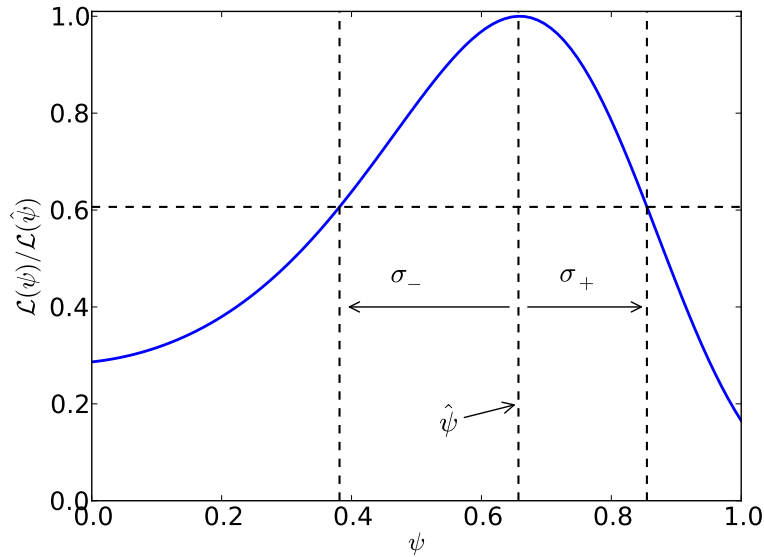


Figure A.1: Illustration of likelihood-based parameter inference. The point estimate for the parameter ψ is given by the best fit point $\hat{\psi}$. The 68% confidence interval is given by $\psi \in [\hat{\psi} - \sigma_-, \hat{\psi} + \sigma_+]$.

and $P(\chi_k^2)$ is the χ_k^2 probability distribution function. This is essentially a relative goodness-of-fit test. Values of ψ outside this interval are unlikely to produce data similar to \mathcal{D} and would be rejected at the $p\%$ level in favour of the hypothesis $\psi = \hat{\psi}$. Equivalently, in terms of the likelihood, we include values of ψ for which

$$\mathcal{L}(\psi) \geq \exp\left(-\frac{1}{2}\gamma(p\%; k)\right) \mathcal{L}(\hat{\psi}). \quad (\text{A.9})$$

This is illustrated in Fig. A.1 for the case of a single parameter of interest.

A.2 Bayesian statistics

In Bayesian statistics, we wish to obtain the *posterior* probability distribution $\mathcal{P}(\boldsymbol{\theta}) = P(\boldsymbol{\theta}|\mathcal{D})$. This is obtained from Bayes' theorem:

$$\mathcal{P}(\boldsymbol{\theta}) = P(\boldsymbol{\theta}|\mathcal{D}) = P(\boldsymbol{\theta}) \frac{P(\mathcal{D}|\boldsymbol{\theta})}{P(\mathcal{D})}. \quad (\text{A.10})$$

Here $P(\mathcal{D})$ is the probability of obtaining the data \mathcal{D} . However, this does not depend on the theoretical parameters $\boldsymbol{\theta}$ and we can therefore take it as an overall normalising factor for the probability distribution. The likelihood enters into the Bayesian framework as the probability of the

data given the model parameters $P(\mathcal{D}|\boldsymbol{\theta}) = \mathcal{L}(\boldsymbol{\theta})$. Finally, the prior $P(\boldsymbol{\theta})$ encodes our *a priori* knowledge about the true value of $\boldsymbol{\theta}$. If the value of a parameter, say θ_1 , is known to be approximately $\theta_1 = \hat{\theta}_1 \pm \sigma_\theta$, we may choose a Gaussian prior to reflect this:

$$P(\theta_1) \propto \exp\left(-\frac{(\theta_1 - \hat{\theta}_1)^2}{2\sigma_\theta^2}\right). \quad (\text{A.11})$$

Alternatively, we may have a very limited knowledge of θ_1 and may choose a linear-flat or log-flat prior over some range of values: $P(\theta_1) \propto 1$ or $P(\log(\theta_1)) \propto 1$. In the case of a linear-flat prior, $\mathcal{P}(\boldsymbol{\theta}) = \mathcal{L}(\boldsymbol{\theta})$ and the Bayesian and frequentist frameworks coincide. In contrast to the likelihood, the posterior distribution is considered a probability distribution, even in the case of small numbers of samples.

As in the frequentist case, we may wish to reduce the dimensionality of the parameter space to include only those parameters of interest $\boldsymbol{\psi}$. When dealing with the posterior probability, this is typically done by marginalisation. The marginalised posterior \mathcal{P}_m is obtained by integrating over the nuisance parameters:

$$\mathcal{P}_m(\boldsymbol{\psi}) = \int \mathcal{P}(\boldsymbol{\psi}, \boldsymbol{\phi}) d\boldsymbol{\phi}. \quad (\text{A.12})$$

Just as \mathcal{P} is a probability distribution function for the parameters $\boldsymbol{\theta}$, \mathcal{P}_m is a probability distribution function for the parameters of interest $\boldsymbol{\psi}$ - specifically, the marginalised probability distribution.

A.2.1 Parameter estimates

In contrast to the frequentist case, there are several possibilities for a point parameter estimate. Because \mathcal{P} and \mathcal{P}_m are probability distributions, they can be described by several location parameters:

Mode - the mode of the probability distribution is the value of $\boldsymbol{\theta}$ which maximises \mathcal{P} . This is also known as the maximum a posteriori (MAP) estimate and can be viewed as analogous to the maximum likelihood estimator.

Median - the median value of the parameter θ satisfies

$$\int_{-\infty}^{\theta_{\text{median}}} \mathcal{P}(\theta) d\theta = \frac{1}{2}. \quad (\text{A.13})$$

This means that there is as much probability density below θ_{median} as above.

Mean - the mean value $\langle \boldsymbol{\theta} \rangle$ is given by

$$\langle \boldsymbol{\theta} \rangle = \int \boldsymbol{\theta} \mathcal{P}(\boldsymbol{\theta}) d\boldsymbol{\theta}. \quad (\text{A.14})$$

Each of these will behave differently for different posterior probability distributions. The MAP estimate indicates where the greatest probability density is and may be useful when the posterior is sharply peaked. The mean and median better reflect the global properties of the posterior probability, but may be misleading if the distribution is multimodal.

We also wish to make statements about the possible range of values for parameters. In a Bayesian framework, we define the p% *credible* interval \mathcal{C}_p such that it encloses p% of the probability distribution. Again, there are several possibilities for how to define $\mathcal{C}_p = [\mathcal{C}_p^{\min}, \mathcal{C}_p^{\max}]$, such as:

Central interval - the interval which has the mean as its central value,

Equal tails interval - the total probability below the interval is the same as above the interval,

$$\int_{-\infty}^{\mathcal{C}_p^{\min}} \mathcal{P}(\boldsymbol{\theta}) d\boldsymbol{\theta} = \int_{\mathcal{C}_p^{\max}}^{\infty} \mathcal{P}(\boldsymbol{\theta}) d\boldsymbol{\theta}, \quad (\text{A.15})$$

Highest density interval - the interval defined by all values $\mathcal{P}(\boldsymbol{\theta}) \geq \gamma$, where γ is defined by

$$\int_{\mathcal{P}(\boldsymbol{\theta} \geq \gamma)} \mathcal{P}(\boldsymbol{\theta}) d\boldsymbol{\theta} = p\%. \quad (\text{A.16})$$

Highest density intervals are useful when $\mathcal{P}(\boldsymbol{\theta})$ is multimodal and disjoint intervals may be required. Again, when we specify a credible interval, we must specify which definition we are using. These definitions can also be extended simply to the case where the parameter space of interest has a higher dimension. In Fig. A.2, we illustrate the MAP estimate and mean for a hypothetical posterior distribution. We also show the 95% credible interval obtained using the equal tails method.

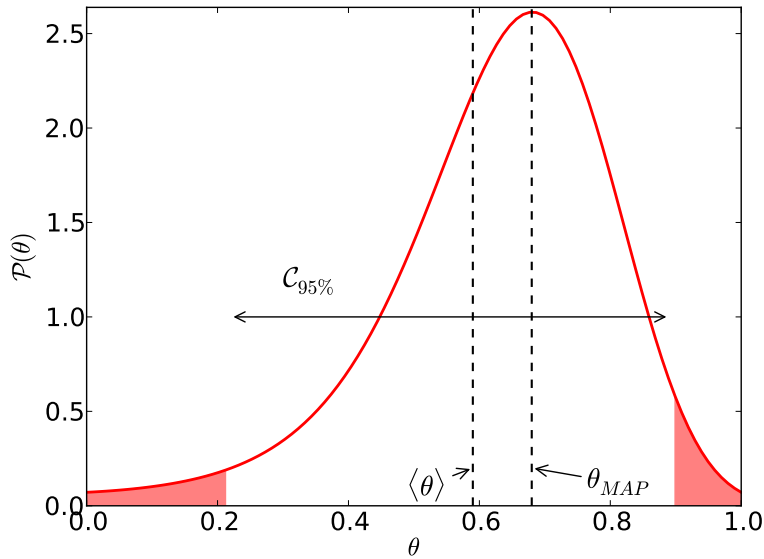


Figure A.2: Illustration of posterior-based parameter inference. We show the difference between the MAP and mean parameter estimates. We also show one possible 95% credible interval - the probability in the shaded tails is equal.

A.3 Exploring the parameter space

So far we have considered how, given $\mathcal{L}(\boldsymbol{\theta})$ or $\mathcal{P}(\boldsymbol{\theta})$, we can make parameter inferences about $\boldsymbol{\theta}$. However, we have not so far considered how we can evaluate these functions. We do not typically know *a priori* where $\mathcal{L}(\boldsymbol{\theta})$ or $\mathcal{P}(\boldsymbol{\theta})$ are maximised or what shape they have. In this section, we will briefly discuss two methodologies for mapping out these functions: Markov Chain Monte Carlo and Nested Sampling.

A.3.1 Markov chain monte carlo

In the Markov chain monte carlo (MCMC) method [407], we generate a chain of points in the parameter space $\{\boldsymbol{\theta}_i\}$. A new point $\boldsymbol{\theta}_{j+1}$ in the chain is generated from the current point $\boldsymbol{\theta}_j$ by picking from some proposal distribution $q(\boldsymbol{\theta}_{j+1}; \boldsymbol{\theta}_j)$. Under the Metropolis-Hastings algorithm [408], the new point is accepted with probability

$$\min \left\{ 1, \frac{\mathcal{P}(\boldsymbol{\theta}_{j+1})q(\boldsymbol{\theta}_j; \boldsymbol{\theta}_{j+1})}{\mathcal{P}(\boldsymbol{\theta}_j)q(\boldsymbol{\theta}_{j+1}; \boldsymbol{\theta}_j)} \right\}. \quad (\text{A.17})$$

Over a large number of points, the chain positions should converge to a stationary distribution. Eventually the number density of chain positions

will be proportional to the posterior $n(\boldsymbol{\theta}) \propto \mathcal{P}(\boldsymbol{\theta})$ (assuming that the proposal distribution is symmetric). In addition, we will also have the value of the likelihood $\mathcal{L}(\boldsymbol{\theta})$ evaluated at all of the points in the chain.

Care must be taken to ensure that the chain has converged before the results can be interpreted. Typically some initial set of points is discarded as ‘burn-in’, after which the chain is deemed to have converged. However, it is often unclear when convergence has been reached. Moreover, each chain position will depend slightly on the previous position. However, we want to obtain independent samples from the posterior distribution. Therefore, the chain is typically thinned (by some factor of order 25-50) [334], with only some of the positions being retained. Finally, we must select how many positions we want to obtain in the chain before we stop the random walk, in the hopes that the chain has adequately explored the parameter space.

When $\mathcal{P}(\boldsymbol{\theta})$ is multimodal, sharply peaked or has strong degeneracies among the parameters, exploration by the chain can be slow. It can be unclear whether convergence has been achieved, especially if the chain becomes trapped in one of the modes of the distribution. One way to improve the rate of convergence is to use high temperature MCMC [335, 407]. We employ a ‘heated’ chain with temperature $T = 2$, meaning that we accept new points with probability

$$\min \left\{ 1, \left(\frac{\mathcal{P}(\theta_{j+1})q(\theta_{j+1})}{\mathcal{P}(\theta_j)q(\theta_j)} \right)^{1/T} \right\}. \quad (\text{A.18})$$

We are now effectively sampling from a flatter posterior distribution, which allows a more rapid mixing and convergence of the chain. However, to achieve the same precision as in the $T = 1$ case, we require a larger number of samples. The distribution of chain positions obtained at the higher temperature is then $n_T(\boldsymbol{\theta}) \propto \mathcal{P}^{1/T}(\boldsymbol{\theta})$. We recover the distribution of positions at $T = 1$ by ‘cooling’ the chain:

$$n(\boldsymbol{\theta}) = n_T(\boldsymbol{\theta}) (\mathcal{P}(\boldsymbol{\theta}))^{1-1/T}. \quad (\text{A.19})$$

One popular, publicly available MCMC code is COSMOMC [334]. This was developed in the context of cosmological parameter estimation, but can be used as a generic MCMC sampler. When the parameter space is of a high dimension or has a number of modes, MCMC methods may prove slow. Such methods also rely on a suitable choice of burn-in and thinning factors, as well as a determination of whether convergence has occurred.

Next, we explore an alternative method for efficiently obtaining samples from the posterior distribution.

A.3.2 Nested sampling

The nested sampling method [409] was originally proposed as a method of calculating the overall normalising factor which appears in Bayes' theorem, $P(\mathcal{D})$. However, it produces as a by-product samples from the posterior distribution and values of the likelihood function. In nested sampling, we take an initial sample of points (so-called ‘live’ points) from the parameter space and evaluate the likelihood at each point. At each subsequent step, the live point with the lowest likelihood \mathcal{L}_0 is removed from the sample and replaced with another point sampled from the parameter space with $\mathcal{L}_i > \mathcal{L}_0$. Thus, the algorithm explores the prior in concentric shells of \mathcal{L} . Each new live point can be assigned a weight w_i , obtained from an estimate of the change in the prior volume between concentric shells. Finally, each point can then be assigned a posterior density

$$p_i = \frac{w_i \mathcal{L}_i}{\mathcal{Z}}. \quad (\text{A.20})$$

The Bayesian evidence $\mathcal{Z} \equiv P(\mathcal{D})$ is obtained by summing $\sum_i w_i \mathcal{L}_i$ and the algorithm continues until this is determined to some desired precision.

In order to continue, we must be able to select points from the prior subject to the hard constraint $\mathcal{L}_i > \mathcal{L}_0$. As the algorithm moves to higher values of \mathcal{L}_0 , points with a higher likelihood than this tend to become localised in very small regions of the parameter space. In addition, if the likelihood is multimodal or has pronounced degeneracies, the sampling of points subject to this constraint becomes highly inefficient. The MULTINEST algorithm [349–351] uses multimodal, ellipsoidal nested sampling to improve performance. As \mathcal{L}_0 increases during the calculation, MULTINEST uses the current live points to approximate the isolikelihood contour by a series of ellipsoidal surfaces. New points are drawn only from within these ellipsoids, increasing the efficiency of the sampling but still ensuring that the constraint $\mathcal{L}_i > \mathcal{L}_0$ is satisfied. The algorithm can also accommodate multiple modes in the posterior which can be explored independently.

In utilising the MultiNest algorithm, we must decide how many live point to use N_{live} . This determines how closely the isolikelihood contours can be followed, how dense the posterior samples will be and, in the case

where there are highly localised modes, how well explored the prior will be. We must also decide the tolerance of the algorithm, `tol`. This determines the precision with which \mathcal{Z} should be determined and therefore how high up the likelihood surface the algorithm should explore. Finally, we can introduce an efficiency `eff`, which is the desired sampling efficiency. In order to (attempt to) achieve this, the algorithm rescales the volume of the bounding ellipsoids to incorporate more or less of the prior volume, as desired.

A.4 Likelihood examples

We have discussed how, given the likelihood and posterior, we can make parameter inferences. We have also explored methods by which these functions can be efficiently explored. Finally, we look at how to evaluate the likelihood for a given data set.

The simplest signal which can be observed is a number of events N_o . We can calculate from the model parameters $\boldsymbol{\theta}$ the expected number of events N_e . The probability of obtaining the data given the model parameters is then given by the Poisson likelihood:

$$\mathcal{L}(N_o|N_e) = \frac{N_e^{N_0}}{N_0!} e^{-N_e}. \quad (\text{A.21})$$

We can extend this definition to incorporate data which has been divided into bins with N_e^i events expected and N_o^i observed in the i^{th} bin:

$$\mathcal{L}(\{N_o^i\}|\{N_e^i\}) = \prod_{i=1,N_{\text{bins}}} \frac{(N_e^i)^{N_o^i}}{(N_o^i)!} e^{-N_e^i}. \quad (\text{A.22})$$

We can also consider the unbinned likelihood by taking the limit as the bin width tends to zero,

$$\mathcal{L}(\mathcal{D}|\boldsymbol{\theta}) = \frac{N_e^{N_0}}{N_0!} e^{-N_e} \prod_{i=1,N_e} P(E_i), \quad (\text{A.23})$$

where N_e and N_o are the number of events expected and observed across the whole experiment. We have assumed here that each event has an associated measurement, the energy E_i , and we take the product over the normalised differential event rates:

$$P(E) = \frac{dR}{dE_R}(E) \left[\int_0^\infty \frac{dR}{dE_R}(E') dE' \right]^{-1}. \quad (\text{A.24})$$

Finally, we may wish to include the effects of backgrounds in the analysis. Then, we must take into account the fact that we do not know whether a given event is due to the signal or background. It will come from the signal with probability

$$f_S = \frac{N_{\text{signal}}}{N_{\text{signal}} + N_{\text{background}}} , \quad (\text{A.25})$$

and from the background with probability $f_{BG} = 1 - f_S$. Thus, we obtain the full likelihood

$$\mathcal{L}(\mathcal{D}|\boldsymbol{\theta}) = \frac{N_e^{N_0}}{N_0!} e^{-N_e} \prod_{i=1, N_e} (f_S P_S(E_i) + f_{BG} P_{BG}(E_i)) . \quad (\text{A.26})$$

Check... Here, N_e and N_o are the total number of expected events including both signal and background. We must also take into account the normalised spectra of the signal $P_S(E)$ and the background $P_{BG}(E)$ separately, multiplying the contributions of both.

For multiple experiments, the total likelihood is then the product of the individual likelihoods for each experiment. When using the binned likelihood, experiments with more bins receive a greater weight in the likelihood. Therefore, we may want to reweight the bins such that each experiment receives equal weight. We write the likelihood contribution of the i^{th} bin in experiment n as $(\mathcal{L}_n^i)^{w_n}$, where w_n is the weight for bins in experiment n . This weight is calculated as

$$w_n = \frac{N_{\text{total}}}{N_{\text{expt}} N_n} \quad (\text{A.27})$$

where N_n and N_{total} are, respectively, the number of bins in experiment n and the total number across all experiments. N_{expt} is the number of experiments. This weighting increases the contribution of experiments with fewer bins than average and decreases the contribution of those with more bins than average. This form also ensures that in the cases of a single experiment and of multiple experiments with the same numbers of bins the weighted likelihood will be identical to the unweighted likelihood.

Appendix B

Calculating the discrete Radon transform

In this appendix, we demonstrate how the Radon transform is calculated for a discretised velocity distribution, as described in Chapter 6. We first consider calculating the azimuthally averaged Radon transform of a general velocity distribution $f(\mathbf{v})$:

$$\begin{aligned}\hat{f}(v_{\min}, \cos \theta) &= \int_0^{2\pi} \hat{f}(v_{\min}, \cos \theta, \phi) d\phi \\ &= \int_0^{2\pi} \left(\int_{\mathbb{R}^3} f(\mathbf{v}) \delta(\mathbf{v} \cdot \hat{\mathbf{q}} - v_{\min}) d^3\mathbf{v} \right) d\phi \\ &= \int_{\phi=0}^{2\pi} \int_{v=0}^{\infty} \oint v f(\mathbf{v}) \delta(v_{\min}/v - \hat{\mathbf{v}} \cdot \hat{\mathbf{q}}) d\Omega_v dv d\phi.\end{aligned}\quad (\text{B.1})$$

We recall that primed angles (θ', ϕ') are associated with the direction of \mathbf{v} , while unprimed angles (θ, ϕ) are associated with the direction of $\hat{\mathbf{q}}$. Thus, the ϕ integral in Eq. B.1 applies only to the δ -function. Expanding the dot product into angular coordinates, we write the ϕ integral as

$$\begin{aligned}I(v_{\min}, \cos \theta, \mathbf{v}) &= \int_0^{2\pi} \delta(\sin \theta \sin \theta' \cos(\phi - \phi') + \cos \theta \cos \theta' - v_{\min}/v) d\phi \\ &\equiv \int_0^{2\pi} \delta(g(\phi)) d\phi.\end{aligned}\quad (\text{B.2})$$

We then rewrite the delta function as a function of ϕ :

$$\delta(g(\phi)) = \sum_i \frac{\delta(\phi - \phi_i)}{|g'(\phi_i)|}. \quad (\text{B.3})$$

Here, we sum over those values of ϕ_i satisfying $g(\phi_i) = 0$,

$$\begin{aligned} g(\phi_i) &= 0 \\ \Rightarrow \cos(\phi_i - \phi') &= \frac{\beta - \cos \theta \cos \theta'}{\sin \theta \sin \theta'} \equiv \gamma, \end{aligned} \quad (\text{B.4})$$

where we have also defined $\beta = v_{\min}/v$. The solutions for $\phi \in [0, 2\pi]$ are:

$$\begin{aligned} \phi_1 &= \phi' + \cos^{-1} \gamma, & \text{for } \phi' \in [0, 2\pi - \cos^{-1} \gamma] \\ \phi_2 &= \phi' + 2\pi - \cos^{-1} \gamma, & \text{for } \phi' \in [0, \cos^{-1} \gamma] \\ \phi_3 &= \phi' + \cos^{-1} \gamma - 2\pi, & \text{for } \phi' \in [2\pi - \cos^{-1} \gamma, 2\pi] \\ \phi_4 &= \phi' - \cos^{-1} \gamma, & \text{for } \phi' \in [\cos^{-1} \gamma, 2\pi]. \end{aligned} \quad (\text{B.5})$$

We note that these solutions exist only for $\beta \in [0, 1]$ (or equivalently $v > v_{\min}$) and for $\gamma \in [-1, 1]$, otherwise Eq. B.4 cannot be satisfied. If these constraints are satisfied, there exist exactly 2 solutions for a given value of ϕ' and therefore 2 δ -functions in Eq. B.3.

For the derivative of $g(\phi)$ we obtain

$$g'(\phi) = -v \sin \theta \sin \theta' \sin(\phi - \phi'). \quad (\text{B.6})$$

Substituting the values of $\phi_{1,2,3,4}$, we see that

$$|g'(\phi_{1,2,3,4})| = v \sqrt{(\sin \theta \sin \theta')^2 - (\beta - \cos \theta \cos \theta')^2}. \quad (\text{B.7})$$

Each of the two δ -functions therefore contributes the same amount to the integral, regardless of the value of ϕ' . Performing the integral, we obtain

$$I(v_{\min}, \cos \theta, \mathbf{v}) = \frac{2C(\gamma)}{v \sqrt{(\sin \theta \sin \theta')^2 - (\beta - \cos \theta \cos \theta')^2}} \Theta(v - v_{\min}), \quad (\text{B.8})$$

where $C(\gamma) = 1$ for $\gamma \in [-1, 1]$ and vanishes otherwise.

We therefore obtain

$$\hat{f}(v_{\min}, \cos \theta) = \int_{-1}^1 \int_{v_{\min}}^{\infty} f(v, \cos \theta') I(v_{\min}, \cos \theta, v, \cos \theta') v^2 dv d \cos \theta', \quad (\text{B.9})$$

where we have performed the ϕ' integral over the velocity distribution,

$$f(v, \cos \theta') = \int_0^{2\pi} f(v, \cos \theta', \phi') d\phi', \quad (\text{B.10})$$

because $I(v_{\min}, \cos \theta, \mathbf{v})$ does not depend on ϕ' . In order to make further progress, we need an explicit form for $f(v, \cos \theta')$. We now consider the discretised velocity distributions discussed in Chapter 6.

B.1 $N = 2$ discretisation

For the $N = 2$ case, we are considering a forward-backward asymmetry in the velocity distribution:

$$f(\mathbf{v}) = \begin{cases} f^1(v) & \text{for } \theta' \in [0, \pi/2] \\ f^2(v) & \text{for } \theta' \in [\pi/2, \pi]. \end{cases} \quad (\text{B.11})$$

From these, we wish to obtain the integrated Radon transforms for the forward and backward directions. Specifically:

$$\hat{f}_1 = \int_0^1 \hat{f}(v_q, \cos \theta) d\cos \theta \quad (\text{B.12})$$

$$\hat{f}_2 = \int_{-1}^0 \hat{f}(v_q, \cos \theta) d\cos \theta. \quad (\text{B.13})$$

We will focus on the first of these, \hat{f}_1 , as the other can be obtained simply by exchanging which directions are forward and backward (that is, by interchanging f_1 and f_2). From now on, we will therefore be working under the assumption that $\cos \theta \in [0, 1]$.

We start with the $\cos \theta'$ integral:

$$\begin{aligned} J &\equiv \int_{-1}^1 f(v, \cos \theta') I(v_{\min}, \cos \theta, v, \cos \theta') d\cos \theta' \\ &= 2\pi \int_0^1 f^1(v) I(\cos \theta') d\cos \theta' + 2\pi \int_{-1}^0 f^2(v) I(\cos \theta') d\cos \theta'. \end{aligned} \quad (\text{B.14})$$

The factor $C(\gamma)$ in the expression for I requires that $|\gamma| < 1$. We can show that this is equivalent to requiring that $\cos \theta' \in [x_-, x_+]$, where

$$x_{\pm} = \beta \cos \theta \pm \sqrt{1 - \beta^2} \sin \theta. \quad (\text{B.15})$$

We show x_{\pm} as a function of $\cos \theta$ in Fig. B.1. Focusing on $\cos \theta \in [0, 1]$, we note that there are two distinct regimes. For $\cos \theta \in [0, \sqrt{1 - \beta^2}]$, x_+ is positive, while x_- is negative. For $\cos \theta \in [\sqrt{1 - \beta^2}, 1]$, however, both x_+ and x_- are positive. We therefore need to treat these two cases separately. Equation B.14 then becomes

$$J = \int_{x_-}^0 \frac{4\pi f^2(v) d\cos\theta'}{v \sqrt{(\sin\theta \sin\theta')^2 - (\beta - \cos\theta \cos\theta')^2}} \quad (B.16)$$

$$+ \int_0^{x_+} \frac{4\pi f^1(v) d\cos\theta'}{v \sqrt{(\sin\theta \sin\theta')^2 - (\beta - \cos\theta \cos\theta')^2}}, \quad \text{for } \cos\theta \in [0, \sqrt{1 - \beta^2}]$$

$$J = \int_{x_-}^{x_+} \frac{4\pi f^1(v) d\cos\theta'}{v \sqrt{(\sin\theta \sin\theta')^2 - (\beta - \cos\theta \cos\theta')^2}}, \quad \text{for } \cos\theta \in [\sqrt{1 - \beta^2}, 1]. \quad (B.17)$$

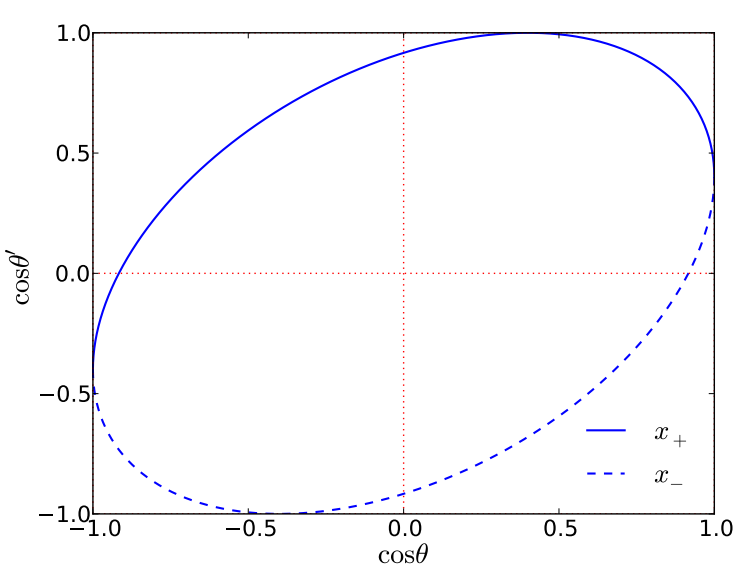


Figure B.1: Integration limits for Eq. B.14 as a function of $\cos\theta$, for a fixed value of β . The value $\cos\theta' = 0$ is denoted with a horizontal dashed line, while $\cos\theta = 0$ is shown with a vertical dashed line.

We note that

$$\int_{x_1}^{x_2} \frac{d\cos\theta'}{\sqrt{(\sin\theta \sin\theta')^2 - (\beta - \cos\theta \cos\theta')^2}} = \left[\sin^{-1} \left(\frac{x - \beta \cos\theta}{\sqrt{1 - \beta^2} \sin\theta} \right) \right]_{x_1}^{x_2}, \quad (B.18)$$

so that J takes the form:

$$\begin{aligned}
J &= \frac{4\pi f^1(v)}{v} \left(\frac{\pi}{2} + \sin^{-1} \left\{ \frac{\beta \cos \theta}{\sqrt{1 - \beta^2} \sin \theta} \right\} \right) \\
&\quad + \frac{4\pi f^2(v)}{v} \left(\frac{\pi}{2} - \sin^{-1} \left\{ \frac{\beta \cos \theta}{\sqrt{1 - \beta^2} \sin \theta} \right\} \right) \quad \text{for } \cos \theta \in [0, \sqrt{1 - \beta^2}] \\
J &= \frac{4\pi^2 f^1(v)}{v}, \quad \text{for } \cos \theta \in [\sqrt{1 - \beta^2}, 1].
\end{aligned} \tag{B.19}$$

We finally perform the $\cos \theta$ integral:

$$\hat{f}^1 = \int_0^1 \int_{v_{\min}}^{\infty} J v^2 dv d \cos \theta. \tag{B.20}$$

Noting that

$$\begin{aligned}
&\int_{x_1}^{x_2} \sin^{-1} \left(\frac{\beta \cos \theta}{\sqrt{1 - \beta^2} \sin \theta} \right) d \cos \theta \\
&= \left[x \sin^{-1} \left(\frac{\beta x}{\sqrt{1 - \beta^2} \sqrt{1 - x^2}} \right) + \tan^{-1} \left(\frac{1}{\beta} \sqrt{1 - \beta^2 - x^2} \right) \right]_{x_1}^{x_2},
\end{aligned} \tag{B.21}$$

we obtain

$$\hat{f}^1 = 4\pi \int_{v_{\min}}^{\infty} v \left(\pi f^1(v) + \tan^{-1} \left(\frac{\sqrt{1 - \beta^2}}{\beta} \right) (f^2(v) - f^1(v)) \right) dv \tag{B.22}$$

$$\hat{f}^2 = 4\pi \int_{v_{\min}}^{\infty} v \left(\pi f^2(v) + \tan^{-1} \left(\frac{\sqrt{1 - \beta^2}}{\beta} \right) (f^1(v) - f^2(v)) \right) dv, \tag{B.23}$$

where \hat{f}^2 is obtained by exchanging $f^1(v)$ and $f^2(v)$.

B.2 $N = 3$ discretisation

The calculation of the forward, backward and transverse Radon transforms for $N = 3$ discretisation proceeds as in the $N = 2$ case. However, we must divide the integration regions of Fig. B.1 into 3 regions rather than into 2 regions. In addition, in the $N = 3$ case, x_{\pm} lie in different ranges of $\cos \theta'$ depending on the value of β . Thus, we must also take care to divide the

range of v into distinct regions depending on which angular bin x_{\pm} fall into. We will not present the result of the calculation here, as its form is not particularly instructive. However, we will note that we require a generalised version of Eq. B.21 in order to perform the calculation:

$$\begin{aligned}
 & \int \sin^{-1} \left(\frac{y - \beta \cos \theta}{\sqrt{1 - \beta^2} \sin \theta} \right) d \cos \theta \\
 &= x \sin^{-1} \left(\frac{y - \beta x}{\sqrt{1 - x^2} \sqrt{1 - \beta^2}} \right) \\
 &\quad + y \tan^{-1} \left(\frac{x - y \beta}{\sqrt{t}} \right) \\
 &\quad + \frac{1}{2} \tan^{-1} \left(\frac{1 - y^2 - \beta^2 - x + y \beta(1 + x)}{(y - \beta) \sqrt{t}} \right) \\
 &\quad - \frac{1}{2} \tan^{-1} \left(\frac{1 - y^2 - \beta^2 + x - y \beta(1 - x)}{(y + \beta) \sqrt{t}} \right) + C \\
 &\equiv K(x; y) + C,
 \end{aligned} \tag{B.24}$$

where it is understood that $K(x; y)$ is a function of β and where

$$t = (1 - x^2)(1 - \beta^2) - (y - \beta x)^2. \tag{B.25}$$

The full results are then in the form of 1-dimensional integrals over these sums of elementary functions. The fact that an analytic integral can be performed for any value of y means that we can calculate the Radon transform for any values of the θ' bin edges and therefore extend the method up to any value of N .

Bibliography

- [1] B. J. Kavanagh and A. M. Green, Phys. Rev. D **86** (2012), arXiv:1207.2039 .
- [2] B. J. Kavanagh, Phys. Rev. D **89** (2014), arXiv:1312.1852 .
- [3] A. G. Riess, *et al.*, Astrophys. J. **116**, 1009 (1998), astro-ph/9805201 .
- [4] S. Perlmutter, *et al.*, Astrophys. J. **517**, 565 (1999), astro-ph/9812133 .
- [5] E. W. Kolb and M. S. Turner, *The Early Universe* (Addison-Wesley, Reading, Massachusetts, 1990) Chap. 9.
- [6] G. R. Blumenthal, S. M. Faber, J. R. Primack, and M. J. Rees, Nature **311**, 517 (1984).
- [7] G. Hinshaw, *et al.*, Astrophys. J. Suppl. Ser. **208**, 19+ (2013).
- [8] C. J. MacTavish, *et al.*, Astrophys. J. **647**, 799 (2005), astro-ph/0507503 .
- [9] K. S. Dawson, *et al.*, Astron. J. **145**, 10+ (2013).
- [10] P. A. R. Ade, *et al.* (BICEP2 Collaboration), (2014), arXiv:1403.3985 .
- [11] T. D. Kitching, *et al.*, (2014), arXiv:1401.6842 .
- [12] L. Fu, *et al.*, “CFHTLenS: Cosmological constraints from a combination of cosmic shear two-point and three-point correlations,” (2014), arXiv:1404.5469 .
- [13] W. J. Percival, *et al.*, Mon. Not. R. Astron. Soc. **327**, 1297 (2001).

- [14] D. G. York, *et al.*, Astron. J. **120**, 1579 (2000), arXiv:astro-ph/0006396 .
- [15] N. Suzuki, *et al.*, Astrophys. J. **746**, 85+ (2011), arXiv:1105.3470 .
- [16] P. A. R. Ade *et al.* (Planck Collaboration), (2013), arXiv:1303.5062 .
- .
- [17] P. A. R. Ade *et al.* (Planck Collaboration), Astron. Astrophys. (2014), arXiv:1303.5076 .
- [18] F. Zwicky, Helv. Phys. Acta. **6**, 110 (1933).
- [19] J. S. Sanders, A. C. Fabian, E. Churazov, A. A. Schekochihin, A. Simionescu, S. A. Walker, and N. Werner, Science **341**, 1365 (2013), arXiv:1309.4866 .
- [20] R. Fusco-Femiano and J. P. Hughes, Astrophys. J. **429**, 545+ (1994).
- [21] N. Makino, Publ. Astron. Soc. Jpn. **46**, 139 (1994).
- [22] N. Okabe, G. P. Smith, K. Umetsu, M. Takada, and T. Futamase, Astrophys. J. **769**, L35 (2013), arXiv:1302.2728 .
- [23] S. Ettori, A. Donnarumma, E. Pointecouteau, T. H. Reiprich, S. Giordini, L. Lovisari, and R. W. Schmidt, Space Sci. Rev. **177**, 119 (2013), arXiv:1303.3530 .
- [24] R. G. Carlberg, H. K. C. Yee, E. Ellingson, R. Abraham, P. Gravel, S. Morris, and C. J. Pritchett, Astrophys. J. **462**, 32+ (1996), arXiv:astro-ph/9509034 .
- [25] V. Springel, *et al.*, Nature **435**, 629 (2005), arXiv:astro-ph/0504097 .
- .
- [26] J. Diemand, M. Kuhlen, and P. Madau, Astrophys. J. **657**, 262 (2006), astro-ph/0611370 .
- [27] V. Springel, J. Wang, M. Vogelsberger, A. Ludlow, A. Jenkins, A. Helmi, J. F. Navarro, C. S. Frenk, and S. D. M. White, Mon. Not. R. Astron. Soc. **391**, 1685 (2008), arXiv:0809.0898 .

- [28] P. Mollitor, E. Nezri, and R. Teyssier, “Baryonic and dark matter distribution in cosmological simulations of spiral galaxies,” (2014), arXiv:1405.4318 .
- [29] M. Vogelsberger, S. Genel, V. Springel, P. Torrey, D. Sijacki, D. Xu, G. Snyder, S. Bird, D. Nelson, and L. Hernquist, *Nature* **509**, 177 (2014), arXiv:1405.1418 .
- [30] M. Vogelsberger, S. Genel, D. Sijacki, P. Torrey, V. Springel, and L. Hernquist, *Mon. Not. R. Astron. Soc.* **436**, 3031 (2013), arXiv:1305.2913 .
- [31] D. Martizzi, R. Teyssier, B. Moore, and T. Wentz, *Mon. Not. R. Astron. Soc.* **422** (2012), arXiv:1112.2752 .
- [32] A. Pillepich, M. Kuhlen, J. Guedes, and P. Madau, *Astrophys. J.* **784**, 161+ (2014), arXiv:1308.1703 .
- [33] G. Stinson, J. Bailin, H. Couchman, J. Wadsley, S. Shen, C. Brook, and T. Quinn, *Mon. Not. R. Astron. Soc.* **408**, 812 (2010), arXiv:1004.0675 .
- [34] M. L. Norman and G. L. Bryan, “Cosmological adaptive mesh refinement,” in *Numerical Astrophysics 1998*, Vol. 240, edited by S. M. Miyama, K. Tomisaka, and T. Hanawa (Springer Netherlands, Dordrecht, 1999) Chap. 3, pp. 19–28, arXiv:astro-ph/9807121 .
- [35] V. Springel, *Mon. Not. R. Astron. Soc.* **401**, 791 (2010), arXiv:0901.4107 .
- [36] G. Lemson and V. Consortium, “Halo and galaxy formation histories from the millennium simulation: Public release of a VO-oriented and SQL-queryable database for studying the evolution of galaxies in the LambdaCDM cosmogony,” (2006), arXiv:astro-ph/0608019 .
- [37] K. Begeman, A. Broeils, and R. Sanders, *Mon. Not. R. Astron. Soc.* **249**, 523 (1991).
- [38] M. Persic, P. Salucci, and F. Stel, *Mon. Not. R. Astron. Soc.* **281**, 27 (1996), astro-ph/9506004 .
- [39] A. Bosma, *Astron. J.* **86**, 1791+ (1981).

- [40] A. Bosma, *Astron. J.* **86**, 1825+ (1981).
- [41] A. J. Deason, V. Belokurov, N. W. Evans, and J. An, *Mon. Not. R. Astron. Soc.: Lett.* **424**, L44 (2012), arXiv:1204.5189 .
- [42] M. López-Corredoira, *Astron. Astrophys.* **563**, A128+ (2014), arXiv:1402.3551 .
- [43] P. Bhattacharjee, S. Chaudhury, and S. Kundu, *Astrophys. J.* **785**, 63+ (2014), arXiv:1310.2659 .
- [44] G. Kauffmann, S. D. White, and B. Guiderdoni, *Mon. Not. R. Astron. Soc.* **264**, 201 (1993).
- [45] M. G. Walker, M. Mateo, E. W. Olszewski, J. Peñarrubia, N. W. Evans, and G. Gilmore, *Astrophys. J.* **704**, 1274+ (2009).
- [46] V. Belokurov, *et al.*, *Astrophys. J. Lett.* **712**, L103 (2010), arXiv:1002.0504 .
- [47] A. Klypin, A. V. Kravtsov, O. Valenzuela, and F. Prada, *Astrophys. J.* **522**, 82 (1999).
- [48] M. Boylan-Kolchin, J. S. Bullock, and M. Kaplinghat, *Mon. Not. R. Astron. Soc. Lett.* **415**, L40 (2011), arXiv:1103.0007 .
- [49] S. Garrison-Kimmel, M. Boylan-Kolchin, J. S. Bullock, and E. N. Kirby, (2014), arXiv:1404.5313 .
- [50] W. J. G. de Blok, *Adv. Astron.* **2010**, 1 (2010), arXiv:0910.3538 .
- [51] J. Dubinski and R. G. Carlberg, *Astrophys. J.* **378**, 496+ (1991).
- [52] J. F. Navarro, C. S. Frenk, and S. D. M. White, *Astrophys. J.* **462**, 563+ (1996), arXiv:astro-ph/9508025 .
- [53] P. Salucci, *Mon. Not. R. Astron. Soc.* **320**, L1 (2001).
- [54] F. Donato, G. Gentile, and P. Salucci, *Mon. Not. R. Astron. Soc.* **353**, L17 (2004), arXiv:astro-ph/0403206 .
- [55] E. Hayashi, J. F. Navarro, C. Power, A. Jenkins, C. S. Frenk, S. D. M. White, V. Springel, J. Stadel, and T. R. Quinn, *Mon. Not. R. Astron. Soc.* **355**, 794 (2004), arXiv:astro-ph/0310576 .

- [56] M. Gritschneider and D. N. C. Lin, *Astrophys. J.* **765**, 38+ (2013).
- [57] N. C. Amorisco, J. Zavala, and T. J. L. de Boer, *Astrophys. J.* **782**, L39+ (2014), arXiv:1309.5958 .
- [58] A. Del Popolo, J. A. S. Lima, J. C. Fabris, and D. C. Rodrigues, “A unified solution to the small scale problems of the λ cdm model,” (2014), arXiv:1404.3674 .
- [59] B. Moore, T. Quinn, F. Governato, J. Stadel, and G. Lake, *Mon. Not. R. Astron. Soc.* **310**, 1147 (1999), astro-ph/9903164 .
- [60] P. Bode, J. P. Ostriker, and N. Turok, *Astrophys. J.* **556**, 93 (2001), astro-ph/0010389 .
- [61] A. V. Macciò and F. Fontanot, *Mon. Not. R. Astron. Soc. Lett.* **404**, L16 (2010).
- [62] M. Milgrom, *Astrophys. J.* **270**, 365 (1983).
- [63] M. Milgrom, *Astrophys. J.* **270**, 371+ (1983).
- [64] M. Milgrom, *Astrophys. J.* **270**, 384+ (1983).
- [65] O. Y. Gnedin, D. H. Weinberg, J. Pizagno, F. Prada, and H.-W. Rix, *Astrophys. J.* , 1115+ (2007).
- [66] S. S. McGaugh, *Astrophys. J.* **632**, 859 (2005), arXiv:astro-ph/0506750 .
- [67] J. D. Bekenstein, *Phys. Rev. D* **70**, 083509+ (2005), arXiv:astro-ph/0403694 .
- [68] M.-C. Chiu, C.-M. Ko, and Y. Tian, *Astrophys. J.* **636**, 565 (2005), arXiv:astro-ph/0507332 .
- [69] C. Skordis, *Phys. Rev. D* **74** (2006).
- [70] R. H. Sanders, *Astrophys. J.* **473**, 117 (1996), arXiv:astro-ph/9606089 .
- [71] W. J. G. de Blok and S. S. McGaugh, *Astrophys. Jo.* **508**, 132 (1998), arXiv:astro-ph/9805120 .

- [72] R. H. Sanders and S. S. McGaugh, Ann. Rev. Astron. Astrophys. **40**, 263 (2002), arXiv:astro-ph/0204521 .
- [73] G. W. Angus, H. Shan, H. Zhao, and B. Famaey, Astrophys. J. **654**, L13 (2006), arXiv:astro-ph/0609125 .
- [74] S. Dodelson and M. Liguori, Phys. Rev. Lett. **97** (2006), arXiv:astro-ph/0608602 .
- [75] A. Slosar, A. Melchiorri, and J. Silk, Phys. Rev. D **72**, 101301 (2005), arXiv:astro-ph/0508048 .
- [76] C. Skordis, D. F. Mota, P. G. Ferreira, and C. Boehm, Phys. Rev. Lett. **96** (2006), arXiv:astro-ph/0505519 .
- [77] J. Zuntz, T. G. Zlosnik, F. Bourliot, P. G. Ferreira, and G. D. Starkman, Phys. Rev. D **81** (2010), arXiv:1002.0849 .
- [78] A. Kudo and M. Yamaguchi, Phys. Lett. B **516**, 151 (2001).
- [79] M. L. Perl, P. C. Kim, V. Halyo, E. R. Lee, I. T. Lee, D. Loomba, and K. S. Lackner, Int. J. Mod. Phys. A **16**, 2137 (2001), hep-ex/0102033 .
- [80] S. N. Gninenko, N. V. Krasnikov, and A. Rubbia, Phys. Rev. D **75**, 075014 (2007), hep-ph/0612203 .
- [81] A. Melchiorri, A. Polosa, and A. Strumia, Phys. Lett. B **650**, 416 (2007), hep-ph/0703144 .
- [82] P. Natarajan, A. Loeb, J.-P. Kneib, and I. Smail, Astrophys. J. **580**, L17 (2002), astro-ph/0207045 .
- [83] X. Chen, S. Hannestad, and R. J. Scherrer, Phys. Rev. D **65**, 123515 (2002), astro-ph/0202496 .
- [84] S. D. L. Amigo, W. M. Cheung, Z. Huang, and S.-P. Ng, J. Cosmol. Astropart. Phys. **2009**, 005 (2009), arXiv:0812.4016 .
- [85] N. F. Bell, A. J. Galea, and K. Petraki, Phys. Rev. D **82** (2010), arXiv:1004.1008 .
- [86] M. Taoso, G. Bertone, and A. Masiero, J. Cosmol. Astropart. Phys. **03**, 022 (2008), arXiv:0711.4996 .

- [87] D. Feldman, Z. Liu, P. Nath, and G. Peim, Phys. Rev. D **81**, 095017 (2010), arXiv:1004.0649 .
- [88] G. Gelmini and P. Gondolo, “DM production mechanisms,” in *Particle Dark Matter*, edited by G. Bertone (Cambridge University Press, Cambridge, 2010) Chap. 7, pp. 121–141, arXiv:1009.3690 .
- [89] K. Griest, Phys. Rev. D **43**, 3191 (1991).
- [90] L. J. Hall, K. Jedamzik, J. March-Russell, and S. M. West, J. High Energy Phys. **2010** (2010), arXiv:0911.1120 .
- [91] D. J. H. Chung, E. W. Kolb, and A. Riotto, Phys. Rev. D **59** (1998), hep-ph/9802238 .
- [92] V. A. Kuzmin and I. I. Tkachev, JETP Lett. **68**, 271 (1998), hep-ph/9802304 .
- [93] T. Gherghetta, G. F. Giudice, and J. D. Wells, Nucl. Phys. B **559**, 27 (1999), hep-ph/9904378 .
- [94] J. R. Bond and A. S. Szalay, Astrophys. J. **274**, 443 (1983).
- [95] D. Boyanovsky, H. J. de Vega, and N. Sanchez, Phys. Rev. D **78** (2008), arXiv:0807.0622 .
- [96] O. Wantz and E. P. S. Shellard, Phys. Rev. D **82**, 123508 (2011), arXiv:0910.1066 .
- [97] V. K. Narayanan, D. N. Spergel, R. Davé, and C.-P. Ma, The Astrophysical Journal **543**, L103 (2000), astro-ph/0005095 .
- [98] K. Abazajian, E. R. Switzer, S. Dodelson, K. Heitmann, and S. Habib, Phys. Rev. D **71**, 043507 (2005), astro-ph/0411552 .
- [99] R. de Putter, *et al.*, Astrophys. J. **761**, 12+ (2012), arXiv:1201.1909 .
- [100] D. Tytler, J. M. O’Meara, N. Suzuki, and D. Lubin, Physica Scripta **T85**, 12+ (2000), arXiv:astro-ph/0001318 .
- [101] B. Fields and S. Sarkar, J. Phys. G. **33**, 1 (2006), astro-ph/0601514 .
- [102] M. Maggiore, Phys. Rep. **331**, 283 (2000), gr-qc/9909001 .

- [103] R. H. Cyburt, B. D. Fields, K. A. Olive, and E. Skillman, *J. Astropart. Phys.* **23**, 313 (2005), astro-ph/0408033 .
- [104] K. Jedamzik, *Phys. Rev. D* **74** (2006), hep-ph/0604251 .
- [105] G. Jungman, M. Kamionkowski, and K. Griest, *Phys. Rep.* **267**, 195 (1995), hep-ph/9506380 .
- [106] G. L. Kane and S. P. Martin, “A supersymmetry primer,” in *Perspectives on Supersymmetry II*, Vol. 21 (WORLD SCIENTIFIC, Singapore, 2011) pp. 1–153, hep-ph/9709356 .
- [107] J. Ellis, J. S. Hagelin, D. V. Nanopoulos, K. Olive, and M. Srednicki, *Nucl. Phys. B* **238**, 453 (1984).
- [108] B. Shakya, “The status of neutralino dark matter,” (2013), arXiv:1312.7505 .
- [109] K.-Y. Choi and O. Seto, *Phys. Rev. D* **88**, 035005 (2013), arXiv:1305.4322 .
- [110] F. D. Steffen, *J. Cosmol. Astropart. Phys.* **2006**, 001 (2006), arXiv:hep-ph/0605306 .
- [111] M. J. Duff, “Kaluza-Klein theory in perspective,” (1994), hep-th/9410046 .
- [112] T. Appelquist, H.-C. Cheng, and B. A. Dobrescu, *Phys. Rev. D* **64**, 035002 (2001), hep-ph/0012100 .
- [113] H.-C. Cheng, K. T. Matchev, and M. Schmaltz, *Phys. Rev. D* **66**, 036005 (2002), hep-ph/0204342 .
- [114] G. Servant and T. M. P. Tait, *Nucl. Phys. B* **650**, 391 (2002), hep-ph/0206071 .
- [115] L. Bergström, *New J. Phys.*, New Journal of Physics **11**, 105006+ (2009), arXiv:0903.4849 .
- [116] C. Amsler, *et al.*, *Phys. Lett. B* **667**, 1 (2008).
- [117] S. Dodelson and L. Widrow, *Phys. Rev. Lett.* **72**, 17 (1994), hep-ph/9303287 .

- [118] X. Shi and G. M. Fuller, Phys. Rev. Lett. **82**, 2832 (1999), astro-ph/9810076 .
- [119] T. Asaka, M. Shaposhnikov, and A. Kusenko, Phys. Lett. B **638**, 401 (2006), hep-ph/0602150 .
- [120] S. H. Hansen, J. Lesgourgues, S. Pastor, and J. Silk, Mon. Not. R. Astron. Soc. **333**, 544 (2002), arXiv:astro-ph/0106108 .
- [121] K. Abazajian and S. M. Koushiappas, Phys. Rev. D **74** (2006), arXiv:astro-ph/0605271 .
- [122] R. D. Peccei and H. R. Quinn, Phys. Rev. Lett. **38**, 1440 (1977).
- [123] G. Raffelt, “Axions in astrophysics and cosmology,” (1995), hep-ph/9502358 .
- [124] P. Sikivie and Q. Yang, Phys. Rev. Lett. **103** (2009), arXiv:0901.1106 .
- [125] A. Arvanitaki, S. Dimopoulos, S. Dubovsky, N. Kaloper, and J. March-Russell, Phys. Rev. D **81** (2010), arXiv:0905.4720 .
- [126] G. Rybka (ADMX collaboration), Phys. Dark Univ. (2014).
- [127] M. Arik, *et al.*, Phys. Rev. Lett. **112** (2013), arXiv:1307.1985 .
- [128] S. W. Hawking, Mon. Not. R. Astron. Soc. **152**, 75 (1971).
- [129] B. J. Carr and S. W. Hawking, Mon. Not. R. Astron. Soc. **168**, 399 (1974).
- [130] B. J. Carr, K. Kohri, Y. Sendouda, and J. Yokoyama, Phys. Rev. D **81** (2010), arXiv:0912.5297 .
- [131] B. J. Carr and M. Sakellariadou, Astrophys. J. **516**, 195 (1999).
- [132] K. Griest, A. M. Cieplak, and M. J. Lehner, Phys. Rev. Lett. **111** (2013).
- [133] P. Pani and A. Loeb, “Tidal capture of a primordial black hole by a neutron star: implications for constraints on dark matter,” (2014), arXiv:1401.3025 .

- [134] J. Kumar, J. L. Feng, G. Alverson, P. Nath, and B. Nelson, AIP Conf. Proc. **1200**, 1059 (2010), arXiv:0909.2877 .
- [135] R. Foot, Int. J. Mod. Phys. A **29**, 1430013+ (2014), arXiv:1401.3965 .
- [136] A. Birkedal, A. Noble, M. Perelstein, and A. Spray, Phys. Rev. D **74** (2006), arXiv:hep-ph/0603077 .
- [137] M. Cirelli, N. Fornengo, and A. Strumia, Nucl. Phys. B **753**, 178 (2007), arXiv:hep-ph/0512090 .
- [138] L. Edelhäuser, T. Flacke, and M. Krämer, J. High Energy Phys. **2013** (2013), arXiv:1302.6076 .
- [139] T. Kakuda, K. Nishiwaki, K.-y. Oda, N. Okuda, and R. Watanabe, “Phenomenological constraints on universal extra dimensions at LHC and electroweak precision test,” (2013), arXiv:1304.6362 .
- [140] ATLAS Collaboration, https://atlas.web.cern.ch/Atlas/GROUPS/PHYSICS/CombinedSummaryPlots/SUSY/ATLAS_SUSY_Summary/ATLAS_SUSY_Summary.pdf (2013).
- [141] CMS Collaboration, https://twiki.cern.ch/twiki/pub/CMSPublic/SUSYSMSSummaryPlots8TeV/barplot_blue_orange_SUSY2013.pdf (2013).
- [142] H. Zhang, Q.-H. Cao, C.-R. Chen, and C. S. Li, J. High Energy Physics **2011** (2011), arXiv:0912.4511 .
- [143] N. Zhou, D. Berge, and D. Whiteson, Phys. Rev. D **87**, 095013 (2013), arXiv:1302.3619 .
- [144] P. J. Fox, R. Harnik, J. Kopp, and Y. Tsai, Phys. Rev. D **85**, 056011+ (2011), arXiv:1109.4398 .
- [145] H. Baer, E.-K. Park, and X. Tata, New J. Phys. **11**, 105024+ (2009), arXiv:0903.0555 .
- [146] O. Buchmueller, M. J. Dolan, and C. McCabe, J. High Energy Phys. **2014** (2014), arXiv:1308.6799 .
- [147] G. Busoni, A. De Simone, E. Morgante, and A. Riotto, Phys. Lett. B **728**, 412 (2013), arXiv:1307.2253 .

- [148] S. A. Malik (CMS collaboration), “Search for dark matter at the LHC using missing transverse energy,” (2012), arXiv:1206.0753 .
- [149] P. Bechtle, *et al.*, Journal of High Energy Physics **2012** (2012), arXiv:1204.4199 .
- [150] P. Bechtle, *et al.*, “Constrained supersymmetry after the higgs boson discovery: A global analysis with fittino,” (2013), arXiv:1310.3045 .
- [151] B. Barish and J. E. Brau, Int. J. Mod. Phys. A **28**, 1330039+ (2013), arXiv:1311.3397 .
- [152] D. Schmeier, “Effective models for dark matter at the international linear collider,” (2013), arXiv:1308.4409 .
- [153] Y. J. Chae and M. Perelstein, Journal of High Energy Physics **2013** (2013), arXiv:1211.4008 .
- [154] M. Ackermann, *et al.* (Fermi-LAT), Physical Review D **86**, 022002 (2012), arXiv:1205.2739 .
- [155] M. Boezio, *et al.*, New J. Phys. **11**, 105023+ (2009).
- [156] M. Aguilar, *et al.* (AMS Collaboration), Physical Review Letters **110** (2013).
- [157] O. Adriani, G. C. Barbarino, G. A. Bazilevskaya, R. Bellotti, M. Boezio, E. A. Bogomolov, L. Bonechi, M. Bongi, V. Bonvicini, and S. Borisov, Astropart. Phys. **34**, 1 (2010).
- [158] M. Ackermann, *et al.*, Phys. Rev. Lett. **108**, 011103+ (2012).
- [159] A. Ibarra, A. S. Lamperstorfer, and J. Silk, Phys. Rev. D **89**, 063539 (2014), arXiv:1309.2570 .
- [160] G. A. Medina Tanco, E. M. de Gouveia Dal Pino, and J. E. Horvath, Astrophys. J. **492**, 200 (1998).
- [161] J. Lavalle, Q. Yuan, D. Maurin, and X. J. Bi, Astron. Astrophys. **479**, 427 (2008), arXiv:0709.3634 .
- [162] M. Ackermann, *et al.* (Fermi-LAT Collaboration), Phys. Rev. D **89**, 042001 (2014), arXiv:1310.0828 .

- [163] C. Weniger, J. Cosmol. Astropart. Phys. **2012**, 007 (2012), arXiv:1204.2797 .
- [164] E. Bloom, E. Charles, E. Izaguirre, A. Snyder, A. Albert, B. Winer, Z. Yang, and R. Essig, “Search of the earth limb fermi data and Non-Galactic center region fermi data for signs of narrow lines,” (2013), arXiv:1303.2733 .
- [165] W. Buchmüller and M. Garny, J. Cosmol. Astropart. Phys. **2012**, 035 (2012), arXiv:1206.7056 .
- [166] T. Cohen, M. Lisanti, T. R. Slatyer, and J. G. Wacker, J. High Energy Phys. **2012** (2012), arXiv:1207.0800 .
- [167] L. Goodenough and D. Hooper, “Possible evidence for dark matter annihilation in the inner milky way from the fermi gamma ray space telescope,” (2009), arXiv:0910.2998 .
- [168] D. Hooper and L. Goodenough, Phys. Lett. B **697**, 412 (2011), arXiv:1010.2752 .
- [169] A. Boyarsky, D. Malyshev, and O. Ruchayskiy, Phys. Lett. B **705**, 165 (2010), arXiv:1012.5839 .
- [170] K. N. Abazajian, J. Cosmol. Astropart. Phys. **2011**, 010 (2011), arXiv:1011.4275 .
- [171] T. Daylan, D. P. Finkbeiner, D. Hooper, T. Linden, S. K. N. Portillo, N. L. Rodd, and T. R. Slatyer, “The characterization of the Gamma-Ray signal from the central milky way: A compelling case for annihilating dark matter,” (2014), arXiv:1402.6703 .
- [172] A. Abramowski, *et al.* (H.E.S.S. Collaboration), Phys. Rev. Lett. **110** (2013), arXiv:1301.1173 .
- [173] J. Aleksić, *et al.*, J. Cosmol. Astropart. Phys. **2014**, 008 (2014), arXiv:1312.1535 .
- [174] V. A. Acciari, *et al.*, Astrophys. J. **720**, 1174 (2010), arXiv:1006.5955 .
- [175] M. Doro, *et al.*, J. Astropart. Phys. **43**, 189 (2013).

- [176] J. Zornoza, Nucl. Instrum. Methods **725**, 76 (2013), arXiv:1204.5290 .
- [177] M. G. Aartsen, *et al.* (IceCube Collaboration), “The IceCube neutrino observatory part IV: Searches for dark matter and exotic particles,” (2013), arXiv:1309.7007 .
- [178] M. W. Goodman and E. Witten, Phys. Rev. D **31**, 3059 (1985).
- [179] A. K. Drukier, K. Freese, and D. N. Spergel, Phys. Rev. D **33**, 3495 (1986).
- [180] R. Bernabei, *et al.*, Eur. Phys. J. C **67**, 39 (2010), arXiv:1002.1028 .
- [181] C. Aalseth, *et al.* (CoGeNT Collaboration), Phys. Rev. Lett. **106**, 131301+ (2011).
- [182] C. E. Aalseth, *et al.*, Phys. Rev. Lett. **107**, 141301+ (2011), arXiv:1106.0650 .
- [183] L. Stodolsky, *et al.*, J. Phys.: Conf. Ser. **384**, 012013+ (2012), arXiv:1203.6835 .
- [184] D. S. Akerib, *et al.* (LUX Collaboration), Phys. Rev. Lett. **112** (2014), arXiv:1310.8214 .
- [185] D. G. Cerdeño and A. M. Green, “Direct detection of WIMPs,” in *Particle Dark Matter*, edited by G. Bertone and G. Bertone (Cambridge University Press, Cambridge, 2010) Chap. 17, pp. 347–369, arXiv:1002.1912 .
- [186] A. Kurylov and M. Kamionkowski, Phys. Rev. D **69**, 063503 (2003), arXiv:hep-ph/0307185 .
- [187] K. Freese, J. Frieman, and A. Gould, Phys. Rev. D **37**, 3388 (1988).
- [188] A. L. Fitzpatrick, W. Haxton, E. Katz, N. Lubbers, and Y. Xu, J. Cosmol. Astropart. Phys. **2013**, 004 (2013), arXiv:1203.3542 .
- [189] J. M. Alarcón, J. M. Camalich, and J. A. Oller, Phys. Rev. D **85**, 051503 (2012), arXiv:1110.3797 .
- [190] G. S. Bali, *et al.* (QCDSF Collaboration), Phys. Rev. D **85**, 054502 (2012), arXiv:1111.1600 .

- [191] M. Shifman, A. Vainshtein, and V. Zakharov, Phys. Lett. B **78**, 443 (1978).
- [192] J. Engel, Phys. Lett. B **264**, 114 (1991).
- [193] J. Engel, S. Pittel, and P. Vogel, Int. J. Mod. Phys. E **01**, 1 (1992).
- [194] M. C. Smith, *et al.*, Mon. Not. R. Astron. Soc. **379**, 755 (2007), astro-ph/0611671 .
- [195] T. Piffl, *et al.*, Astron. Astrophys. **562**, A91+ (2014), arXiv:1309.4293 .
- [196] R. Helm, Phys. Rev. **104**, 1466 (1956).
- [197] M. Ressell and D. Dean, Phys. Rev. C **56**, 535 (1997), hep-ph/9702290 .
- [198] S. Scholl and J. Jochum, J. Phys.: Conf. Ser. **375**, 012020+ (2012).
- [199] E. Aprile, *et al.*, J. Phys. G **40**, 115201+ (2013), arXiv:1306.2303 .
- [200] A. Münster, *et al.*, “Radiopurity of CaWO₄ crystals for direct dark matter search with CRESST and EURECA,” (2014), arXiv:1403.5114 .
- [201] R. Bernabei, *et al.*, Nucl. Instrum. Methods A **592**, 297 (2008), arXiv:0804.2738 .
- [202] M. Kuźniak, M. Boulay, and T. Pollmann, J. Astropart. Phys. **36**, 77 (2012), arXiv:1203.1576 .
- [203] C. Galbiati, *et al.*, J. Phys.: Conf. Ser. **120**, 042015+ (2008), arXiv:0712.0381 .
- [204] K. Abe, J. Hosaka, T. Iida, M. Ikeda, K. Kobayashi, Y. Koshio, A. Minamino, M. Miura, S. Moriyama, and M. Nakahata, Astropart. Phys. **31**, 290 (2009).
- [205] E. Aprile, T. Yoon, A. Loose, L. W. Goetzke, and T. Zelevinsky, Rev. Sci. Instrum. **84**, 093105+ (2013), arXiv:1305.6510 .
- [206] Z. Ahmed, *et al.*, Physical Review Letters **102**, 011301 (2009).
- [207] Z. Ahmed *et al.* (CDMS Collaboration), (2009), arXiv:0912.3592 .

- [208] Z. Ahmed, *et al.* (CDMS Collaboration), Phys. Rev. Lett. **106** (2011), arXiv:1011.2482 .
- [209] R. Agnese, *et al.*, Phys. Rev. Lett. **111** (2013), arXiv:1304.4279 .
- [210] G. Angloher, *et al.*, Eur. Phys. J. C **72** (2012), arXiv:1109.0702 .
- [211] C. E. Aalseth, *et al.*, Phys. Rev. D **88** (2013), arXiv:1208.5737 .
- [212] C. E. Aalseth, *et al.*, “Search for an annual modulation in three years of CoGeNT dark matter detector data,” (2014), arXiv:1401.3295 .
- [213] C. E. Aalseth, *et al.*, “Maximum likelihood signal extraction method applied to 3.4 years of CoGeNT data,” (2014), arXiv:1401.6234 .
- [214] E. Armengaud, *et al.*, Phys. Lett. B **702**, 329 (2011), arXiv:1103.4070 .
- [215] D. Akimov, *et al.*, Phys. Lett. B **709**, 14 (2012), arXiv:1110.4769 .
- [216] E. Aprile, *et al.* (XENON Collaboration), Phys. Rev. Lett. **107**, 131302+ (2011), arXiv:1104.2549 .
- [217] A. Marchionni, *et al.*, J. Phys.: Conf. Ser. **308**, 012006+ (2011), arXiv:1012.5967 .
- [218] A. Badertscher, *et al.*, J. Instrum. **8**, C09005+ (2013).
- [219] M. Boulay and B. Cai (DEAP/CLEAN Collaboration), Journal of Physics: Conference Series **136**, 042081+ (2008).
- [220] E. Behnke, *et al.*, Phys. Rev. Lett. **106**, 021303+ (2011).
- [221] M. Felizardo, *et al.* (SIMPLE Collaboration), Phys. Rev. Lett. **108** (2012), arXiv:1106.3014 .
- [222] S. Archambault, *et al.* (PICASSO Collaboration), Phys. Lett. B **711**, 153 (2012), arXiv:1202.1240 .
- [223] S. K. Kim, H. J. Kim, and Y. D. Kim, New J. Phys. **12**, 075003+ (2010).
- [224] R. Bernabei, *et al.*, Eur. Phys. J. C **56**, 333 (2008), arXiv:0804.2741 .

- [225] R. Bernabei, *et al.*, Eur. Phys. J. C **73** (2013), arXiv:1308.5109 .
- [226] H. S. Lee, *et al.*, Phys. Rev. Lett. **99** (2007), arXiv:0704.0423 .
- [227] B. Ahmed, *et al.*, J. Astropart. Phys. **19**, 691 (2003), arXiv:hep-ex/0301039 .
- [228] R. Bernabei, *et al.*, Riv. Nuovo Cimento **26**, 1 (2003), arXiv:astro-ph/0307403 .
- [229] P. Belli, R. Bernabei, A. Bottino, F. Cappella, R. Cerulli, N. Fornengo, and S. Scopel, Phys. Rev. D **84**, 055014 (2011), arXiv:1106.4667 .
- [230] C. Savage, G. Gelmini, P. Gondolo, and K. Freese, J. Cosmol. Astropart. Phys. **2009**, 010 (2009), arXiv:0808.3607 .
- [231] D. Hooper, J. I. Collar, J. Hall, D. McKinsey, and C. Kelso, Phys. Rev. D **82**, 123509+ (2010), arXiv:1007.1005 .
- [232] R. Agnese, *et al.*, “Search for Low-Mass WIMPs with SuperCDMS,” (2014), arXiv:1402.7137 .
- [233] J. H. Davis, C. McCabe, and C. Boehm, “Quantifying the evidence for dark matter in CoGeNT data,” (2014), arXiv:1405.0495 .
- [234] N. Bozorgnia, G. B. Gelmini, and P. Gondolo, J. Cosmol. Astropart. Phys. **2010**, 019 (2010), arXiv:1006.3110 .
- [235] K. Blum, “DAMA vs. the annually modulated muon background,” (2011), arXiv:1110.0857 .
- [236] R. Bernabei, *et al.*, Eur. Phys. J. C **72**, 1 (2012), arXiv:1202.4179 .
- [237] M. Fairbairn and T. Schwetz, J. Cosmol. Astropart. Phys. **2009**, 037 (2009), arXiv:0808.0704 .
- [238] J. Herrero-Garcia, T. Schwetz, and J. Zupan, Phys. Rev. Lett. **109** (2012), arXiv:1205.0134 .
- [239] P. J. Fox, J. Liu, and N. Weiner, Phys. Rev. D **83** (2011), arXiv:1011.1915 .

- [240] M. T. Frandsen, F. Kahlhoefer, C. McCabe, S. Sarkar, and K. Schmidt-Hoberg, J. Cosmol. Astropart. Phys. **2012**, 024 (2012), arXiv:1111.0292 .
- [241] M. R. Buckley and W. H. Lippincott, Phys. Rev. D **88**, 056003 (2013), arXiv:1306.2349 .
- [242] J. L. Feng, J. Kumar, D. Marfatia, and D. Sanford, Phys. Lett. B **703**, 124 (2011), arXiv:1102.4331 .
- [243] D. Smith and N. Weiner, Phys. Rev. D **64**, 043502 (2001), arXiv:hep-ph/0101138 .
- [244] R. Foot, Phys. Lett. B **728**, 45 (2014), arXiv:1305.4316 .
- [245] T. Schwetz and J. Zupan, J. Cosmol. Astropart. Phys. **2011**, 008 (2011), arXiv:1106.6241 .
- [246] E. Aprile, *et al.* (XENON Collaboration), Phys. Rev. Lett. **111** (2013), arXiv:1301.6620 .
- [247] E. Aprile, *et al.* (XENON Collaboration), Phys. Rev. Lett. **109**, 181301 (2013), arXiv:1207.5988 .
- [248] E. Aprile, “The Xenon1T dark matter search experiment,” in *Sources and Detection of Dark Matter and Dark Energy in the Universe*, Vol. 148, edited by D. Cline (Springer Netherlands, Dordrecht, 2012) Chap. 14, pp. 93–96, arXiv:1206.6288 .
- [249] P. Gorel, “Search for dark matter with liquid argon and pulse shape discrimination: Results from DEAP-1 and status of DEAP-3600,” (2014), arXiv:1406.0462 .
- [250] D. C. Malling, *et al.*, “After LUX: The LZ program,” (2011), arXiv:1110.0103 .
- [251] H. Kraus, *et al.*, Nucl. Phys. B: Proc. Suppl. **173**, 168 (2007).
- [252] S. Roth, C. Ciemniak, C. Coppi, F. Feilitzsch, A. Gütlein, C. Isaila, J. Lanfranchi, S. Pfister, W. Potzel, and W. Westphal, J. Opt. Mater. **31**, 1415 (2009), arXiv:0810.0423 .
- [253] L. Baudis (DARWIN consortium), J. Phys.: Conf. Ser. **375**, 012028+ (2012), arXiv:1201.2402 .

- [254] J. Monroe and P. Fisher, Phys. Rev. D **76** (2007), arXiv:0706.3019 .
- [255] J. Billard, E. Figueroa-Feliciano, and L. Strigari, Phys. Rev. D **89**, 023524 (2014), arXiv:1307.5458 .
- [256] A. Drukier, K. Freese, D. Spergel, C. Cantor, G. Church, and T. Sano, “New dark matter detectors using DNA for nanometer tracking,” (2012), arXiv:1206.6809 .
- [257] A. Lopez, A. Drukier, K. Freese, C. Kurdak, and G. Tarle, “New dark matter detector using nanoscale explosives,” (2014), arXiv:1403.8115 .
- [258] A. A. Aguilar-Arevalo, *et al.* (DAMIC Collaboration), “DAMIC: a novel dark matter experiment,” (2013), arXiv:1310.6688 .
- [259] P. deNiverville, D. McKeen, and A. Ritz, Phys. Rev. D **86**, 035022 (2012), arXiv:1205.3499 .
- [260] R. Essig, A. Manalaysay, J. Mardon, P. Sorensen, and T. Volansky, Phys. Rev. Lett. **109** (2012), arXiv:1206.2644 .
- [261] R. Essig, J. Mardon, and T. Volansky, Phys. Rev. D **85**, 076007 (2012), arXiv:1108.5383 .
- [262] B. Borasoy and Ulf-G, Phys. Lett. B **365**, 285 (1995), arXiv:hep-ph/9508354 .
- [263] M. M. Pavan, I. I. Strakovsky, R. L. Workman, and R. A. Arndt, “The pion-nucleon sigma term is definitely large: results from a G.W.u. analysis of pion nucleon scattering data,” (2001), arXiv:hep-ph/0111066 .
- [264] L. Alvarez-ruso, T. Ledwig, M. J. Vicente Vacas, and J. Martin-camalich, Int. J. Mod. Phys.: Conf. Ser. **26**, 1460089+ (2014), arXiv:1402.1031 .
- [265] J. Ashman, *et al.*, Phys. Lett. B **206**, 364 (1988).
- [266] R. L. Jaffe and A. Manohar, Nucl. Phys. B **337**, 509 (1990).
- [267] D. Adams, Phys. Rev. D **56**, 5330 (1997), arXiv:hep-ex/9702005 .
- [268] D. Qing, X.-S. Chen, and F. Wang, Phys. Rev. C **57**, R31 (1998).

- [269] A. Thomas, Phys. Rev. Lett. **101**, 102003+ (2008).
- [270] J. D. Lewin and P. F. Smith, Astropart. Phys. **6**, 87 (1996).
- [271] G. Fricke, C. Bernhardt, K. Heilig, L. Schaller, L. Schellenberg, E. Shera, and C. Dejager, At. Data. Nucl. Data Tables **60**, 177 (1995).
- [272] G. Dda, A. Kemper, and P. Gondolo, J. Cosmol. Astropart. Phys. **2007**, 012 (2007), arXiv:hep-ph/0608035 .
- [273] G. Co', V. De Donno, M. Anguiano, and A. M. Lallena, J. Cosmol. Astropart. Phys. **2012**, 010+ (2012).
- [274] C. Ya-Zheng, C. Jun-Mou, L. Yan-An, S. Hong, and L. Xue-Qian, Chin. Phys. C **36**, 505+ (2012).
- [275] M. Cannoni, Phys. Rev. D **87**, 075014 (2013), arXiv:1211.6050 .
- [276] J. Engel and P. Vogel, Phys. Rev. D **40**, 3132 (1989).
- [277] F. Iachello, L. M. Krauss, and G. Maino, Phys. Lett. B **254**, 220 (1991).
- [278] J. Ellis and R. A. Flores, Nucl. Phys. B **307**, 883 (1988).
- [279] D. G. Cerdeno, M. Fornasa, J.-H. Huh, and M. Peiro, Phys. Rev. D **87**, 023512 (2012), arXiv:1208.6426 .
- [280] J. Kumar, Int. J. Mod. Phys.: Conf. Ser. **10**, 115 (2012), arXiv:1201.0217 .
- [281] K. Hamaguchi, S. P. Liew, T. Moroi, and Y. Yamamoto, “Isospin-Violating dark matter with colored mediators,” (2014), arXiv:1403.0324 .
- [282] K. Schmidt-Hoberg, F. Staub, and M. W. Winkler, Phys. Lett. B **727**, 506 (2013), arXiv:1310.6752 .
- [283] H. An, L.-T. Wang, and H. Zhang, “Dark matter with \$t\$-channel mediator: a simple step beyond contact interaction,” (2014), arXiv:1308.0592 .

- [284] M. Pospelov and T. T. Veldhuis, Phys. Lett. B **480**, 181 (2000), arXiv:hep-ph/0003010 .
- [285] C. M. Ho and R. J. Scherrer, Phys. Lett. B **722**, 341 (2013), arXiv:1211.0503 .
- [286] J. Fan, M. Reece, and L.-T. Wang, J. Cosmol. Astropart. Phys. **2010**, 042 (2010), arXiv:1008.1591 .
- [287] M. Cirelli, E. D. Nobile, and P. Panci, J. Cosmol. Astropart. Phys. **2013**, 019 (2013), arXiv:1307.5955 .
- [288] R. Catena and P. Ullio, J. Cosmol. Astropart. Phys. **2010**, 004 (2010), arXiv:0907.0018 .
- [289] M. Weber and W. de Boer, Astron. Astrophys. **509**, A25+ (2010), arXiv:0910.4272 .
- [290] F. Nesti and P. Salucci, J. Cosmol. Astropart. Phys. **07**, 016 (2013), arXiv:1304.5127 .
- [291] S. Garbari, C. Liu, J. I. Read, and G. Lake, Mon. Not. R. Astron. Soc. **425**, 1445 (2012), arXiv:1206.0015 .
- [292] F. Iocco, M. Pato, G. Bertone, and P. Jetzer, J. Cosmol. Astropart. Phys. **11**, 029 (2011), arXiv:1107.5810 .
- [293] P. Salucci, F. Nesti, G. Gentile, and C. Frigerio Martins, Astron. Astrophys. **523**, A83+ (2010), arXiv:1003.3101 .
- [294] C. Moni Bidin, G. Carraro, R. A. Méndez, and R. Smith, Astrophys. J. **751**, 30+ (2012), arXiv:1204.3924 .
- [295] J. Bovy and S. Tremaine, Astrophys. J. **756**, 89 (2012), arXiv:1205.4033 .
- [296] J. I. Read, “The local dark matter density,” (2014), arXiv:1404.1938 .
- [297] A. M. Green, Mod. Phys. Lett. A **27**, 1230004 (2012), arXiv:1112.0524 .
- [298] F. J. Kerr and D. Lynden-Bell, Mon. Not. R. Astron. Soc. **221**, 1023 (1986).

- [299] M. Feast and P. Whitelock, Mon. Not. R. Astron. Soc. **291**, 683 (1997), arXiv:astro-ph/9706293 .
- [300] R. Schönrich, Mon. Not. R. Astron. Soc. **427**, 274 (2012), arXiv:1207.3079 .
- [301] J. Bovy, *et al.*, Astrophys. J. **759**, 131+ (2012), arXiv:1209.0759 .
- [302] J. Binney and S. Tremaine, *Galactic dynamics*, 2nd ed. (Princeton University Press, Princeton, NJ, 2008).
- [303] N. W. Evans, C. M. Carollo, and P. T. de Zeeuw, Mon. Not. R. Astron. Soc. **318**, 1131 (2000), arXiv:astro-ph/0008156 .
- [304] L. M. Widrow, Astrophys. J. Suppl. Ser. **131**, 39 (2000).
- [305] M. Lisanti, L. E. Strigari, J. G. Wacker, and R. H. Wechsler, Phys. Rev. D **83**, 023519 (2011), arXiv:1010.4300 .
- [306] P. Bhattacharjee, S. Chaudhury, S. Kundu, and S. Majumdar, Phys. Rev. D **87**, 083525 (2013), arXiv:1210.2328 .
- [307] M. Fornasa and A. M. Green, Phys. Rev. D **89** (2013), arXiv:1311.5477 .
- [308] M. Vogelsberger, A. Helmi, V. Springel, S. D. M. White, J. Wang, C. S. Frenk, A. Jenkins, A. Ludlow, and J. F. Navarro, Mon. Not. R. Astron. Soc. **395**, 797 (2009), arXiv:0812.0362 .
- [309] M. Kuhlen, N. Weiner, J. Diemand, P. Madau, B. Moore, D. Potter, J. Stadel, and M. Zemp, J. Cosmol. Astropart. Phys. **02**, 030 (2010), arXiv:0912.2358 .
- [310] Y.-Y. Mao, L. E. Strigari, R. H. Wechsler, H.-Y. Wu, and O. Hahn, Astrophys. J. **764**, 35 (2012), arXiv:1210.2721 .
- [311] M. Kuhlen, M. Lisanti, and D. N. Spergel, Phys. Rev. D **86**, 063505 (2012), arXiv:1202.0007 .
- [312] K. Freese, P. Gondolo, H. Newberg, and M. Lewis, Phys. Rev. Lett. **92**, 111301 (2004).
- [313] A. Helmi, S. D. M. White, and V. Springel, Phys. Rev. D **66** (2002), arXiv:astro-ph/0201289 .

- [314] M. Vogelsberger, S. D. M. White, A. Helmi, and V. Springel, Mon. Not. R. Astron. Soc. **385**, 236 (2007), arXiv:0711.1105 .
- [315] J. I. Read, L. Mayer, A. M. Brooks, F. Governato, and G. Lake, Mon. Not. R. Astron. Soc. **397**, 44 (2009), arXiv:0902.0009 .
- [316] J. I. Read, *et al.*, AIP Conf. Proc. **1240**, 391 (2010), arXiv:0901.2938 .
- [317] A. M. Green, J. Cosmol. Astropart. Phys. **10**, 034 (2010), arXiv:1009.0916 .
- [318] A. H. G. Peter, Phys. Rev. D **83**, 125029 (2011), arXiv:1103.5145 .
- [319] M. Fairbairn, T. Douce, and J. Swift, J. Astropart. Phys. **47**, 45 (2013), arXiv:1206.2693 .
- [320] L. E. Strigari and R. Trotta, J. Cosmol. Astropart. Phys. **2009**, 019 (2009), arXiv:0906.5361 .
- [321] A. H. G. Peter, Phys. Rev. D **81**, 087301+ (2010), arXiv:0910.4765 .
- [322] C. Arina, G. Bertone, and H. Silverwood, Phys. Rev. D **88** (2013), arXiv:1304.5119 .
- [323] M. Pato, L. Baudis, G. Bertone, R. R. de Austri, L. E. Strigari, and R. Trotta, Phys. Rev. D **83** (2011), arXiv:1012.3458 .
- [324] M. Pato, L. E. Strigari, R. Trotta, and G. Bertone, J. Cosmol. Astropart. Phys. **2013**, 041 (2013), arXiv:1211.7063 .
- [325] M. Drees and C.-L. Shan, J. Cosmol. Astropart. Phys. **2007**, 011 (2007), arXiv:astro-ph/0703651 .
- [326] M. Drees and C.-L. Shan, J. Cosmol. Astropart. Phys. **2008**, 012+ (2008), arXiv:0803.4477 .
- [327] B. Feldstein and F. Kahlhoefer, “A new halo-independent approach to dark matter direct detection analysis,” (2014), arXiv:1403.4606 .
- [328] P. Gondolo and G. B. Gelmini, J. Cosmol. Astropart. Phys. **2012**, 015 (2012), arXiv:1202.6359 .

- [329] E. D. Nobile, G. Gelmini, P. Gondolo, and J.-H. Huh, *J. Cosmol. Astropart. Phys.* **2013**, 048 (2013), arXiv:1306.5273 .
- [330] E. Aprile, (2009), <http://xenon.astro.columbia.edu/> presentations/Aprile_SJTU09.pdf.
- [331] A. M. Szelc (WArP collaboration), *AIP Conf. Proc.* **1115**, 105 (2009).
- [332] T. Bruch (CDMS collaboration), (2010), arXiv:1001.3037 .
- [333] E. Aprile, L. Baudis, B. Choi, K. L. Giboni, K. Lim, A. Manalaysay, M. E. Monzani, G. Plante, R. Santorelli, and M. Yamashita, *Phys. Rev. C* **79**, 045807+ (2009), arXiv:0810.0274 .
- [334] A. Lewis and S. Bridle, *Phys. Rev. D* **66**, 103511 (2002), astro-ph/0205436 .
- [335] S. Kirkpatrick, C. D. Gelatt, and M. P. Vecchi, *Science* **220**, 671 (1983).
- [336] J. Skillingm, “Foundations and algorithms,” in *Bayesian Methods in Cosmology*, edited by M. P. Hobson, A. H. Jaffe, A. R. Liddle, P. Mukherjee, and D. Parkinson (Cambridge University Press, Cambridge, 2009) Chap. 1, pp. 3–32.
- [337] C. Sturge, R. Trotta, G. Bertone, A. H. G. Peter, and P. Scott, *Phys. Rev. D* **86**, 023507 (2012), arXiv:1201.3631 .
- [338] C. W. Purcell, J. S. Bullock, and M. Kaplinghat, *Astrophys. J.* **703**, 2275 (2009), arXiv:0906.5348 .
- [339] J. Diemand, M. Kuhlen, P. Madau, M. Zemp, B. Moore, D. Potter, and J. Stadel, *Nature* **454**, 735 (2008), arXiv:0805.1244 .
- [340] W. H. Press, S. A. Teukolsky, W. T. Vetterling, and B. P. Flannery, “Chebyshev approximation,” in *Numerical recipes : the art of scientific computing* (Cambridge University Press, Cambridge, 2007) Chap. 5.8, 3rd ed.
- [341] W. Gautschi, in *Recent advances in numerical analysis*, edited by C. De Boor and G. H. Golub (Academic Press, New York, 1978) pp. 45–72.

- [342] J. H. Wilkinson, in *Studies in numerical analysis*, edited by G. H. Golub (Mathematical Association of America, 1984) p. 3.
- [343] J. C. Mason and D. C. Handscomb, *Chebyshev polynomials*, 1st ed. (Chapman & Hall/CRC, 2002).
- [344] E. Aprile, “XENON1T at LNGS: Proposal April 2010,” www.bo.infn.it/xenon/docs/xe1t_proposal_v2.pdf (2010).
- [345] P. Benetti *et al.*, J. Astropart. Phys. **28**, 495 (2007), arXiv:astro-ph/0701286 .
- [346] L. Grandi, *WARP: an argon double phase technique for Dark Matter search*, Ph.D. thesis, Department of Nuclear and Theoretical Physics, University of Pavia (2005).
- [347] D. Bauer, “SuperCDMS SNOLAB,” <https://indico.fnal.gov/getFile.py/access?sessionId=1&resId=0&materialId=0&confId=6584> (2013).
- [348] D. Bauer, “SuperCDMS update,” www.fnal.gov/directorate/program_planning/all_experimenters_meetings/special_reports/Bauer_supercdms_status_02_04_13.pdf (2013).
- [349] F. Feroz and M. P. Hobson, Mon. Not. R. Astron. Soc. **384**, 449 (2007), arXiv:0704.3704 .
- [350] F. Feroz, M. P. Hobson, and M. Bridges, Mon. Not. R. Astron. Soc. **398**, 1601 (2008), arXiv:0809.3437 .
- [351] F. Feroz, M. P. Hobson, E. Cameron, and A. N. Pettitt, “Importance nested sampling and the MultiNest algorithm,” (2014), arXiv:1306.2144 .
- [352] G. Cowan, K. Cranmer, E. Gross, and O. Vitells, Eur. Phys. J. C **71**, 1 (2013), arXiv:1007.1727 .
- [353] S. S. Wilks, Ann. Math. Stat. **9**, 60 (1938).
- [354] G. Schwarz, Ann. Stat. **6**, 461 (1978).
- [355] A. Green and B. Morgan, Phys. Rev. D **77**, 027303 (2008).
- [356] W. H. Press and D. N. Spergel, Astrophys. J. **296**, 679+ (1985).

- [357] J. Silk, K. Olive, and M. Srednicki, Phys. Rev. Lett. **55**, 257 (1985).
- [358] T. Gaisser, G. Steigman, and S. Tilav, Phys. Rev. D **34**, 2206 (1986).
- [359] M. Srednicki, K. A. Olive, and J. Silk, Nucl. Phys. B **279**, 804 (1987).
- [360] K. Griest and D. Seckel, Nucl. Phys. B **283**, 681 (1987).
- [361] A. Gould, Astrophys. J. **321**, 571+ (1987).
- [362] A. Gould, Astrophys. J. **388**, 338+ (1992).
- [363] W. J. Kaufmann, *Universe* (W.H. Freeman, 1991).
- [364] A. Gould, Astrophys. J. **368**, 610+ (1991).
- [365] A. H. G. Peter, Phys. Rev. D **79**, 103532 (2009), arXiv:0902.1347 .
- [366] S. Sivertsson and J. Edsjo, Phys. Rev. D **85**, 123514 (2012), arXiv:1201.1895 .
- [367] A. Gould, Astrophys. J. **321**, 560+ (1987).
- [368] L. Krauss, M. Srednicki, and F. Wilczek, Phys. Rev. D **33**, 2079 (1986).
- [369] G. Busoni, A. De Simone, and W.-C. Huang, J. Cosmol. Astropart. Phys. **2013**, 010 (2013), arXiv:1305.1817 .
- [370] M. Blennow, J. Edsjo, and T. Ohlsson, J. Cosmol. Astropart. Phys. **2008**, 021+ (2008), arXiv:0709.3898 .
- [371] T. Sjöstrand, Computer Physics Communications **82**, 74 (1994).
- [372] P. Gondolo, J. Edsjo, P. Ullio, L. Bergstrom, M. Schelke, and E. A. Baltz, J. Cosmol. Astropart. Phys. **2004**, 008 (2004), arXiv:astro-ph/0406204 .
- [373] P. Gondolo, J. Edsjö, P. Ullio, L. Bergström, M. Schelke, E. Baltz, T. Bringmann, and G. Duda, <http://www.darksusy.org> (2014).
- [374] S. Adrian-Martinez *et al.* (ANTARES collaboration), J. Cosmol. Astropart. Phys. **2013**, 032 (2013).
- [375] R. Abbasi, *et al.* (IceCube collaboration), Phys. Rev. Lett. **102**, 201302 (2009), arXiv:0902.2460 .

- [376] R. Abbasi, *et al.*, Astropart. Phys. **35**, 615 (2012), arXiv:1109.6096 .
- [377] M. Aartsen, *et al.* (IceCube collaboration), Phys. Rev. Lett. **110** (2013), arXiv:1212.4097 .
- [378] K. Choi, C. Rott, and Y. Itow, J. Cosmol. Astropart. Phys. **2014**, 049 (2014), arXiv:1312.0273 .
- [379] M. T. Ressell, M. B. Aufderheide, S. D. Bloom, K. Griest, G. J. Mathews, and D. A. Resler, Phys. Rev. D **48**, 5519 (1993), arXiv:hep-ph/9307228 .
- [380] V. Dimitrov, J. Engel, and S. Pittel, Phys. Rev. D **51**, 291 (1995), hep-ph/9408246 .
- [381] J. Menéndez, D. Gazit, and A. Schwenk, Phys. Rev. D **86** (2012), arXiv:1208.1094 .
- [382] P. Scott, *et al.*, J. Cosmol. Astropart. Phys. **2012**, 057 (2012), arXiv:1207.0810 .
- [383] D. Cerdeño, *et al.*, J. Cosmol. Astropart. Phys. **2013**, 028 (2013), arXiv:1304.1758 .
- [384] M. Aartsen *et al.* (IceCube-PINGU collaboration), “Letter of intent: The precision IceCube next generation upgrade (PINGU),” (2014), arXiv:1401.2046 .
- [385] P. Gondolo, Phys. Rev. D **66** (2002), arXiv:hep-ph/0209110 .
- [386] C. J. Copi, J. Heo, and L. M. Krauss, Phys. Lett. B **461**, 43 (1999), arXiv:hep-ph/9904499 .
- [387] C. J. Copi and L. M. Krauss, Phys. Rev. D **63**, 043507 (2001).
- [388] B. Morgan, A. Green, and N. Spooner, Phys. Rev. D **71**, 103507 (2005), arXiv:astro-ph/0408047 .
- [389] E. Daw, *et al.*, Astropart. Phys. **35**, 397 (2012), arXiv:1010.3027 .
- [390] E. Daw, *et al.*, EAS Publ. Ser. **53**, 11 (2012), arXiv:1110.0222 .
- [391] K. Miuchi, *et al.*, Phys. Lett. B **686**, 11 (2010), arXiv:1002.1794 .
- [392] K. Miuchi, *et al.*, EAS Publ. Ser. **53**, 33 (2012), arXiv:1109.3099 .

- [393] Q. Riffard, *et al.*, “Dark matter directional detection with MIMAC,” (2013), arXiv:1306.4173 .
- [394] D. Santos, *et al.*, J. Phys.: Conf. Ser. **469**, 012002+ (2013), arXiv:1311.0616 .
- [395] J. Monroe (DMTPC Collaboration), EAS Publ. Ser. **53**, 19 (2012).
- [396] J. B. R. Battat (DMTPC Collaboration), J. Phys.: Conf. Ser. **469**, 012001+ (2013).
- [397] S. Vahsen, H. Feng, M. Garcia-Sciveres, I. Jaegle, J. Kadyk, Y. Nguyen, M. Rosen, S. Ross, T. Thorpe, and J. Yamaoka, EAS Publ. Ser. **53**, 43 (2012).
- [398] J. Billard, F. Mayet, and D. Santos, J. Cosmol. Astropart. Phys. **2012**, 006 (2012), arXiv:1202.3372 .
- [399] S. Burgos, *et al.*, Astropart. Phys. **31**, 261 (2008), arXiv:0809.1831 .
- [400] T. Naka, M. Kimura, M. Nakamura, O. Sato, T. Nakano, T. Asada, Y. Tawara, and Y. Suzuki, EAS Publ. Ser. **53**, 51 (2012), arXiv:1109.4485 .
- [401] S. Ahlen, *et al.*, Int. J. Mod. Phys. A **25**, 1 (2009), arXiv:0911.0323 .
- [402] D. S. M. Alves, S. E. Hedri, and J. G. Wacker, “Dark matter in 3D,” (2012), arXiv:1204.5487 .
- [403] M. Kuhlen, J. Diemand, P. Madau, and M. Zemp, J. Phys.: Conf. Ser. **125**, 012008+ (2008), arXiv:0810.3614 .
- [404] S. K. Lee, “Harmonics in the Dark-Matter sky: Directional detection in the Fourier-Bessel basis,” (2014), arXiv:1401.6179 .
- [405] C. McCabe, J. Cosmol. Astropart. Phys. **2014**, 027 (2014), arXiv:1312.1355 .
- [406] S. D. Biller and S. M. Oser, “Another look at confidence intervals: Proposal for a more relevant and transparent approach,” (2014), arXiv:1405.5010 .

- [407] A. Lewis and S. Bridle, “Parameter estimation using monte carlo sampling,” in *Bayesian Methods in Cosmology*, edited by M. P. Hobson, A. H. Jaffe, A. R. Liddle, P. Mukherjee, and D. Parkinson (Cambridge University Press, Cambridge, 2009) Chap. 3, pp. 57–78.
- [408] N. Metropolis, A. W. Rosenbluth, M. N. Rosenbluth, A. H. Teller, and E. Teller, *J. Chem. Phys.* **21**, 1087 (1953).
- [409] J. Skilling, in *BAYESIAN INFERENCE AND MAXIMUM ENTROPY METHODS IN SCIENCE AND ENGINEERING: 24th International Workshop on Bayesian Inference and Maximum Entropy Methods in Science and Engineering*, Vol. 735 (AIP, 2004) pp. 395–405.